AGB Evolution and Nucleosynthesis: Understanding the Uncertainties

Bryce Alexander Remple

München 2024

AGB Evolution and Nucleosynthesis: Understanding the Uncertainties

Bryce Alexander Remple

Dissertation
an der Fakultät für Physik
der Ludwig–Maximilians–Universität
München

vorgelegt von
Bryce Alexander Remple
aus Ortonville, MN, USA

München, den 17.12.2024

Erstgutachter: Prof. Dr. Achim Weiss
Zweitgutachter: Prof. Dr. Rolf-Peter Kudritzki
Tag der mündlichen Prüfung: 12.03.2025

Contents

List of Figures

List of Tables

Zusammenfassung

Diese Arbeit stellt eine umfassende Untersuchung der Unsicherheiten bei Sternentwicklungs- und Nukleosynthesemodellen für asymptotische Riesenaststerne (AGB) durch die Analyse von zwei Schlüsselprozessen der Nukleosynthese, dem intermediären und dem langsamen Neutroneneinfangsprozess (*i*-Prozess und *s*-Prozess), dar. Das Forschungsprojekt kombiniert die Modellierung der Sternentwicklung mit Berechnungen der Nukleosynthese, um unser Verständnis von der Produktion schwerer Elemente in Universum zu verbessern.

Zur Untersuchung des *i*-Prozesses wurde eine Reihe von Modellen mit unterschiedlichen Überschießenswerten und Massen betrachtet. Ein Protoneningestionsereignis (PIE) tritt in Sternen mit niedriger Masse und Metallizität auch ohne Überschießen auf. Ich entwickle und validiere ein neuartiges, auf einer Zeitskala basierendes Kriterium, um zu bestimmen, wann PIEs in Sternmodellen auftreten. Dabei stelle ich fest, dass diffusives Überschießen sowohl das Auftreten als auch die Eigenschaften von PIEs beeinflusst. Der Zeitpunkt der Aufspaltung der pulsgetriebenen Konvektionszone (PDCZ) während eines PIE wirkt sich entscheidend auf die chemische Zusammensetzung der Sternenoberfläche aus. Ein Vergleich der modellierten und beobachteten Elementhäufigkeiten zeigt, dass die Modelle zu viel Kohlenstoff produzieren und Schwierigkeiten haben, die Elementhäufigkeiten des ersten Peaks von CEMP-r/s-Sternen korrekt darzustellen. Eine wichtige Erkenntnis ist die Identifizierung von „fehlgeschlagenen" *i*-Prozessen als mögliche Erklärung für einige CEMP-r/s- und CEMP-s-Sterne, was auf ein differenzierteres Bild der Produktion schwerer Elemente in metallarmen AGB-Sternen hindeutet.

Des Weiteren wurde eine systematische Studie zur Nukleosynthese des *s*-Prozesses in 3-$M_{\odot}$-Sonnen-Metallizitäts-Modellen durchgeführt, in denen zentrale physikalische Aspekte verändert wurden. Die Ergebnisse zeigen, dass das Überschießen der konvektiven Hülle, die atomare Diffusion und die Wahl der Zustandsgleichung den größten Einfluss auf die Eigenschaften der ^{13}C-Tasche und die AGB-Entwicklung haben. Die Erträge an schweren Elementen weisen relativ geringe Schwankungen (innerhalb eines Faktors von 2) auf, während die Produktion leichter Elemente empfindlicher auf die physikalischen Eingangsgrößen reagiert.

Diese Ergebnisse liefern wichtige Einschränkungen für galaktische chemische Entwicklungsmodelle und zeigen Bereiche für zukünftige Forschungsprojekte auf, einschließlich der Notwendigkeit eines besseren Verständnisses der PDCZ-Aufspaltung des PIE und der Auswirkungen von Unsicherheiten der Kernrate und Mischungseffekten.

Abstract

This thesis presents a comprehensive investigation of the modeling uncertainties of asymptotic giant branch (AGB) stellar evolution and nucleosynthesis through the examination of two key nucleosynthetic processes: the intermediate and slow neutron-capture processes (*i*-process and *s*-process). The research combines stellar evolution modeling with detailed post-processing nucleosynthesis calculations to advance our understanding of heavy element production in the universe.

To study the *i*-process, I run a grid of models with different overshoot values and masses. A proton ingestion event (PIE) is found to occur in low-mass, low-metallicity stars even without overshoot. I develop and validate a novel timescale-based criterion for determining when PIEs occur in stellar models. I find that diffusive overshooting significantly influences both PIE occurrence and characteristics. The timing of the split of the pulse driven convection zone (PDCZ) during a PIE crucially affects the final surface abundances. Comparison of the modeled and observed surface abundances show that the models overproduce carbon and have difficulty in matching the first-peak element abundances of CEMP-r/s stars. A key finding is the identification of "failed" *i*-process events as a potential explanation for both some CEMP-r/s and CEMP-s stars, suggesting a more nuanced picture of heavy element production in metal-poor AGB stars.

Complementing the *i*-process investigation, I conducted a systematic study of *s*-process nucleosynthesis in 3 $M_{\odot}$, solar-metallicity models by varying key physics choices. The results reveal that convective envelope overshooting, atomic diffusion, and the equation of state have the greatest effect on the characteristics of the ^{13}C pocket and the AGB evolution. While heavy element yields show on average relatively modest variations (within a factor of 2), light element production demonstrates greater sensitivity to the input physics.

These findings provide important constraints and uncertainties for galactic chemical evolution models and highlight areas for future research, including the need for better understanding of the PDCZ splitting during the PIE, the impact of nuclear rate uncertainties, and the further exploration of mixing effects.

Chapter 1

Introduction

Non est ad astra mollis e terris via

Seneca, *Hercules Furens*

There are approximately 300 isotopes which are known to occur in nature and almost as many which are known to be present in the Sun. Figure 1.1 shows the solar abundance distribution up to lead (Pb). As one can see, there are a number of striking features to this distribution such as local peaks. The goal of explaining the origin of these isotopes and the features of this distribution has been a driving force for nuclear physics and astrophysics for nearly a century. The road to this lofty goal winds its way through the history of chemistry, astronomy and optics, nuclear physics, quantum mechanics, and astrophysics. The terminus of this road has not yet been reached, but our understanding of the origin of the elements has come a long way.

It is now understood that all the isotopes in the universe are forged in stars, with the exception of the H, He, and trace amounts of Li which were formed in the Big Bang and some light isotopes formed by cosmic ray spallation. In some cases these isotopes are created in the deep interiors of stars, in other cases they are born from the violent explosions which end a star's life, and in some cases both are true. Whatever the case may be for a specific isotope, an essential criterion is that its formation must be followed by an escape from the star and an incorporation into the interstellar medium (ISM), lest it be trapped in the compact objects, i.e. white dwarfs, neutron stars, and black holes, which populate the stellar graveyard. Once in the ISM, the isotopes can be incorporated into the next generation of stars or into the planetary bodies which can form around stars.

In this research a particular emphasis will be placed on the formation of elements heavier than iron. These elements are formed from a successive series of neutron captures on iron and other heavy elements followed by β^--decays, a decay in which a neutron turns into a proton and emits an electron and an anti-neutrino.

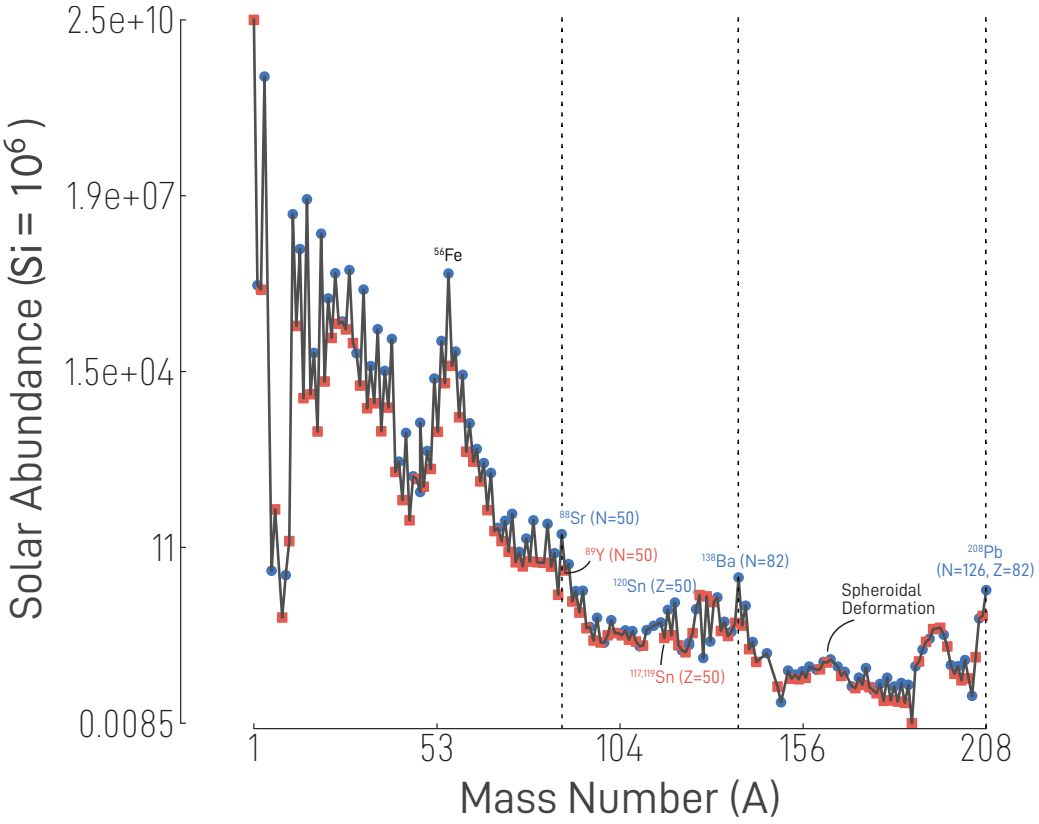

Figure 1.1 The solar abundance distribution in number of atoms relative to Si as given by Lodders (2021). Nuclei with even mass number are marked in blue and nuclei with odd mass number are marked in red. As is common practice, the abundances have been normalized such that Si has an abundance of 10^6. The annotations will be explained in the course of the work.

In this way one is able to form heavier and heavier elements as long as there is a sufficient number of neutrons. This requirement greatly limits the possible number of astrophysical sites where such nucleosynthesis processes could occur. Neutrons decay into protons in approximately 10 minutes under stellar conditions and, therefore, must be constantly produced in order for these neutron captures to occur. The efficiency of the neutron captures, which is directly tied to the neutron production efficiency, as compared to the β^--decays is used to categorize the neutron capture processes into three regimes: the slow neutron-capture process (*s*-process), the intermediate neutron-capture process (*i*-process), and the rapid neutron-capture process (*r*-process).

This investigation focuses specifically on the neutron-capture processes which occur in evolved stars of initial masses between 0.8 $M_\odot$–8.0 $M_\odot$. These so-called asymptotic giant branch (AGB) stars provide ideal conditions for neutron captures. At low metallicities they have the potential of activating the *i*-process, while at intermediate to high metallicities they are known to be a site for the *s*-process. Unfortunately, our lack of understanding of certain key physical processes, e.g.

convection and mass loss, introduce large uncertainties in the modeling of the *i*- and *s*-process in AGB stars.

Understanding the uncertainties in AGB stellar modeling is crucial for multiple fields of astrophysics. The nucleosynthetic yields from these stars provide essential input for galactic chemical evolution models, while their structural properties inform our understanding of stellar physics and constrain theories of convection and mass loss. Additionally, as the primary site of the *s*-process, AGB stars are key to explaining the observed abundances of roughly half of all elements heavier than iron (Kobayashi et al. 2020).

The goal of this work is to better understand how the uncertainties in our modeling of these poorly understood physical phenomena affects the evolution of these stars and the nucleosynthetic output of our simulations. To do this we will study the *s*-process and the *i*-process separately. For the *i*-process portion of this study, a grid of models was run with varying mass and overshoot values. These models were then post-processed to determine the heavy element nucleosynthesis. For the *s*-process a similar approach was used, though in this case the mass and metallicity were fixed and only the choice of physics was varied; the atmosphere treatment, opacity in outer layers, mass loss, equation of state, atomic diffusion, and overshoot values were all considered.

This thesis is organized as follows. Chapter 2 provides the prerequisite theoretical understanding for the entirety of what follows. Chapter 3 is a detailed history and literature review of the *s*-process, *i*-process, and AGB stellar evolution. While not exhaustive it does provide both the historical context of how we arrived at our current understanding of these phenomena as well as the more recent context needed to understand this works place in the current research landscape. Chapter 4 will delve into the numerical methods and codes which have been used. The results are split into two chapters, Chapter 5 and Chapter 6, covering the *i*- and *s*-process, respectively. Finally, the conclusions will be presented in Chapter 7. A list of acronyms used in this work can be found in Appendix A.

Chapter 2

Theory

Die Sonne strahlt bekannter Weise
In polytroper Sphären Glanz
Und ihre vorgeschreib'ne Reise
Bestätigt meine Formeln ganz.
Ihr Anblick gibt Lemaitre Stärke,
Wenn keiner sie ergründen mag.
Die unbegreiflich hohen Werke
Sind herrlich wie am ersten Tag.

The Character of Prof. Eddington,
Faust. Eine Historie

In 1926, Arthur Eddington published a series of lectures named "*Stars and Atoms*" (Eddington 1927). In the beginning of the first chapter he briefly addresses the audience directly:

> From his central position man can survey the grandest scales of Nature with the astronomer, or the minutest works with the physicist. To-night I ask you to look both ways. For the road to a knowledge of the stars leads through the atom; and important knowledge of the atom has been reached through the stars. (Eddington 1927)

The current landscape of AGB stars and their nucleosynthesis was formed by the research, theories, and observations from both fields: astrophysics and nuclear physics. I will begin this chapter with a overview of nuclear physics, then move on to stellar evolution, and finally discuss observations. In all sections the discussion will be limited to only those concepts which are necessary for the understanding of the current work. Readers can consult the references therein for more details on specific topics.

2.1 Nuclear Physics

All atomic nuclei consist of protons and neutrons, known collectively as nucleons. The number of neutrons in the nucleus, denoted by N, and the *atomic number*, or number of protons in the nucleus, denoted by Z, together uniquely identify a nucleus' species. The sum of Z and N gives one the total number of nucleons in the nucleus and is called the *mass number*, denoted by A. Any particular nuclear species is referred to as a *nuclide*. Nuclides with the same proton number all belong to the same element. Isotopes are distinct nuclides of the same chemical element. Thus, they share a common atomic number but have a different number of neutrons.[1]

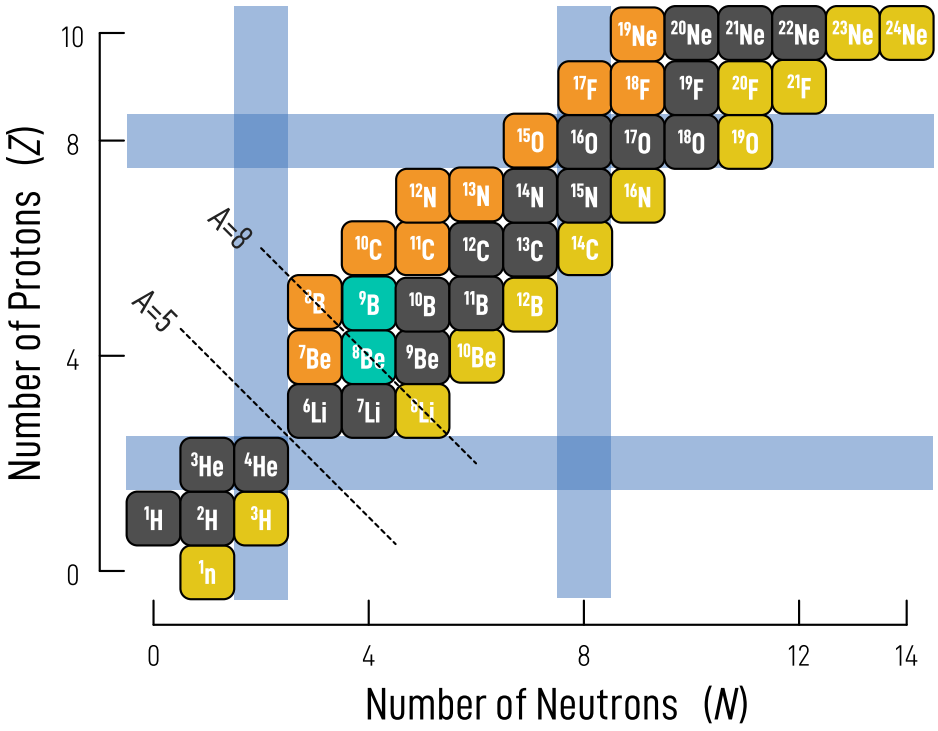

Figure 2.1 A Chart of nuclides for $N \leq 14$ and $Z \leq 10$. Nuclides which are colored in black are stable, those in yellow decay via β^--decay, those in orange decay via β^+-decay, and those in turquoise decay via α-decay. The blue shaded regions denote magic numbers.

Nuclides can be nicely visualized by plotting them on what is called the *chart of nuclides*. Figure 2.1 is an example of such a chart where isotopes colored in gray are stable, those in yellow decay via β^--decay, those in orange decay via β^+-decay, where a proton is converted to a neutron and emits a positron and a neutrino, and those in turquoise decay via α-decay, which is the emission of a He nucleus. As one can see, nuclides are plotted based on the number of protons

[1] The references for this section will be Iliadis (2007, Ch. 1) and Kippenhahn et al. (2013, Ch. 18) unless otherwise stated

and neutrons they have with the x-axis showing the run of neutron number and the y-axis showing the run of proton number. Isobars, or lines of constant atomic weight, lie along diagonal lines from lower right to upper left. Analyzing charts like this can provide useful insights. For instance, here one can see that there are no stable isotopes along the isobars with a mass number of 5 or 8 — we will return to this point in the next chapter. In the course of this section we will return to this figure a few times and explain more of its concepts.

Another property of the atomic nucleus, and, in fact, the most fundamental one, is its mass. Measurements of atomic nuclei showed that, contrary to what one would expect, the rest mass of a nucleus, m_{nuc}, is less than the sum of the mass of its constituents, i.e.

$$m_{\mathrm{nuc}} = Zm_{\mathrm{p}} + Nm_{\mathrm{n}} - \Delta m, \tag{2.1}$$

where m_{p} is the mass of the proton, m_{n} is the mass of the neutron, and Δm is known as the *mass defect*. According to Einstein's famous equation one can relate this mass defect to an equivalent energy: $\mathrm{BE} = \Delta E = \Delta mc^2$. This energy, BE, is referred to as the *binding energy* of the nucleus which is a measure of the energy it would take to separate a given nucleus into its constituent nucleons. Thus, the binding energy is intimately related to the stability of a nucleus. The binding energy can also be written as

$$\mathrm{BE}(Z,N) = \left(Zm_{\mathrm{p}} + Nm_{\mathrm{n}} - m_{\mathrm{nuc}}\right)c^2.$$

A plot of binding energy per nucleon versus mass number can be seen in Figure 2.2. Notice that the most tightly bound isotopes are around ^{56}Fe (^{62}Ni and ^{58}Fe have higher binding energies per nucleon but are not plotted in this figure). These isotopes make up what is known as the "iron peak". On either side of this peak the binding energies decrease.

There are a number of theoretical models to explain the characteristics of nuclei. One of the most famous is known as the *shell model*. A proper derivation of the shell model is beyond the scope of this work, but a brief discussion is in order. Conceptually, the nuclear shell model is the nuclear analogue of the atomic shell model, which is very successful in describing the properties of atoms. In the case of the atomic shell model the nucleus represents the heavy center of a Coulomb field in which electrons move. If one solves Schrödinger's equation for this system it describes a series of shells characterized by various quantum numbers that set the properties for these shells: energy, how many electrons can occupy each shell, etc.

Attempting to apply this conceptual model to the nucleus comes with complications. For one, there are two types of elementary particles involved, protons and neutrons, as opposed to just one, electrons. Also, nuclear interactions are not governed by the Coulomb force, but rather the strong force, so the potential is not

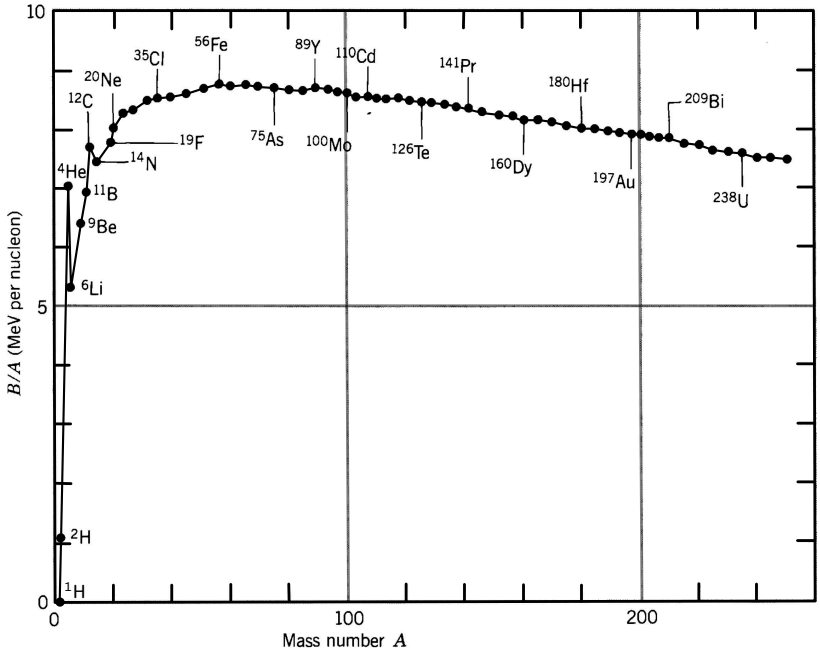

Figure 2.2 Binding energy per nucleon versus mass number from Krane & Halliday (1987), slightly modified by me.

known precisely. The basic assumption of the shell model is that the interaction of one nucleon with all other nucleons can be approximated by some average potential. Nevertheless, this theory is very successful in describing a number of properties of nuclei.

One key feature which is apparent when this theory is applied is, just as there are particularly stable configurations in the atomic shell model when electron shells are full (the noble gasses), there are particularly stable configurations in the nuclear shell model when a nucleus' major shells are full. This happens when the number of protons or neutrons in a nucleus is 2, 8, 20, 28, 50, 82, and 126. These are called the *magic numbers*. If a nucleus has a magic number of both protons and neutrons, then it is known as being doubly magic. Looking again at Figure 2.1, the light blue regions denote magic numbers. As one can see, ^{16}O is a doubly magic nuclide as it has 8 protons and 8 neutrons. The list of stable magic number nuclei can be found in Table 2.1 and some are also labeled in Figure 1.1 along with their magic number(s) in parentheses. It should stressed that just because a nucleus is magic or even doubly magic does not mean that it is stable, only that it is more stable than would otherwise be expected. ^{56}Ni is a good example of a nucleus which is doubly magic but nevertheless decays with a relatively short half-life. The increased stability of magic-number isotopes is responsible for the abundance peaks after Fe in the solar abundance distribution marked by the dotted lines in Figure 1.1.

An alternate theory of the nucleus also exists. The *liquid drop model* models

the forces on the outermost nucleons of the nucleus similarly to the modeling of surface tension in a water droplet. These two models of the nucleus can broadly be placed into two categories based on which of the following two fundamental assumptions are made: the nucleus can be described as a collection of nucleons freely moving in an average potential (shell model), or each nucleon feels the force of all other individual nucleons in the nucleus forming a sort of coupling between all nucleons (liquid drop model). Both theories are able to accurately describe certain phenomenon. For example, as we have just discussed, the shell model describes the stability of the magic-number isotopes. The liquid drop model on the other hand can be used to explain the properties of nuclei of very high mass and away from the magic numbers. The abundance "hill" labeled "spheroidal deformation" in Figure 1.1 can be explained with this theory. Far from a closed shell the nucleus may be significantly deformed as can be ascertained from measurements of quadrupole moments and rotational level structure (Bohr & Mottelson 1953a,b, Nilsson 1955). This spheroidal deformation results in lower energy levels for extra neutrons and thus more stable nuclei which explains the increased abundance of the nuclei with mass number around 160 (Burbidge et al. 1957).

Having established some foundational knowledge of the nucleus, we will now move onto discussing nuclear reactions. A *nuclear reaction* is simply a process through which at least one nuclide is transformed into another. Imagine a nuclear reaction involving four nuclei. One nucleus of species 1 and one of species 2 interact to form one nucleus of species 3 and one of species 4. One can write this reaction as

$$1 + 2 \rightarrow 3 + 4 \qquad \text{or} \qquad 1\,(2,\,3)4.$$

In the event that species 1 and 2 are identical to species 3 and 4, then the interaction is called a *scattering*. Otherwise, the interaction is a nuclear reaction. Species 1 and 2 are called the *reactants* and species 3 and 4 the *products*.

One of the primary properties of a nuclear reaction is how much energy it produces or requires. If a reaction produces/requires energy it is known as an *exothermic/endothermic* reaction. The energy of the reaction, commonly referred to as the reaction's *Q-value*, can be calculated via

$$Q_{1\,(2,3)4} = \left(\mathrm{BE}_3 + \mathrm{BE}_4\right) - \left(\mathrm{BE}_1 + \mathrm{BE}_2\right). \tag{2.2}$$

Therefore, the reactants must have less binding energy than the products for the reaction to generate energy. Given what we know about the iron peak this means that for isotopes lighter than ^{56}Fe nuclear fusion will produce energy, whereas for isotopes heavier than ^{56}Fe nuclear fusion will require energy input. This can be seen graphically in Figure 2.2. Additionally, the slope of the binding energy curve is steepest for lightest isotopes meaning that fusing the lightest isotopes

Table 2.1 The stable magic number nuclides. Nuclides in bold are doubly magic and therefore appear once under both the "Protons" and "Neutrons" headings.

2	8	20	28	50	82	126
			Protons			
^{3}He	**^{16}O**	**^{40}Ca**	^{58}Ni	^{112}Sn	^{204}Pb	
^{4}He	^{17}O	^{42}Ca	^{60}Ni	^{114}Sn	^{206}Pb	
	^{18}O	^{43}Ca	^{61}Ni	^{115}Sn	^{207}Pb	
		^{44}Ca	^{62}Ni	^{116}Sn	**^{208}Pb**	
		^{46}Ca	^{64}Ni	^{117}Sn		
		^{48}Ca		^{118}Sn		
				^{119}Sn		
				^{120}Sn		
				^{122}Sn		
				^{124}Sn		
			Neutrons			
^{4}He	^{15}N	^{36}S	**^{48}Ca**	^{86}Kr	^{136}Xe	**^{208}Pb**
	^{16}O	^{37}Cl	^{50}Ti	^{87}Rb	^{138}Ba	^{209}Bi
		^{38}Ar	^{51}V	^{88}Sr	^{139}La	
		^{39}K	^{52}Cr	^{89}Y	^{140}Ce	
		^{40}Ca	^{54}Fe	^{90}Zr	^{141}Pr	
				^{92}Mo	^{142}Nd	
					^{144}Sm	

together, say protons to ^{4}He, will generate more energy than fusing two ^{12}C nuclei to generate ^{24}Mg.

In order for the reaction to take place at all the nuclei of species 1 and 2 must be brought close enough together that the strong but short-ranged nuclear forces dominate over the weaker but farther-reaching Coulomb force. The nuclei, being both positively charged, will resist this. The picture is sketched in Figure 2.3. Without loss of generality we will for now assume the stationary rest frame of the nucleus of species 1 which has a charge Z_1. The nucleus of species 2 with charge Z_2 approaches 1 with an energy E. If we assume the nuclear force will begin to dominate at a distance r_0 from 1 then the *Coulomb barrier* which nuclei 2 must overcome is approximately $V_c = Z_1 Z_2 e^2 / r_0$. In a star the energy of the incoming nuclei is a result of its kinetic energy from thermal motion, hence, why these reactions are referred to as *thermonuclear reactions*. However, if one estimates the average kinetic energy of a nucleus at the temperature at the center of the Sun, roughly $T \approx 10^7$ K, then one finds that it is a factor of 10^3 smaller than the Coulomb barrier. Since there are a distribution of kinetic energies in an ideal gas of a particular temperature, one could turn the question around and ask what the probability is of finding a particle in the high-energy tail of the Maxwell-

Boltzmann distribution which has the energy to overcome the Coulomb barrier. Unfortunately, at this energy, the exponential factor of the Maxwell-Boltzmann distribution drops to $e^{-1000} \approx 10^{-434}$. This means that even given the some 10^{57} nuclei in the Sun, there is effectively no chance for a nuclear reaction to take place. Yet, we know they happen.

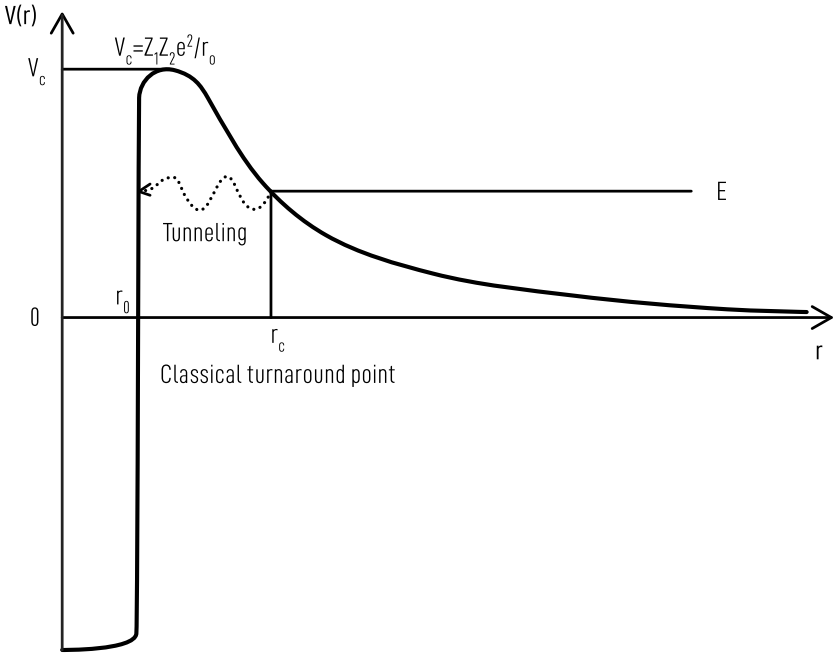

Figure 2.3 A diagram depicting quantum tunneling and the Coulomb barrier. V_c is the maximum of the Coulomb potential, r_c is the classical turn around point for a particle with energy E, and r_0 is the distance from the nucleus at which the nuclear forces exceed the Coulomb force.

The way out of this predicament came from quantum mechanics and George Gamow. Quantum mechanics allows for a small but finite probability that a particle will penetrate or "tunnel" its way through the Coulomb barrier despite having an energy that is classically not sufficient to overcome it. The probability, P, for this to happen is

$$P \propto E^{-1/2} e^{-2\pi\eta}\,, \qquad \text{where } \eta = \left(\frac{m}{2}\right)^{1/2} \frac{Z_1 Z_2 e^2}{\hbar E^{1/2}} \tag{2.3}$$

is called the Sommerfeld factor, E is the relative kinetic energy of nucleus 1 and 2, and m is the reduced mass of nucleus 1 and 2. If one assumes $Z_1 Z_2 = 1$ and $T \approx 10^7$K, then P is of the order 10^{-20}. Since $P \propto e^{Z_1 Z_2}$, in order to burn heavier nuclei one needs higher temperatures. This results in the well separated burning phases we know from stars.

To see if the tunneling probability is large enough to allow for reactions to occur one can take the product of the tunneling probability distribution and the

Maxwell-Boltzmann distribution to get the true probability of a reaction taking place. This is shown in Figure 2.4. The tunneling probability is plotted with a dot-dashed line and the Maxwell-Boltzmann distribution with the dashed line. The product of the two is shown in the solid line. The peak in the product of the two distributions is known as the *Gamow peak* and gives an estimate of the energy, and thus the temperature, at which a reaction is likely to take place in a star.

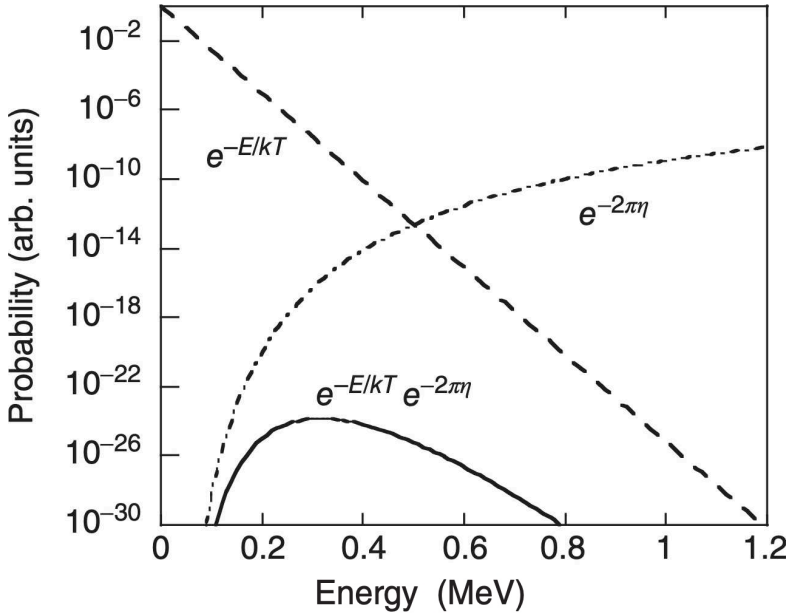

Figure 2.4 Panel a of Figure 3.13 from (Iliadis 2007). See text for description

So we have now seen that nuclear reactions depend on the energy of the reactants (which in stars is directly tied to the temperature of the plasma) and the charge of the reactants. Theory gives a good understanding of how and why certain reactions are or are not probable, but to quantitatively determine the probability one relies on experiment whenever possible. In experiments the probability that an interaction will occur is called the *cross-section* of the interaction. To determine cross-sections an experimentalist needs three things: a beam of particles, a target, and a detector. If the reaction being studied is 1 (2, 3)4, then a beam of particles of species 1 would be shot at a target made ideally 100% of particles of species 2 and the detector would be set to detect particles of species 3 or 4. The cross-section, σ, would then be

$$\sigma = \frac{R}{I_1 N_2}$$

where R is the rate of detections, I_1 is the number of particles of species 1 incident on the target per unit time per unit area, and N_2 is the number of particles of species 2 that are exposed to the beam. σ then has dimensions of area and is reported with the unit barn (b)[2] where $1\,\mathrm{b} = 100\,\mathrm{fm}^2$. While this clearly means

the cross-section is not exactly the probability of a reaction occurring, the two are proportional. It should also be noted that the cross-section will depend on the energy of the particles in the beam. Thus, this experiment must be done for a range of energies to see how the cross-section would change at different energies (and thus temperatures in a star). In Figure 2.5 one can see a sketch of what a plot of cross-section against energy might look like.

As one can see from the cross-section curve, it generally is a smooth curve but it also has peaks. These peaks are called *resonances*. To discuss this a small digression must first be made to the topic of the Bohr picture of the nucleus (Bohr 1936). In this picture the nuclear reaction can be seen as consisting of two steps. First, a nucleus of species 1 and one of species 2 form a *compound nucleus*, C^*, which is always formed in an excited state, denoted by the $*$ in the exponent. The compound nucleus is assumed to be excited as it has not only the binding energy of 1 and 2 but also their kinetic energies. Second, C^* decays via a particular "channel". The primary assumption of the Bohr picture is that the first and second step are independent of one another and the channel in which C^* decays only depends on the properties of C^* and not on how it was formed. Possible decay channels are shown below. (Weiss et al. 2004)

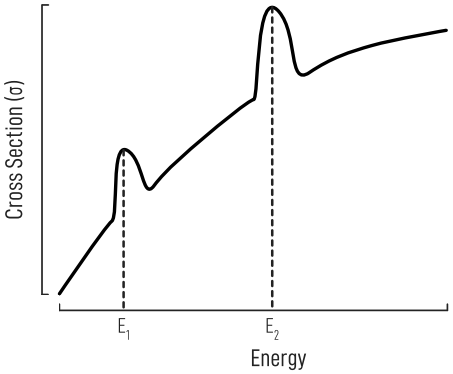

Figure 2.5 A hypothetical cross-section versus energy curve. E_1 and E_2 mark resonant energies. Based on Figure 18.4 in Kippenhahn et al. (2013)

$$1+2 \rightarrow C^* \begin{cases} 1+2 & \text{Elastic Scattering} \\ 3+4 & \text{Particle Emission} \\ \vdots & \\ C+\gamma & \gamma\text{-ray emission} \end{cases}$$

Via which channel C^* decays will depend on a number of factors, one of which being the energy levels of the C^* nuclei from nuclear shell theory. Looking at Figure 2.6, one can see that, for the compound nucleus C^*, the energy it would take to remove a nucleon from the ground state is E_{min}. The energy levels below E_{min} in energy can only decay via γ-emission which is unlikely. Thus, these states are referred to as *stationary states*. However, if a particle's energy is above E_{min} it will not necessarily be expelled immediately. The sharp rise of the Coulomb

[2]The name "barn" was established by scientists in the Manhattan Project after other potential candidates including "Oppenheimer", "Bethe", and "Manly" were excluded for various reasons (Baker & Holloway 1947). The name is meant to reflect the fact that the barn is a very large area for nuclear purposes.

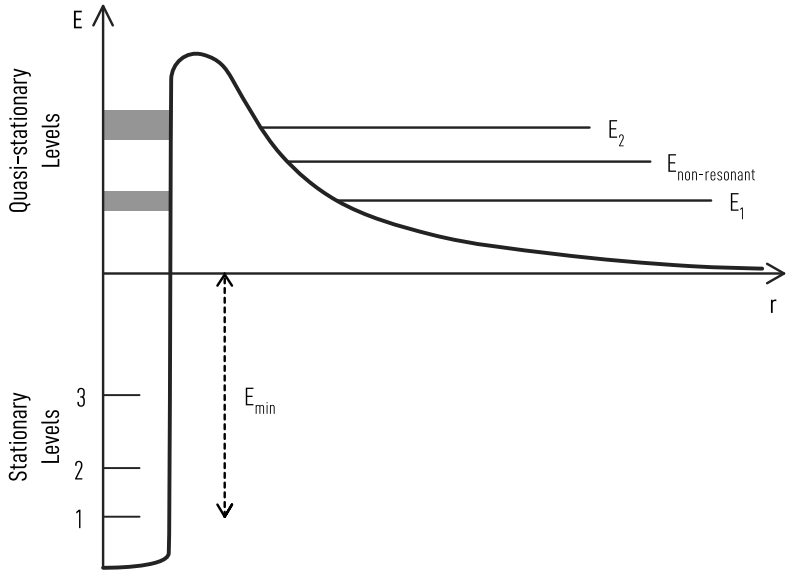

Figure 2.6 A sketch of energy levels in a compound nucleus C^*. The energy levels E_1 and E_2 correspond to the same energies as in Figure 2.5. $E_{\text{non-resonant}}$ marks one of many non-resonant energies. See text for more details. Based on Figure 18.3 in Kippenhahn et al. (2013).

potential still acts like a wall for particles on the left side just as it does for those on the right. These particles can exist in these *quasi-stationary levels* for some time, but eventually the particles will escape via tunneling. These quasi-stationary states lead to these peaks in the cross-section curve which we set out to explain. For example, to form C^* from 1 and 2 with gradually increasing energy E of their relative motion, the tunneling probability will increase according to Equation (2.3) as long as E does not correspond to a quasi-stationary level. If, however, E does correspond to a quasi-stationary level, then the colliding particles find a resonance and can form C^* much more easily. At these resonant energies the reaction probability is enhanced by orders of magnitude.

Now that the requisite concepts have been laid out, the time has come to discuss thermonuclear reaction rates. Again the reaction 1 (2, 3)4 will be considered. Suppose that one charged particle of species 1 is moving with a velocity v relative to all charged particles[3] of species 2. If there are n_2 particles of species 2 per unit volume and the cross-section for the reaction is σ, then it is easy to see that the rate per unit volume at which a particle of species 1 will interact with a particle of species 2 is $n_2\sigma v$. If we now assume that there is not only one particle of species 1 but rather n_1 particles of species 1 per unit volume then

$$r_{12} = n_1 n_2 \sigma v,$$

[3]If one of the reactants has no charge, i.e. a photon or a neutron, then the Coulomb barrier need not be overcome and the general picture changes.

where r_{12} is the *reaction rate per pair of particles* and n_1 is the *number density* of species 1. However, this does not account for the case where species 1 and 2 are the same. In this case the number of unique particle pairs is given by

$$\frac{n_1(n_1-1)}{2} \approx \frac{n_1 n_1}{2},$$

where the approximate equality holds in the limit of large particle numbers (a safe assumption in our case). Substituting that into the equation for r_{12} yields

$$r_{12} = \frac{1}{1+\delta_{12}} n_1 n_2 \sigma v \ ,$$

where δ_{12} is the Kronecker delta function,

$$\delta_{12} = \begin{cases} 0, & \text{species 1} \neq \text{species 2} \\ 1, & \text{species 1} = \text{species 2} \end{cases}.$$

Without this extra factor one would be double counting particles when species 1 and 2 are the same. This would effectively be allowing for the nucleus to interact with itself to form heavier nuclei.

At this point one of our assumptions must be removed as it is incorrect. It was assumed that all particles of species 1 move with relative velocity v. Because σ depends on v, this is a critical assumption. A more realistic assumption is that the relative velocities of the particles follow a Maxwell-Boltzmann distribution. Switching from v to E, one finds that the fraction of all particle pairs in the energy interval $[E, E+\mathrm{d}E]$ is

$$f(E)\mathrm{d}E = \frac{2}{\sqrt{\pi}} \frac{E^{1/2}}{(kT)^{3/2}} e^{-E/kT} \mathrm{d}E.$$

To get the reaction rate per unit time and volume one must integrate over all energies:

$$r_{12} = \frac{1}{1+\delta_{12}} n_1 n_2 \int_0^\infty \sigma(E) v \, f(E) \mathrm{d}E.$$

The integral itself is an important quantity called the *average cross-section* or the *reactivity* which is denoted as

$$\langle \sigma v \rangle = \int_0^\infty \sigma(E) v \, f(E) \mathrm{d}E.$$

The final quantity which is not yet known is $\sigma(E)$. A derivation of this quantity will not be done here (interested readers can find an in depth derivation in Weiss et al. (2004, Sec. 17.11)) and instead the result will simply be stated as

$$\sigma(E) = \frac{S}{E} e^{-2\pi\eta}.$$

where the exponential quantity comes from the tunneling probability, η is the same as defined in Equation (2.3), and S is known as the astrophysical cross-section factor or the *astrophysical S-factor*. This factor contains all of the intrinsic nuclear properties of the particular reaction at hand. In theory it can be calculated, but one rather relies on experimental measurements when possible. Measurements of S are not always possible. Even when it is possible, it can only be done at very high energies since the cross-sections are too low at low energies to be accurately measured in terrestrial laboratories. This means that the energies for which S is known are much higher than those of astrophysical relevance. Thus, the experimental data for S must be extrapolated down to the low energies relevant for stars. This can be done reliably for non-resonant reactions as S is nearly constant with energy in this case. If, however, there are resonances, known or unknown, in the lower energies, then S can vary greatly with energy, and the results can be uncertain. Finally, we have arrived at the final expression for the average cross-section for the case of non-resonant reactions,

$$\langle \sigma v \rangle = \frac{2^{3/2}}{(m\pi)^{1/2}} \frac{1}{(kT)^{3/2}} \int_0^\infty S(E) e^{-E/kT - \bar{\eta}/E^{1/2}} \mathrm{d}E,$$

where

$$\bar{\eta} = 2\pi\eta E^{1/2},$$

and η, once again, is the same as defined in Equation (2.3). m is the reduced mass of particles 1 and 2 and comes from replacing v with E via $E = \frac{1}{2}mv^2$. If there are resonances more work must be done to get an accurate cross-section. Luckily, the stellar physicist need not calculate this quantity. $\langle \sigma v \rangle$ is measured experimentally and provided in large databases such that in practice one needs only the following rate equation:

$$r_{12} = \frac{1}{1+\delta_{12}} n_1 n_2 \langle \sigma v \rangle_{12}. \tag{2.4}$$

There is only one factor missing from our rate equation, but it can make a large difference in the rate: *electron screening*. In most regions of the star the nuclei are largely or fully ionized meaning that there are many free electrons in the stellar plasma. At high densities each nucleus tends to attract neighboring electrons due to their positive charge and forms a negative “charge cloud” around it. From the perspective of a second nearby nucleus this charge cloud partially shields the positive charge of the first nucleus and lowers the peak of the Coulomb barrier. Hence, the reaction rate for that reaction will be higher than if one ignored

this effect.

Electron screening can be taken into account by simply multiplying the reaction rate by a screening factor,

$$f = e^{U_0/kT}, \text{ where } U_0 = Z_1 Z_2 e^2 / r_D.$$

This is only valid in the so-called "weak screening limit" as first defined by Salpeter (1954), where the electrostatic energy between the particles when r_D apart is less than the mean thermal energy per particle. r_D is the Debye length and can be thought of as approximately the radius of the charge cloud. For the remainder of this work the factor f will be omitted from the equations as is customary, but it must be stressed that f is not included in the reactivity values which one finds in the nuclear databases and as such must be computed separately for each reaction involving charged particles and for each temperature.

With the tools to calculate rates one might logically next want to determine how the abundances of the reactants and products would change over time given a particular reaction rate. Again, using our canonical hypothetical reaction 1 (2, 3)4, let us consider what the change of the abundance of species 1 would be. The amount of particles of species 1 should be decreasing since it is a reactant, and it should depend on the amount of particles of species 1 and 2 since without those particles the reaction cannot take place. Finally, it should depend on the cross-section of the reaction. Putting that together one gets

$$\frac{\mathrm{d}\mathrm{Y}_1}{\mathrm{d}t} = -\frac{1}{1+\delta_{12}} \rho N_A \mathrm{Y}_1 \mathrm{Y}_2 \langle \sigma v \rangle_{12}$$

which of course is just the rate expression from Equation (2.4) with a negative sign since the abundance of species 1 is decreasing. The Y's are mole fractions, defined as $\mathrm{Y}_1 = n_1/(\rho N_A)$, where N_A is Avogadro's number. The *mole fraction* of the isotopes is used instead of the mass fraction or number density as it is insensitive to changes in mass density, i.e. compression or expansion of the stellar gas, which is not true of the mass fraction or the number density.

As a brief aside, we have now encountered three different ways of expressing the abundance of a species of nuclides: number density, mass fraction, and mole fraction. The mole fraction was just defined, and you will recall that number density is the number of particles of species i per unit volume and is denoted as n_i or N_i. The *mass fraction* of species i is the fraction of the total mass which is due to the mass of all particles of species i. It is defined as

$$X_i = \frac{n_i M_i}{\rho N_A},$$

where M_i is called the *relative mass fraction* of species i and is calculated via $M_i = m_{\mathrm{nuc},i}/m_u$ and m_u is the *unified atomic mass unit*. m_u is defined as one-

twelfth the mass of an atom of ^{12}C. Since neutrons and protons have very nearly the same amount of mass (the neutron is about 0.2% less massive) and electrons have about four orders of magnitude less mass, m_u is effectively the mass of a nucleon, and M_i is approximately the isotope's mass number.

Up until now we have always assumed that a reaction involves two reactants and two products. This is not always the case: a β-decay only has one reactant, for example. Triple body reactions are also possible. The above equation can be expanded to allow for this,

$$\frac{\mathrm{d}Y_i}{\mathrm{d}t} = \sum_j C^i_j Y_j + \sum_{j,k} C^i_{j,k} \rho N_A Y_j Y_k \langle \sigma v \rangle_{j,k} + \sum_{j,k,l} C^i_{j,k,l} \rho^2 N_A^2 Y_j Y_k Y_l \langle \sigma v \rangle_{j,k,l}, \quad (2.5)$$

where

$$\begin{aligned} j,k,l,i &\text{ may be n, p, } \alpha, \gamma, e^{+,-}, \nu, {}^{12}\mathrm{C}, \text{ etc.} \\ C^i_j &= c_i \\ C^i_{j,k} &= c_i / \left(1+\delta_{j,k}\right)! \\ C^i_{j,k,l} &= c_i / \left(1+\delta_{j,k}+\delta_{j,l}\right)! \,. \end{aligned}$$

In Equation (2.5) I have switched from numbers to letters for the indices to indicate the generality of this expression (it is not only valid for the reaction 1(2,3)4). The $C^i_{j,k}$ ($C^i_{j,k,l}$) terms handle the double counting issue when $j = k$ ($j = k$, or $k = l$, or $l = j$, or $j = k = l$). The c_i's themselves specify how many particles of species i are created or destroyed in a reaction. It is also important to note that the c_i's, and thus the $C^i_{j,k}$'s and $C^i_{j,k,l}$'s, can be positive or negative depending on whether the isotope i is created or destroyed. For example, in a $^{12}\mathrm{C} + {}^{12}\mathrm{C}$ reaction $C^{^{12}\mathrm{C}}_{^{12}\mathrm{C},^{12}\mathrm{C}} = -2/2$.

Naturally, one wants to follow the change of the abundance of all species in the reaction. Thus, one has many of these equations; one for each species to be considered. This creates a stiff system of coupled differential equations. In practice, a stiff numerical system is one for which the time evolution of different components of the system are described by a wide range of timescales. To get a sense for how stiff this system of equations is one can consider the first two reactions of the *pp*-chain, the process by which the Sun produces its energy. The first reaction of the *pp*-chain, $^1\mathrm{H}(\mathrm{p}, e^+ + \nu)^2\mathrm{H}$, has a reaction timescale on the order of 10 billion years. Step two of the *pp*-chain, $^2\mathrm{H}(\mathrm{p}, \gamma)^3\mathrm{He}$ has a timescale of just seconds. Hence, even for the Sun, the timescales involved in nuclear burning can differ by over 17 orders of magnitude!

Such a stiff system must be solved via an implicit numerical scheme. Commonly,

this is done via the backward Euler method combined with a Newton-Raphson method (Hix & Meyer 2006). That works as follows. From the backward Euler method one has the usual equation:

$$\frac{\mathrm{Y}(t+\delta t)-\mathrm{Y}(t)}{\Delta t} = \dot{\mathrm{Y}}(t+\Delta t). \tag{2.6}$$

Rearranging this equation one can cast it into a root finding problem,

$$Z = \frac{\mathrm{Y}(t+\delta t)-\mathrm{Y}(t)}{\Delta t} - \dot{\mathrm{Y}}(t+\Delta t) = 0, \tag{2.7}$$

which can be solved via the Newton-Raphson method. The change in the abundances is then

$$\Delta \mathrm{Y} = (J_Z)^{-1} Z, \tag{2.8}$$

where the terms of J_Z, the Jacobian of Z, are

$$J(i,j) = \frac{\delta_{ij}}{\Delta t} - J_{\dot{\mathrm{Y}}}(i,j), \tag{2.9}$$

where Δt is the time step and δ_{ij} is the Kronecker delta function. $J_{\dot{\mathrm{Y}}}$, the Jacobian of $\dot{\mathrm{Y}}$, is calculated in the usual fashion as

$$J_{\dot{\mathrm{Y}}}(i,j) = \frac{\partial \dot{\mathrm{Y}}_\mathrm{i}}{\partial \mathrm{Y}_\mathrm{j}}, \tag{2.10}$$

where the first index runs over all reactants and products and the second index runs over all reactants.[4] Once the change in abundance has been calculated, the energy generation rate of all the nuclear reactions can be calculated via

$$\epsilon_\mathrm{nuc} = \sum_i \frac{\mathrm{dY}_i}{\mathrm{d}t} M_{\mathrm{exc},i} N_A c^2, \tag{2.11}$$

where $M_{\mathrm{exc},i}$ is the mass excess of species i and is equal to

$$M_{\mathrm{exc},i} = m_{\mathrm{nuc},i} - A_i m_u. \tag{2.12}$$

A program which solves these equations is called a *nuclear network*. Nuclear networks are contained in all modern stellar evolution codes. Depending on what stars one is interested in modeling and how detailed one wants to investigate the nucleosynthesis, the nuclear network will track the abundances of tens, hundreds, or even over a thousand isotopes. The time it takes to solve the equations increases quickly, as $\mathcal{O}\left(n^3\right)$, with increasing number of isotopes, n (Hix & Meyer 2006).

[4] This is technically not true. The second index also runs over all the reactants and products as well, but, as the mole fraction of the products does not enter into the equations for $\dot{\mathrm{Y}}$, the derivatives with respect to product mole fraction are all zero.

Moreover, this system of equations must be solved at least once per grid point where nuclear burning is happening and per time step in a stellar model. This means that the nuclear network can greatly slow down the stellar evolution code if one wants to track many isotopes at a time.

One way around this is to use a *post-processing* code. A post-processing code takes the thermodynamic output from a stellar evolution code with a small nuclear network as input for a nucleosynthesis calculation using a much larger nuclear network. In the post-processing approach the thermodynamic input is considered as fixed. No feedback of the assumed mixing processes or energy release by the reactions considered in the post-processing calculation on the stellar structure is possible. Because of this, all reactions which are important for the energy generation, and thus which affect the stellar structure, must be included in the nuclear network in the stellar evolution code and any reactions that are considered in the post-processing are assumed to be energetically irrelevant. More information on the detailed workings of a post-processing code will be given in Section 4.2. Some form of post-processing has been in use since at least Peters (1968) who used it to calculate the nucleosynthesis of the weak component of the *s*-process. A key to the method becoming more popular were the papers of Arnett & Truran (1969) and Wagoner (1969) wherein efficient algorithms for solving the nuclear network equations were developed. After this, a number of studies utilized these algorithms to calculate the nucleosynthesis of the *s*-process (Shorin et al. 1971, Peters et al. 1972, Couch et al. 1974). To the best of my knowledge the first application of post-processing to *s*-process calculations on the AGB is the work of Truran & Iben (1977).

While this approach does introduce some inconsistencies it allows for following large numbers of isotopes. Due to modern computational speeds as well as better algorithms for solving stiff equations and taking advantage of the sparseness of the matrix formed from the system of equations, large networks can now be implemented directly in stellar evolution codes (the interested reader should consult Timmes (1999) for a comparison of the different solving methods as well as the advantages of sparse algorithms). Nevertheless, there are still computational efficiency advantages to using a post-processing code.

2.2 Stellar Evolution

In the following section the aspects of stellar evolution as it relates to this thesis will be discussed. It is assumed that the reader has a basic understanding of stellar evolution and, as such, some details will be skipped. This includes the stellar structure equations. If a topic is unfamiliar Kippenhahn et al. (2013) is

a standard reference for stellar evolution.[5]

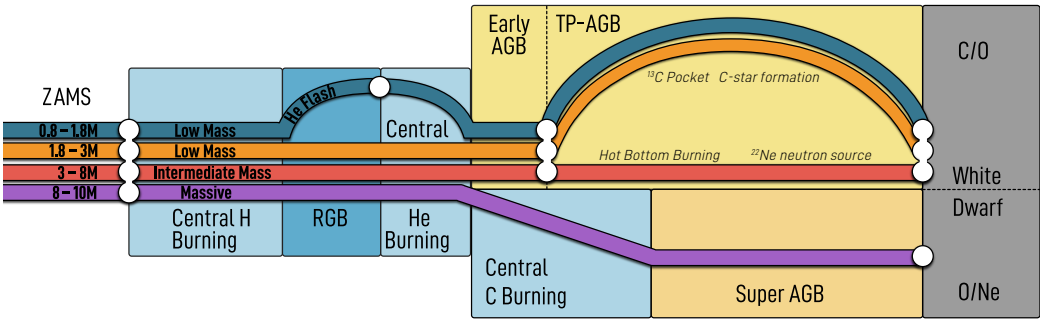

Figure 2.7 A diagram depicting the evolution of stars with different initial masses. The stars evolve from left to right. Different phases of evolution are denoted by colored regions.

The property of a single star that has the greatest impact on its evolution and end fate is the mass it has when it forms. In Figure 2.7, one can see the different paths which stars take through their evolution based on the mass they are born with. The exact values for each mass range also depend on other properties such as metallicity. To aid in the discussion we will follow the evolution of a $1\,M_\odot$ (the blue path in Figure 2.7) and a $5\,M_\odot$ (the red path in Figure 2.7) star. The "massive stars" ($8\,M_\odot$–$10\,M_\odot$) will not be discussed.

Irrespective of mass, all stars begin their life on the *main sequence* (MS). Everything before that is considered part of the formation of the star. The MS begins at the *zero-age main sequence* or ZAMS when H burning begins in the core of the star. We will begin our discussion of the evolution of these stars here. The discussion will be split into two parts: the evolution of a $1\,M_\odot$ star up to the AGB and the evolution of a $5\,M_\odot$ star up to the AGB.

2.2.1 Pre-AGB Evolution of a $1M_\odot$ Star

For stars up to roughly $1.2\,M_\odot$ the core of the star on the MS is radiative and the bulk of the energy is produced via the *proton-proton chain* or *pp*-chain. The *pp*-chain is the process by which these stars create helium from protons. There are multiple paths for the *pp*-chain, denoted with roman numerals, three of four of which are shown in Figure 2.8. Regardless of the path the *pp*-chain takes, the net result is always $4\mathrm{p} \rightarrow {}^4\mathrm{He} + 2e^+ + 2\nu$. The neutrinos are assumed to leave the star without interaction and remove energy from the star. The timescale for completing the chain is controlled by the slowest reaction in the chain which is the first reaction: $\mathrm{p}(\mathrm{p}, e^+ + \nu)^2\mathrm{H}$. This reaction is infamous for having such a low cross-section that it cannot be measured in terrestrial laboratories. When one estimates this cross-section theoretically one finds that on average a proton

[5] Kippenhahn et al. (2013) along with Habing & Olofsson (2004) are the references for all content in this section unless otherwise stated.

must wait on the order of 8×10^9 yr in the core of the Sun before undergoing this reaction.

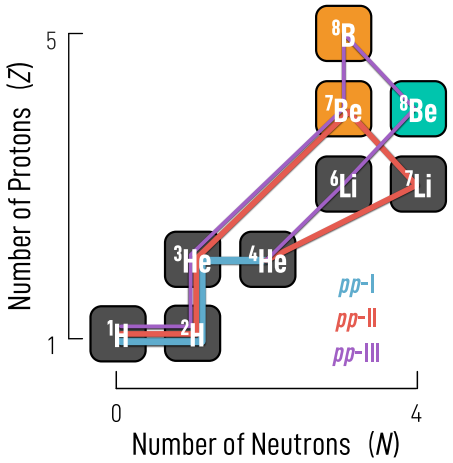

Figure 2.8 A schematic depiction of the *pp*-chain. Isotope colors have the same meaning as in Figure 2.1.

As more protons are converted to helium in the core, the molecular weight of that material increases. This leads to an increase in the central temperature and density. Once the core has exhausted its supply of protons it "turns-off", or leaves, the MS and crosses the Hertzsprung Gap. During this time the He-rich core is too cool to ignite He burning and so it contracts to the point that degeneracy sets in. At the same time H burning is establishing itself in a shell outside the core. For reasons which are still not fully understood (interested readers can consult Miller Bertolami 2022) this combination of processes causes the star to expand in radius. The cooling of the outer layers turns them convective and by the time the star reaches the *Hayashi line*, the border between stars in hydrostatic equilibrium and those that are not, the convective envelope (CE) already extends deep into the star. The "barrier" for stable stars demarcated by the Hayashi line pushes the star to higher luminosity at near constant effective temperature along the *red giant branch* (RGB). As the star ascends the RGB the CE continues to penetrate deeper into the star until it reaches material which has already been processed by H burning. This causes material enriched mainly in ^{4}He, ^{13}C, and ^{14}N to be brought to the surface of the star. This phenomenon is known as the *First Dredge-up* (FDU). The FDU leaves behind a discontinuity in the molecular weight gradient between the homogeneous, H-rich envelope and the He-enriched layers below. Later, as the H shell continues to move outwards in the star, it will reach this discontinuity at which point the luminosity of the star drops briefly before continuing to increase. This creates the so-called "bump" on the RGB.

As the star continues to ascend the RGB, the degenerate He core continues to contract and heat. Neutrino losses from star's center cause the temperature maximum in the star to migrate away from the center. At the tip of the RGB He burning is ignited at the location of the temperature maximum in an off-center ignition. This violent episode causes the luminosity generated by the star to exceed 1×10^9 solar luminosities and is called the *core helium flash*. The energy generated in this event is not radiated from the star but instead is used to lift the degeneracy of the core, and the star then proceeds towards the *horizontal branch* (HB). Here the star is gently burning helium in its core, which is now convective. The most

important nuclear reaction in this phase is the *triple-α reaction*: $^{4}\mathrm{He}\,(2\,\alpha,\gamma)^{12}\mathrm{C}$. Other α-capture reactions such as $^{12}\mathrm{C}\,(\alpha,\gamma)^{16}\mathrm{O}$ also take place but account for at most a couple percent of the energy generation. Following He exhaustion the star enters an analogous phase to that it was in just after the MS. The now carbon- and oxygen-rich core begins to contract and becomes degenerate while He burning begins in a shell above the core and below the H shell. The star then begins to ascend the giant branch for a second time as it enters the *early-AGB* (E-AGB) phase.

2.2.2 Pre-AGB Evolution of a $5\,M_\odot$ Star

For stars above roughly $1.2\,M_\odot$ the *CNO cycle* rather than the *pp*-chain dominates the energy production during the MS. Because of the CNO cycle's higher dependence on the temperature ($T^{13\ldots20}$ as compared to $T^{3.5\ldots5.5}$) the core of the star becomes convective. The result of each cycle is the same as for the *pp*-chain, that is, $4\mathrm{p} \rightarrow 4\mathrm{He} + 2e^{+} + 2\nu$. In the CNO cycle, though, heavier elements are used as catalysts for this to occur. In each cycle, C, N, O, or F nuclei act only as catalysts, in the sense that the total abundance of the heavier nuclei together is not altered and only hydrogen is consumed. The relative abundances of the individual catalysts will change. As can be seen in Figure 2.9, proton captures on C, N, and O are used to build up to an isotope which then decays by emitting a helium nucleus. Just as the *pp*-chain has multiple paths, so too in the CNO cycle there are 4 cycles. Only the first two are depicted in Figure 2.9 as they are the most relevant for the stellar mass range considered in this work.

Each cycle overlaps with the next one and one isotope acts as a critical junction for determining if a cycle will be completed or if the next cycle will be entered. For CNO-I and CNO-II that junction isotope is $^{15}\mathrm{N}$ which can either undergo a (p,α) reaction thereby completing the CNO-I cycle, or undergo a (p,γ) reaction and enter the CNO-II cycle. In the case of the CNO-I cycle, the timescale for completing a cycle is set by the slowest reaction which is $^{14}\mathrm{N}\,(\mathrm{p},\gamma)^{15}\mathrm{O}$.

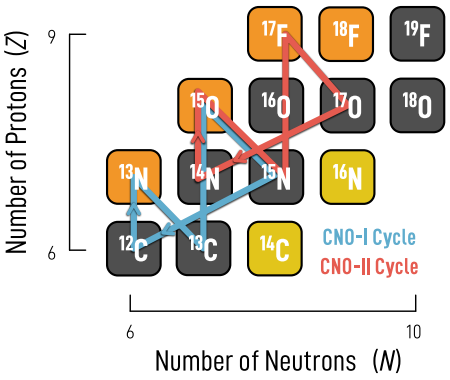

Figure 2.9 A schematic depiction of the CNO cycle. The lines show the reaction pathways. Isotope colors have the same meaning as in Figure 2.1.

The star ends the MS much as the $1\,M_\odot$ star did, crossing the Hertzsprung Gap as H-shell burning establishes itself. These stars likewise climb the RGB and experience the FDU just as their lower mass counterparts do. The main difference here is that the core does not become degenerate and instead He burning ignition occurs non-violently at the center of the star under

non-degenerate conditions.

At this point the star settles on the horizontal branch burning helium in a convective core and hydrogen in a shell. The competition between these two energy sources will determine how far into the blue the star will travel, i.e. how hot the surface of the star will be. Following the end of central He burning the star is forced by the rising He shell to expand. The expansion cools the outer layers enough that the H shell is extinguished and the CE delves deeper into the star. Eventually, the CE will encounter the region formally occupied by the now extinguished H shell and the star will undergo its second dredge-up phase. The *second dredge-up* (SDU) will significantly enhance the surface abundance of ^{4}He, ^{12}C, and ^{14}N. Following SDU, the H shell reignites and the star climbs the giant branch a second time entering the E-AGB phase.

2.2.3 On the AGB

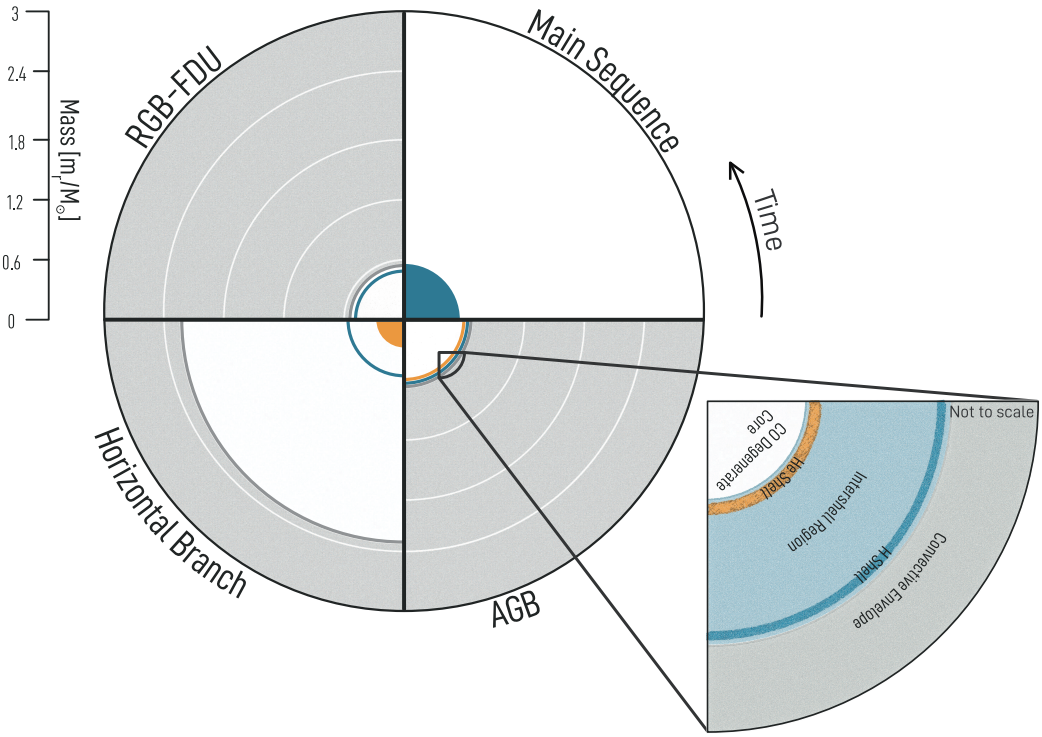

Figure 2.10 Cross-sections of a 3 $M_{\odot}$ stellar model at different points in the evolution. Each section of the plot is labeled with the evolutionary phase depicted. Blue denotes H burning, orange denotes He burning, and gray denotes convection. The white lines are shells of constant mass at the values shown in the scale to the left. Time runs counter clockwise, though each quarter circle only shows a snapshot of the structure of the star in that phase. The inset is not to scale and shows the most interesting part of the structure of the AGB star. Here, the light blue color denotes the intershell region.

Regardless of initial mass, at the start of the AGB the structure of the star is

qualitatively the same. The star consists of a C/O degenerate core, a He shell, an intershell region, a H shell, and a CE. The structure of a star in different phases of its evolution is shown in Figure 2.10. The inset shows a zoomed in view of the AGB phase, where the components are no longer to scale so as to better see each of them. The AGB phase is split into two parts: the E-AGB, where the star is simply climbing the giant branch with increasing luminosity generated by the two burning shells, and the thermally pulsing AGB (TP-AGB) phase, where the characteristic thermal pulses (TPs) have begun. TPs refer to the characteristic oscillations in the H and He luminosities of the star along the AGB. To understand how these TPs occur, a full pulse and interpulse phase is depicted in Figure 2.11 and will be described in detail.

Before discussing a TP cycle though, there is an important question to answer first. Why do the pulses occur at all? The TPs on the AGB are due to a thermal instability of the thin He shell. There is a relatively simply mathematical model which can be used to show this and will aid us later in discussing the finer details of the He-shell flashes. The argument that follows comes in large part from Sackmann (1977) but utilizes instead the equations from Kippenhahn et al. (2013).

If one compares the density-radius relationship for the case of central burning and for the case of a burning shell one finds (Equations 33.3–4 in Kippenhahn et al. 2013)

$$\frac{\mathrm{d}\rho}{\rho} = -3\frac{\mathrm{d}r}{r} \text{ for the center} \tag{2.13}$$

$$\frac{\mathrm{d}\rho}{\rho} = -\frac{r}{D}\frac{\mathrm{d}r}{r} \text{ for the shell,} \tag{2.14}$$

where r is the radial coordinate and D is the thickness of the shell source. We then assume that the layers above the shell expand or contract homologously. Thus, we can apply a homology relationship for the pressure in the shell

$$\frac{\mathrm{d}P}{P} = -4\frac{\mathrm{d}r}{r},$$

and, using Equation (2.14), we get

$$\frac{\mathrm{d}P}{P} = \frac{4}{n}\frac{\mathrm{d}\rho}{\rho},$$

where I have defined $n = r/D$. It is worth stressing here that the way n is defined means that a thinner shell has a larger n than a thicker shell.

Next, we notice from Equation (2.14) that to go from the case of central burning to shell burning all one must do is replace the factor of 3 with n. Applying this to Eq. 25.27 from Kippenhahn et al. (2013) we get our next equation:

$$\frac{\mathrm{d}P}{P} = \frac{4\delta}{4\alpha - n}\frac{\mathrm{d}T}{T}.$$

Combining the previous two equations we get our third equation

$$\frac{\mathrm{d}T}{T} = \frac{4\alpha - n}{\delta n}\frac{\mathrm{d}\rho}{\rho}.$$

The factors of α and δ have their usual meaning in the Kippenhahn book. They quantify the deviation of the gas from an ideal gas and come from the equation of state. If radiation pressure would be considered then

$$\alpha = \frac{1}{\beta}$$

and

$$\delta = \frac{4 - 3\beta}{\beta},$$

where

$$\beta = \frac{P_{\mathrm{gas}}}{P} = \frac{1 - P_{\mathrm{rad}}}{P}.$$

For now we will assume an ideal gas meaning $\alpha = \delta = \beta = 1$. We will remove this assumption later. All together, we have

$$\frac{\mathrm{d}P}{P} = \frac{4}{n}\frac{\mathrm{d}\rho}{\rho} \tag{2.15}$$

$$\frac{\mathrm{d}P}{P} = \frac{4}{4 - n}\frac{\mathrm{d}T}{T} \tag{2.16}$$

$$\frac{\mathrm{d}T}{T} = \left(\frac{4}{n} - 1\right)\frac{\mathrm{d}\rho}{\rho}, \tag{2.17}$$

and I will give each coefficient its own variable name

$$G_1 = \frac{4}{n} \tag{2.18}$$

$$G_2 = \frac{4}{4 - n} \tag{2.19}$$

$$G_3 = \frac{4}{n} - 1. \tag{2.20}$$

It should be clear from Equations (2.15) to (2.17) that $n = 4$ is some sort of critical point (G_2 is not even well defined at that point). Specifically, if $n > 4$ then

$G_3 < 0$ meaning that density decreases with increasing temperature. This means as the shell expands the temperature will increase. Additionally, the relative change in pressure is less than the change in density when $n > 4$. These two criteria are a perfect combination for a thermonuclear runaway. Note, that this is a completely different kind of thermonuclear runaway from that which occurs during the core He flash. There, the runaway occurs due to the equation of state of degenerate material. Under degenerate conditions the temperature decouples from the pressure and density. Here, the runaway is caused by a purely geometrical effect. If the shell is thin enough it is unstable.

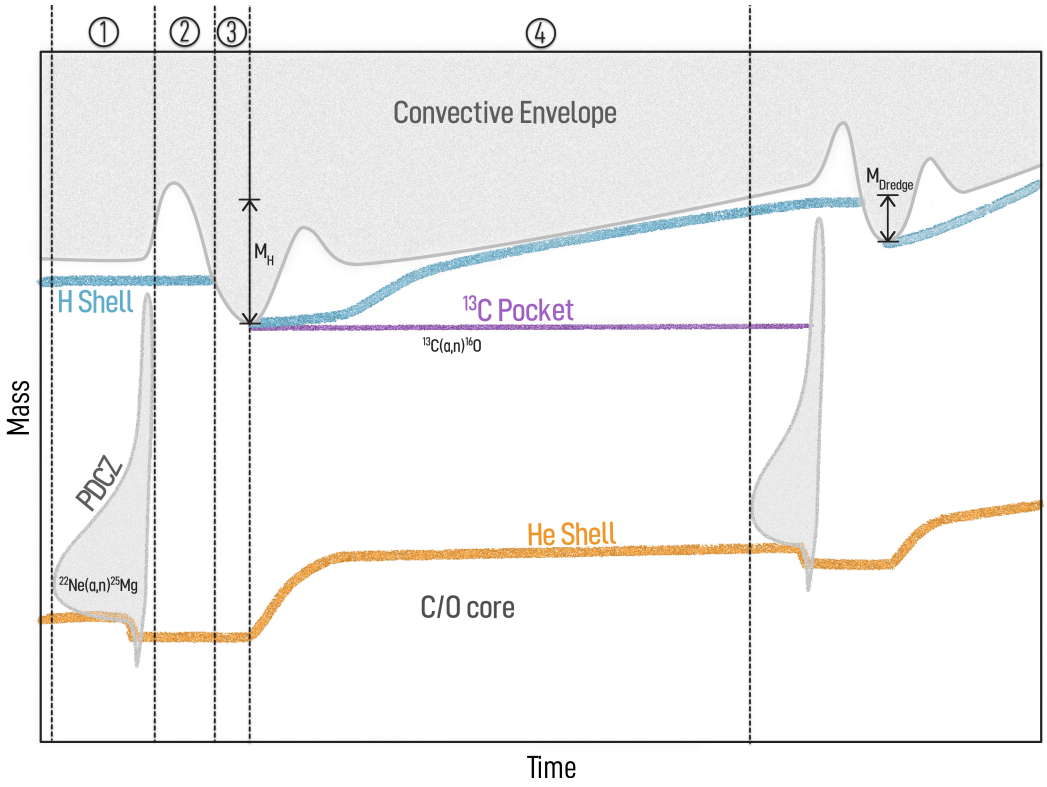

Figure 2.11 A sketch of a Kippenhahn diagram of two TPs. As in Figure 2.10, orange denotes the He shell, blue denotes the H shell, and gray denotes convection. The purple line is the ^{13}C pocket. The regions of the plot labeled 1, 2, 3, and 4 refer to the pulse, power down, TDU, and interpulse phase of the TP cycle, respectively. M_H is the distance that the H shell travels outward during the interpulse and $M_{\rm dredge}$ is the mass of material dredged up during the TDU. Finally, the neutron-source reactions are written at the location in the star where they would be active.

A TP cycle can be roughly broken up into 4 parts: pulse, power-down, third dredge-up, and interpulse. These correspond to zones 1, 2, 3, and 4 in Figure 2.11, respectively. Starting with zone 1 and the pulse, the thin He shell is unstable as we have shown and a thermonuclear runaway occurs with the shell luminosity able to reach up to 1×10^8 L$_\odot$. The energy release drives a convective zone in the intershell region known as the pulse-driven convection zone (PDCZ) as well as

causing the expansion of the layers above the He shell. At this point it is prudent to think about what stops the flash. This seemingly simple question is complicated by the fact that there are three different maxima during the flash that one must explain: The maximum helium luminosity (L_{He}), the maximum temperature at the base of the He shell (T_{He}), and the maximum extent of the PDCZ. None of the maxima occur at the same point in time. We can use Equations (2.15) to (2.20) to understand the first two maxima.[6]

The luminosity of the He shell is driven almost exclusively by the triple-α reaction. The energy generation rate due to the triple-α reaction is

$$\epsilon_{\mathrm{nuc}} \propto \rho^2 T^{\nu}$$

and so

$$\frac{\mathrm{d}\epsilon}{\epsilon} = 2\frac{\mathrm{d}\rho}{\rho} + \nu\frac{\mathrm{d}T}{T}. \tag{2.21}$$

ν is a purely nuclear physics term. From the rate in Harris et al. (1983) one can see that, in the temperature regime of interest, $\nu = -3 + 44.0/T_8$, where $T_8 = T/1 \times 10^8\,\mathrm{K}$. Secondly, we can use Equation (2.17) to express the relative change in the energy generation purely in terms of temperature:

$$\frac{d\epsilon}{\epsilon} = \left(-3 + \frac{44}{T_8} + \frac{2}{G_3}\right)\frac{\mathrm{d}T}{T} = \left(-3 + \frac{44}{T_8} + \frac{2}{\frac{4}{n} - 1}\right)\frac{\mathrm{d}T}{T}. \tag{2.22}$$

It is clear that if the result of the terms in the parentheses is positive, then the energy from He burning will continue to grow, and if it is negative it will subside. So now we can ask, how does this expression change during the flash? In the beginning of the flash the shell is thin meaning $n \gg 4$, and the temperature is around 100 MK so the expression is

$$-3 + 44 - 2 = 39.$$

So the He shell is extremely sensitive to temperature and the burning is happening extremely quickly. As the flash continues and the He shell expands, n will approach the critical value of 4 but still be slightly higher than 4. This will cause the third term in the expression to become more negative rapidly. Additionally, the temperature is still increasing, now being roughly 250 MK, which suppresses the second term. If we take $n = 4.1$ and $T_8 = 2.5$ then the expression is

$$-3 + 17.6 - 82 = -67.4.$$

[6] We will again be following the argument of Sackmann (1977), but essentially the same argument was already made by Weigert (1966) to explain the separation of the luminosity and temperature maxima

This means that we have entered a regime where increasing the temperature will actually decrease the energy generation rate! This explains why the maximum of the He luminosity always occurs before the maximum in temperature. This third term in the expression carrying the geometrical thickness factor becomes increasingly negative as the shell approaches the boundary between thin and thick and greatly suppresses the energy generation rate.

However, the shell is still thin and thus the continued expansion of the shell leads to a continued increase in temperature even if the nuclear burning is slowing. The temperature will reach its peak exactly when $n = 4$ as can easily be seen by Equation (2.17), at which point with decreasing n the temperature will also decrease. One may ask what is the critical value of n which will cause the peak L_{He}? If we assume that this peak will occur at, say, 225 MK then one can easily solve for where the expression has its root and find

$$n = 4.5496.$$

As a final point to make here, one can consider what would happen if I do not assume that the radiation pressure is negligible. In that case we have, in place of Equations (2.18) to (2.20),

$$G_1 = \frac{4}{n} \tag{2.23}$$

$$G_2 = \frac{4}{n}\frac{4-3\beta}{\frac{4}{n}-\beta} \tag{2.24}$$

$$G_3 = \frac{\frac{4}{n}-\beta}{4-3\beta}. \tag{2.25}$$

Thus, the criterion for a thin shell changes to $n > 4/\beta$. However the criterion for the percentage change of pressure being less than the percentage change in density is still achieved at $n > 4$. Both must be fulfilled for the instability. Carrying the new G coefficients through to Equation (2.22), we now have

$$\frac{\mathrm{d}\epsilon}{\epsilon} = \left(-3 + \frac{44}{T_8} + \frac{2}{G_3}\right)\frac{\mathrm{d}T}{T} = \left(-3 + \frac{44}{T_8} + \frac{2(4-3\beta)}{\frac{4}{n}-\beta}\right)\frac{\mathrm{d}T}{T}.$$

If, as before, we assume the peak of the He luminosity will occur at 225 MK, then our new expression is

$$-3 + 19.5 + \frac{2(4-3\beta)}{\frac{4}{n}-\beta} = 0,$$

and we solve for n to get

$$n = \frac{4}{-\frac{2}{16.5}(4-3\beta)+\beta}.$$

Here we see that an increasing contribution of the radiation pressure will lead to the transition of the shell from thin to thick to happen at a larger value of n, i.e. earlier. This in turn will slightly dampen the maximum He luminosity and temperature achieved during the flash.

Shortly after the peak in temperature the PDCZ will reach its maximum extent. Despain & Scalo (1976) argue that the maximum extent of the PDCZ is not governed by the hydrostatic readjustment of the star but rather by a thermodynamic one. Their argument is based on the paper by Schwarzschild & Härm (1965) who showed that the two criteria for the instability of the shell source are:

1. A positive perturbation in entropy leads to a positive perturbation in temperature.

2. The shell is thick enough that the excess heat will not diffuse away faster than the instability can grow, but thin enough to be unstable.

During a pulse, they argue, the intershell region does expand hydrostatically, but this expansion has little impact on the layers above the H shell because they are hydrostatically decoupled from the intershell region. This decoupling is due to the energy generation in the H shell which provides a strong restoring force against perturbations in radius (Stein 1966). However, the thermal perturbations of the He shell can be communicated to the outer layers by means of radiative diffusion.

They define the timescale for the growth of the instability as

$$\tau_e \approx \frac{C_p T}{\epsilon_n},$$

where C_p is the specific heat capacity, and the timescale for radiative diffusion from the He shell to the H shell as

$$\tau_{\text{diff}} \approx \frac{3}{128\sigma}\left(\int_{r1}^{r2}\sqrt{\frac{\kappa C_p}{T^3}}\rho\, dr\right)^2,$$

where κ is the opacity. As long as $\tau_e < \tau_{\text{diff}}$ the PDCZ will grow because the instability is growing faster than the outer layers can receive the information, but when $\tau_e \gtrsim \tau_{\text{diff}}$ the outer layers can adjust to any changes from the He shell as quickly as they occur and the PDCZ will cease to grow and recede. One year later Fujimoto (1977) carried out a similar analysis. While the timescales were defined somewhat differently, their computations support the argument. As it turns out these timescales are equal only after the maximum temperature is reached when τ_{He} in increasing and τ_{diff} is decreasing.

As the PDCZ recedes and the He luminosity and temperature continue to dwindle, the star has entered the phase known as power-down, shown in zone 2 of Figure 2.11. With the H shell extinguished there is no longer a strong entropy barrier holding back the CE and so it moves inward in mass. If the CE moves into the formerly convective region of the PDCZ, it will dredge-up material enriched from partial He burning as well as elements heavier than iron which have been produced via a series of neutron captures known as the *s*-process (this will be discussed in more detail in Section 2.2.6). This is known as the *third dredge-up* (TDU) and is shown in zone 3 in Figure 2.11. The efficiency of the TDU, denoted by λ, is a key quantity in AGB models and is not empirically well known. It is defined as

$$\lambda = \Delta M_{\mathrm{dredge}} / \Delta M_{\mathrm{H}}, \tag{2.26}$$

where $\Delta M_{\mathrm{dredge}}$ is the mass dredged up after a TP and ΔM_{H} is the distance traversed by the H shell during the preceding interpulse phase (see Figure 2.11 for a visual representation of these quantities) (Lattanzio 1989). At this point the star has entered zone 4 which denotes the interpulse phase. Here the star has again begun contracting and the H shell attains H-burning temperatures again. At the same time *s*-process nucleosynthesis is happening in the ^{13}C pocket (this will be discussed in more detail in Section 2.2.6). As the temperature and densities continue to rise, the He shell contracts until it is once again thin and thus unstable leading to another thermonuclear runaway. TPs and TDUs can occur many times during the AGB. The AGB phase finally ends when the envelope has been completely stripped due to mass loss.

One important change to this picture for stars above 3 $M_\odot$–5 $M_\odot$ is the occurrence of hot-bottom burning (HBB) — the colorful name being coined by Scalo et al. (1975). HBB refers to a situation where the base of the CE is hot enough that hydrogen burning can occur there. This gives the H-burning region access to abundant fuel for nuclear burning and leads to a higher luminosity of the star than one would expect from the AGB core mass-luminosity relationship. Furthermore, since the burning is occurring in the envelope it will alter the surface composition. The main effect is to reduce the C abundance and increase the N abundance as one would expect from a region subjected to CNO-cycle burning.

The AGB phase finally ends when mass loss has fully, or mostly, eroded the envelope leaving behind a core of mostly C and O and perhaps a very thin envelope. The core is in turn surrounded by a thick shroud of dust and gas — the former envelope of the star which was lost during the AGB. This material is endowed with the nucleosynthetic signature of the star and enriches the interstellar medium (ISM) or could be accreted by a companion star in the event that the AGB star was in a multiple system like a binary.

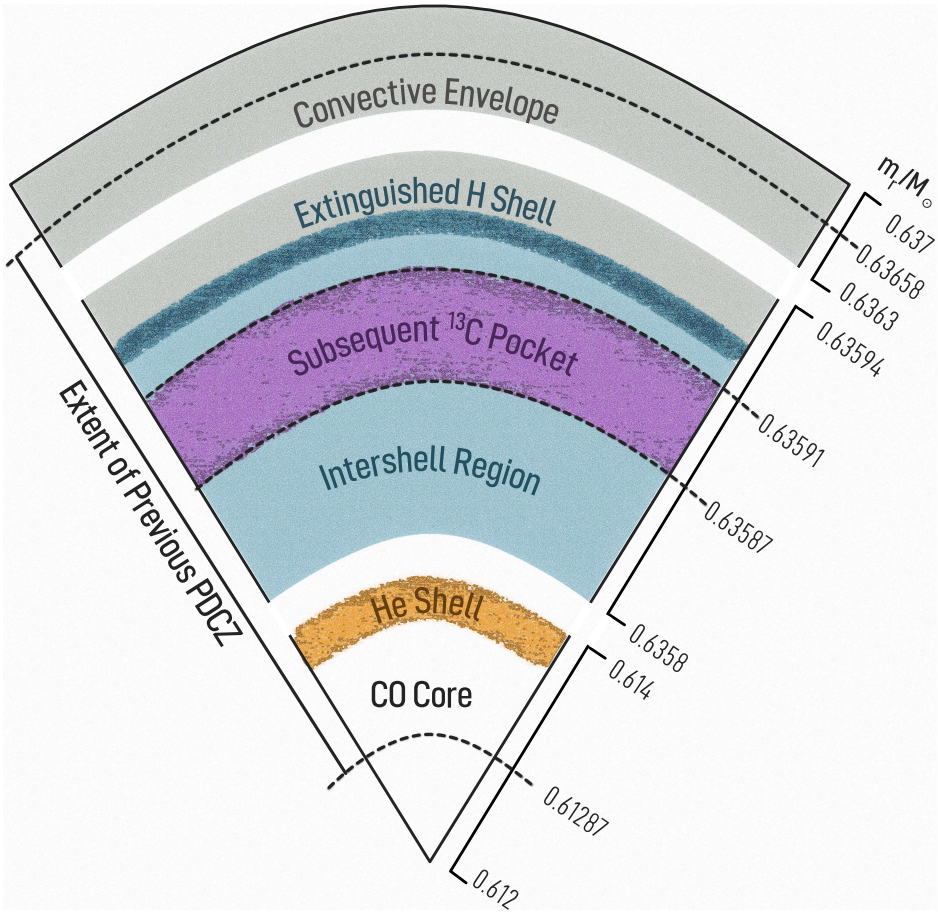

Figure 2.12 A Diagram depicting the structure of a 3 $M_\odot$ AGB star during a TDU at the time of the deepest extent of the CE. The extent of the PDCZ in the preceding pulse and the subsequent ^{13}C pocket are shown as well.

2.2.4 Convection

Before continuing on to discuss some further details of AGB evolution, a brief aside is in order. In the preceding discussion of evolution a number of convective zones have been mentioned. The modeling of convection in 1D is one of the biggest sources of uncertainties in stellar models. Convection in real stars is an extremely turbulent process and spans regions where the temperature, pressure, and density may change by many orders of magnitude. The only way to properly model it is to fully solve the Navier-Stokes equations in 3D. This is however so computationally expensive that it can only be done for small parts of a star for very short (in comparison to stellar evolutionary timescales) times. As such, stellar modelers are forced to use some sort of approximative 1D theory. By far the most common such theory is the *mixing length theory* (MLT). The simple mixing length picture of convection involves a parcel of matter which rises a set length, the *mixing length*, due to a dynamical instability. The neutral buoyancy point where

this instability ends is known as the *Schwarzschild boundary* (Schwarzschild 1906), and it marks the end of the convective zone. The mixing length is a free parameter in this theory which in stellar models usually takes a value between 1.5–2.

Once one has solved the mixing length equations one has the necessary temperature gradients to determine where in the star convection should occur and one has the convective velocities (or diffusion coefficients) which describe the convective motions. However, MLT on its own does not specify how the actually mixing should be calculated. For that one needs an additional theory. There are two main approaches to mixing in stellar evolution codes: the diffusive approach where one uses the diffusion coefficients from MLT and the advective or linear approach where one uses the convective velocities (these will be discussed in more detail in Chapter 4). These mixing schemes are known to give different results. This is studied in detail in (Goriely & Siess 2018) where both mixing schemes are implemented in the same stellar evolution code, `STAREVOL`, and compared to each other. Even with all other code details kept the same, the different mixing schemes produce different results.

The MLT is known to suffer from a number of issues, one of which involves the boundary of the convective zone. It is known from 3D hydrodynamical simulations that there is in fact some mixing which takes place beyond the Schwarzschild boundary. This is referred to as extra mixing or convective boundary mixing (CBM). Additionally, there are observations, such as the turn off point of the MS in star clusters (Magic et al. 2010) or the properties of eclipsing binary stars (Remple et al. 2021), which can only be matched by stellar evolution models when CBM is accounted for. Overshoot, which will be discussed in more detail in Section 4.1.1, is an extra mixing process which is commonly used in stellar evolution codes. This is discussed here as the uncertainties in convection will rear their head almost any time one attempts to investigate a phenomenon in stars in detail.

2.2.5 Mass Loss on the AGB

A typical assumption in the calculations of stellar evolution before around 1980 is that the mass of the star does not change despite the observations which showed that stars do lose mass. The first direct observational evidence of mass loss from a star came from Biermann (1951) who determined that the deflection of comet tails could not solely be explained by the momentum transfer of solar photons, and instead was due to a flow of particles coming from the Sun. A few years later Deutsch (1956) was able to deduce that the M-type red giant star in the α Her binary system was losing mass at a rate six orders-of-magnitude higher than the Sun. Shklovskii (1957) was the first to suggest that the mass loss of cool extended red giants may be the source of the circumstellar material surrounding

planetary nebulae. The study of mass loss in stars was greatly helped by the IRAS space survey in 1983, the first all-sky survey at infrared wavelengths. Using this data Olofsson et al. (1990) were able to determine that the shells of planetary nebulae were indeed consistent with episodic mass loss due to TPs on the AGB.

As already discussed, the AGB terminates when mass loss fully erodes the CE of the star. The most widely accepted mass loss picture for AGB stars at present involves two components. First, shock waves, driven by the radial pulsations of the star and strengthening as they propagate through the sharply decreasing density of the star's outer layers, act as a levitation mechanism driving the radial extension of the atmosphere. These shocks compress, heat, and push the material as it travels through. Second, the material which has been pushed further from the star undergoes radiative cooling and leads to dust grain formation. These dust grains feel the pressure of the radiation field generated by the star providing the momentum for the so-called *dusty winds*.

Despite having this picture, the mass loss of AGB stars is not quantitatively well understood, so mass loss laws used in modeling tend to be based on empirical or simple theoretical estimates. These laws all attempt to connect the properties of the stars to their mass loss rates. The most well known and widely used mass loss parameterization is Reimers' wind (Reimers 1975). Based on observations of red giants and supergiants, Reimers developed the mass-loss relationship:

$$\dot{M}_{\text{Reimers}} = -4 \times 10^{-13} \eta_{\text{R}} LR/M.$$

This relationship had the advantage of being observationally motivated and simple to incorporate in stellar evolution codes. It soon became clear, however, that, depending on evolutionary stage, it was prone to under- or overestimating the mass loss. For this reason the calibrating parameter, η_{R}, was added to the formula which is not necessarily constant throughout the evolution. Many variations of this general formula were developed in the following years in order to improve the estimate (for a discussion see Bloecker (1995)).

In Iben & Renzini (1983) the authors included a new type of mass loss: a *superwind*. This superwind was invoked by Renzini (1981) as a way to produce the characteristic sturctures observed in the ejecta surrounding planetary nebulae. In their models the superwind mass loss is switched on once a certain critical luminosity is reached.

A different approach is taken by Vassiliadis & Wood (1993) who use an empirical relation which is solely dependent on the period, P, of the linear pulsations of the star and its mass. The period itself is calculated via another empirical relationship which relates the mass and radius of the star to its period. It can be argued that this is a more physical description as the pulsations of the star are thought to be part of the mechanism behind the mass loss.

One important variable which is not taken into account in these mass loss

prescriptions is the C/O ratio at the surface of the star. This situation was rectified in Wachter et al. (2002) and van Loon et al. (2005) who developed mass loss prescriptions specifically for C-rich and O-rich stars, respectively. The mass-loss prescription of Wachter et al. (2002) is based on pulsating wind models whereas van Loon et al. (2005) used observations of O-rich AGB stars to develop their parameterization.

In recent years the field has shifted from attempting to provide simple formulae to instead providing tables to be interpolated. The data from these tables come from increasingly advanced and complicated simulations of the outer layers of AGB stars and atmospheres. A far from exhaustive list of these kinds of studies includes: Mattsson et al. (2010), Eriksson et al. (2014), Bladh et al. (2019), Siess et al. (2022), and Sandin et al. (2023).

A shared feature of all AGB mass-loss rates is the increased mass loss with increased luminosity. This leads to brief spikes in the mass loss with every pulse resulting in thin circumstellar shells around the star. Effective temperature is also included in some mass loss prescriptions with lower effective temperature leading to higher mass loss. Aside from luminosity and effective temperature, the C/O ratio at the surface of the star also plays a significant role in the mass loss of AGB stars. The greater the C/O ratio the more dust is formed in the outer layers, the more the opacity increases, and the stronger the winds are. On the AGB each TDU will increase the C/O ratio at the surface. Once the C/O ratio exceeds unity the star is a carbon star and the mass loss increases dramatically. This can be seen in Figure 2.13. Because of this effect it is now standard practice to use opacity tables for various C/O mixtures.

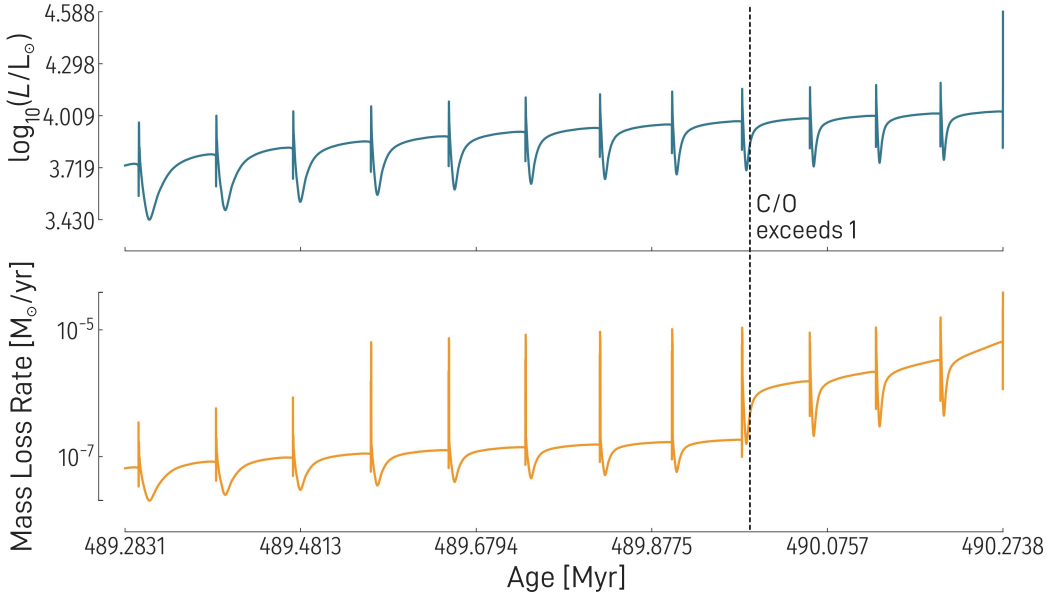

Figure 2.13 Mass loss rate and luminosity as a function of time on the AGB for a 3 $M_\odot$ star. The dashed line indicates when the C/O ratio exceeds unity

Another critically important consequence of the mass loss on the AGB is that it enriches the ISM with the nucleosynthetic products of the star. This includes the *s*-process isotopes which were dredged-up in the TDUs. Because of this, AGB stars are of great importance to galactic chemical evolution models. These models rely in part on *nucleosynthetic yield tables* from AGB models. These yield tables simply tabulate the total amount of all isotopes which were lost in the winds of an AGB model and thus went into the ISM.

A *yield* can be calculated for each isotope tracked in the stellar evolution code. The exact way of calculating the yield can differ from study to study so it is important to be careful when interpreting results across studies. Generally, there are two formulae

$$\mathscr{M}_i = \int_0^{\tau_{\text{star}}} \dot{M}(t) X_i^{\text{surface}}(t) dt \tag{2.27}$$

and

$$\mathscr{Y}_i = \int_0^{\tau_{\text{star}}} \left(X_i^{\text{surface}}(t) - X_i(0)\right) \dot{M}(t) \mathrm{d}t. \tag{2.28}$$

where τ_{star} is the current age of the star, $\dot{M}(t)$ is the mass loss rate at time t, $X_i^{\text{surface}}(t)$ is the surface mass fraction of isotope i at time t, and $X_i(0)$ is the initial mass fraction of isotope i. $\mathscr{M}_i$ gives the total mass of isotope i expelled into the ISM and is always positive, whereas $\mathscr{Y}_i$ only keeps track of the isotope creation or destruction relative to the initial abundance of the star and can be positive or negative. Both will be used in this work, thus, for the purposes of disambiguation, we will refer to $\mathscr{M}$ as the mass yield and $\mathscr{Y}$ as the net yield. Similar to $\mathscr{Y}_i$, one can define an overproduction factor for an isotope i in terms of $\mathscr{M}_i$ as,

$$\mathscr{F}_i = \frac{\mathscr{M}_i}{(M_{\text{ini}} - M_{\text{final}}) X_i(0)}. \tag{2.29}$$

2.2.6 *S*-PROCESS

It has already been discussed on the basis of Figure 2.2 that nuclear fusion up to iron results in energy generation and nuclear fusion past iron requires energy. This alone strongly suggests that the generation of elements heavier than iron is likely not a large factor in the evolution of stars, but rather a process which generates trace element abundances.

Recalling the discussion from Section 2.1, as Z increases the Coulomb barrier becomes harder to overcome and tunneling becomes less effective. For this reason it was quickly hypothesized that heavy element production is the result of successive neutron captures. Since the neutron has no charge it does not feel the Coulomb potential of the nucleus. Of course neutron captures alone will not result in a change of Z and thus to a new element. However, a nucleus can not

indefinitely capture neutrons. As one adds more neutrons the nucleus will become more unstable and will eventually undergo β^--decay, turning one neutron into a proton, and thus arriving at the next row up in the chart of nuclides. The swath of the chart of nuclides where elements are stable to β-decays is referred to as the *Valley of Beta Stability*. Figure 2.14 shows a sketch of the valley of stability for one element — this is essentially a cross-section of the chart of nuclides for constant atomic weight, A, i.e. an isobar. The orange dots on the left are unstable neutron-poor isotopes, while the yellow dots on the right are neutron-rich unstable isotopes, and the black dots are stable isotopes. Successive neutron captures will push the nucleus farther to the right where the isotopes get more and more unstable. How far the nucleus gets depends on the interplay of the neutron density, or similarly the time between neutron captures, and the lifetime of the isotope before it decays. Here one can identify two extremes: the neutron captures dominate over the β^--decays, or vice versa. The first case we call the *r*-process with typical neutron densities of $N_\mathrm{n} \gtrsim 10^{20}\,\mathrm{cm}^{-3}$, and the second case we call the *s*-process with typical neutron densities of $N_\mathrm{n} \gtrsim 10^{8}\,\mathrm{cm}^{-3}$.

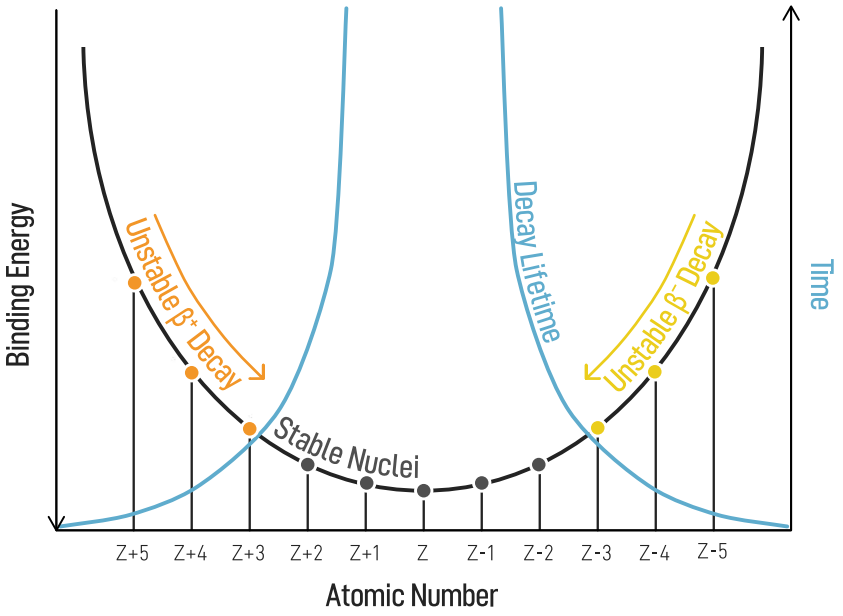

Figure 2.14 A sketch of the valley of beta stability for constant A. Based on Fig. 12.13 in Shaviv (2012).

To get a better picture of the behavior of the *s*-process one can ask how the abundances of isotopes would change if subjected only to neutron captures and β-decays. Recall that the slowness of the neutron captures as compared to the β-decays is the defining characteristic of the *s*-process. Using Equation (2.5) one can see that the equation for the number abundance, N_A, of a nuclide with mass number A, is

$$\frac{\mathrm{d}N_{\mathrm{A}}}{\mathrm{d}t} = N_{\mathrm{n}}N_{\mathrm{A}-1}\lambda_{\mathrm{nA}-1} - \left(\lambda_{\beta} + \lambda_{\mathrm{nA}}\right)N_{\mathrm{n}}N_{\mathrm{A}}. \tag{2.30}$$

where N_{n} is the neutron number density, λ_{β} is the β-decay rate, and λ_{nA} is the neutron capture rate for the nuclide with mass number A. To simplify things $\lambda = \langle \sigma v \rangle$ is often written as σv_T where σ is some average cross-section and v_T is the thermal velocity of the neutrons. This is valid as $\langle \sigma v \rangle$ for neutron captures is very insensitive to temperature changes, and the temperature at which neutron-capture processes take place is largely constant for a particular neutron exposure epoch (Clayton 1983). This further implies that $\langle \sigma \rangle$ and v_T are constant.

We can then define a new quantity, $\Phi = N_{\mathrm{n}}v_T$, called the *neutron flux* and rewrite Equation (2.30) as

$$\frac{\mathrm{d}N_{\mathrm{A}}}{\mathrm{d}t} = \sigma_{n\mathrm{A}-1}N_{\mathrm{A}-1}\Phi - \left(\sigma_{\beta} + \sigma_{\mathrm{nA}}\right)N_{\mathrm{A}}\Phi. \tag{2.31}$$

We will now assume that all nuclei on the *s*-process path are either stable or the isotope is very short lived. Thus, we can treat a two-step reaction, such as

$$(Z,A) + n \rightarrow (Z,A+1) + \gamma \rightarrow (Z+1,A+1) + \beta^{-} + \bar{\nu}, \tag{2.32}$$

as a one-step reaction

$$(Z,A) + n \rightarrow (Z+1,A+1) + \gamma + \beta^{-} + \bar{\nu}. \tag{2.33}$$

In this way we can ignore the β-decays in our equations and eliminate σ_{β} from Equation (2.31). Additionally, we will replace t in Equation (2.31) with the time-integrated neutron flux, or *neutron exposure*, which is equal to $\tau = \int \Phi \, \mathrm{d}t$, to get

$$\frac{\mathrm{d}N_{\mathrm{A}}}{\mathrm{d}\tau} = \sigma_{n\mathrm{A}-1}N_{\mathrm{A}-1} - \sigma_{\mathrm{nA}}N_{\mathrm{A}}. \tag{2.34}$$

This description of the *s*-process is called the *classical* s*-process* and proved to be a very useful phenomenological tool. In Clayton et al. (1961) it was used to show that a single neutron irradiation event cannot reproduce the solar *s*-process abundance distribution. Seeger et al. (1965) then showed that a good solution can be found if one assumes a distribution of exponential neutron exposures of the form

$$\rho(\tau) = \frac{f N_{^{56}\mathrm{Fe}}}{\tau_0} \exp^{-\tau/\tau_0} \tag{2.35}$$

where τ_0 is a parameter which controls the mean neutron exposure, f is a constant, and $N_{^{56}\mathrm{Fe}}$ is the abundance of ^{56}Fe which is assumed to be the *seed*, or starting point, of the *s*-process. ^{56}Fe is assumed to be the seed for the *s*-process for a

number of reasons. It has a higher neutron-capture cross-section than many of the elements lighter than it, yet it is comparably abundant to the light elements which cannot be said of the elements heavier than it. This gives us a boundary condition for the *s*-process which is needed to solve these equations. The analytical solution to the system of equations of the type seen in Equation (2.34) looks like:

$$\sigma_{\mathrm{nA}} N_{\mathrm{A}} = \frac{f N_{^{56}\mathrm{Fe}}}{\tau_0} \prod_{i=56}^{\mathrm{A}} \left(1 + (\sigma_{ni}\tau_0)^{-1}\right)^{-1}. \tag{2.36}$$

As more abundance and nuclear data became available it was determined that three different exponential distributions of neutron exposures would be required in order to explain the observed *s*-process abundance.

1. *The Weak Component*: This mainly produces elements between Fe and Sr.
2. *The Main Component*: This mainly produces elements between Sr and Pb.
3. *The Strong Component*: This mainly produces Pb.

The weak component is believed to occur in the cores of massive stars during central He burning, whereas the main component occurs in AGB stars. The strong component may also be produced in AGB stars of low metallicity. For the remainder of the section we will focus on the main component.

Now, we must discuss the shortcomings of the classical *s*-process model. First, Equation (2.34) tends to a solution for which $\sigma_{n\mathrm{A}-1} N_{\mathrm{A}-1} \approx \sigma_{\mathrm{nA}} N_{\mathrm{A}}$ (Clayton 1983). While for long sections of the *s*-process path σN is *locally* near constant it is not constant at the magic numbers or over long spans of the path. This can be seen in Figure 2.16. You will recall that nuclei with magic numbers of protons or neutrons are particularly stable as explained via nuclear shell theory. Just as atoms with full electron shells are reluctant to gain or lose electrons, nuclei with full nuclear shells are resistant to changes in their nucleon number. This means that isotopes near magic numbers have very small neutron-capture cross-sections. This creates bottlenecks in the *s*-process path and abundances will build up into peaks at these magic numbers. This also means that large neutron exposures are required to get past these peaks. There are three main peaks in the *s*-process path at N=50, 82, and 126 which can be clearly seen in Figure 1.1. Peak one is located around ^{88}Sr, peak two is located around ^{138}Ba, and peak three is located around ^{208}Pb. These peaks will be missed in the classical *s*-process analysis. The second shortcoming of the classical approach is that it ignores the presence of *branching points*. Recall that one assumption made in the classical approach is that all isotopes are either fully stable, i.e. $\lambda_\beta \ll \lambda_n$, or decay immediately, i.e. $\lambda_\beta \gg \lambda_n$. This is not always the case. There are a number of places along the *s*-process path where, for a particular isotope, $\lambda_\beta \approx \lambda_n$. Here the *s*-process path will split as some of the nuclei of the branching isotope decay and some capture

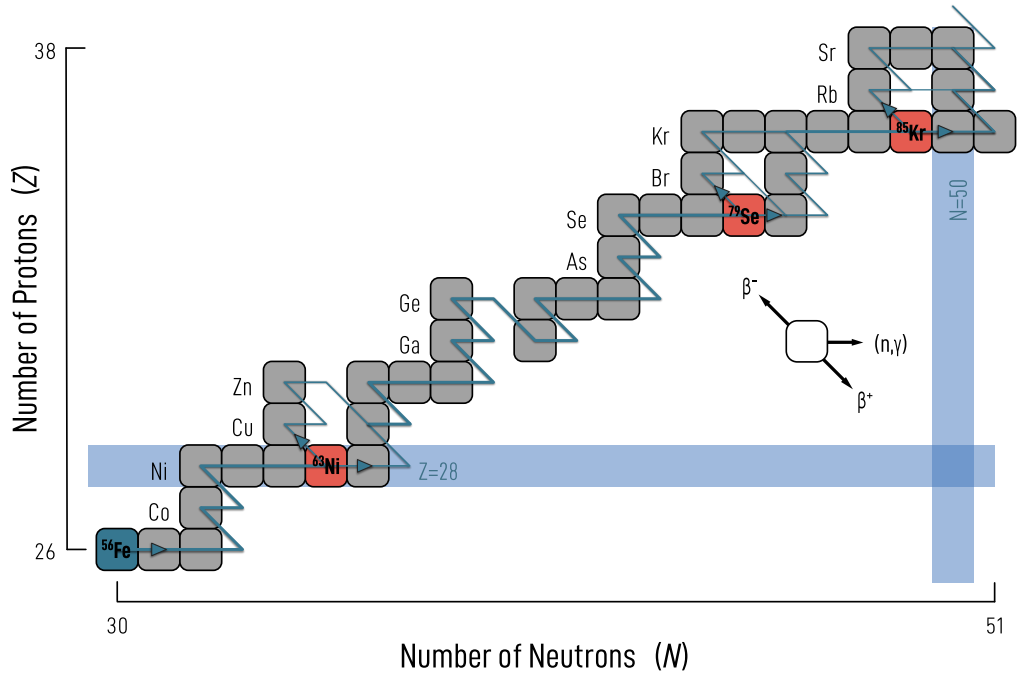

Figure 2.15 A depiction of the *s*-process path from the seed to the first peak. Isotopes with a red background denote branching points. The seed, ^{56}Fe, is colored dark blue

neutrons. This branching can be seen in Figure 2.15 where a number of branching isotopes are shown in red and the *s*-process path is shown in blue.

One way in which branching points can be useful is that they serve as a way of determining the neutron density of *s*-process enriched material, or, if one assumes a particular neutron source reaction, as a thermometer for the temperature at which the *s*-process occurred. As an example we will look at the branching point at ^{85}Kr, which controls whether the *s*-process path flows through ^{85}Rb or ^{87}Rb. In a high-neutron-density environment ^{85}Kr will capture a neutron to get to the stable isotope ^{86}Kr which will again undergo a neutron capture to ^{87}Kr, which will then β-decay (in just over an hour) to stable ^{87}Rb. In a low-neutron-density environment, however, ^{85}Kr will simply β-decay to ^{85}Rb. Because of this behavior the ratio of ^{85}Rb/^{87}Rb or the ration of Rb to the first peak elements of Sr, Y, and Zr can provide information of the condition where the *s*-process occurs (Wallerstein et al. 1997).

In AGB stars the *s*-process can occur in two places (see Figure 2.11 again). For stars above roughly 3 $M_\odot$ the *s*-process can take place at the base of the PDCZ. In these stars the temperatures here can exceed 300 MK and thus activate the ^{22}Ne$(\alpha, n)^{25}$Mg reaction. This produces neutron densities of 10^{11} cm^{-3} for a period of tens of years. This is sometimes referred to as the convective *s*-process as the neutron captures are happening in a convective environment. In stars below

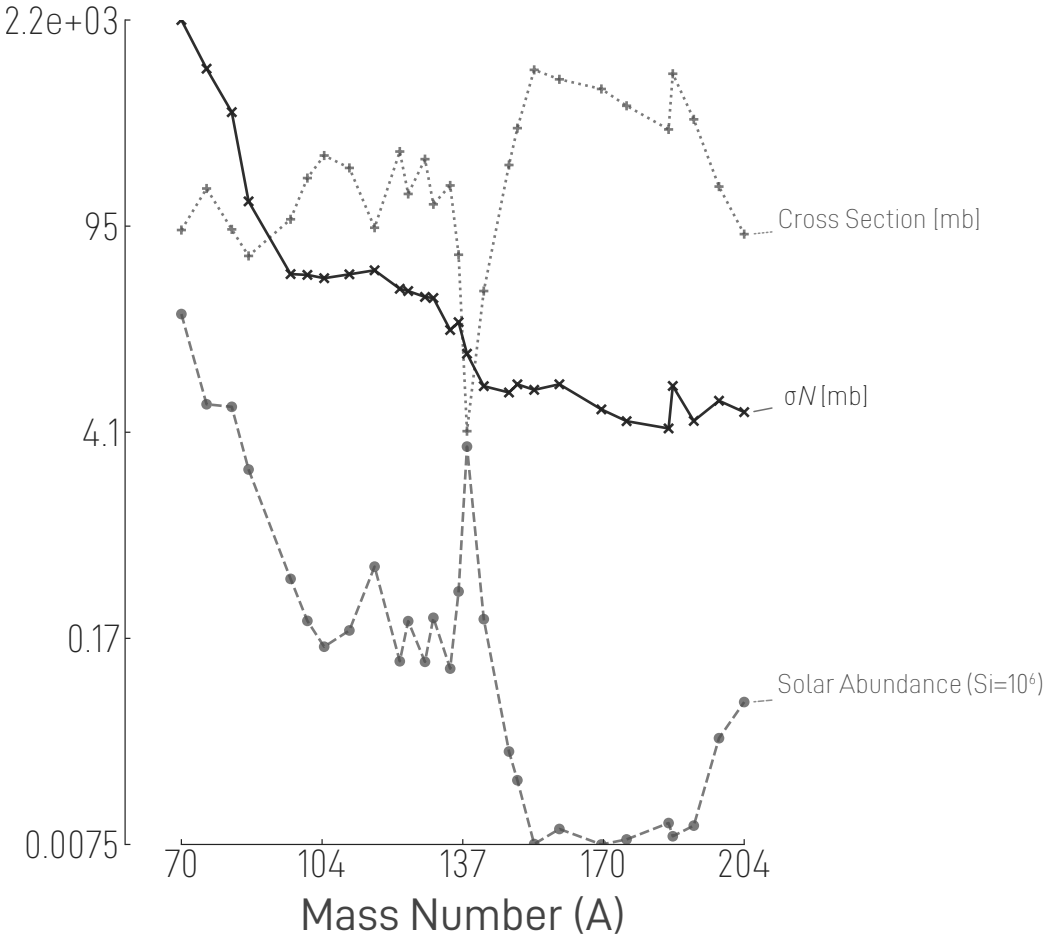

Figure 2.16 The solar abundance distribution from Lodders (2021), neutron-capture cross-sections from the KADoNiS Database (Dillmann et al. 2014), and their product σN as a function of mass number for *s*-only isotopes as given by Seeger et al. (1965).

this mass the main site for the *s*-process is the ^{13}C pocket mentioned briefly in Section 2.2.3 and shown in Figure 2.11. Here temperatures are lower at only 100 MK and the neutron density is also lower at $\leq 10^7$ cm^{-3}. However, because the ^{13}C pocket lasts on the order of 40 000 yr–50 000 yr the total neutron exposure is actually higher than for the convective *s*-process. The neutrons here are generated via the $^{13}\mathrm{C}(\alpha, \mathrm{n})^{16}\mathrm{O}$ reaction in a radiative environment.

The formation of the ^{13}C pocket itself is one of the most important open questions in AGB stellar modeling and depends highly on the treatment of convection. The general theory of its formation goes as follows. At the deepest extent of the CE during TDU some amount of protons are mixed beyond the base of the CE. This is necessary because there is not enough ^{13}C in the intershell region to generate the necessary neutron exposure for the *s*-process. These protons are then captured by the abundant ^{12}C to form ^{13}N which subsequently undergoes β^+-decay to ^{13}C. This ^{13}C can then capture an α to create a neutron. If too many protons are

mixed beyond the convective border however, then the ^{13}C may capture another proton and become ^{14}N which is a *neutron poison*. The term neutron poison simply refers to an isotope which can efficiently capture neutrons thereby impeding the *s*-process. The ^{13}C pocket is normally defined as the region of the star where the effective ^{13}C mass, $X^{\text{eff}}_{^{13}\text{C}}$, is greater than 1×10^{-4}, where $X^{\text{eff}}_{^{13}\text{C}} = X_{^{13}\text{C}} - \frac{13}{14} X_{^{14}\text{N}}$. The details behind the process, including how deep into the star the CE goes during TDU, how the protons are mixed beyond the convective border, and how many protons are mixed, are all still unknown. These factors all fundamentally rely on the modeling of convection which, as discussed, is very uncertain. To underscore the challenge of modeling the ^{13}C pocket and why even small uncertainties may be important, it is useful to think about the scales involved. According to models, an AGB star has a radius on the order of 100 000 000 km, the overshoot region of the CE, which is responsible for the extra mixing of protons for the ^{13}C pocket, extends over approximately 100 000 km, and the ^{13}C pocket itself is only on the order of 100 km wide.

The best way to try and understand the properties of the ^{13}C pocket are to compare the results of stellar models with observations, either spectroscopic or meteoritic (see Section 2.3), in order to constrain what is allowed. One example of this is is the use of [hs/ls] as a proxy for neutron exposure as determined by Luck & Bond (1991). This quantity represents the average abundance ratio of the elements between Ba and Sm (hs) and those between Sr and Zr (ls). In practice one is usually limited to using only a handful of the elements in each range to calculate [hs/ls] due to the limited number of abundance determinations possible from observations. For example, one could calculate [hs/ls] as[7]

$$\begin{aligned}[\text{hs/ls}] &= [\text{hs/Fe}] - [\text{ls/Fe}] \\ &= \frac{[\text{Ba/Fe}] + [\text{La/Fe}] + [\text{Ce/Fe}]}{3} - \frac{[\text{Sr/Fe}] + [\text{Zr/Fe}]}{2}.\end{aligned} \tag{2.37}$$

AGB stars of solar metallicity are observed to have $-0.5 \leq [\text{hs/ls}] < 0.0$ (Busso et al. 1995).

2.2.7 *i*-PROCESS

In addition to the *s*-process, Cowan & Rose (1977), also proposed the idea of an intermediate neutron-capture process, or *i*-process, which they claimed could occur in evolved red giants. The *i*-process, as the name suggests, is defined by having neutron exposures intermediate to those of the *s*-process and *r*-process, $N_{\text{n}} \approx 10^{12}\,\text{cm}^{-3}$–$10^{16}\,\text{cm}^{-3}$. This idea has gained traction in the last two decades as research into so-called CEMP-r/s stars, carbon-enhanced metal-poor stars with

[7] [X/Fe] is referred to as spectroscopic notation. $[\text{X/Fe}] = \log_{10}(N_{\text{X}}/N_{\text{Fe}})_* - \log_{10}(N_{\text{X}}/N_{\text{Fe}})_\odot$.

both *r*- and *s*-process features in their heavy element abundance patterns, has shown that it may be necessary to invoke the *i*-process to explain the strange abundance patterns of these stars.

Though the location at which the *i*-process occurs remains uncertain, the common thread among all the hypotheses is the need for protons to be mixed to regions of high temperature actively undergoing He burning. This is generally referred to as a proton-ingestion event (PIE), but other names such as H-ingestion event (HIE), He-flash driven deep mixing (He-FDDM), and dual flashes among others can be found in the literature.[8] The protons, having been mixed into a He-burning region, are captured by the abundant ^{12}C to form ^{13}C. The neutrons for the *i*-process are then released via the ^{13}C neutron source reaction which is very active at typical He-burning temperatures of 200 MK–300 MK. This results in neutron densities much higher than those of the *s*-process where the same reaction is occurring but at typical temperatures around 90 MK–100 MK. A number of candidate astrophysical sites for the *i*-process have been put forth by various authors. The idea proposed by Denissenkov et al. (2017) and Denissenkov et al. (2019) is that the *i*-process occurs in rapidly accreting white dwarf stars (RAWDs). In this scenario the white dwarf is accreting proton rich material from its binary companion. An unstable He-burning shell is formed by the burning of the proton-rich material. The He shell ignites and drives a convection zone resulting in protons being mixed into the He burning regions leading to *i*-process levels of neutron densities. Another possible site is the core He flash of low-mass extremely metal-poor stars when the flash driven convection zone penetrates the H-rich region of the star (Fujimoto et al. 2000, Campbell et al. 2010, Cruz et al. 2013). Super-AGB stars (AGB stars with initial masses between 7 $M_\odot$–10 $M_\odot$) have also been suggested (Siess 2007, Jones et al. 2016).

In this work we focus on the final potential site, the thermally pulsing AGB (TP-AGB) phase of low-mass metal-poor stars (Fujimoto et al. 2000, Iwamoto 2009, Cristallo et al. 2009a, Suda & Fujimoto 2010, Choplin et al. 2021, Goriely et al. 2021, Choplin et al. 2022, 2024). In this scenario the large He-burning luminosity during the pulses drives a PDCZ between the He and H shells, as is the case in the higher-metallicity AGB stars. However, at low metallicity, PDCZ can overcome the relatively small entropy barrier of the H shell and thereby mix protons to the base of the PDCZ to be burned. The penetration of the PDCZ into the H shell is only possible at low metallicity as the dearth of metals, especially CNO, forces the H shell to become hotter to compensate for the reduced number of catalysts and thus reduces the entropy of the shell (Fujimoto et al. 2000). Here, as was the case for the *s*-process, the details of the PIE are strongly linked to the modeling of convection in 1D and the uncertainties associated with that.

[8] In this work PIE will be used.

2.3 Observations

Having dedicated the majority of this chapter to theory, it is now time to discuss the observational side of things. The most important observational techniques related to AGB stars and their nucleosynthesis are *spectroscopy* and *meteorite analysis*. Additionally, *variability* is another critical observational characteristic of many AGB stars. Here a brief introduction to these topics will be given. Unless otherwise specified the reference for Sections 2.3.1 and 2.3.2 will be Habing & Olofsson (2004). For Section 2.3.3 the reference is Encrenaz et al. (2004).

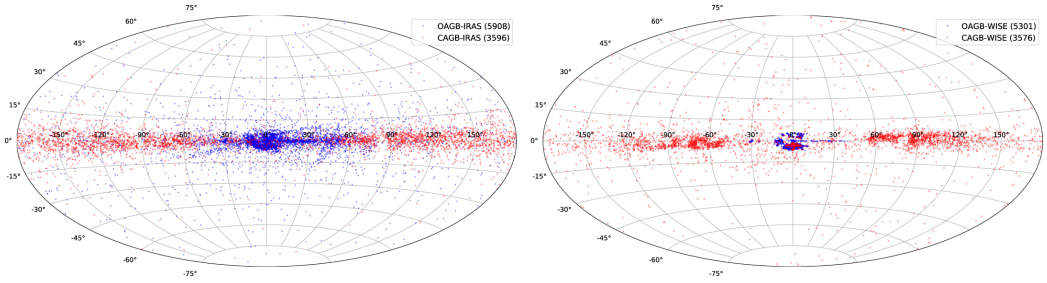

Figure 2.17 Spatial Distribution of AGB stars in the Milky Way from two surveys: IRAS (left) and WISE (right). Blue dots mark the O-rich AGB stars, while red dots mark the C-rich AGB stars. This is Figure 13 in Suh (2021)

2.3.1 Spectroscopy

The first recorded observation of spectral lines in the solar spectra came from Wollaston (1802), who used a very narrow aperture on his spectroscope allowing him to get a much cleaner spectrum. Figure 2.18 shows his drawing of the spectrum he observed. Stellar spectroscopy in general can trace its origin back to Joseph von Fraunhofer who, in 1817, discovered that the spectrum he obtained from Sirius is very different from the one he obtained from the Sun (von Fraunhofer 1817, pg. 220 to 221). The realization that the features of spectra could be attributed to chemical elements and the work of determining these attributions began with Kirchhoff & Bunsen (1860). Shortly after, large catalogues of stellar spectra were already being formed. Secchi (1868) at the Vatican observatory observed and collected spectra from as many as 4000 stars. Among these stars were a small group of red stars which he noticed had different spectra than most red stars. In particular the spectral lines likely associated with carbon were much stronger than usual.

Starting in the late nineteenth century, work on the prolific Henry Draper Catalogue began at Harvard. This catalogue contained the spectra of hundreds of thousands of stars. One publication of this work included the division of stars into specific classes based on the width of their spectral lines (Maury & Pickering 1897). As more and more stars were assigned a spectral classification,

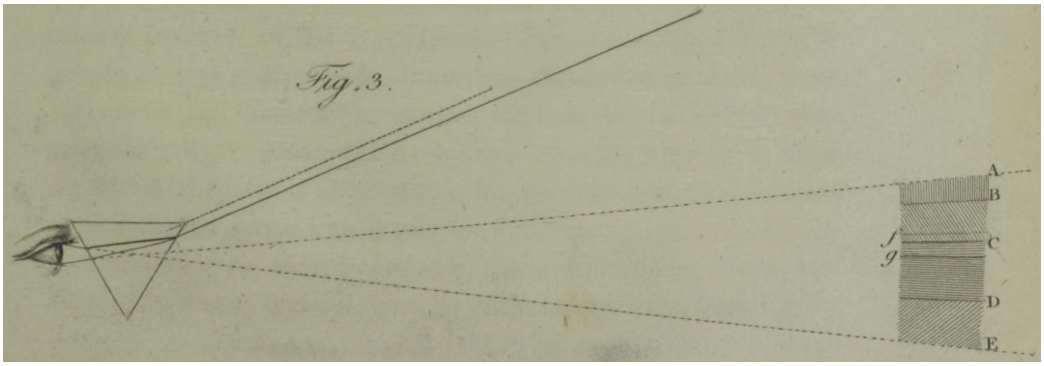

Figure 2.18 Figure 3 from Wollaston (1802) showing the solar spectrum. The letters denote different lines in the spectrum.

Hertzsprung (1911) and independently Russell (1914) developed what came to be known as the *Hertzsprung-Russell diagram* (HRD) — the name being coined later by Strömgren (1933) — which shows the location of stars in the magnitude-spectral classification plane, or, equivalently, the luminosity-effective temperature plane (see Figure 2.19).[9]

There are three primary spectral classifications to which AGB stars belong: M, S, and C. *M stars* are characterized by TiO-bands, *S stars* show ZrO-bands which is an indication that *s*-process elements have already begun being dredged up to the surface of the star, and *C stars* lack metallic oxides and instead have molecular bands from carbon compounds, most notably CN and C_2. The C class corresponds to the set of peculiar stars first noticed by Secchi (1868) and are also called *carbon stars*. It is also possible that a star belongs to more than one spectral classification. For example, there are stars whose spectra contain both TiO and ZrO bands. These stars are then classified as MS stars.

These spectral classifications can also be understood as a temporal progression. Stars at the beginning of the AGB will have spectral type M. As multiple TDUs occur the surface of the star will become enriched in C and *s*-process elements. The carbon will quickly cling to any excess O atoms and form CO leaving strong *s*-process lines indicative of an S type star. Further C enrichment will cause CN and C_2 molecules and a C type spectrum.

There are two classifications related to AGB stars which will be referred to in this work. Barium (Ba) stars, first identified by Bidelman & Keenan (1951), defied explanation for a long time as their evolutionary status was well before the AGB, yet they exhibited clear signs of *s*-process enhancement. It wasn't until McClure et al. (1980) that it was found that all Ba stars are actually in binary systems with a white dwarf companion. The explanation then was clear; the Ba

[9] Interestingly, one year before Hertzsprung, Rosenberg (1910) published a diagram plotting the stars in the Pleiades cluster on an apparent magnitude vs strength of calcium and hydrogen lines plot which is effectively an HRD.

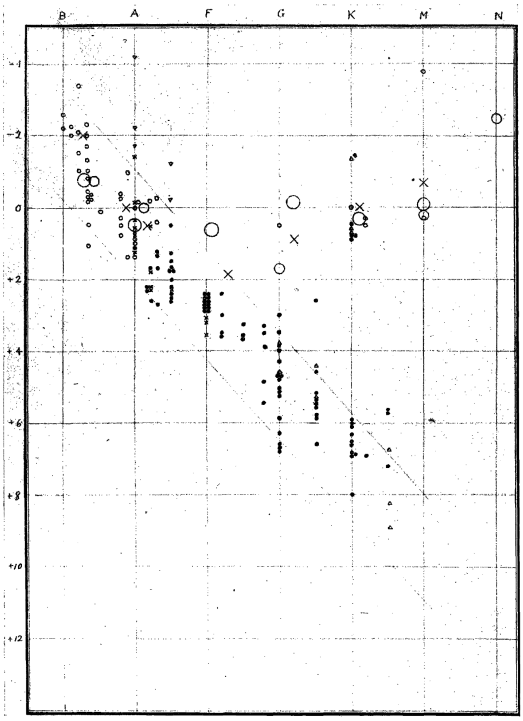

Figure 2.19 An HRD from Russell (1914). The different marker types correspond to membership to different moving cluster. One can see that the MS is denoted with the diagonal lines (though it is not yet referred to as such in the publication).

stars became *s*-process enhanced during a mass transfer phase with the more evolved companion while the companion was in the AGB phase.

Similarly, there are observations that have shown that there are many more extremely metal-poor stars with strong carbon enhancement than predicted (Beers et al. 1992, Beers 1999, Rossi et al. 1999, Aoki et al. 2007, Suda et al. 2011). These carbon-enhanced metal-poor (CEMP) stars are further sub-categorized based on whether the surface abundances show no signs of heavy element enhancement (CEMP-no), signs of *s*-process enhancement (CEMP-s), signs of *r*-process enhancement (CEMP-r), or signs of both *r*- and *s*-process enhancement (CEMP-r/s) (Beers & Christlieb 2005). The *i*-process has been invoked to explain the abundance signatures of the CEMP-r/s stars as multiple studies have determined that these star's abundances cannot be explained by a linear combination of *r*- and *s*-process contamination (Jonsell et al. 2006, Lugaro et al. 2012, Dardelet et al. 2014, Hampel et al. 2016). Again in the case of CEMP stars the abundance of neutron capture elements is assumed to be the result of contamination by a companion star, where the *i*-process actually occurred, which is now a white dwarf.

To be labeled a CEMP star the star must have $[\mathrm{Fe/H}] < -1$ and $[\mathrm{C/Fe}] > 1$ (Beers & Christlieb 2005). The criteria for classifying the CEMP stars into their various sub-classifications is complicated and has continued to develop over

the years. Originally, the focus was primarily on Ba and Eu. Ba is traditionally considered an *s*-process element and Eu an *r*-process element. So one could analyze the spectra of a CEMP star and try and match the resulting abundances to a solar *s*- or *r*-process abundance curve which had been scaled to the appropriate metallicity. For a CEMP-s star the Ba abundance would be a good match for the scaled solar *s*-process abundance curve. A CEMP-r star would have a Eu abundance which matches well to the scaled solar *r*-process abundance curve. A CEMP-no star would have no unusual heavy element abundances. Finally, a CEMP-r/s star would have a Ba abundance which matches a scaled solar *s*-process, but it would also have a Eu abundance which matches well to the scaled solar *r*-process curve. One of the original ideas to explain this was to assume the star was born from ISM material with a high *r*-process enrichment and then was contaminated with *s*-process enriched material by a companion star (Jonsell et al. 2006). Research into these stars revealed that the abundance pattern of the CEMP-r/s stars cannot be replicated by assuming a star which has undergone and/or been contaminated by material enriched by both the *r*-process and the *s*-process (Lugaro et al. 2012). Furthermore, the Eu and Ba abundances of CEMP-r/s stars as a group are actually correlated. This would also be difficult to explain under the paradigm where CEMP-r/s stars are a mixture of *r*-process and *s*-process material. Why should the abundances of two different elements created via different nuclear burning processes in different astrophysical locations be correlated? This all points to the need for a single nucleosynthetic process which can explain these stars. As it would seem that this nucleosynthetic process should have properties between that of the *r*-process and the *s*-process, the *i*-process is a logical candidate.

As more CEMP stars were observed the classification of these stars into their various subgroups became more complicated. Additionally, different researchers would use slightly different criteria. A classification system that was widely used was the one of Beers & Christlieb (2005). Their classification system worked as follows:

- CEMP-s: $[\mathrm{Ba/Eu}] > 0.5$
- CEMP-r/s: $0.0 < [\mathrm{Ba/Eu}] < 0.5$
- CEMP-r: $[\mathrm{Ba/Eu}] < 0.0$ and $[\mathrm{Eu/Fe}] > 0.0$

This system works well but some researchers still felt it was not able to handle all CEMP stars. In Karinkuzhi et al. (2021) they propose a more elaborate classification scheme. Their approach involves calculating the "distance" between a CEMP star's abundance distribution and the solar *r*-process abundance distribution. To do so one must choose a set of heavy elements, they use Y, Zr, Ba, La, Ce, Nd, and Sm, and then calculate the signed distance as

$$d_S = \frac{1}{N} \sum_{x_i} \left(\log_{10} \epsilon_{x_i,*} - \log_{10} \epsilon_{x_i,\mathrm{norm}(r,*)} \right) \tag{2.38}$$

and the root mean square distance as

$$d_{\mathrm{rms}} = \left(\frac{1}{N} \sum_{x_i} \left(\log_{10} \epsilon_{x_i,*} - \log_{10} \epsilon_{x_i,\mathrm{norm}(r,*)} \right) \right)^{1/2} \tag{2.39}$$

where the sum is over the set of heavy elements chosen, the $*$ subscript refers to the observed star, and $\log_{10} \epsilon_{x_i} = \log_{10}(n_{x_i}/n_{\mathrm{H}}) + 12$. The quantity $\log_{10} \epsilon_{x_i,\mathrm{norm}(r,*)}$ is the standard r-process abundance profile, $\log_{10} \epsilon_{x_i,r}$, normalized to the star's Eu abundance: $\log_{10} \epsilon_{x_i,r} + (\log_{10} \epsilon_{\mathrm{Eu},*} - \log_{10} \epsilon_{\mathrm{Eu},r})$. Using these quantities they then define the following criterion for the demarkation of CEMP-s and CEMP-r/s stars:

- CEMP-s: $d_S > 0.6$
- CEMP-r/s: $d_S < 0.6$.

In Figure 2.20 one can see an example of the abundance distribution for a CEMP-r/s, CEMP-s, and CEMP-r star. The data points are observations of actual CEMP stars and the solid lines are model predictions from a stellar evolution code.

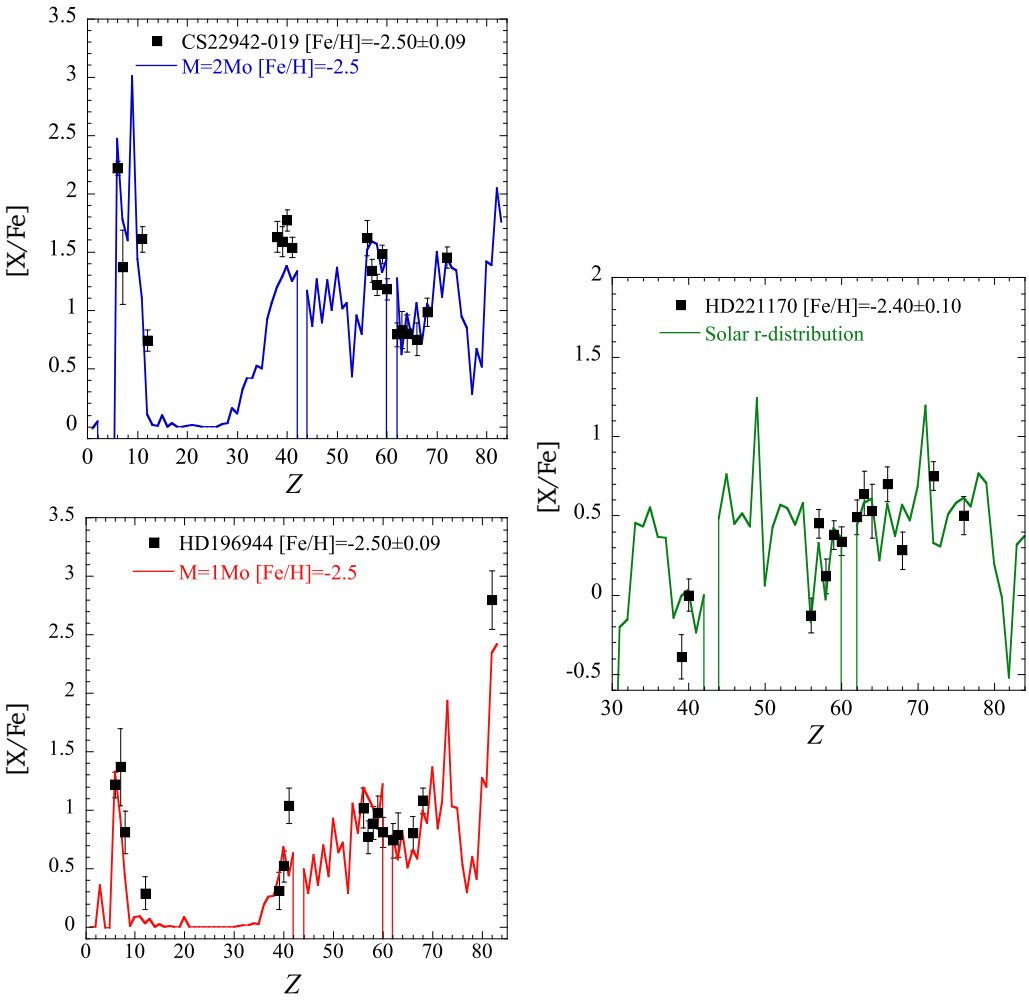

Figure 2.20 A comparison of the abundance pattern for three CEMP stars: CEMP-r/s in red, CEMP-s in blue, and CEMP-r in green. The data points are observations of the star which is shown in the legend. Solid lines are model predictions for a model with the parameters shown in the legend. This is taken from Fig. 11 in Karinkuzhi et al. (2021).

2.3.2 Variability

As many as 90% of TP-AGB stars are what are known as *long-period variables* or LPVs. LPVs are, as the name suggests, characterized by long-period variations in their flux. This separates them from shorter period variables such as Cepheids whose variability is shorter and has a different physical origin. The observation of the first LPV occurred in 2 steps. In 1596 the East Frisian (now days The Netherlands) clergyman and astronomer Fabricius was studying Jupiter and noticed that a star in the constellation of the whale (Cetus) disappeared (Hoffleit 1997). He originally believed it to be a "Stella Nova" — Tycho Brahe had discovered the first stella nova (Tycho's Supernova) two decades earlier in 1572 (Brahe 1573) — but he saw the star had reappeared in later observations. In 1638 the Dutch

astronomer Holwarda observed that the star dis- and reappeared with a period of about one year. This star received the name "Stella Mira", the "miraculous" or "amazing star" and is the prototypical Mira variable star (Habing & Olofsson 2004).[10]

Now days LPVs are split into four classifications: *Mira-like* (M), *semi-regular of type a* (SRa), *semi-regular of type b* (SRb), and *Irregular* (L). The classifications are based on the amplitude of the variations of the flux in the V-band as well as how consistent the period of variability is. Mira-like variables have the largest amplitude and most consistent period while Irregular variables have small amplitudes and irregular periods. Variability is one of the most important criteria observers have to separate E-AGB stars from their thermally pulsing elders.

2.3.3 Meteorites

In 1794, Ernst Florens Friedrich Chladni was the first to recognize the extraterrestrial origin of meteorites, which he referred to as „Weltenspäne" [*"World shavings"*][11] (Chladni 1794). It was a common belief at the time that meteorites were of a volcanic origin (Society 1802). It came to be accepted that meteorites were not only of extraterrestrial origin but that they also are among the oldest objects in the solar system, dating back to its formation. The analysis of meteorites has impacted both nuclear physics and astrophysics. Meteorite analysis done by Harkins (1917) first revealed the odd-even effect of atomic number on abundance. This phenomenon, still sometimes referred to as the "Harkin Effect", shows that nuclei with even number of nucleons are more abundant than their odd neighbors. This was eventually explained with the nuclear shell model (see Section 2.1). Additionally, Noddack & Noddack (1930), Goldschmidt (1937), and Suess & Urey (1956) compiled the early abundance distribution catalogues using data from meteorites as well as solar observations. These abundance distributions proved to be invaluable tools for many astrophysical researchers.

The oldest solid bodies in the solar system are found in meteorites. These *calcium-aluminum-rich inclusions* or CAIs are found in the most primitive of meteorites. CAIs are one of the major components of *chondrites*, a subclass of *stony meteorites*. These meteorites are "undifferentiated" meaning they did not suffer mass fractionation which occurs, for example, with any change of phase such as melting in the core of large asteroids. On the other hand, "differentiated" meteorites, such as *iron* and *stony-iron* meteorites have undergone these processes. Undifferentiated meteorites can be used to date the formation of the meteorites and thus the Solar System and the Sun. To do this one must leverage our understanding of radioactive decay chains and the half-lives of the participating

[10] It is possible, though unclear, that Mira was observed by astronomers as far back as Aratus (315–245 B.C.), Hipparchus (134 B.C.), and Chinese observers (1070 A.D.) (Hoffleit 1997).

[11] Translation mine

isotopes. Differentiated meteorites are not suited for this task as the process of differentiation itself will produce isotopic anomalies which cannot be confidently separated from the expected changes arising from radioactive decay.

The key to all meteorite analysis, including dating the meteorite, is the *law of radioactive decay*. Consider a parent isotope, P, and a daughter isotope, D, where $P(t)$ and $D(t)$ are the abundances of the parent and daughter isotope respectively at time t. Using the radioactive decay law (Rutherford & Soddy 1903) we know that $P(0) = P(t)e^{\lambda t}$, where $\lambda = \ln(2)/t_{1/2}$ is the *decay constant* and $t_{1/2}$ is the half-life of the decay from P to D. Thus,

$$D(t) = D(0) + P(t)\left(e^{\lambda t} - 1\right), \tag{2.40}$$

and we would like to solve for t. $P(t)$ and $D(t)$ can be measured but $D(0)$ is unknown and cannot be measured. The way around this impasse is to consider a third, stable isotope, S, which is of the same element as D. The assumption being that the two isotopes would experience the formation of the meteorite the same and thus the quantity $D(0)/S(0)$ is identical from one sample to another. Therefore, Equation (2.40) can then be written

$$\frac{D(t)}{S(t)} = \frac{D(0)}{S(0)} + \frac{P(t)}{S(t)}\left(e^{\lambda t} - 1\right) \tag{2.41}$$

One may recognize this as the equation of a line where the unknown quantity, $D(0)/S(0)$, is the y-intercept. Thus, one need only take multiple samples measuring $D(t)$, $S(t)$, and $P(t)$ and plot them to find $D(0)/S(0)$ at which point one can solve for t. A classic example of a set of such isotopes is $P = {}^{87}\mathrm{Rb}$, $D = {}^{87}\mathrm{Sr}$, and $S = {}^{86}\mathrm{Sr}$.

But meteorites hold more information than simply their age. The first hint of the existence of what came to be known as *stardust grains* appeared in the 1960s when analysis of the composition of the noble gases Ne (Black & Pepin 1969) and Xe (Reynolds & Turner 1964) trapped inside old carbonaceous chondrite meteorites showed the presence of exotic components with isotopic compositions completely different to the "normal" Solar System material. Eventually microscopic dust grains were recovered from meteorites, displaying enormous anomalies in their isotopic compositions relative to the solar composition. These are too large to be attributed to fractionation or cosmic rays. In Figure 2.21 one can see the large variation in isotopic abundances found in different star dust grains attributed to various astrophysical sources. The white rectangle shows the range of the isotopic abundances which are found in "normal" Solar System material. Where the dashed lines cross is the solar value of these isotopic ratios.

The stardust grains originated as dust grains in the gas surrounding stars. One obvious, and observationally confirmed, candidate location for the formation of dust is the wind-driven, outer layers of AGB stars. Another astrophysical site

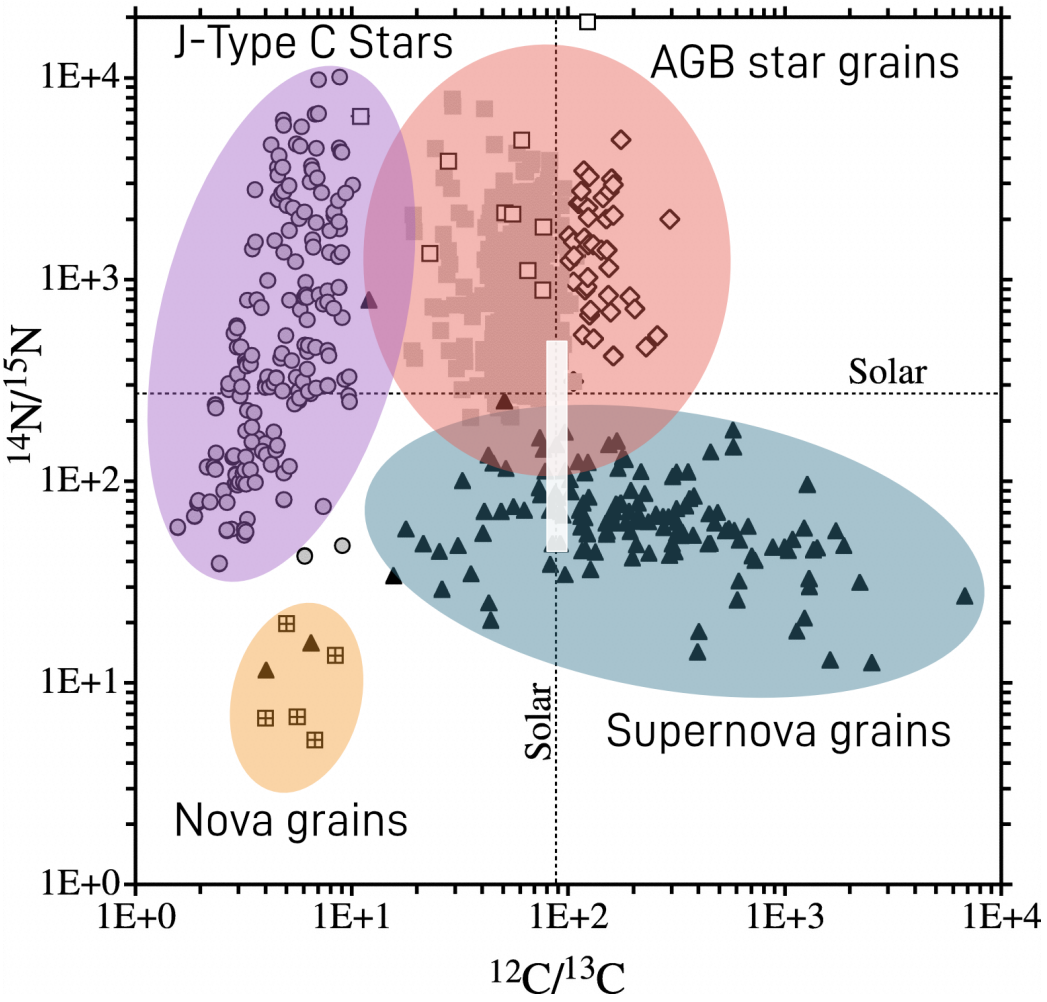

Figure 2.21 N and C isotopic ratios of individual presolar SiC grains. The solar value of the isotopic ratios is given by the dashed lines. The shape of the markers correspond to the type of stardust grain the measurement comes from. The colored ellipses show those stardust grains which are thought to have originated at a particular astrophysical source given by the labels near the ellipses. The white rectangle roughly shows the range of the isotopic abundances which are found in "normal" solar system material. This figure is Figure 1 from Zinner et al. (2006). The annotations are mine based on a similar figure from Hoppe (2010).

where dust is observed to form is the cooled ejecta of core-collapse supernova explosions. When the Sun and Solar System formed some of the stardust grains had traveled from their formation site and became trapped inside meteorites from which they are recovered today. Since stardust grains carry the detailed signature of the isotopic composition of the gas that surrounds stars, they are effectively small shavings of stars. While the bulk of the solar system material comes from many different stars as a result of the chemical evolution of the Galaxy, each stardust grain instead carries the nucleosynthetic signature of the particular site of its formation.

The analysis of stardust grains is very similar to that done for dating meteorites. For various combinations of D, S, and P, one can determine $\frac{D(0)}{S(0)}$ to glean information on the abundance of the material from which the meteorite formed. The value of this ratio for a material can show an excess in a daughter nucleus as compared to standard solar system material and is a sign that it is a stardust grain. For example, a large excess of ^{26}Mg as compared to the stable Mg isotope, ^{24}Mg, is a sign that the meteorite formed with ^{26}Al which decays into ^{26}Mg (Lugaro et al. 2018). These excesses are measured as per mil or per ten thousand variations with respect to some lab standard, denoted as δ- or ϵ-values, respectively:

$$\delta\left(^{26}\mathrm{Mg}/^{24}\mathrm{Mg}\right) = \left(\frac{\left(^{26}\mathrm{Mg}/^{24}\mathrm{Mg}\right)_{\mathrm{measured}}}{\left(^{26}\mathrm{Mg}/^{24}\mathrm{Mg}\right)_{\mathrm{standard}}} - 1 \right) \times 1000. \tag{2.42}$$

A linear correlation between the excess and the elemental ratio, $\delta(^{26}\mathrm{Mg}/^{24}\mathrm{Mg})$ vs Al/Mg, proves that ^{26}Al was incorporated into the sample. The abundances of certain radioactive isotopes, such as ^{135}Cs or ^{205}Pb, in stardust grains provide tight constraints on the nucleosynthesis in stellar sources such as AGB stars (Lugaro et al. 2018).

Chapter 3

History

> ...the heaven's glorious sun
> That will not be deep-search'd with saucy looks:
> Small have continual plodders ever won
> Save base authority from others' books
>
> — William Shakespeare, *Love's Labour's Lost*

The development of our understanding of stellar nucleosynthesis spans a century of scientific inquiry, marked by crucial theoretical advances and observational discoveries. This chapter examines this development in two distinct periods: from 1920 to 1995 (Section 3.1), when the fundamental concepts were established, and from 1995 to the present (Section 3.2), focusing on recent refinements in our understanding of AGB nucleosynthesis. While the reader may proceed directly to Section 3.2, the ability to place discoveries and advancements in a historical context and to understand how our knowledge has progressed will provide the reader with a greater appreciation of the field as a whole and the value of our scientific inheritance. Hopefully, the reader leaves the section with a much more optimistic view of the progress science has made than Biron in *Love's Labour's Lost* (see epigraph). Section 3.2 will begin with a timeline of the important milestones covered in Section 3.1 for those who skipped that section. All readers are recommended to read this section.

3.1 1920 to 1995

"We are pulling at the wrong end of the tangle, which has to be unravelled by a different approach." So opined Arthur Eddington in his 1920 paper on the internal constitution of stars (Eddington 1920). The "tangle" he referred to was the

question of how the Sun produces its energy. In this paper Eddington asserts that Lord Kelvin was "pulling at the wrong end of the tangle" by trying to explain this energy production via gravitational contraction which, as was known even then from geological evidence, grossly underestimates the lifetime of the Sun. Instead he proposed a different approach; what if this energy came from nuclear processes? Specifically, the fusion of H to He could provide the energy needed. This was not the first time that it was suggested that the energy of the atom powers the Sun. In 1903, Rutherford and Soddy calculated the energy released via the nuclear decay of heavy elements like radium (Rutherford & Soddy 1903). They found that it is more energetic than any known chemical reaction. Realizing that this decay energy is necessarily only a small part of the internal energy of the atom they suggested that

> The maintenance of solar energy, for example, no longer presents any fundamental difficulty if the internal energy of the component elements is considered to be available, i.e. if processes of sub-atomic change are going on. (Rutherford & Soddy 1903, pg. 591)

Nevertheless, Eddington's conjecture was concrete, identifying the specific process via which the internal energy of the atom could be released (H fusing to He), and also, for the time, bold. Only one year earlier the first artificial nuclear reaction (i.e. excluding decays which happen naturally without intervention) was produced: $^{14}\mathrm{N}(\alpha, \mathrm{p})^{17}\mathrm{O}$. Again it was Rutherford who had published the experiment in which protons were seen being ejected by nitrogen atoms being bombarded with α-particles (Professor Sir E. Rutherford F.R.S. 1919), and, as Eddington wrote, "…what is possible in the Cavendish Laboratory may not be too difficult in the Sun." (Eddington 1920) It remained unclear, however, how this process would work. The neutron was unknown at the time, not to be discovered for another 12 years, and a He nucleus was thought to be composed of 4 protons and 2 electrons. This meant all six constituents would have to meet simultaneously to form He.

There were, however, other ideas for powering the Sun. James Jeans had two ideas. The first was that the energy generation was the result of the annihilation of protons and electrons (Jeans 1924). The main benefit of this theory was that it explained why stars seem to lose mass. This was quickly challenged on the grounds that a proton and electron are unlikely to annihilate given their vastly different properties, such as mass (Schumann 1925). His second idea was that the Sun was composed of "super-heavy elements" which were heavier than any found on Earth (Jeans 1925a). These elements would then decay providing the energy needed for the Sun. Henry Russell, on the other hand, thought that there are a series of critical points at which some process comes into play which can annihilate some new portion of material to release energy and cause the Sun to lose mass (Russell 1925). White dwarfs are then composed of some immutable substance which

cannot be annihilated. The primary difference between the models is that Jeans' hypothesis implies no dependence of the energy generation on temperature. In the words of Jeans, "If my stellar matter is compared to uranium, Russell's must be compared to gunpowder." (Jeans 1925b)

A key pillar of our understanding of nuclei was erected over the course of a series of papers by Aston in the early 1920's (Aston 1919, 1920a,b,c, 1921, 1922). Using a machine of his own invention, the mass-spectrograph, Aston was able to show definitively that not every atom of an element is the same. Most known elements actually consist of atoms with the same charge but different weights: the isotope. This was not a new idea. The name had been coined years earlier by Soddy (Soddy 1913). At that time research into radioactive elements had shown that certain decay chains lead to elements with different weights but identical chemical properties. This was, however, thought to be unique to the radioactive elements. Aston was able to show that, not only was it not unique to radioactive elements, it is almost a ubiquitous property of elements across the entire periodic table of elements. He was also able to reason from his accurate mass determinations that the difference in weight between isotopes was equal to the weight of a proton. Thus, he naturally concluded that "Nature uses the same standard bricks in the construction of the atoms of all elements, and that these standard bricks are the primordial atoms of positive and negative electricity, protons and electrons." An isotope then, he claims, is simply the result of adding or subtracting a proton-electron pair to the nucleus, changing the mass by that of effectively one proton (electrons being roughly 1/1000 as massive as protons) but not affecting the charge.

He was also able to draw a further critical conclusion from his weight measurements. A He nucleus weighs less than 4 protons and 2 electrons. He correctly proposes that the missing weight is due to the energy which binds the nucleus together which he associates with how densely "packed" the electrons and protons of the nucleus are. The implication of this as it relates to energy release is not lost on him:

> it is the first step towards what may well be the greatest achievement of the human race, the release and control of the so-called "atomic energy." … If we could transmute the hydrogen contained in one pint of water the energy so liberated would be sufficient to propel the *Mauretania* across the Atlantic and back at full speed. (Aston 1922, pg. 705)

These studies by Aston were among the primary evidence used by Eddington to support his energy source hypothesis.

Three years later Condon used Einstein's famous equation, $E = mc^2$ (Einstein 1905a), to provide an alternative estimate for the lifetime of the Sun (Condon 1925). The idea, Condon explains, comes directly from Einstein's paper

where he states „Die Masse eines Körpers ist ein Maß für dessen Energieinhalt; ändert sich die Energie um L, so ändert sich die Masse in demselben Sinne um $L/9 \times 10^{20}$, wenn die Energie in Erg und die Masse in Grammen gemessen wird.“ [*“The mass of a body is a measure of its energy content; if the energy changes by L, then the mass changes in the same way by $L/9 \times 10^{20}$, where energy is measured in erg and mass in grams.”*][1] (Einstein 1905a). Thus, considering the luminosity of the Sun as well as its mass, Condon estimates the lifetime of the Sun to be on the order of 10^{12} years. However, the actual source of this energy is not considered:

> It is necessary to bear in mind that, from the manner of its derivation, the equation [$E = mc^2$] necessitates that loss of mass by a system accompany loss of energy as a result of radiation. We do not need to inquire into the source of the energy lost by radiation. (Condon 1925, pg. 126)

However, the estimate Condon obtains is not far off from Eddington's estimate of 15 billion years based on an atomic energy source, and both are far closer to being in agreement with the geological data than the prediction of Lord Kelvin.

Around this time important observational results came to light. Firstly, Harkins (1917) noticed two things when studying isotopic abundances measured from meteorites. One, the abundance of nuclei with an even number of nucleons is higher than that of their odd neighbors, and, two, the so-called α-elements (^{12}C, ^{16}O, etc.) have much higher abundances than their neighboring isotopes. This implies that these isotopes are particularly stable. Secondly, Aston (1924), continuing his work on isotopes, showed that almost all elements have isotopes and that the relative abundance of the isotopes of an element vary from element to element. Finally, Goldschmidt (1930) saw that when the abundance of isotopes was plotted as a function of mass number, and not atomic number as was standard practice at the time, there are peaks in the abundance distribution. All of these observations call for some theory of the structure of the nucleus in order to explain them. This would spawn many competing theories. Harkins, for example, saw the stability of the α-elements as evidence that the nucleus contained α-particles as the basic building blocks, a theory which was widely purported for many years.[2]

Additionally, there were still the succession of atomic models from the Cavendish laboratory at Cambridge which were the standard models of the time. Beginning with the infamous “plum pudding model” of J. J. Thomson (Thomson 1904) in which the electrons are embedded in a positive volume like plums in a plum

[1] Translation mine

[2] In the late 1920s Schrödinger criticized his colleagues for their belief in this model: “Just because you see an α-particle coming out of the nucleus, you should not necessarily conclude that inside they exist as such!”. He was correct. Both for α- and β-decays, particles emitted from nuclei are only created at the moment of escape (Jensen 1965)

pudding. His student Ernest Rutherford updated this model after the famous "gold-foil experiment" (Rutherford 1911). In this model, the Rutherford model, the electrons orbit a massive positively charged nucleus. Interestingly, seven years earlier Nagaoka (1904) had already proposed the idea of a "Saturnian" model of the atom in which rings of electrons orbit a central positive charge, though the idea lacked experimental backing or a theoretical explanation for why such a system should be stable. The issue of stability plagued the Rutherford model as well. Additionally, that same year, Van Den Broek (1911) was the first person who realized that the position of the elements in the periodic table was due to the charge of its nucleus. Before that the ordering was largely based on the atomic weight except for in certain cases such as Ni and Co where the ordering by atomic weight was not kept due largely to the intuition of chemists whose experiments showed the properties of the elements suggested an alternate ordering. This idea supports the Rutherford model of a central positive charge surrounded by a cloud of electrons.

Around this time, we see the first attempts at incorporating the new field of quantum mechanics into a model of the atom. Haas (1910) had already established the relationship between Planck's constant and atomic dimensions, being the first person to accurately estimate what would come to be known as the Bohr radius, and Nicholson (1912a) and Nicholson (1912b) first associated the spectral line radiation he observed in the solar corona as being due to the quantized nature of the energy of electrons in an atom. These ideas were solidified by Rutherford's student Niels Bohr[3] who added quantum mechanical effects to Rutherford's model deriving the electron shell structure of the atom and solving the model's stability issue (Bohr 1913). That same year a series of experiments conducted by Henry Mosely (Moseley 1913, 1914) effectively proved not only the Rutherford/Bohr model's central positive mass surrounded by electrons but also the ordering of the elements on the periodic table being due to the charge of the nucleus. Furthermore, he was able to show that there were missing gaps in the periodic table. One example is the gap at atomic number 43. This would later be identified as Technetium (Tc) which has no stable isotopes. We will see that this will have important consequences later. The Bohr model, while very successful as an atomic model, proved not very useful in penetrating the mysteries of the nucleus itself. Those mysteries would have to wait.

The study of abundances once again lead to a surprise at the end of the 1920's. Unsöld (1928) and later Russell (1929) determined that the abundance of H and He in the Sun is vastly different than on Earth. This defied the conventional wisdom of the time that the composition of both bodies was roughly the same. In fact, this result was so surprising that Russell himself had refused to believe the same conclusions which were presented in Cecilia Payne's Ph.D. thesis (Payne

[3] One of 11 future Nobel laureates trained by Rutherford (Rhodes 2012, pg. 66).

1925b) four years earlier and convinced her to back off from her conclusions in the resulting paper (Payne 1925a). In that paper, Payne writes "Hydrogen and helium are omitted from the table. The stellar abundance deduced for these elements is improbably high, and is almost certainly not real." The new abundance measurements meant that there are significantly more protons available for Eddington's energy source, but the question of how these reactions would occur was still unanswered.

One of the most important steps in solving this conundrum came by way of Gamow. In 1925, an experiment by Rutherford and Chadwick showed that α-particles emitted by uranium have less energy than than they should gain from the repulsive Coulomb field of the uranium nucleus (Rutherford & Chadwick 1925). To solve this apparent paradox, in his 1928 paper, Gamow describes the phenomenon of quantum tunneling (Gamow 1928)[4]. The α-particle tunnels its way through the Coulomb field of the uranium nucleus and thus the Coulomb field only imparts its energy on the α-particle from the point where it is done tunneling onward. While the theory was developed to explain how particles can escape a nucleus during decays, it also makes it easier for a nucleus to capture an incoming particle. This allows reactions to occur at higher rates and at lower temperatures than previously thought possible since the Coulomb barrier of a nucleus need not be entirely overcome. Two years after this success Gamow would attempt to also explain the structure of the nucleus by assuming that Harkins was correct and that nuclei are built from α-particles. His model consists "…of a nucleus built from α-particles in a way very similar to a water-drop held together by surface tension." In his model, though, a certain number of protons and electrons can be bound to the aggregations of α-particles (Gamow 1930).

The possible implications of quantum tunneling on nuclear reactions was immediately clear. Atkinson & Houtermans (1929) investigated the application of quantum tunneling on nuclear reactions in stars. They find that protons are likely able to penetrate lighter elements and that

> Daraus ergibt sich die Möglichkeit, die Energieentwicklung der Sterne aus den Massendefekten der Elemente zu erklären, wobei die Annahme von Sechserstößen für den He-Aufbau vermieden wird. [*This raises the possibility of explaining stellar energy generation from elemental mass defects, avoiding the assumption of six-particle collisions for He buildup.*][5] (Atkinson & Houtermans 1929, pg. 656)

Additionally, they note that, even with quantum tunneling, they see no way of creating the heavy radioactive elements via direct fusion. Atkinson would continue to research the idea of nuclear reactions in stars and, in 1931, published

[4] Independently, Gurney and Condon developed the same theory in Gurney & Condon (1929), which was published only a few months after Gamow's paper.

[5] Translation mine

two papers (d'Escourt Atkinson 1931a,b) on his ideas for creating He in stars without the need for a six-particle reaction. The process he proposes involves a series of proton captures on light elements until an unstable isotope is reached which would then decay via the emission of an α-particle. He referred to this as a "regenerative process" because the abundance of the light element which initially captured a proton would not change.

Part three of the paper series by Atkinson (d'Escourt Atkinson 1936) was not written until 1936. By this time two very important new discoveries caused Atkinson to revisit his original ideas. In 1932, Chadwick correctly explained the energetic, neutral radiation, which had been observed by others, such as Curie & Joliot (1932), as the neutron (Chadwick 1932), and, in 1932, Urey et al. (1932) had discovered deuterium based on the prediction of Birge & Menzel (1931). Atkinson argues that, in light of these new discoveries, the only option for the first step of a proton-to-He reaction chain in stars is $\mathrm{p}\,(\mathrm{p}, e^+ + \nu)^2\mathrm{H}$.

The discovery of the neutron had a profound impact on the study of nuclear structure. The α-particle model of Harkins and Gamow was jeopardized and the Bohr model of the atom remained unable to explain the properties of the nucleus itself. The time was ripe for new theories. Bartlett (1932) attempted to explain why certain isotopes such as ^{4}He and ^{16}O are particularly stable by assuming that the nucleus has a shell structure in analogy to the atomic shell structure. ^{4}He and ^{16}O then correspond to closed shells which are particularly stable configurations. Elsasser (1934) attempted to explain the abundance peaks seen by Goldschmidt as being due to those nuclei having a "special" number, later to be known as "magic number"[6], of neutrons and/or protons which would lead to particularly stable nuclei. He correlated these numbers with closed shells following Bartlett (1932). At the same time, Bohr (1936) and Bohr & Kalckar (1937) proposed an alternate view of the nucleus, extending the idea first proposed by Gamow (1930), which would come to be known as the "liquid drop model" due to the similarities between the modeling of the forces on the outermost nucleons of the nucleus and the modeling of surface tension in a water droplet[7]. In this case though, they dropped Gamow's original assumption that He nuclei are the building blocks of all nuclei. A great debate raged for many years over the two models, and, as it turns out, both models are successful in explaining certain aspects of nuclear physics and Nobel prizes would be awarded to scientists for work on both models (Shaviv 2012).

Finally, 19 years after Eddington's hypothesis, the foundation of stellar nucleosynthesis would come into being in the span of only 2 years. In 1939, Hans Bethe

[6]The term magic number was coined by Eugene Wigner as a pejorative moniker for the idea. Indeed a number of prominent physicists viewed magic numbers as an exercise in numerology and not as real physics (Jensen 1965, Mayer 1964).

[7]Interestingly, the first paper Bohr ever published was on determining the surface tension of water (Bohr 1909).

published his paper showing that the conversion of protons to He — what would one day be called the proton-proton chain — could provide the energy which powers stars (Bethe & Critchfield 1938). Additionally, Carl von Weizsäcker and Hans Bethe had independently derived the CNO cycle in 1938 and 1939, respectively (von Weizsäcker 1937, 1938, Bethe 1939a,b). Both processes validated the predictions by Atkinson. The proton-proton chain begins with the reaction which he predicted would be the first step from synthesizing protons to He, and the CNO cycle could be classified as a regenerative process. While these papers established a theoretical basis for nuclear burning in stars, there was still no observational evidence proving nuclear burning occurred in stars at all. But all the isotopes we observe must come from somewhere.

One alternate attempt to explain the origin of the elements was the famous "Alpher–Bethe–Gamow"[8] paper (Alpher et al. 1948). This paper, which correctly determines the relative abundances of H and He due to Big Bang nucleosynthesis, suggested that the abundances of *all* atomic nuclei are due to neutron captures immediately following the Big Bang[9]. Gamow reasoned that the elements could not have been created in an equilibrium scenario. His argument was as follows. The binding energy of nuclei increases with atomic weight, i.e. $A \propto \mathrm{BE}$. Thus, any equilibrium process would lead to an exponential decrease in abundance. However, observations only show this is true up to Fe. Heavy elements show strong deviations from this trend and, thus, require non-equilibrium conditions such as those found during the Big Bang. As an interesting side note, the calculations for this paper were only possible due to 97 papers from the Manhattan Project being declassified and presented at the 272nd American Physical Society Meeting in 1946. This included crucial neutron capture data (Shaviv 2012).

The main stumbling block for the "hot Big Bang" theory, as it came to be known, came with the realization that there are no stable isotopes with an atomic mass of 5 or 8 (recall Figure 2.1 where this was already pointed out). This creates an impassable roadblock for neutron captures to overcome. However, the gap at $\mathrm{A} = 5$ and $\mathrm{A} = 8$ was a problem for stellar nucleosynthesis as well, having already been a stumbling block for Bethe when trying to determine how stars could synthesize C from He. If He captures a proton the resultant nuclide will have $\mathrm{A} = 5$ and decay back to an $\mathrm{A} = 4$ nuclide thus not climbing any higher in mass. Similarly, two He nuclei reacting will produce a nuclide with $\mathrm{A} = 8$ and also decay to lower A.

In 1954, Hoyle, a long time advocate for the idea that the synthesis of the

[8]The paper is also referred to as the $\alpha\beta\gamma$ paper due to the similarity of the author's last names to the Greek letters. In fact, Gamow added Bethe as an author on the paper exactly for this reason (Gamow 1961, pg. 64).

[9]The name "Big Bang" only came about later via Fred Hoyle who used the image of a big bang to help explain the theory in 1949 on a BBC radio show. It may or may not have been denigratory (Kragh 2013).

elements occurred in stars, pointed out that the gap at A = 8 was not an issue in stars because the high densities allowed for the possibility of a triple body reaction: $\alpha + \alpha + \alpha \rightarrow {}^{12}\mathrm{C}$ (Hoyle 1954). His work on what would come to be known as the triple-α reaction is best known for his prediction of an energy level in C. Based purely on astrophysical arguments such as the relative abundance of C to O, he was able to predict that the ^{12}C nucleus had an energy level at around 7.7 MeV corresponding to a resonance which would allow for the triple-α reaction to occur. The energy level was later experimentally confirmed to exist (Dunbar et al. 1953).

Mayer (1948) finalized the explanation of the magic numbers. Mayer summarized the then available data showing that nuclei with proton or neutron numbers of 20, 50, 82 and 126 are particularly stable and that these nuclei would have very low neutron-capture cross-sections. One year later she was able to use the nuclear shell model to explain why magic nuclei are particularly stable by including a strong spin-orbit coupling term (Mayer 1949). The inclusion of this term causes the energy levels of certain states to change drastically. Where there would otherwise have been available energy levels there are now large gaps with no available energy levels. The proton or neutron number where these gaps occur are the magic numbers. This can be see in Figure 3.1. Interestingly, in Haxel et al. (1949) and Jensen et al. (1949), the spin-orbit coupling was independently proposed. The first paper, Haxel et al. (1949), was rejected by the journal Nature under the accusation that "it is not really physics but rather playing with numbers" (Jensen 1965).

Finally, in 1952, the question of whether stellar nucleosynthesis occurs was answered. Paul Merrill discovered the spectral lines of Tc I in several giant stars (Merrill 1952). Given that Tc, one of Henry Mosely's missing gap elements, has no stable isotopes and any Tc isotope would decay within a few million years at most (Greenstein 1954), the discovery was irrefutable evidence that Tc is made *in situ* in these stars via nuclear processes. This undoubtedly came as a shock at the time. One of the few people who had seriously considered the idea of stars creating elements heavier that helium was Fred Hoyle (Hoyle 1946, 1954). He proposed that the elements between C and Fe could be created via nuclear reactions in certain very hot stars. Tc on the other hand is even heavier than Fe and there was no clear way in which a star could produce it.

One year later a seemingly unrelated discovery was made through observations of the M 92 globular cluster. Recent advancement in photovisual plates and photoelectric techniques had lead observers to unprecedentedly accurate color-magnitude diagrams (CMD), and in Arp et al. (1953) they noticed a new feature of the CMD of M 92. There appeared to be a "bifurcation" of the giant branch (see Figure 3.2), the meaning of which was unclear to them. In the same year observations of M 3 revealed the same feature (Sandage 1953). The explanation of this feature would remain elusive for a time.

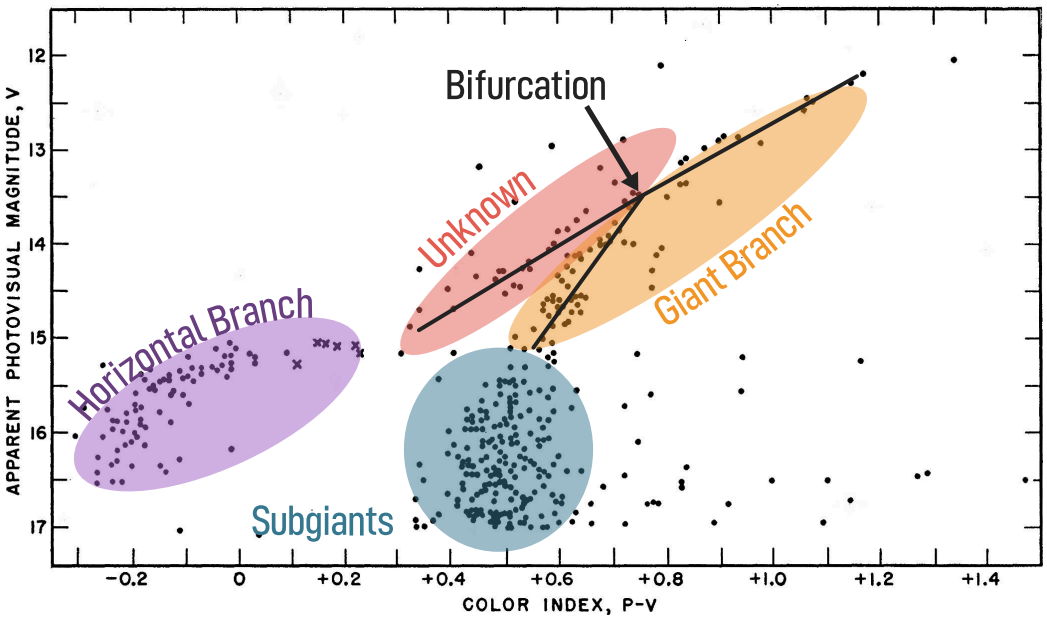

Figure 3.2 Figure 2 from Arp et al. (1953) showing the bifurcation of the giant branch. The annotations are mine.

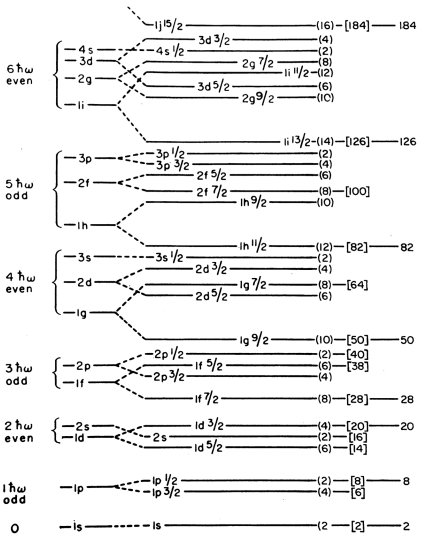

Figure 3.1 A schematic diagram showing the energy levels for protons in a nucleus. The splitting of the dotted lines shows the effect of the spin-coupling term. Figure 6 in Mayer (1964).

An explanation for Tc in stars, however, did not have to wait long. Cameron (1955) laid out a proposal that neutron captures in giants could produce isotopes up to lead and bismuth at which point the neutron-capture path terminates in a closed loop due to the isotopes above Pb and Bi being unstable. Such a process would require a neutron-source reaction, a reaction which can continually produce neutrons, since the lifetime of a free neutron in stellar conditions is on the order of 10 min. The source of the neutrons, he determined, is the $^{13}\mathrm{C}(\alpha, \mathrm{n})^{16}\mathrm{O}$ reaction for which he calculated the rate and found it can efficiently produce neutrons at temperatures around 1×10^8 K.

This remarkably accurate picture was then further analyzed that same year by Fowler et al. (1955). In this paper the authors encounter the issue that in order to explain the roughly constant abundance of heavy elements with $A > 100$ in the solar abundance pattern, one needs roughly 20 neutrons per metal nucleus. If one calculates the equilibrium abundance of $^{13}\mathrm{C}$ after CNO burning there are

only approximately 2.4 ^{13}C nuclei per metal nucleus. Furthermore, they note that there is a potential problem due to a neighboring isotope. If ^{14}N is produced via p-capture on ^{13}C, then the production of heavy elements will be suppressed since ^{14}N has a large neutron-capture cross-section. Ultimately, they conclude that "…neutron production follows any building of heavier nuclei by helium as long as hydrogen can be introduced into the core by some mixing process…". However, no such mixing process was known to occur in stars.

The correct identification of the second neutron-source reaction in 1960 also came from Cameron (Cameron 1960). He proposes that the ^{22}Ne$(\alpha, n)^{25}$Mg reaction would be a logical candidate for a neutron source as ^{22}Ne is already readily available during He burning and, thus, avoids the issues associated with the ^{13}C source. Amidst this burst of theoretical progress a crucial piece of observational work was published. Suess & Urey (1956) compiled the most comprehensive and accurate solar abundance catalogue to date. Taking observational evidence from meteoritic analysis, spectroscopy, geological studies, as well as relying on previous compilations (Noddack & Noddack (1930) and Goldschmidt (1937) being among the first attempts at such a compilation), they were able to give estimates of the abundances of isotopes from ^{1}H up to ^{238}U.

In a few short years the landscape of nucleosynthesis, in particular in stars, had completely changed, and, in 1957, Margaret Burbidge, Geoffrey Burbidge, William A. Fowler, and Fred Hoyle published their landmark paper, Burbidge et al. (1957), often referred to as B^{2}FH due to the initials of the authors. The paper begins "Man inhabits a universe composed of a great many elements and their isotopes" and in its over 100 pages reviews and organizes the theory of stellar nucleosynthesis and argues for the origin of these great many elements. This was the first attempt at systematically organizing stellar nucleosynthesis into a discrete number of processes each with their own stellar sites. The abundances from Suess & Urey (1956) provided crucial constraints and insights into possible mechanisms. They postulate 8 nuclear processes are responsible for creating all the isotopes: H burning, He burning, α-process, *e*-process, *s*-process, *r*-process, *p*-process, and *x*-process. The *s*-process, or *slow* neutron-capture process, is the name they gave to the neutron capture process discussed by Cameron (1955) and Fowler et al. (1955). This name was chosen because the neutron captures occur on a timescale which is generally slower than the intervening β-decays. As can be seen in Figure 3.3, the *s*-process path roughly follows the valley of stability and can produce isotopes up to Pb.

With a roadmap of the *s*-process and a goal of reproducing the solar abundance pattern, researchers went to work. Clayton et al. (1961) showed using the classical *s*-process approach that no single neutron exposure event could properly reproduce the solar abundance of elements which are only associated with the *s*-process, so-called *s*-only nuclei. However, Seeger et al. (1965) determined that an exponential distribution of neutron exposures could work. Finally, Clayton &

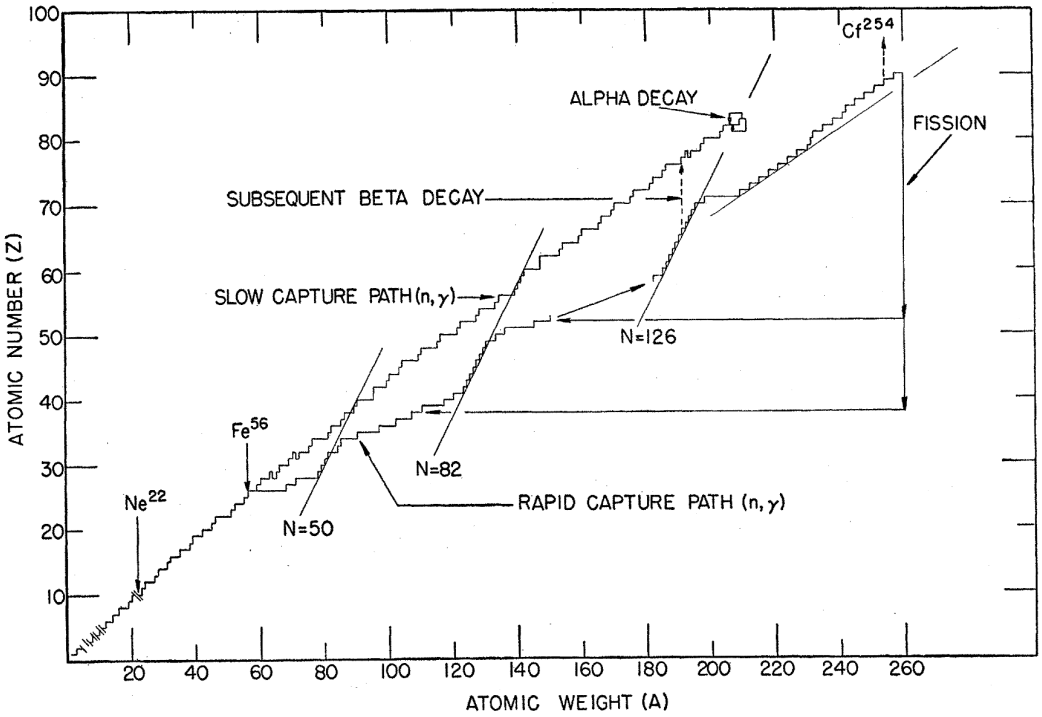

Figure 3.3 The *s*-process and *r*-process paths. The magic numbers N=50, 82 and 126 are also marked. This is Fig. V,2 in Burbidge et al. (1957)

Rassbach (1967) and later Clayton & Ward (1974) found that three different exponential distributions of neutron exposures were necessary. This meant that the *s*-process likely had multiple stellar origins.

There was another issue which was encountered when trying to explain the observations of Merrill (1952); how did the Tc make its way to the surface of the star? The *s*-process was believed to be occurring in the core of the star and there was no known mechanism which would convectively connect the envelope and core of a giant star to transport these products to the surface (Greenstein 1954, Fowler et al. 1955, Burbidge et al. 1957).

Over the course of the 1950's and 1960's a new tool was introduced which revolutionized the field and dominates astrophysical research to this day: computers. The increased computational power of computers was described by Martin Schwarzschild in 1958: "A person can perform more than twenty integration steps a day… for a typical single integration consisting of, say, forty steps, less than two days are needed." (Schwarzschild 1958). Clearly an efficient algorithm for solving the equations of stellar structure was needed to make the computational time feasible. In a series of papers (Henyey et al. 1959, 1964), Henyey outlined just such a numerical method for solving the stellar structure equations efficiently: the Henyey method. For the first time numerical simulations of the evolution of a star could be carried out in detail.

These simulations quickly lead to many question being answered as well

as some surprises. One such surprise was uncovered by Weigert (1966) and Schwarzschild & Härm (1965) independently. They found that after central He burning the star evolved with two small nuclear burning shells: one H shell and one He shell. The surprise came when they noticed the star to be thermally unstable. Previously, the only thermal instability known in stars was due to the ignition of helium in a star with a degenerate core (Schwarzschild & Härm 1965). This new thermal instability caused the star to pulse and the luminosities of the shell sources to vary violently. In a follow-up study Schwarzschild & Härm (1967) showed that during each TP (which they referred to as "relaxation oscillations") a convective zone appeared between the H and He shells (the PDCZ), and, in the case on one pulse (pulse #9), the convective zone extended very slightly beyond the lower border of the H shell. This would provide the mixing of protons into a He rich zone which was required by the theory of Fowler et al. (1955). This category of star, characterized by two burning shells over a degenerate core, was later identified by Iben & Rood (1970) to be responsible for the bifurcation of the giant branch first observed by Arp et al. (1953) (see again Figure 3.2). These stars were dubbed AGB stars (Sandage & Walker 1966). As it turns out it was not a bifurcation of the branch but rather a second giant branch which asymptotically approaches the red giant branch in a CMD.

The detailed investigation of pulse #9 and any associated nucleosynthesis was left to Sanders (1967). Sanders concluded that only a very small number of protons mixed into the PDCZ would be necessary to release enough neutrons to produce isotopes all the way up to lead. The conclusion of Sanders (1967) was, however, quickly challenged. Subsequent simulations carried out by other authors (Rose & Smith 1972, Sweigart 1974, Sugimoto & Nomoto 1975, Iben 1975b,a, Truran & Iben 1977, Schoenberner 1979), as well as Weigert (1966) the year before, showed that the PDCZ does approach the H shell, but that it never penetrates the H shell. The lack of consideration of the radiation pressure is pinned as the cause of the PDCZ extending too far in the Schwarzschild & Härm simulation (Iben 1976). It was shown in Section 2.2.3 how ignoring radiation pressure leads to more violent flashes. These more violent flashes would drive larger PDCZs. Additionally, Iben (1975a) finds that, in higher mass AGB stars, the $^{22}\mathrm{Ne}(\alpha, \mathrm{n})^{25}\mathrm{Mg}$ neutron source proposed by Cameron (1960) can reproduce much of the *s*-process abundance pattern without needing to invoke some form of proton mixing. The temperatures required for the activation of this source, though, limits its applicability to intermediate-mass AGB stars.

Numerical simulations, assuming the $^{22}\mathrm{Ne}$ source, with a post-processing nuclear network covering the typical *s*-process path were done the subsequent year (Truran & Iben 1977). In this study, the authors modeled the pulse phases as "square wave episodes" where the temperature and density vary as a square wave over the pulse phase. The resulting *s*-process abundances were critical in determining which neutron source is active in stars based on observations. This

study was only made possible by two important studies from the end of the 1960's. Arnett & Truran (1969) and Wagoner (1969) developed two different methods for solving the system of equations needed to calculate abundance changes of isotopes due to nuclear reactions. Previous attempts at solving the equations via direct integration (Truran et al. 1966) only produced solutions with a great deal of effort due to the highly stiff nature of the equations.

Iben (1976) was not, however, the last word on the possibility of the PDCZ mixing protons into the He shell. Despain & Scalo (1976) show through a thermodynamic timescale argument that there is no physical reason why a sufficiently intense flash would not be able to make contact with the H-rich region, and, in fact, they simulate such a flash by artificially increasing the triple-α rate by a factor of 200. This conclusion was corroborated in Fujimoto (1977). Iben (1976) identifies the entropy barrier between the PDCZ and the H-burning shell as the primary hurdle one must overcome for this to occur. This barrier is smaller for lower core masses (Iben 1977) and lower metallicities (Fujimoto et al. 1984).

The calculation of such an event had already been attempted by Sweigart (1974). Although he finds that there is no mixing of protons into the intershell region, he runs models for which he artificially injects protons into the intershell region. He notes that when he injects protons at a rate ten times faster than is seen in the simulation of Schwarzschild & Härm (1965), the PDCZ splits into two during the ingestion which could have an effect on the continued evolution. Despain (1977) extends the work done earlier by Christy-Sackmann et al. (1974) by analyzing models which have a convective zone that is forced to extend from the surface of the star to the base of the He shell where temperatures are around 200 MK. The light element nucleosynthesis is followed with a proper nuclear network including neutron-source reactions and the *s*-process nucleosynthesis is calculated analytically using the method of the classical *s*-process. He finds that the "rapid *s*-process" which occurs in this star leads to abundances which are not typical for either the *s*- or the *r*-process:

> In particular, some nuclei that are thought to be produced only by the *s*-process are bypassed in the deeply mixed envelope, and other nuclei thought to be synthesized in the *r*-process are produced. However, the abundances of the *r*-process nuclei differ greatly from both solar system and normal *r*-process calculations. (Despain 1977, pg. 785)

Cowan & Rose (1977) also show that the resulting release of neutrons from such an event would be too high for the *s*-process but too low for the *r*-process. Thus, they proposed the idea of an intermediate neutron-capture process, or *i*-process. The *i*-process, they said, would have neutron densities of $N_n \approx 10^{15}\,\mathrm{cm}^{-3}$–$10^{17}\,\mathrm{cm}^{-3}$ resulting from the mixed protons being captured by ^{12}C to form ^{13}C which would subsequently undergo the neutron-producing reaction $^{13}\mathrm{C}(\alpha, \mathrm{n})^{16}\mathrm{O}$. It is important to note, however, that all of these models

achieved the mixing of protons into the intershell in an artificial way. Because of this, the idea of an *i*-process would mostly die out for the time being.

Around the same time, Ulrich (1973) showed that the recurring TPs seen in the AGB models could provide the exponential neutron exposures which were deemed necessary by Seeger et al. (1965) and Clayton & Rassbach (1967) for the *s*-process to reproduce the solar abundance pattern. Ulrich was agnostic regarding the source reaction of the neutrons and only assumed that the *s*-process was occurring in the PDCZ.

While the results of Ulrich (1973) seemed to corroborate the mechanism Iben proposed — which indeed is the correct one for intermediate-mass AGB stars — it became clear that it alone cannot explain the *s*-process abundance pattern of all stars. For one, there exist AGB stars which show clear signs of *s*-process enhancement but with distributions that cannot be matched when assuming the ^{22}Ne source and with low luminosities which imply masses that are too low for the activation of the ^{22}Ne source (Clegg et al. 1979, Blanco et al. 1980, Scalo 1981, Smith & Lambert 1986). Furthermore, measurements of *s*-process anomalies in meteoritic SiC grains yielded isotopic ratios of noble gases which could only be explained by nucleosynthesis at relatively low temperatures typical of the ^{13}C source (Gallino et al. 1990). Finally, in numerical simulations carried out by Boothroyd & Sackmann (1988b), among others, the temperatures in the PDCZ in low-mass AGB stars were confirmed to not be high enough to activate the ^{22}Ne source.

This of course reintroduces the issue originally discussed by Fowler et al. (1955) of trying to explain how protons can be mixed into the He-burning region and in the correct proportions to produce enough ^{13}C for the neutron-source reaction and not too much ^{14}N while also bringing the nucleosynthetic products to the surface. As one would expect, many ideas were put forth: “plume mixing” (Ulrich 1973, Scalo & Ulrich 1973), “deep mixing” (Sackmann et al. 1974), semiconvection (Iben 1982, Hollowell & Iben 1988, Sackmann & Boothroyd 1991), diffusion (Prialnik et al. 1981, Iben 1982, Kovetz et al. 1984, Busso et al. 1992), and overshoot (Iben 1976, Hollowell & Iben 1988, Sackmann & Boothroyd 1991) to name a few.

In 1975, Iben demonstrated that his models, which included overshoot, showed the CE extend deep into the star’s interior after each pulse, as had been seen by others (see, for example, Weigert 1966, Schwarzschild & Härm 1967, Sweigart 1973, Sugimoto & Nomoto 1975). However, now the envelope was able to penetrate regions of the star which had previously been occupied by the PDCZ (Iben 1975b). Now there was a way for the nuclear burning products to reach the surface and, in this case, it would occur many times during the AGB. Similar results were also obtained in the simulations of Sugimoto & Nomoto (1975) for more massive AGB stars that same year. In this case overshoot was not used, but rather the authors increased the mixing length parameter to achieve

this effect. This phenomenon came to be known as the TDU.

This result along with the work done much earlier in Russell (1934) finally solved the riddle of the C stars first discovered by Secchi (1868). Russell (1934) had shown that the binding energy of CO leads to M type spectra if the abundance of O exceeds that of C and to C type spectra otherwise. Now there was an explanation for how a star's surface could become so C rich; the material in the intershell region is rich in C due to He burning and the TDU brings this material to the surface.

Further investigation of the TDU phenomenon lead investigators to a possible solution for the other issue plaguing the ^{13}C source since Fowler et al. (1955): some mixing process is required to get protons into He burning regions. In Iben & Renzini (1982), they notice that at the deepest extent of the CE during a TDU protons can be carried away by semiconvection into the C-rich region between the burning shells and form a ^{13}C-rich region. The semiconvection zone is the result of the increased opacity in that region due to the ^{12}C-rich intershell region being pushed outward to low enough temperatures that C provides a large contribution to the opacity (Sackmann 1980). The authors then suggest that this ^{13}C-rich region would be engulfed by the convective shell in the subsequent pulse and create *s*-process elements. Unfortunately, it was found that this effect is only seen in very low-metallicity stars (Hollowell & Iben 1988). Also, other authors were either unable to reproduce the effects of semiconvection or found the effect to be orders of magnitude weaker (Lattanzio 1987, Boothroyd & Sackmann 1988c).

At this time the crucial neutron capture cross-section measurements were greatly improved and expanded by two studies: Bao & Käppeler (1987) and Beer et al. (1989). The status of the neutron capture cross-section measurements relevant to the *s*-process at that time is summarized in Table 2 of Kappeler et al. (1989). 286 cross-sections had been experimentally measured with varying degrees of accuracy, leaving roughly 70 unmeasured.

Finally, in Straniero et al. (1995) we arrive at the current picture of low-mass AGB *s*-process nucleosynthesis. In their simulations the authors artificially mix protons into the C-rich intershell at the deepest extent of the TDU. This creates a ^{13}C pocket, as they call it, which, instead of being engulfed by the convective shell in the subsequent pulse, burns radiatively in the interpulse period. The neutron density created by the ^{13}C source at this temperature is a much better match to the observations.

3.2 Recent Developments: 1995 to Present

Before continuing, a summary of the important events from Section 3.1 are shown in Table 3.1 for those readers who skipped Section 3.1. At the end of the previous section we had finally come to the currently accepted picture of low-mass AGB

Table 3.1 A timeline of milestones from 1920 to 1995

1920	Eddington first suggests that stars are powered by fusing H to He.
1928	Gamow derives quantum tunneling overcoming a critical roadblock to nuclear fusion in stars.
1932	Chadwick discovers the neutron.
1937-39	Bethe and von Weizsäcker discover the *pp*-chain and CNO cycle.
1948	Mayer explains the magic numbers with nuclear shell theory by including a strong spin-orbit coupling term.
1952	Merrill discovers Tc in a stellar spectra, proving stellar nucleosynthesis does occur.
1955	Cameron correctly identifies the ^{13}C neutron-source reaction and proposes heavy element synthesis via a series of successive neutron captures.
1957	B^{2}FH organize stellar nucleosynthesis into a discrete number of processes each with their own stellar sites.
1960	Cameron correctly identifies the second neutron source reaction: the ^{22}Ne source.
1961	Clayton et al. show that no single neutron exposure event can reproduce the *s*-process abundance pattern.
1964	Henyey et al. describe the Henyey method, an efficient algorithm for solving the stellar structure and evolution equations.
1965	Seeger et al. show that an exponential distribution of neutron exposures is necessary to explain the *s*-process abundances.
1965-66	Weigert and Schwarzschild & Härm independently discover TPs in their AGB simulations.
1973	Ulrich shows that the recurring TPs on the AGB could provide the exponential neutron exposures needed for the *s*-process.
1975	Iben shows that the ^{22}Ne source is indeed active in intermediate mass AGB stars.
1975	Iben shows his models with overshoot experience TDU explaining how *s*-process elements reach the surface of AGB stars and why AGB stars become C rich.
1977	Cowan & Rose propose the existence of an *i*-process with neutron densities between those of the *r*- and *s*-process.
1995	Straniero et al. identify the correct location for the *s*-process in low-mass AGB stars: the ^{13}C pocket during the interpulse phase.

s-process nucleosynthesis from Straniero et al. (1995). A small amount of protons is mixed beyond the formal Schwarzschild boundary of the CE during the TDU forming a ^{13}C pocket which burns radiatively during the interpulse period thereby producing *s*-process elements. In their paper the extra-mixing of protons was done in an entirely artificial way. This of course side-steps the fundamental question of how these protons get into the intershell region, which remains unanswered. The details of the ^{13}C pocket — how it forms, how large it should be, etc. — have dominated the research of the *s*-process ever since. It is a complicated question as it is dependent on the uncertainties in both the nucleosynthesis as well as the stellar structure. Additionally, understanding how neutron sources, mass loss, and mixing change as a function of mass and metallicity and using this information to match observations became the focus of many researchers. These two pursuits are the main focus of the coming subsection. The subsequent subsection will be dedicated to the developments related to low-metallicity AGB stars and the *i*-process. The topics have been split up to avoid an excessive amount of jumping from one topic to the next.

3.2.1 *S*-PROCESS AND THE AGB

Following Straniero et al. (1995), there was a push to test the new theory. The analysis of Lambert et al. (1995) confirmed earlier results (see, e.g., Malaney 1987) that the low ratio of Rb/Sr at the surfaces of the target stars heavily favors the ^{13}C source over the ^{22}Ne source as the neutron source for the *s*-process in low-mass AGB stars. Furthermore, the match is even better if one assumes the ^{13}C source is active not in the He shell during the pulse but in the intershell region during the interpulse phase where the temperatures are lower. This still left the mechanism responsible for the extra mixing undetermined.

This extra mixing had been problematic for some time. Though it had been recognized from early on that extra mixing was required in order for TDU to occur (Iben 1976), there were still instances in which studies found TDU without any additional mixing (Lattanzio 1989, Straniero et al. 1997). Furthermore, studies were split on what the metallicity and mass cutoffs were for the TDU. Lower metallicity and higher mass seemed to make TDU easier to achieve (Busso et al. 1999). The answer to the first problem came from Pols et al. (2001). They found that the Schwarzschild boundary at the base of the CE in stellar models is unstable, at least in the sense that any mixing of protons beyond it will cause the boundary to move deeper as well. The codes which achieved TDU without extra-mixing were, they claimed, doing so by accidentally mixing protons below the Schwarzschild boundary due to numerics. This caused the Schwarzschild boundary to move deeper into the star and, thus, a TDU could occur. The second problem is largely the result of our lack of understanding of how convection really operates in stars. This is still an open question and lead to the development of a

number of different hypotheses regarding the physical origin of the extra mixing needed for AGB stars.

In 1996, Freytag and collaborators performed a 2D hydrodynamical simulation of a shallow surface convective zone (Freytag et al. 1996). In their simulation they see clear evidence of mixing beyond the formal convective boundary which they describe as overshoot. The vertical velocities of the material, which are non-zero when they reach the edge of the formally convective region, decay exponentially as the material advances through the overshoot region and away from the Schwarzschild boundary. Additionally, they provide a 1D approximative parameterization for the behavior of mixing in the overshoot region. Herwig et al. (1997) implemented this as

$$D(z) = D_0 \exp \frac{-2z}{f H_p}, \tag{3.1}$$

where f is the free parameter, H_p is the pressure scale height, z is the radial distance from the Schwarzschild boundary, and D_0 sets the scale of diffusive speed and is proportional to H_p. They find that using this overshoot prescription one is able to produce a ^{13}C pocket during the TDU, however, this comes at the cost of introducing a free parameter which can not be calibrated observationally. This parameter controls the size of the overshoot region. Furthermore, the inclusion of overshoot in the PDCZ can have a large effect on the characteristics of the pulse and the intershell abundances. Nevertheless, there was at least a possible physical explanation for the ^{13}C pocket now. Furthermore, models which used overshoot had intershell abundances of O and C which are a much better match to observations of PG1159 stars (Herwig 2000). These stars are post-AGB stars at the center of planetary nebulae and their surface abundances should match the intershell abundances of AGB models.

It was around this time that it became clear that the stellar models, with the help of the improved nuclear data, were now superseding the classical *s*-process approach. Using the ^{13}C-pocket approach, Gallino et al. (1998) found that the final surface abundance of *s*-process elements in their stellar models could not be reproduced by the simple exponential law of neutron irradiations as was assumed in the classical *s*-process. Furthermore, a study by Arlandini and collaborators used the recently updated (n, γ) cross-sections to show that the classical *s*-process analysis leads to inescapable internal inconsistencies, in particular around magic number nuclei (Arlandini et al. 1999). These inconsistencies arise largely from the fact that the classical approach to *s*-process nucleosynthesis assumes average quantities, such as the effective values for the neutron density and temperature, which do not map well to the true features of the stellar models.

Observations were also providing critical insights. Abia & Wallerstein (1998) analyzed the spectra of SC, S, and Ba stars and determined the abundance of some *s*-process elements. In particular using the ratio of ^{85}Rb/^{87}Rb they are

able to provide estimates of the neutron density in the star which the material was subjected to prior to dredge-up. Comparing these surface enhancements to the models of Gallino et al. (1998) and Straniero et al. (1997) they find that some stars experienced neutron exposures expected for the ^{13}C source, while some experienced the activation of the ^{22}Ne source. In a follow-up study Abia and collaborators extended their spectroscopic observations to more stars (Abia et al. 2001). In doing so they make a number of important conclusions. First, the increase in C abundance at the surface of the stars correlates to the degree of *s*-process enhancement in the star. This observationally confirms that the TDU is bringing both the C and the *s*-process elements to the surface as had been previously suggested by e.g. Smith & Lambert (1990). Secondly, they determine that almost all the C stars they find have a mass $M \lesssim 3\,\mathrm{M}_{\odot}$. These results in combination with the physically motivated overshoot briefly made it seem as though the puzzle of AGB stars was close to solved.

The overshoot approach quickly ran into issues, though. Herwig (2000) finds that the size of the ^{13}C pockets produced via overshoot are orders of magnitude smaller than estimated for the *s*-process. They also find that in addition to a ^{13}C pocket there is a partially overlapping ^{14}N pocket at a slightly higher mass coordinate. This is important because ^{14}N acts as a neutron poison effectively consuming neutrons and leaving few to none for the *s*-process. This limits the region where the *s*-process is expected to occur to those regions where the number abundance of ^{13}C is greater than that of ^{14}N. Thus, there was still room to test other theories. Langer et al. (1999) simulated the effect of rotational induced mixing at the base of the CE. They find that the maximum ^{13}C abundance in the ^{13}C pocket is similar to that found by Herwig et al. (1997), however, there is an important fundamental difference between the two mixing schemes. Overshoot only mixes the regions just beyond the convective zone and thus only mixes for as long as the convective zone is nearby. Rotational mixing on the other hand is always mixing, even after the CE begins to recede. Thus, the rotational mixing spreads the ^{13}C peak out before the neutron production begins. They still achieve *s*-process neutron densities and a larger pocket (in mass) than Herwig (2000), however they fail to include the ^{14}N neutron poison reaction in their simulations. Yet, the two mixing processes are not mutually exclusive and Herwig & Langer (2001) run simulations including both effects. They find that the rotational mixing not only spreads out the ^{13}C but also the ^{14}N such that once the ^{13}C neutron source is active the ^{14}N pocket has completely overlapped the ^{13}C pocket, effectively choking off the *s*-process. This casts serious doubt on rotational mixing being the missing extra mixing process, at least as implemented in Herwig & Langer (2001).

A slight modification of the overshoot prescription by Herwig et al. (1997) was used in Chieffi et al. (2001) to calculate the AGB evolution of a zero-metallicity star. While Herwig et al. (1997) use a diffusive overshoot approach,

meaning the exponential decay is applied to the diffusion coefficients in the models, Chieffi et al. (2001) applies the exponential decay directly to the convective velocities. This is strictly speaking a more direct implementation of the results from Freytag et al. (1996), but it requires the use of an advective mixing scheme. In this paper they establish that TPs do in fact happen for primordial stars and that these zero-metallicity stars can even become carbon stars. This method was then applied to AGB models of population II stars where it was found that the ^{13}C pocket produced via this prescription is larger by a factor of 10 than in the diffusive mixing approach (Cristallo et al. 2001).

An important study in understanding the effect of the characteristics of the ^{13}C pocket on the *s*-process came in 2000. Goriely & Mowlavi (2000) calculate the nucleosynthesis resulting from different ad hoc H profiles left behind by the TDU. First, they confirm the conclusion of Gallino et al. (1998) that the ^{13}C pocket will form around the region where the proton-to-^{12}C ratio is approximately 0.1 after the TDU. Secondly, they find that the shape of the proton profile left behind by the TDU has very little effect on the end nucleosynthesis. The extent of the profile is, however, key and, of course, dependent on the TDU.

There were a number of studies done to investigate the TDU efficiency, λ, and its dependency on fundamental stellar parameters. Lattanzio (1989) finds that λ increases with increasing core mass and decreasing metallicity. The dependency on metallicity had been found also a year earlier in Boothroyd & Sackmann (1988c). Karakas et al. (2002) attempted to find fitting formula for the efficiency of TDU for use in synthetic models. In doing so they determine that mass loss can decrease the value of λ. Comparison of models to observational evidence from, e.g. Girardi et al. (1999), showed that codes likely do not predict sufficiently efficient TDU episodes (Karakas et al. 2002). Because of this new ideas were necessary to explain how TDUs could be made to be more efficient.

Herwig & Austin (2004) showed that when varying the ^{14}N(p, γ)^{15}O and triple-α reaction rates within the given uncertainties, λ is uncertain within a factor of two. Furthermore, Herwig (2000) showed that overshoot at the base of PDCZ during the pulse also impacts λ. In both cases the reason for this is that the peak He luminosity is impacted by these variables. The stronger the pulse the stronger the subsequent dredge up due to the greater expansion and cooling of the upper layers of the intershell region.

Another idea put forth was internal gravity waves (IGWs) (Denissenkov & Tout 2003). IGWs are excited by perturbations in any fluid subject to a gravitational field. In stars the perturbations come from convective eddies which reach the base of the convective zone. The IGWs can then propagate through the stellar material, and, in the radiative layers adjacent to the convection zone, lead to additional mixing. The ^{13}C pocket formed by IGWs is two orders of magnitude larger than typical values for the diffusive overshoot prescription. This result is not seen in all codes however (see Goriely & Siess 2018).

Progress was being made on including different physics in other parts of the AGB star as well. Marigo (2002) showed convincingly that the structure of the outer envelope of AGB is acutely sensitive to the opacities. In particular, including the molecular opacities for C-enriched envelopes dramatically reduces the effective temperature of these stars and brings their colors into much better agreement with observations.

All the while neutron-capture cross-section measurements were being constantly improved and expanded, providing critical input for the *s*-process studies. A proper review of these studies is beyond the scope of this work, but a few papers will be mentioned here for the interested reader. Kaeppeler et al. (1994) provided updated reaction rates for various α-capture reactions as well as the ^{22}Ne neutron-source reaction. Building upon the work of Kappeler et al. (1989), Bao and colleagues conducted extensive experiments to measure neutron-capture cross-sections for various isotopes. Their research included measurements on isotopes like ^{99}Tc and ^{175}Lu, which are crucial for *s*-process nucleosynthesis. These measurements significantly expanded the database of known cross-sections and improved the accuracy of *s*-process models (Bao et al. 2000). This study also formed the basis of the Karlsruhe Astrophysical Database of Nucleosynthesis in Stars (KADoNiS) database. Further updates to the neutron-capture cross-section measurements in this database can be found in Dillmann et al. (2006, 2008) and Dillmann et al. (2014). Jaeger et al. (2001) updated the neutron-capture cross-section for the ^{22}Ne neutron-source reaction. In 2008, Heil and collaborators conducted experimental studies of the ^{13}C(α, n)^{16}O reaction at stellar energies (Heil et al. 2008). More recently the LUNA collaboration has provided an updated cross-section measurement for the ^{13}C neutron-source reaction (Ciani et al. 2021).

As can be plainly seen in this discussion, there are many variables and physical phenomenon which can impact the evolution of an AGB star. Furthermore, the relevancy and relative importance of these variables can change within the stellar parameter space. In an attempt to help bring order to this picture, as well as to provide useful results for other fields, some researchers took it upon themselves to create grids of AGB models including the abundance yields of these models. There are a number of grids of different sizes run with different codes by different groups. Here we will focus on the three most widely used grids in the literature: The Monash grid (Karakas & Lattanzio 2007, Karakas 2010, Karakas & Lugaro 2016), the FRUITY grid (Cristallo et al. 2009b, 2011, 2015), and the NuGrid models (Battino et al. 2016, Pignatari et al. 2016). These grids provide not only structural information about all of the models in the grid but also the yields of those models. These results can then be used as input in galactic chemical evolution studies.

While all of these studies perform the same task, there are some key differences in the numerical methods employed in each. Here we will discuss the key

differences. The stellar evolution tracks of the Monash grid are run using the mass loss prescription of Vassiliadis & Wood (1993) on the AGB, a mixing length parameter of 1.75, and no convective overshoot at any point during the evolution, though there are select models with some overshoot used. These tracks are then post-processed to determine the final yields. One distinguishing feature of the post-processing code is the use of an artificial ^{13}C pocket (Lugaro et al. 2003, Karakas 2010). Instead of resolving the ^{13}C pocket in the stellar evolution code and having the post-processor calculate the nucleosynthesis of it, the post-processor itself forces the mixing of extra protons past the base of the CE at its deepest points of mixing during the TDU. The amount of protons mixed and the profile of the proton abundance is fully customizable making it extremely flexible for testing the effect of different mixing possibilities. It is however also fully heuristic and, thus, not necessarily physical or consistent with the stellar track. It should also be noted that the models do not include opacity tables with large variations in C/O.

The NuGrid models are also post-processed but with a different post-processing code which does not use the same artificial-pocket approach, instead opting to let the evolutionary code resolve the pocket. The models of Pignatari et al. (2016) are with the mass loss prescription of Bloecker (1995) with $\eta_B = 0.01$. This value is then changed to $\eta_B = 0.04$ for tracks less than 3 $M_\odot$ and $\eta_B = 0.08$ for the 3 $M_\odot$ track once the star becomes a C star. The code does not, however, use C/O-variable opacities. These models do include overshoot with a value of $f_{\rm ov} = 0.014$ being used everywhere during the pre-AGB phase. On the AGB, $f_{\rm ov} = 0.008$ is used for the PDCZ and, during TDU, they switch to $f_{\rm ov} = 0.126$ for the CE. The models of Battino et al. (2016) (B16) include an extension of the usual convective overshoot method. In addition to the standard exponentially decaying overshoot profile, the authors add a second shallower mixing profile to simulate the effect of IGWs.

Finally, the FRUITY models are the only models of the three where no post-processor is used. Instead a full network of 500 isotopes is built directly into the evolution code itself, avoiding the need for any post-processing. Additionally, the mixing scheme used in these models is not the diffusive based mixing scheme used in the other grids. Here an advective mixing scheme is applied wherein the degree of mixing between two grid points is linearly dependent on the time step and the mixing timescale between the two grid points (Chieffi et al. 2001, Straniero et al. 2006). Overshoot is then implemented, analogously to Equation (3.1), via an exponential decay of the convective velocities:

$$v = v_{\rm bce} \exp \frac{-d}{\beta H_p}. \tag{3.2}$$

Here, d is the distance to formal convective boundary, $v_{\rm bce}$ is the velocity at

the Schwarzschild boundary, H_p is the pressure scale height, and β is the free parameter. One important consequence of this scheme as it is implemented in Cristallo et al. (2009b) is that there is no overshoot at the base of the PDCZ. This is because they find that $v_{\rm bce}$ is zero at the lower boundary of the PDCZ, i.e. the radiative gradient is equal to the adiabatic gradient. In addition, C/O variable opacities and the mass loss prescription of Vassiliadis & Wood (1993) are used.

Despite the popularity of these studies, very little work has gone into properly comparing the results of the grids, in particular the evolutionary models themselves, against each other. Lugaro et al. (2003) conducted a very nice comparison of the codes in question (or older versions of these codes). However, due to the very different physics which were used for each code, it is hard to know whether the results have any generality. For instance, all the codes use different mass loss descriptions and each code handles overshoot differently including one code where it was ignored entirely. One additional comparison is found in the following figure from Yagüe López et al. (2022). In Figure 3.4 one can see the final surface enhancements of various models of a 3 $M_\odot$, solar metallicity star. Even from this one comparison it is clear how much uncertainty there is in the results and how much code differences can play a role.

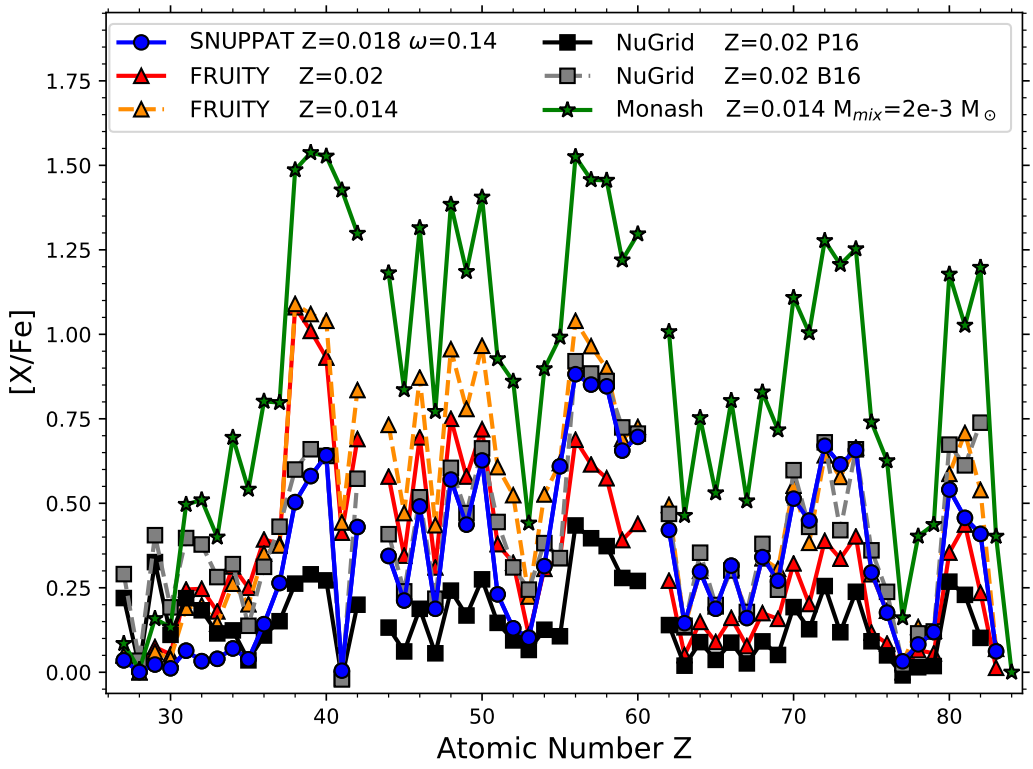

Figure 3.4 Figure 7 from Yagüe López et al. (2022). The final surface abundances of 3 $M_\odot$, solar metallicity models from different AGB model grids are shown as well as a model from the original paper which is labeled as SNUPPAT.

In addition to these studies, where the focus was more on the nuclear synthesis, there is also the study of Weiss & Ferguson (2009) where a grid of AGB models was run using GARSTEC, the same stellar evolution code used in this work, with a focus on solely the structure and evolution of such models. They find that the C/O ratio has a large impact on the effective temperatures of their models when using the new C/O-variable opacities. Additionally, since they use mass loss prescriptions which take into account C/O, the mass loss was also very high in these models leading to short AGB lifetimes and fewer pulses as compared to other studies. Finally, they find that the overshoot at the base of the PDCZ inhibits the growth of the core along the AGB and puts some of their models in contention with observations.

Work on AGB stars with GARSTEC continued in Wagstaff & Weiss (2018) and Wagstaff et al. (2020). These studies extended the physics available in GARSTEC to include spherical atmospheres, Planck mean opacities, and convective-zone-specific overshoot parameters. Wagstaff & Weiss (2018) focused on the affect of the outer boundary condition on the models. It was determined that there is little to no difference between models with an Eddington gray atmosphere and a spherical atmosphere. The use of the Planck mean opacities in the outermost layers of the star does however shift the star to cooler temperatures. Ultimately, this was found to have a negligible affect on the structure and evolution of the star. The primary affect is simply to increase the mass loss as a direct result of the lower effective temperature. Wagstaff et al. (2020) then investigated how overshoot at different convective boundaries alters the evolution of AGB models. It was found the overshoot at the lower boundary of the CE and the lower boundary of the PDCZ have the largest impact on the models. A grid of models with varying overshoot parameters were run and compared to observations such as the Carbon star count, PG1159 surface abundances, and the initial-final mass relationship. Ultimately, there was no set of overshoot parameters which could simultaneously match all observational constraints. Neither of these studies sought to study the *s*-process and so the ^{13}C pocket was not resolved.

3.2.2 *i*-process and the AGB

In 1985 the HK survey was launched. The name comes from the fact that the survey used a narrowband interference filter to restrict the bandpass to the H and K lines of Ca II. The goal of this survey was to study the nucleosynthesis of the first population of stars by analyzing the abundance distribution of extremely metal-poor stars, whose composition is only the result of big bang nucleosynthesis and the pollution of the first generations of stars (Beers et al. 1985). Analysis of the data provided a serendipitous result; there were far more metal-poor stars with carbon enhancement than expected. Additionally, these CEMP stars, as they became to be known, have differing neutron-capture-element enhancements (Norris et al.

1997a,b, Beers 1999). Some exhibiting signs of *r*-process enhancements (Sneden et al. 1996), some exhibiting signs of *s*-process enhancement[10], some which appear to have enhancements somewhere between *r*- and *s*-process (Hill et al. 2000, Cohen et al. 2003), and still others with no heavy element enhancement (Norris et al. 1997b). This implies, among other things, that the *s*-process must be activated in AGB stars of extremely low metallicity. Additionally, the CEMP-r/s stars must be properly explained.

Work had already been done on modeling the *i*-process in AGB stars (see the discussion in Section 3.1) and had continued. In Malaney (1986b) a post-processing nuclear network, covering only the light elements, including a simple mixing scheme was used to calculate what would happen if protons were injected into the PDCZ. He finds that the rate at which the protons are ingested has the greatest impact on the maximum neutron density achieved. He finds neutron densities ranging from $1 \times 10^9\,\mathrm{cm}^{-3}$–$1 \times 10^{14}\,\mathrm{cm}^{-3}$ depending on the ingestion rate. Furthermore, he runs some models where he artificially splits the PDCZ in a way which matches the behavior seen by Sweigart (1974) and finds that this also has a large impact on the neutron densities. A follow-up study was conducted with a nuclear network extending out to $N = 50$ and finds that the abundance distribution of such an event is much different than that of a typical AGB scenario (Malaney 1986a). As in the other earlier studies of the *i*-process, the ingestion of protons by the PDCZ was achieved artificially in these simulations.

Fujimoto et al. (2000) computed evolutionary models spanning a mass range of $0.8\,\mathrm{M}_\odot$–$5.0\,\mathrm{M}_\odot$ and a metallicity of $[\mathrm{Fe/H}] = -2$–0. They categorize the behaviour of their models into five different cases. In case II′, which corresponds to $[\mathrm{Fe/H}] \lesssim -2.0$ and $1\,\mathrm{M}_\odot \lesssim M \lesssim 3\,\mathrm{M}_\odot$, their models exhibit a PIE. They claim these stars will evolve into more N-rich C stars with the additional enhancement of *s*-process elements. These results along with the observation of the CEMP-r/s stars revived interest in the idea of an *i*-process.

An important point of this paper is that the PIE was achieved naturally and not artificially. As we saw in Section 3.1 none of the pre-2000 models had a PIE event occur naturally except Schwarzschild & Härm (1965), though as Iben (1976) showed this was due to the lack of consideration of the radiation pressure. As we will see in the remainder of this section, post-2000 models easily find PIEs happening. This naturally begs the question of what had changed in that time. Certainly the models improved, the input physics improved, etc. However, this is not the deciding factor. If one looks at Table 3.2 one will notice that the old studies were modeling stars in the wrong part of the parameter space. Of course they did not have the benefit of the observations of CEMP-r/s stars to guide their simulations. In the modern studies the authors focused on extremely metal-

[10] this category had been known for some time and were originally designated as CH stars (Keenan 1942) and studied by a number of authors, e.g. Vanture (1992). It was only now that they were determined to be a subcategory of CEMP stars.

Table 3.2 The mass and metallicities of the models of previous *i*-process studies.

Reference	Mass [$M_\odot$]	[Fe/H]	PIE
Schwarzschild & Härm (1965)	1	−1.25*	yes**
Weigert (1966)	5	0.38*	no
Rose & Smith (1972)	0.85	−0.25*	no
Sweigart (1974)	0.7	−1.25*	no
Iben (1975a,b, 1976)	7	Pop I	no
Fujimoto et al. (2000)	1–3	−2.5 to −5	yes
Iwamoto et al. (2004), Iwamoto (2009)	1–3	−2.7	yes
Campbell & Lattanzio (2008)	1–3	−2.5 to −5	yes
Suda & Fujimoto (2010)	1.2–3.4	−3 to −5	yes
Cristallo et al. (2009a)	1.5	−2.44	yes
Choplin et al. (2021)	1.0	−2.5	yes

* calculated from the Z value given in the paper by assuming $Z_\odot = 0.018$.
** due to lack of consideration of radiation pressure.

poor and lower-mass stars for which the PIEs do occur. The reason that lower metallicities and lower masses make PIEs easier is that both affect the entropy barrier of the H shell. It can be shown that the entropy barrier of the H shell is smaller for lower core masses (Iben 1977) and lower metallicities (Fujimoto et al. 1984). The lower the entropy barrier is the easier it is for the PDCZ to overcome it and ingest protons.

The work of Fujimoto et al. (2000) was improved and extended by Suda & Fujimoto (2010) with a grid of models spanning masses of 0.9 $M_\odot$–9 $M_\odot$ and [Fe/H] of −5– − 2 as well as 0. They find that region of the parameter space for case II′ is bounded by [Fe/H] $\lesssim -3$ and $1.2\,M_\odot \lesssim M \lesssim 3.4\,M_\odot$. Detailed nucleosynthesis of heavy elements is again not conducted, but they do state that the case II′ stars will again be N-rich C stars with *s*-process enhancement. A similar study was conducted by Lau et al. (2009) with qualitatively similar results. This is also the first study which attempts to include convective overshoot into the calculations. Unfortunately, numerical difficulties prevent them from drawing any firm conclusions. They do however claim that the inclusion of overshoot during the TP-AGB phase "does not significantly affect the subsequent evolutionary behaviour" and that it only shifts the range in parameter space where one would expect certain phenomena to occur.

A year earlier Cristallo et al. (2009a) calculated the evolution of a Z=5 × 10^{-5}, 1.5 $M_\odot$ star. They find a PIE occurs in the first fully formed pulse leading to neutron densities of $N_n \approx 10^{15}\mathrm{cm}^{-3}$. Additionally, they find that the CNO energy release in the PDCZ can exceed that of the triple-α energy release. When this occurs there develops a temperature inversion in the PDCZ and the convection zone will split in two and does not re-merge. After the PIE the star evolves as

a usual AGB star. As a final note, they find, in agreement with Iwamoto et al. (2004) and Iwamoto (2009), that a large amount of ^{7}Li is produced via the Cameron-Fowler mechanism (Cameron 1955, Cameron & Fowler 1971) as a result of the PIE.

The possible origins of the CEMP-r/s stars were addressed in Jonsell et al. (2006) by considering 9 different origin scenarios, including: the star formed from *r*-process rich material and created the *s*-process enhancement itself, the star formed from *r*-process rich material and accreted the *s*-process material from a companion star, and a scenario where the star is in a triple system and accretes the *r*-process rich material from one companion and the *s*-process rich material from the other companion. None of the 9 scenarios proves to be convincing in explaining the observations.

A similar study is conducted by Lugaro et al. (2012) wherein detailed *s*-process post-processing nucleosynthesis calculations are done on AGB models from two different stellar evolution codes and compared to the observations of different CEMP stars. The simulated *s*-process abundances provide a good match to the CEMP-s stars, but fail to match the Eu abundance observed in CEMP-r/s stars by at least an order of magnitude. Secondly, they find that Ba and Eu abundances in CEMP-r/s stars are correlated suggesting that the either a single process is responsible for the r/s enhancement or that the *s*-process and *r*-process which enriched the material must be correlated, which is unlikely. This result was also confirmed by Cristallo et al. (2016) in self-consistent stellar models.

In addition to the comparisons to spectroscopic evidence, there is also some meteoritic evidence to support the idea of an *i*-process. Several works have shown that pre-solar grains may bear the isotopic signature of *i*-process nucleosynthesis. In one case strongly negative values of $\delta\left(^{134}\mathrm{Ba}/^{136}\mathrm{Ba}\right)$ are shown to be incompatible with *s*-process models but expected of the *i*-process (Liu et al. 2014) while the other study points to anomalies in Ca and Ti which can only be explained by neutron densities typical for the *i*-process (Jadhav et al. 2013).

Based on these results, some researchers began looking for a separate "r/s" process with a natural candidate being the *i*-process. Dardelet et al. (2014) carried out a one-zone nucleosynthesis simulation with the temperature and density being taken from the PDCZ of an AGB model. An arbitrary amount of H is included in the composition to simulate the effect of protons being entrained from the envelope. They find that almost all of the ^{12}C is consumed within the first second of the simulation. After ten minutes the ^{13}C has formed and begins producing a neutron density of $N_{\mathrm{n}} \approx 10^{14}\,\mathrm{cm}^{-3}$–$10^{16}\,\mathrm{cm}^{-3}$ depending on the initial amount of H in the zone. The resulting abundances match the observations of CEMP-r/s stars well.

Using a similar approach, Hampel et al. (2016) addressed the question of what neutron density best reproduces the CEMP-r/s abundance pattern. To do so they performed detailed nucleosynthesis calculations with different neutron

densities which were kept constant throughout the simulation. All simulations were continued until a time integrated neutron exposure of 495 mb^{-1} was reached. Their primary conclusion is that the CEMP-r/s observations are best matched by a constant neutron density of $1 \times 10^{14} cm^{-3}$.

Most recently, in a series of papers (Choplin et al. 2021, Goriely et al. 2021, Choplin et al. 2022, 2024), the Brussels group investigate the *i*-process with the STAREVOL stellar evolution code with a fully coupled network of 1160 isotopes. The first paper provides an in depth analysis of a single evolutionary track for a 1 $M_\odot$, [Fe/H] = −2.5 star. As was seen in Cristallo et al. (2009a), the authors find that a PIE occurs early in the AGB phase, in this case during the third pulse. The ingestion of H into the He shell causes a huge burst of energy from the CNO cycle. This energy eventually exceeds that of the triple-α reaction and creates a temperature inversion, splitting the PDCZ into two separate convection zones which do not remerge. In disagreement with Cristallo et al. (2009a), they find that the split occurs after the peak in the neutron density which reaches $N_n = 4.3 \times 10^{14}\,cm^{-3}$. However, the neutron density remains very large in the lower convection zone even after the split. The products of the nucleosynthesis in the lower shell never reach the surface and remain locked in the star. On the other hand, the material in the upper convective zone reach the surface. Clearly the timing of the splitting of the convective zone is crucial. If it were to split before the maximum neutron density is reached than the final surface abundances would be very different.

After the PIE, the merging of the upper part of the split PDCZ with the CE brings the *i*-process enriched material to the surface. Along with it comes a vast amount of carbon raising the surface ^{12}C abundance by over 3 dex. Thus, the star becomes a carbon star triggering rapid mass loss which ends the AGB before any further pulses can occur. This is in disagreement with the models of Cristallo et al. (2009a) which find that their AGB star continues its expected evolution. The authors suggest a few explanations including the different masses of the modeled stars (1 $M_\odot$ as opposed to 1.5 $M_\odot$) as well as the roughly 1 dex difference in CNO enhancement at the surface of the stars.

Another key aspect of this first paper is a test of the dependency of the PIE on the spatial and temporal resolution of the simulation. They find that when decreasing the spatial and temporal resolution the PIE "resists" strongly suggesting it is not a numerical artifact. Furthermore, they find that some final surface abundances may vary by up to 0.6 dex depending on resolution settings. Finally, if the spatial or temporal resolution is too coarse it is possible to miss the PIE entirely and have the star evolve along a typical AGB evolution.

The second paper of the series concentrates on the nuclear uncertainties and their affect on the *i*-process and PIEs (Goriely et al. 2021). Their findings show that, in general, the final elemental surface abundances are uncertain within ±0.4 dex due to the nuclear uncertainties. Interestingly, they find that the

uncertainty related to the ^{13}C neutron source reaction rate and the β-decay rates have only a minor impact on the final surface abundances. Of course this may be different if one were able to consider isotopic rather than elemental abundances.

The third paper presents a grid of models with initial masses of 1, 2, and 3 $M_\odot$ and metallicities of [Fe/H] = −3.0, −2.5, −2.3, and −2.0 (Choplin et al. 2022). They find that PIEs occur in models with masses of 1 $M_\odot$ and 2 $M_\odot$ and with metallicities of [Fe/H] = −3, −2.5, and −2.3 during the first or second TP. The peak neutron density remains relatively unchanged over this parameter range with $N_n = 10^{14}$ cm^{-3}–10^{15} cm^{-3}. They find that the PIE effectively terminates the AGB phase for their 1 $M_\odot$ models, but the 2 $M_\odot$ models continue along the AGB after the PIE. The authors expect that this is due to the larger envelopes (in mass) of the 2 $M_\odot$ stars which dilutes the carbon enrichment and, thus, avoids triggering the rapid mass loss which goes along with a high C/O abundance. None of their models with a mass of 3 $M_\odot$ or a metallicity of [Fe/H] = −2.0 experience a PIE as the entropy barrier of the H shell is too large in these stars.

The fourth paper focuses on the impact of overshoot on the *i*-process in AGB stars (Choplin et al. 2024). Various overshoot values for the top and bottom of the PDCZ as well as the bottom of the CE are tested on their standard 1$M_\odot$, [Fe/H] = −2.5 model. Their calculations are, however, not carried out until the end of the AGB. Instead they apply a so-called dilution method to approximate the final surface abundances based on the structure and abundances of the star when the PDCZ splits, which is where they stop their evolutionary models. They find that the overshoot value at the top of the PDCZ, which they vary from 0.0 to 0.2 pressure scale heights, is the most impactful of the overshoot parameters in determining whether a PIE will occur and in determining the final surface abundances. Additionally, they find that the parameter space within which a PIE can be expected to occur is enlarged in both mass and metallicity when overshoot is added to the models. Specifically, for low-mass stars they find PIEs occurring at nearly solar metallicity and at low metallicity they find PIEs in stars up to 3$M_\odot$.

Chapter 4

Numerical Methods

> Science is what we understand well enough to explain to a computer. Art is everything else we do.
>
> Donald Knuth, *Foreward to A=B*

Since the advent of the Henyey method, numerical calculations have played an integral role in the study of stellar evolution. While computational power has grown exponentially since the 1950s, the numerical tools used have in turn grown in complexity, seeking to leverage the now available resources. Despite the progression of this computational arms race, researchers are still forced to weigh the costs and potential rewards of increasing the complexity of their codes. One example which has already been mentioned (Section 2.1) is the splitting of AGB nucleosynthesis calculations into an evolutionary part, handled by a stellar evolution code, and a nucleosynthesis part, handled by a post-processing code. In this chapter the codes which handle these tasks will be discussed in more detail, beginning with the stellar evolution code.

4.1 GARSTEC

For the purposes of generating the stellar evolution models for this work the Garching Stellar Evolution Code or `GARSTEC` (Weiss & Schlattl 2008) was used. It is a general purpose stellar evolution code capable of calculating stellar models from the pre-main sequence to early white-dwarf stage for low-mass stars, or carbon burning for higher mass stars. More information on the specific workings of the code can be found in Weiss & Schlattl (2008) and Weiss & Ferguson (2009)[1], but the discussion here will be limited to those physical processes which are of particular importance for this study or which are specific to the AGB branch of the code used here. The solar abundances used throughout this work is that of

Grevesse & Sauval (1998).

4.1.1 Convective Mixing and Overshooting

In GARSTEC, convection is handled by the standard mixing-length formulation of Kippenhahn et al. (2013). As already discussed, the mixing length provides the temperature gradients necessary to determine where convection is occurring in stars as well as convective velocities. The mixing scheme in GARSTEC is, however, diffusive. The diffusion coefficients, $D_{\rm conv}$, are calculated from the conevctive velocities, $v_{\rm conv}$, from MLT via

$$D_{\rm conv} = \frac{1}{3} v_{\rm conv} \alpha H_P, \tag{4.1}$$

where α is the mixing length parameter and H_p is the pressure scale height. For the models run in this work, $\alpha = 1.68$. Once the diffusion coefficients are calculated the mixing is performed by solving

$$\frac{\partial X_i}{\partial t} = \frac{\partial}{\partial m_r}\left(\left(4\pi r^2 \rho\right)^2 D \frac{\partial X_i}{\partial m_r} \right), \tag{4.2}$$

where D is the sum of the convective and overshoot diffusion coefficients, X_i is the mass fraction of isotope i, and m_r is the mass coordinate. To calculate the overshoot diffusion coefficient one needs a theory for convective overshoot.

Convective overshooting, whether in the form of material overshooting the boundary or other proposed extra mixing processes, is a physical process which certainly takes place at all convective boundaries. As already discussed in Section 2.2.4, in the simplified picture of MLT there is no convective motion beyond the Schwarzschild boundary. However, the Schwarzschild boundary marks where the acceleration of the convective elements is zero. The material will reach this point with a non-zero velocity and, thus, will overshoot the boundary by some amount. This is what is known as convective overshoot. It should be noted that in the literature overshoot is often used as a catch-all term for CBM and its application in stellar models is also often meant to be an amalgamation of any number of CBM processes (Angelou et al. 2020). Convective overshooting is implemented in GARSTEC with the description by Freytag et al. (1996). The overshoot diffusion coefficient is defined as

$$D_{\rm over}(z) = D_0 \exp \frac{-2z}{f H_p}, \tag{4.3}$$

where f is the free parameter, H_p is the pressure scale height, z is the radial distance from the Schwarzschild boundary, and D_0 sets the scale of diffusive

[1] Unless otherwise indicated, these will be the references for all details of the code in the next four sections.

speed and is proportional to H_p. The area where overshoot is occurring is often referred to as the overshoot region, and the convective region excluding the overshoot region is sometimes referred to as the formal convective zone.

Using this description, problems may occur when running models for stars with very small convective cores. As H_p grows ever larger towards the center of the star, the overshooting region would become unrealistically large. This is handled in `GARSTEC` by applying a *geometrical cut-off*. In Equation (4.3), the H_p is replaced by

$$H_p^* = H_p \min\left[1, \left(\frac{\Delta R_{CZ}}{2H_p}\right)^2\right], \tag{4.4}$$

which ensures that the overshooting region is restricted to a fraction of the radial extent of the convective zone, ΔR_{CZ}. This feature is common in stellar evolution codes, though the specific implementation can vary (for a detailed discussion, see Section 2.7 of Anders & Pedersen 2023).

As an additional extension in the AGB branch of the code, the option for setting different overshoot parameters for different convective boundaries was implemented (Wagstaff 2018, Wagstaff et al. 2020). During the course of the life of a star many different convective zones will come and go. Normally, the same overshoot value is used for all convective zones and applies to both the upper and lower boundaries. There is, however, no reason to think that this overshoot parameter would not change for qualitatively different convective zones or even for the upper and lower boundaries of the same convective zone due to the different thermal and structural conditions (see, e.g., the discussions in Miller Bertolami (2016) and Wagstaff et al. (2020)). More concretely, many studies have shown that during the AGB a very large overshoot parameter is required at the base of the CE in order to inject enough protons into the deeper layers to facilitate the formation of the ^{13}C pocket. However, using such a large overshoot for, say, the core during H burning would be incongruous with the findings that a much lower overshoot parameter causes models to match the observed turn-off of the main sequence seen in clusters (Magic et al. 2010). Separate overshoot parameters can be set for the core convective zone during H burning (`fCHB`), the core convective zone during He burning (`fCHeB`), the bottom of the convective envelope (`fCE`), the bottom of the PDCZ (`fPDCZb`), and the top of the PDCZ (`fPDCZt`).

4.1.2 Diffusion

Diffusion, which we will refer to as atomic diffusion to avoid ambiguity with diffusive mixing, in stars is the result of gradients. In chemically inhomogeneous regions concentration gradients power concentration diffusion. Even in chemically

homogeneous stars, temperature and pressure gradients cause heavier elements to migrate towards the center of the star via temperature or pressure diffusion (Kippenhahn et al. 2013).

Atomic diffusion is a slow process. Under solar conditions the characteristic time it would take for an element to diffuse a solar radius is roughly 6×10^{13} years (Thoul et al. 1994). This suggests that atomic diffusion only plays a role in low-mass stars where the timescale of evolution is long enough to allow for atomic diffusion to be effective. Nevertheless, when discussing the ^{13}C pocket isotopes traveling even short distances may have an important effect. Therefore, atomic diffusion has been tested in a number of the models in this work.

Atomic diffusion is handled in GARSTEC using the description of Thoul et al. (1994). This approach assumes all elements are ionized and neglects the effects of radiation pressure but is otherwise quite general. By default, the atomic diffusion scheme in GARSTEC only considers H and He, however, other elements can be specified too. For the present study, when atomic diffusion was applied, it was done so for ^{1}H, ^{4}He, all C, N, and O isotopes, and neutrons.

4.1.3 Equation of State

Most models were run using the OPAL equation of state (EoS) (Rogers & Nayfonov 2002). The tables are interpolated on a grid of 4x4 tables via a smoothed quadratic interpolation as per OPAL recommendations (Weiss & Schlattl 2008). In special cases the EoS used by the code was not the OPAL EoS but rather FreeEOS (Irwin 2012). This EoS is calculated using an equilibrium-constant approach to minimize the Helmholtz free-energy. The equilibrium-constant approach gives numerical solutions of high quality with thermodynamic consistency which is typically better than 1 part in 10^{11}.

4.1.4 Nuclear Network

In the AGB branch of GARSTEC the nuclear network has been expanded. This was originally done as part of the work by Cruz et al. (2013). This was necessary in order to account for the neutron sources and neutron poisons important for the *s*-process. Additionally, they needed more isotopes to follow the nuclear burning processes during the proton ingestion episodes that may occur in extremely low- to zero-metallicity RGB stars.

The old network had 15 isotopes and approximately 21 reactions. The new network has 34 isotopes with 119 reactions. See Figure 4.1 for an overview of the two networks. Note that ^{26}Al requires special treatment. At temperatures present in stars one cannot assume that all ^{26}Al nuclei are in the ground state, some may be in what is called a metastable or isomeric state. That is to say in an energetic state. These two states are treated as separate isotopes in the network.

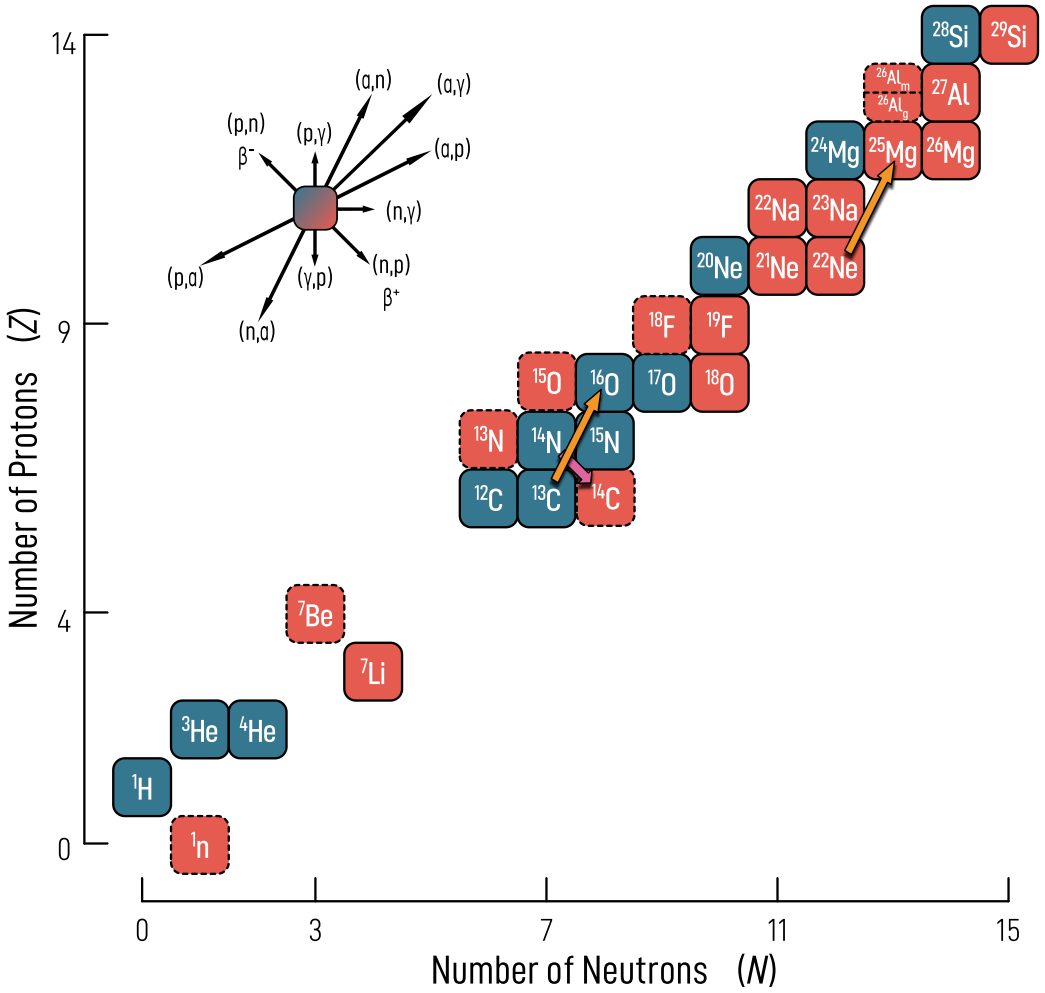

Figure 4.1 The nuclear network of GARSTEC in this work. The blue squares represent those isotopes which are in the nuclear network in the main branch of GARSTEC. Red isotopes are ones which have been added to the network in the AGB branch. Isotopes with a solid outline are stable, those with a dashed outline are unstable. The main neutron-source reactions and the primary neutron-poison reaction are marked with arrows.

Additionally, some reactions in the network are what will be referred to as *implicit reactions*. These are two step reactions which have been condensed into one reaction to avoid needing to include even more isotopes. This is a valid approximation so long as the second step of these implicit reactions is a β-decay with a short half-life. Short, in this case, means the half-life of the decay must be shorter than the time step taken by GARSTEC, and, thus, the time resolution is not fine enough to distinguish between the reaction proceeding in two steps or one. The energy generation of both reactions is of course accounted for.

The nuclear network tracks the energy and composition changes due to nuclear reactions by solving a system of equations. In general, the composition of any material subject to nuclear burning will evolve according to Equation (2.5) and

the energy generation can be calculated with Equation (2.11) as discussed in Section 2.1. This creates a stiff system of coupled differential equations. Being a stiff system of equations, one must use an implicit solver to calculate a solution. In GARSTEC, this is handled via a backwards-differencing scheme. Special care is taken to regulate the nuclear time steps such that abundance changes are kept at a level of at least 10% per step.

While the framework of this extended network was in place prior to the current work, I spent a great deal of time improving and extending the network. In fact, the network was almost completely rewritten such that the system of equations is set up programmatically by the code itself instead of being hardcoded. Furthermore, comparisons of the network to that of the LPCODE code (Althaus et al. 2015, and references therein) were conducted to ensure that all important isotopes and reactions were accounted for. Additionally, a basic method for interpolating reaction rates from rate tables was implemented.

The reaction rates used by GARSTEC in this work come from different sources. With a few exceptions the rates come from either the NACRE collaboration (Angulo et al. 1999, Xu et al. 2013) or the recommended JINA Reaclib database rates (Cyburt et al. 2010). The important exceptions are listed below:

- $^{13}\mathrm{C}(\alpha, \mathrm{n})^{16}\mathrm{O}$ (Ciani et al. 2021)
- $^{22}\mathrm{Ne}(\alpha, \mathrm{n})^{25}\mathrm{Mg}$ (Jaeger et al. 2001)
- $^{12}\mathrm{C}(\alpha, \gamma)^{16}\mathrm{O}$ (Kunz et al. 2002).

4.1.5 Opacities

The possibility of using "non-standard" opacities in GARSTEC is the result of the work of Kitsikis (2008) and Kitsikis & Weiss (2007). The possibilities for opacities were then subsequently expanded by Graham Wagstaff during his PhD (Wagstaff 2018, Wagstaff & Weiss 2018).

C/O Opacities

Usually, for main sequence stellar evolution one would use opacities from OPAL (Iglesias & Rogers 1996) for all models except for those models with low effective temperatures. In that case, one would use the tables from Ferguson et al. (2005). These tables all assume that the abundance distribution of metals is similar to that of the solar abundance. However, during the TP-AGB phase, the star will undergo a number of TDU events. These events will dredge-up large amounts of C to the surface, increasing the star's surface C/O ratio. In order to better model the outer layers in this phase, one needs opacity tables for which C/O is varied. Otherwise, the opacity will be underestimated. The opacity as a

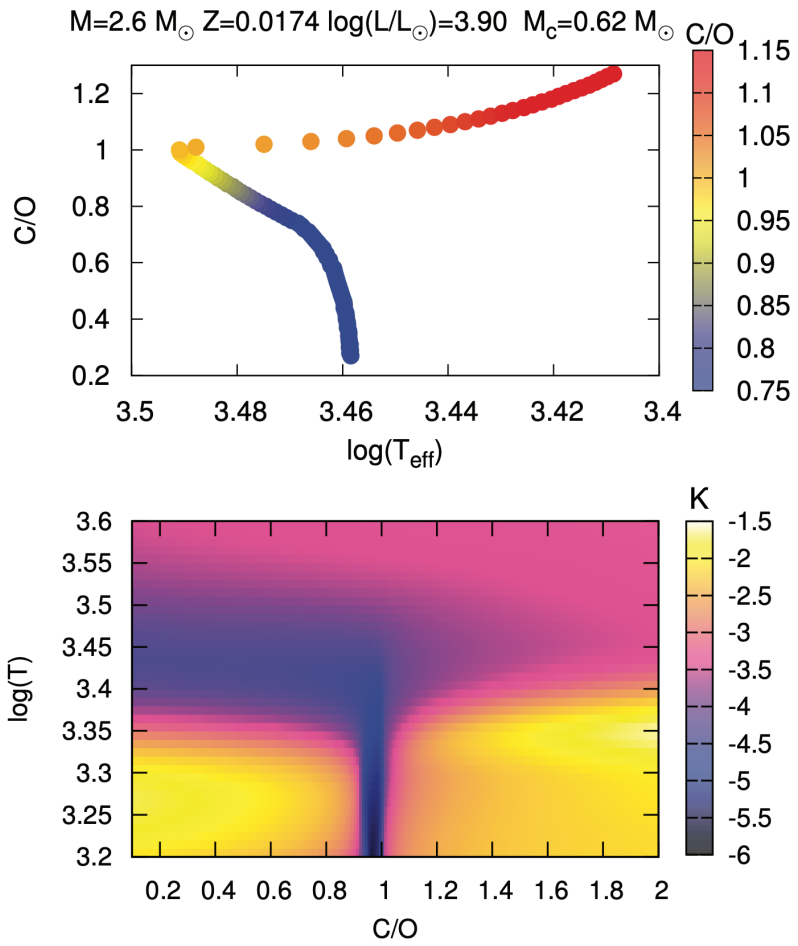

Figure 4.2 Figure 3 from Marigo et al. (2011). The top panel shows the evolution of the effective temperature of a TP-AGB model with initial mass of 2.60 $M_\odot$, from the first TP up to the post-AGB phase. The color-coding corresponds to the current surface C/O ratio. The bottom panel shows the Rosseland mean opacity as a function of the temperature and increasing C/O ($Z = 0.02$, $X = 0.7$).

function of temperature and C/O ratio is shown in Figure 4.2. Kitsikis (2008) added C/O-variable opacity tables to GARSTEC which are automatically switched to based on the current abundances. The C/O values for the tables are 0.17, 0.48, 0.9, 1.0, 1.1, 3.0, and 20.0.

Rosseland vs. Planck

It has already been discussed how the change in opacity due to composition, specifically C/O ratio, cannot be ignored in AGB stars, however, there is a more fundamental issue to be considered when it comes to opacity.

To avoid time consuming and complicated radiative transfer calculations a definition of a frequency independent, or grey, opacity is required. Assuming

Local Thermodynamic Equilibrium (LTE) and the *Diffusive Approximation*[2], which are strictly valid only in the stellar interior, one can derive the *Rosseland Mean* (RM) opacity (Rosseland 1924), denoted by κ_R, as

$$\frac{1}{\kappa_R(\rho, T)} = \frac{\int_0^\infty \frac{1}{\kappa(\nu)} \frac{\partial \mathrm{B}_\nu}{\partial r} \mathrm{d}\nu}{\int_0^\infty \frac{\partial \mathrm{B}_\nu}{\partial T} \mathrm{d}\nu},$$

where B_ν is the Planck function. This is the standard treatment for opacities in the atmospheric calculations in stellar evolution codes.

In the outer layers of a star, the diffusive approximation breaks down and the use of RM opacitites is no longer justified. An alternative to the RM opacity is the *Planck mean* (PM) opacity, κ_P, as outlined in Eddington (1921, 1916), defined as

$$\frac{1}{\kappa_P(\rho, T)} = \frac{\int_0^\infty \kappa(\nu) \mathrm{B}_\nu \mathrm{d}\nu}{\int_0^\infty \mathrm{B}_\nu \mathrm{d}\nu},$$

which does not rely on the diffusive approximation.

The RM opacities tend to allow the radiation flux to pass through at frequencies of least resistance, leading to an undersampling of the actual mean opacity in a stellar atmosphere. On the other hand, the PM opacities tend to lead to opacities which are larger than the RM opacities. Wagstaff & Weiss (2018) found that the AGB models using the PM opacities have cooler effective temperatures than those using RM opacities and, thus, have different temperatures at the base of the convective envelope which could have an impact on the TDUs.

The ability to use PM opacities is included in `GARSTEC` (Wagstaff 2018). Specifically, the code is able to use PM opacities in the outer layers of the star and transition to RM opacities in the inner layers (Wagstaff 2018, Wagstaff & Weiss 2018).

4.1.6 Atmosphere Treatment

The options for modeling the atmosphere in `GARSTEC` were also extended in Wagstaff (2018). A full solution of the stellar atmosphere including radiation transport is costly in terms of time so simplified models are used in stellar evolution codes. The most widely used model by far is the *Eddington gray atmosphere* model (Eddington 1959, pg. 320).

The Eddington gray atmosphere model uses a number of assumptions:

1. The absorption coefficient has no dependence on frequency.

[2]The Diffusion Approximation states that if the mean free path of a photon is 'short' then the transport of photons in that material can be modeled as a diffusive process.

2. The atmosphere has a plane-parallel geometry.

3. The atmosphere is in thermal radiative equilibrium.

The first assumption allows us to ignore many of the complications that arise from a full radiative transport calculation. The second assumption means that we consider the atmosphere to consist of parallel sheets stacked upon one another. Within these sheets all quantities of interest (radius, luminosity, etc.) are constant. In other words, all quantities only depend on the depth in the atmosphere. Altogether, this allows the equation of hydrostatic equilibrium to be combined with the definition of optical depth, τ_d, and thus the temperature stratification can be solved for.

This model works reasonably well, in particular for solar-like stars, and is therefore used in almost all stellar evolution calculations. The problem one encounters in AGB stars (and really in any star once it leaves the main sequence) is the plane-parallel geometry assumption is no longer valid. The atmosphere of an AGB star is very extended and should be calculated assuming a spherical geometry. To test what impact this may have Wagstaff (2018) implemented a spherical grey atmosphere, as outlined in Lucy (1976).

Within this framework, the effective temperature is taken analogously with the Eddington solution, i.e. $T_{\rm eff} = T_*$ at $\tau_d = 2/3$, where T_* is referred to as the photospheric temperature to acknowledge the lack of a unique definition for effective temperature in an extended atmosphere. This approach has the advantage of reducing to the Eddington plane-parallel atmosphere already implemented within `GARSTEC`, when the geometric extent of the atmosphere is negligible.

The temperature stratification is given by

$$T^4 = \frac{1}{2} T_*^4 \left[2W + \frac{2}{3}\tau \right],$$

where W is the geometric dilution factor

$$W = \frac{1}{2}\left(1 - \sqrt{1 - (R/r)^2}\right),$$

and the optical depth is defined as

$$\frac{d\tau_d}{dr} = -\kappa r \left(\frac{R}{r}\right)^2.$$

4.1.7 Mass Loss

The mass loss rates on the AGB can reach extreme values of up to $10^{-4}\,M_\odot\,yr^{-1}$ and is critical in determining the lifetime of the AGB phase. As discussed in Section 2.2.5, our theoretical understanding of mass loss on the AGB is insufficient

to derive mass loss rates directly from physical laws. Instead, parameterized mass-loss relation, both empirical and theoretical, are employed in stellar evolution codes. In this study, different mass loss prescriptions were used in different evolutionary phases which will be described below.

Prior to the AGB, Reimers' wind (Reimers 1975) was used,

$$\dot{M}_{\mathrm{Reimers}} = -4 \times 10^{-13} \eta_{\mathrm{R}} \frac{(L/\mathrm{L}_\odot)(R/\mathrm{R}_\odot)}{M/\mathrm{M}_\odot}, \tag{4.5}$$

with $\eta_{\mathrm{R}} = 0.4$. Once on the AGB, the mass loss rates will depend on the linear pulsation period, estimated as

$$\log_{10}(P) = -1.92 - 0.73 \log_{10}(M/\mathrm{M}_\odot) + 1.86 \log_{10}(R/\mathrm{R}_\odot) \tag{4.6}$$

as determined by Ostlie & Cox (1986) on the basis of linear pulsation models. If the period as given by Equation (4.6) is less that 400 days then Reimers' mass loss is used. If, however, the period exceeds 400 days the mass loss switches to one of two options depending on the surface composition. For O-rich surface compositions the mass loss formula of van Loon et al. (2005) is used,

$$\log_{10}(\dot{M}_{\mathrm{AGB}}) = -5.65 + 1.05 \log_{10}\left(10^{-4} \frac{L}{\mathrm{L}_\odot}\right) - 6.3 \log_{10}\left(\frac{T_{\mathrm{eff}}}{3500\mathrm{K}}\right), \tag{4.7}$$

whereas, for C-rich surface compositions the parameterization of Wachter et al. (2002) is used,

$$\log_{10}(\dot{M}_{\mathrm{AGB}}) = -4.52 + 2.47 \log_{10}\left(10^{-4} \frac{L}{\mathrm{L}_\odot}\right) - 6.81 \log_{10}\left(\frac{T_{\mathrm{eff}}}{2600\,\mathrm{K}}\right) - 1.95 \log_{10}\left(\frac{M}{\mathrm{M}_\odot}\right). \tag{4.8}$$

4.2 ANT

The post-processing code used in this work is the Astrophysical Nucleosynthesis Tool (`ANT`) (Battich et al. 2023). Given a series of sequential stellar models calculated with a 1D stellar evolution code like `GARSTEC`, `ANT` reads the density, temperature, and mixing information (convective velocities or diffusion coefficients) from the models, and calculates the nucleosynthesis and the mixing of chemical elements, decoupled from each other. By default, the abundances are read by `ANT` from `GARSTEC` for the initial model after which the abundances are evolved without any information of the abundances in `GARSTEC`.

The number of isotopes and reactions which `ANT` follows is flexible and can be adjusted based on the problem being investigated. For example, for the *i*-process

calculations in this work a network of 1190 isotopes is used. For the *s*-process only 343 isotopes are followed. Below, I cover the important details of the workings of `ANT`.

4.2.1 Nuclear Network

The nuclear network of `ANT` includes reactions of up to three reactants. The basics of nuclear networks including the system of equations which needs to be solved (Equation (2.5)) has already been covered and will not be repeated here. However, the way of solving those equations is different in `ANT` than in `GARSTEC`. This is mainly due to the fact that the network in `ANT` is significantly larger and so more efficient methods are required to solve the network equations in a reasonable amount of time. As already discussed, Equation (2.5) is a very stiff set of equations and requires an implicit scheme to solve. `ANT` uses the Bader-Deuflhard method (Bader & Deuflhard 1983). The linear algebra package for solving the system of equations is the MA48 package (HSL 2013) which uses Gaussian elimination to solve a sparse unsymmetric system of equations. This implementation follows the suggestion of Timmes (1999).

In general, one can understand the Bader-Deuflhard method as follows. The system of equations to resolve is composed of one equation for each isotope in the network. These equations can be written as

$$\frac{\mathrm{d}\vec{y}}{\mathrm{d}t} = \vec{f}(\vec{y}), \qquad \vec{y} = (y_1, \ldots, y_{N_{\mathrm{isot}}}) \tag{4.9}$$

$$\vec{y}(t_0) = \vec{y}_0 \tag{4.10}$$

where y_i is the abundance (in mole fraction) of isotope i and f_i is the corresponding function for the time derivative of that isotope. The functions $f_i(\vec{y})$ depend on products of the abundances and are, therefore, non-linear. This is an initial value problem with y_0 being the initial abundances provided at time t_0. In practice these abundances are taken from a stellar evolution code. The algorithm used to solve this initial value problem is the semi-implicit mid-point method, combined with a Richardson extrapolation.

The implicit mid-point method begins with an implicit form of the mid-point-rule equation

$$\vec{y}_{n+1} - \vec{y}_{n-1} = 2h\vec{f}\left(\frac{\vec{y}_{n+1} + \vec{y}_{n-1}}{2}\right). \tag{4.11}$$

One then converts this into a semi-implicit form by linearizing about $\vec{f}(\vec{y}_n)$:

$$\left[1 - h\frac{\partial \vec{f}}{\partial \vec{y}}\right]\vec{y}_{n+1} = \left[1 - h\frac{\partial \vec{f}}{\partial \vec{y}}\right]\vec{y}_{n-1} + 2h\left[\vec{f}(\vec{y}_n) - \frac{\partial \vec{f}}{\partial \vec{y}}\vec{y}_n\right]. \tag{4.12}$$

Now, for a given time, t_0, and time step, H, one divides the time step from t_0 to $t_0 + H$ into sub-time-steps of size $h = H/n$, for a given n. Note, that we have yet to specify what n should be so that one can calculate h. This is where the Richardson extrapolation enters. The idea of Richardson extrapolation is to calculate the solution from t to $t + H$ a certain number of times using different subdivisions, h, of the time step, H, and then extrapolate the different solutions to $h = 0$. In this sense one is considering the final answer of the numerical calculation itself as an analytical function of h which we probe by seeing how it changes with different values of h. In this way one is often able to take larger time steps. For stiff problems, Bader & Deuflhard (1983) propose the sequence:

$$n = 2, 6, 10, 14, 22, 34, 50, \ldots . \tag{4.13}$$

The extrapolation is then performed with a polynomial function. The number of attempts one makes to cross the interval H with different values of h (how many numbers of the sequence 4.13 use) depends on the precision required.

For a given n the reaction network is then advanced over the n sub-time-steps of h totaling a complete time step of H via the following series of matrix equations:

$$\vec{\Delta}_0 = \left[1 - h\frac{\partial \vec{f}}{\partial \vec{y}}\right]^{-1} h\vec{f}(\vec{y}_0) \tag{4.14}$$

$$\vec{y}_1 = \vec{y}_0 + \vec{\Delta}_0, \tag{4.15}$$

$$\vec{\Delta}_k = \vec{\Delta}_{k-1} + 2\left[1 - h\frac{\partial \vec{f}}{\partial \vec{y}}\right]^{-1} [h\vec{f}(\vec{y}_k) - \vec{\Delta}_{k-1}] \tag{4.16}$$

$$\vec{y}_{k+1} = \vec{y}_k + \vec{\Delta}_k, \qquad k = 1, \ldots, n-1 \tag{4.17}$$

$$\vec{\Delta}_n = \left[1 - h\frac{\partial \vec{f}}{\partial \vec{y}}\right]^{-1} [h\vec{f}(\vec{y}_n) - \vec{\Delta}_{n-1}] \tag{4.18}$$

$$\vec{y}_n = \vec{y}_n + \vec{\Delta}_n, \tag{4.19}$$

where the Jacobian matrix, $J = \partial \vec{f}/\partial \vec{y}$, is always evaluated at t_0 and the function $\vec{f}$ is reevaluated at each sub-time-step h.

4.2.2 Convection

By default, `ANT` implements convection via the advective mixing mechanism described by Chieffi et al. (2001), which itself is based on the mixing description from Sparks & Endal (1980). In this scheme one calculates the mass fraction abundance of isotope k in shell i, X_i^k, from the unmixed abundance, ${}^0X_i^k$, as

$$X_i^k = {}^0X_i^k + \frac{1}{M_{\text{convec}}} \sum_{j \in M_{\text{convec}}} \left({}^0X_j^k - {}^0X_i^k\right) f_{ij} \Delta m_j, \tag{4.20}$$

where M_{convec} is the mass of the convective zone and Δm_j is the mass of shell j. The sum runs over all grid points in the convective zone. The quantity f_{ij}, known as the mixing factor[3], is defined as

$$f_{ij} = \min\left(\frac{\Delta t}{\tau_{ij}}, 1\right), \tag{4.21}$$

where Δt is the time step over which the material is to be mixed and

$$\tau_{ij} = \int_{r_i}^{r_j} \frac{\mathrm{d}r}{v_{\text{MLT}}} = \sum_{l=i}^{j} \frac{\Delta r_l}{v_{\text{MLT}_l}}. \tag{4.22}$$

Here Δr_l is the width of shell l and v_{MLT_l} is the convective velocity in shell l as computed via mixing length theory. One can think of τ_{ij} as a characteristic timescale of convective motions between shells i and j. This mixing scheme has the advantage that it is fast to implement, but it is an advective mixing scheme whereas in `GARSTEC` the mixing is diffusive. This introduces an additional inconsistency between the stellar evolution code and the post-processor. To improve this situation, the mixing scheme was altered. In Einstein (1905b, Section 4) the derivation of the frequency distribution of the distance traveled by a particle via diffusion from a point source is shown. Unsurprisingly, this distribution is Gaussian. The mean of the distribution is 0 and its standard deviation is $\sqrt{2Dt}$ where D is the diffusion coefficient and t is the time elapsed. Leveraging the properties of the Gaussian distribution, we can then say the root mean square of the distance traveled by a particle with diffusion coefficient D in time t is also $\sqrt{2Dt}$.

We can now use this information to rewrite the expression for f_{ij} based on the timescale for diffusion. Thus, we have

$$f_{ij} = \min\left(\frac{\Delta t}{\tau^D_{ij}}, 1\right), \text{ where } \tau^D_{ij} = \sum_{l=i}^{j} \frac{\Delta r_l^2}{2D_l\alpha^2}, \tag{4.23}$$

D_l is the diffusion coefficient for shell l, and α is a constant whose meaning will be discussed now. In the Chieffi mixing scheme there was a clear criterion for full mixing; If the velocity is high enough to allow for a particle to traverse the entire distance to the next grid point in the allotted time, then $f_{ij} = 1$. In this new mixing scheme it is not so clear what the criterion for full mixing is. For instance, consider a simple case where we have a two-grid-point-wide convective zone. The mixing factor for the mixing between grid points 1 and 2 is then

[3] In Chieffi et al. (2001) this is called the damping factor as opposed to the mixing factor as it is called in Sparks & Endal (1980). Given that larger values of f mean increased mixing the original nomenclature of Sparks & Endal (1980) makes more sense and will be used here.

$$f_{12} = \frac{\Delta t}{\frac{\Delta r_1^2}{2D_1\alpha^2}} = \frac{2D_1\Delta t\alpha^2}{\Delta r_1^2}. \tag{4.24}$$

We can then ask what does it mean if $f_{12} = 1$ in this case? Well, it implies that

$$\Delta r_1 = \alpha\sqrt{2D_1\Delta t} = \alpha\sigma. \tag{4.25}$$

This means, if we assume for the time being that $\alpha = 1$, that $f_{12} = 1$ implies that the distance to the next grid point is exactly equal to the 1σ value of the Gaussian distribution which have assumed for our diffusion process. However, if the next grid point is 1σ away that means 34.1% of the particles originally in shell 1 have moved a distance less than Δr_1, i.e. the particles are still in shell 1. This is far from fully mixed. Now by changing the value of α we can change the σ-value at which we assume full mixing. So if $\alpha = 1/4$, then $f_{12} = 1$ when $\Delta r_1 = 1/4\sigma$. This α is effectively a free parameter in this scheme which will be kept at $1/4$ for the entirety of this work. I made one final change to the mixing scheme. The form of f_{ij} was changed to

$$f_{ij} = \begin{cases} 1.0 & \text{if } \Delta t/\tau_{ij}^D > 1.0 \\ 1.0 - (1.0 - \Delta t/\tau_{ij}^D)^4 & \text{else.} \end{cases} \tag{4.26}$$

This change improves the agreement between `GARSTEC` and `ANT` marginally and is not essential.

Below one can see some tests of the new mixing scheme. One important thing to keep in mind for these tests is that the reaction rate sources for `ANT` and `GARSTEC` are not necessarily the same. Thus, even for the reactions which the two networks both include, the rate may be different, and so some of the abundance differences in the following tests are due to this. These differences however will be the same for both mixing schemes since neither mixing scheme relies on changes to the networks of either code. First, a $3\,M_\odot$, solar metallicity track was run from the ZAMS to the end of the MS without overshoot. This track was then post-processed by `ANT` once with the standard Chieffi mixing scheme and once with the new Einstein-Sparks-Chieffi (ESC) mixing scheme described above. The results can be seen in Figure 4.3 where the solid lines show the abundances from `GARSTEC` and the dashed line shows the abundances from `ANT`. There is hardly any difference between the two mixing schemes and both reproduce the abundances of `GARSTEC` quite well. This is not surprising since the convective velocities in the core are high and the time steps which `GARSTEC` takes are quite large on the MS. Together this means that $f_{ij} \approx 1$ throughout the convection zone and so the mixing schemes are mathematically identical.

Figure 4.4 again shows the results of the mixing schemes on the MS, but the stellar models now include overshooting. In this case there is a noticeable

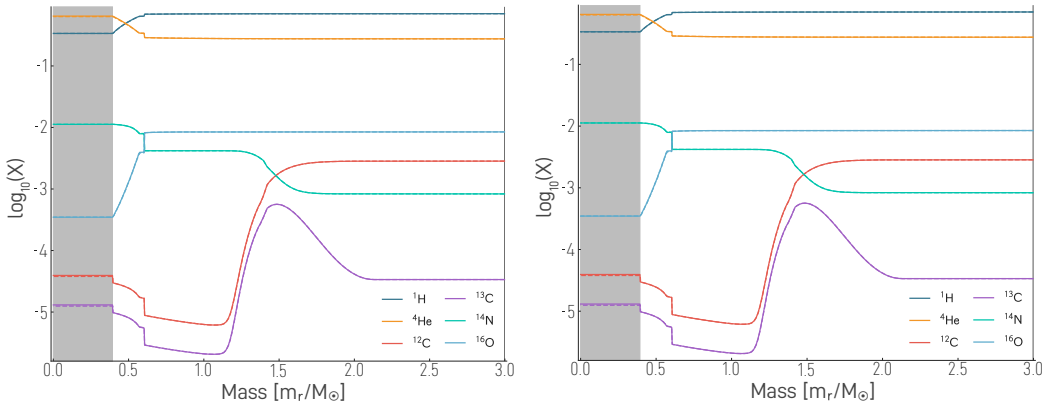

(a) Chieffi mixing scheme **(b)** ESC mixing scheme

Figure 4.3 A comparison of the Chieffi mixing scheme (left) and the ESC mixing scheme (right) in `ANT` on the MS for a model without overshoot. Solid lines are the abundances from `GARSTEC` and dashed lines are the post-processed abundances from `ANT`. Dark regions denote convection zones.

difference between the two mixing schemes. This difference is due to the behavior of the mixing scheme in the overshoot regions where $f_{ij} < 1$. Here the Chieffi mixing scheme overestimates the value of f_{ij} and over mixes. The ESC mixing scheme on the other hand much better matches the abundance profiles from `GARSTEC` in this region, implying a much more accurate determination of f_{ij}.

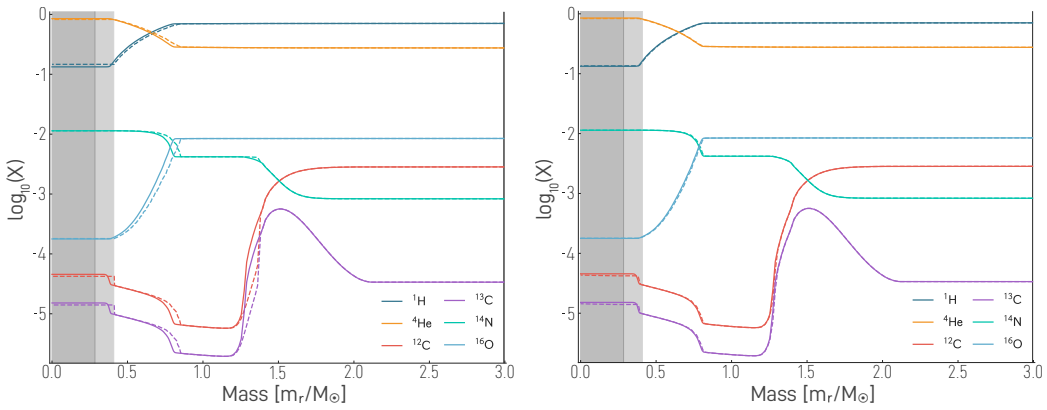

(a) Chieffi mixing scheme **(b)** ESC mixing scheme

Figure 4.4 A comparison of the Chieffi mixing scheme (left) and the ESC mixing scheme (right) in `ANT` on the MS for a model with overshoot. Solid lines are the abundances from `GARSTEC` and dashed lines are the post-processed abundances from `ANT`. Dark gray areas denote formally convective regions and light gray areas denote overshoot regions.

Next, the mixing schemes were tested during the central He-burning phase of the same track including overshoot. To be clear, for this test the post-processing was done only from the start of central He burning instead of from the ZAMS. In doing so we avoid the complications arising from determining which abundance

irregularities are from this phase and which are perhaps cumulative effects from the previous evolution. Here again one can see that the ESC mixing scheme better matches convection in GARSTEC in particular in the overshoot regions.

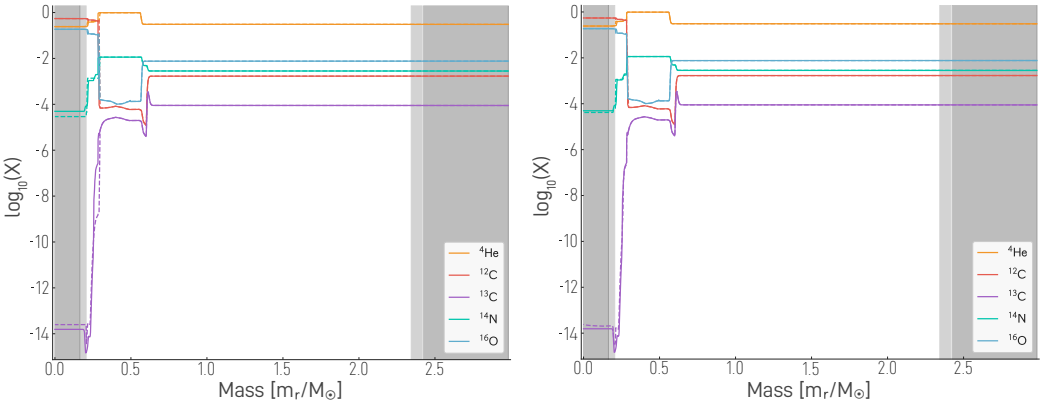

(a) Chieffi mixing scheme **(b)** ESC mixing scheme

Figure 4.5 A comparison of the Chieffi mixing scheme (left) and the ESC mixing scheme (right) in ANT during central He burning for a model with overshoot. See Figure 4.4 for an explanation of the plot elements.

Finally, a test of the mixing schemes was run for the PDCZ, again including overshoot. Figure 4.6 shows a snapshot of the star as the PDCZ is diminishing in size. Again one can see that in the formally convective region the results of the two mixing schemes are quite similar. Both show a fair amount of deviation for ^{13}C and ^{14}N, though these isotopes have relatively low abundances. This may very well be due to different reaction rate sources in ANT and GARSTEC. Additionally, the ESC mixing scheme seems to do a better job of reproducing the abundance profiles of ^{16}O and ^{4}He in this region. The largest differences between the schemes is in the formerly convective region below the PDCZ where the extended overshoot region would have been located ($0.585 \lesssim m_r/\mathrm{M}_\odot \lesssim 0.59$). Here one can see that both mixing schemes again have difficulties matching the ^{13}C and ^{14}N isotope profiles, though the ESC mixing scheme at least matches the location and magnitude of the abundance peaks near $m_r/M_* \approx 0.59$ for these isotopes. Where the difference is most pronounced is in the abundance profiles for ^{4}He, ^{12}C, and ^{16}O. It is clear that the Chieffi mixing scheme over mixes these elements. This is the same behavior as was seen in Figure 4.4.

In summary, these comparisons show that the Chieffi mixing scheme is perfectly appropriate for formally convective regions, but to use overshoot an adjustment of the mixing scheme is needed. The ESC mixing scheme is much more suited to these situations and is simple to implement in a code which already has the Chieffi mixing scheme implemented. Of course no mixing scheme will exactly match what is done in GARSTEC except for the mixing scheme used in GARSTEC, and there will always be some deviations due to different networks, reaction rate

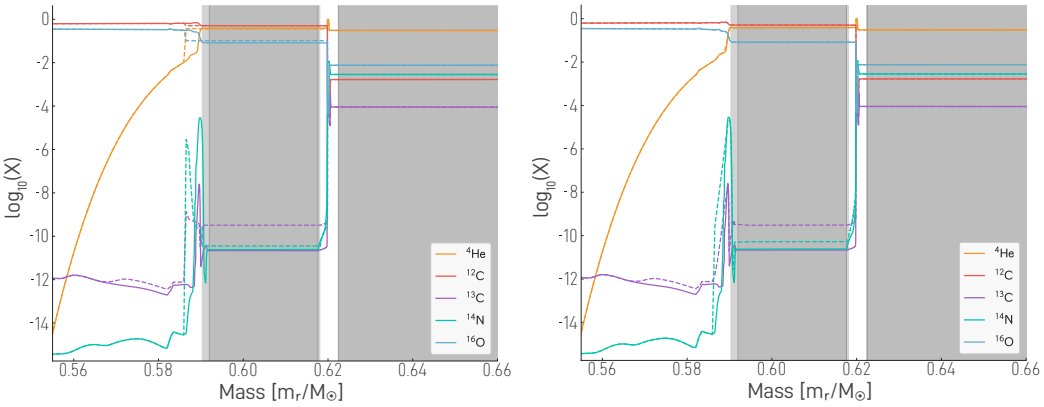

(a) Chieffi mixing scheme **(b)** ESC mixing scheme

Figure 4.6 A comparison of the Chieffi mixing scheme (left) and the ESC mixing scheme (right) in ANT during a PDCZ for a model with overshoot. See Figure 4.4 for an explanation of the plot elements.

sources, and numerics.

4.2.3 Abundances from GARSTEC

By default ANT only reads the abundances from GARSTEC for the first model after which the abundances of the two codes are completely independent. This has the drawback that, for example, the neutron densities reported for the models run in GARSTEC may not be in agreement with the neutron densities in ANT. I thus devised a way that the neutron densities in the two codes are in better agreement. To do this I edited ANT such that at every time step the code reads the abundances of ^{1}H, ^{13}C, and ^{14}N from GARSTEC. In this way the most important isotopes in determining the neutron density are in exact agreement between both codes. For the case of the *i*-process where the neutron captures are happening in a convective region, ANT also ignores the neutrons in the mixing scheme. This is valid since the decay time for neutrons is around 10 minutes and the capture time for neutrons in the PIE may be even shorter. Thus, the neutrons are never mixed far from where they were produced before they are destroyed. Note that this handling of the abundances was not implemented for the tests of the mixing scheme shown in the previous section.

Figure 4.7 and Figure 4.8 show the abundance comparisons of ANT and GARSTEC for a PIE of a 1 $M_\odot$ model without overshoot and the ^{13}C pocket for a 3$M_\odot$ model with overshoot. In both cases the neutron densities are in very good agreement. This is the desired behavior. Note, ^{1}H, ^{13}C, and ^{14}N are excluded from these plots since they are forced to be in perfect agreement via this method.

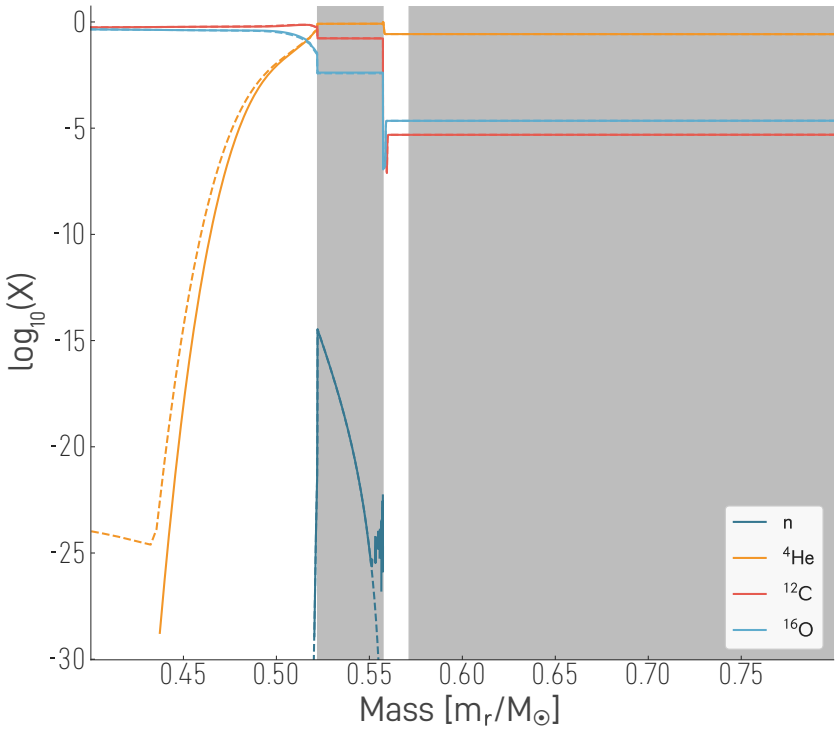

Figure 4.7 A comparison of the abundances of `ANT` and `GARSTEC` during a PIE for a $1M_{\odot}$ model without overshoot. See Figure 4.4 for an explanation of the plot elements. ^{1}H, ^{13}C, and ^{14}N are forced to agree with `GARSTEC` and, as such, are not shown.

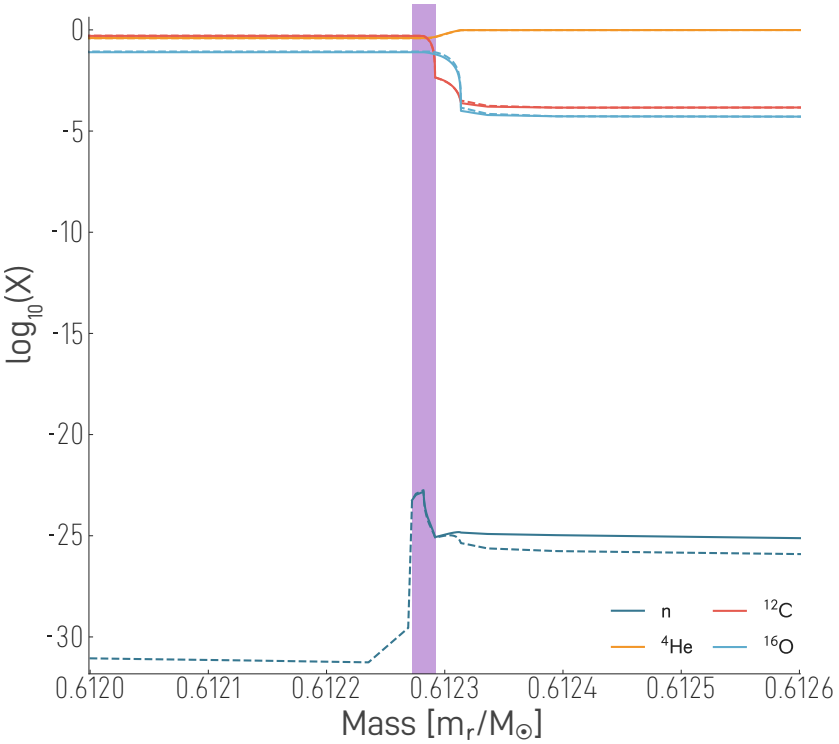

Figure 4.8 A comparison of the abundances of `ANT` and `GARSTEC` in the ^{13}C pocket (purple region) for a $3M_{\odot}$ model with overshoot. See Figure 4.4 for an explanation of the plot elements. ^{1}H, ^{13}C, and ^{14}N are forced to agree with `GARSTEC` and, as such, are not shown.

Chapter 5

Investigations of the *i*-process

> What we observe is not nature itself, but nature exposed to our method of questioning.
>
> Werner Heisenberg, *Physics and Philosophy*

As has been shown in the previous chapters, there is much we still do not know about the *i*-process including where in the universe it occurs. Even if one assumes that it occurs in low-mass, low-metallicity AGB stars there are still unknowns related both to the stellar structure, such as where and when the PDCZ splits during a PIE and which stars experience PIEs, as well as to the nuclear processes, such as what sort of final surface abundances one could expect from these stars. In my investigations into the *i*-process I sought to address these questions by means of running and analyzing stellar evolution models coupled to a post-processing code. I will first discuss in detail the stellar evolution models and the results related to the stellar structure and light-element nucleosynthesis before discussing the heavy-element nucleosynthesis in detail. The results related to the structure and light-element nucleosynthesis of the $1.2\,M_\odot$ models have already been published in Remple et al. (2024).

5.1 Structure and Light-Element Nucleosynthesis

5.1.1 The Fiducial Model

We begin by discussing in detail the evolution of a $M_{\text{initial}} = 1.2\,M_\odot$, $Z = 5 \times 10^{-5}$ ($[\text{Fe/H}] = -2.56$) evolutionary model. This model will act as a fiducial model for comparing what happens when we add or change the physics in other models. The values of mass and metallicity were chosen to allow for a comparison to

both Cristallo et al. (2009a) and Choplin et al. (2021). For this model, overshoot was only applied to the convective core with overshoot parameters of `fCHB` = `fCHeB` = 0.016. This value is calibrated to match observations of main-sequence stars in clusters (Maeder & Meynet 1991, Stothers & Chin 1992, Weiss & Schlattl 2008, Magic et al. 2010). There is no clear way of calibrating the core overshoot for the HB so I followed the typical practice of using the same value as for the MS (Wagstaff et al. 2020). It should be mentioned that there are studies which suggest, based on model matching to asteroseismology observations, that higher or lower values of `fCHeB` are needed during the central He burning (Bossini et al. 2017, Brogaard et al. 2023). The dependence of the results on the core overshoot parameter for the MS and HB were not tested.

pre-AGB

The evolution up to the AGB phase proceeds in the expected manner. H burning in the core occurs under radiative conditions until the exhaustion of H at an age of 2.5 Gyr. The star then crosses the Hertzsprung gap and ascends the RGB. The core He flash occurs off-center in the degenerate central regions of the star before the star settles on the HB, burning He in its core for another 100 Myr.

The AGB

After the exhaustion of He in the core on the HB, the star once again ascends the giant branch — in this case the AGB. The E-AGB phase sees the two, mostly dormant, burning shells moving outward in the star until the ignition of the H shell. The TP-AGB phase for this star begins with a typical cycle of pulse, power down, and interpulse phase. The H-free core mass of this model just before the first instability is $0.56\,M_\odot$. Despite this first pulse being rather weak, the He luminosity peaks at $\log_{10} L_{\rm He}/L_\odot = 5.6$, it is nevertheless able to drive a PDCZ in the intershell region. The pulse is not followed by a TDU. After the flash the models exhibit a series of sub-flashes with progressively weaker peak He luminosities and smaller PDCZs. This is something present in all of our models for the first few instabilities, after which the sub-flashes disappear. This is a known phenomenon (see, for example, Sackmann 1977). In the second instability the He luminosity exceeds $\log_{10} L_{\rm He}/L_\odot = 6.5$ and the PDCZ spans over $3.0 \times 10^{-2}\,M_\odot$. The pulse is followed by one sub-flash and, as before, no TDU.

The third instability is where the PIE occurs. This flash is again stronger than the previous ones with He luminosities in excess of $\log_{10} L_{\rm He}/L_\odot = 7.2$ even before the PIE. The PDCZ, driven by the large release of energy at its base, begins to extend into the H-rich regions near the H shell. The protons ingested there are quickly brought deeper into the PDCZ where temperatures are in excess of 200 MK and the $^{12}\mathrm{C}(\mathrm{p},\gamma)^{13}\mathrm{N}$ reaction proceeds with rapidity. The freshly synthesized

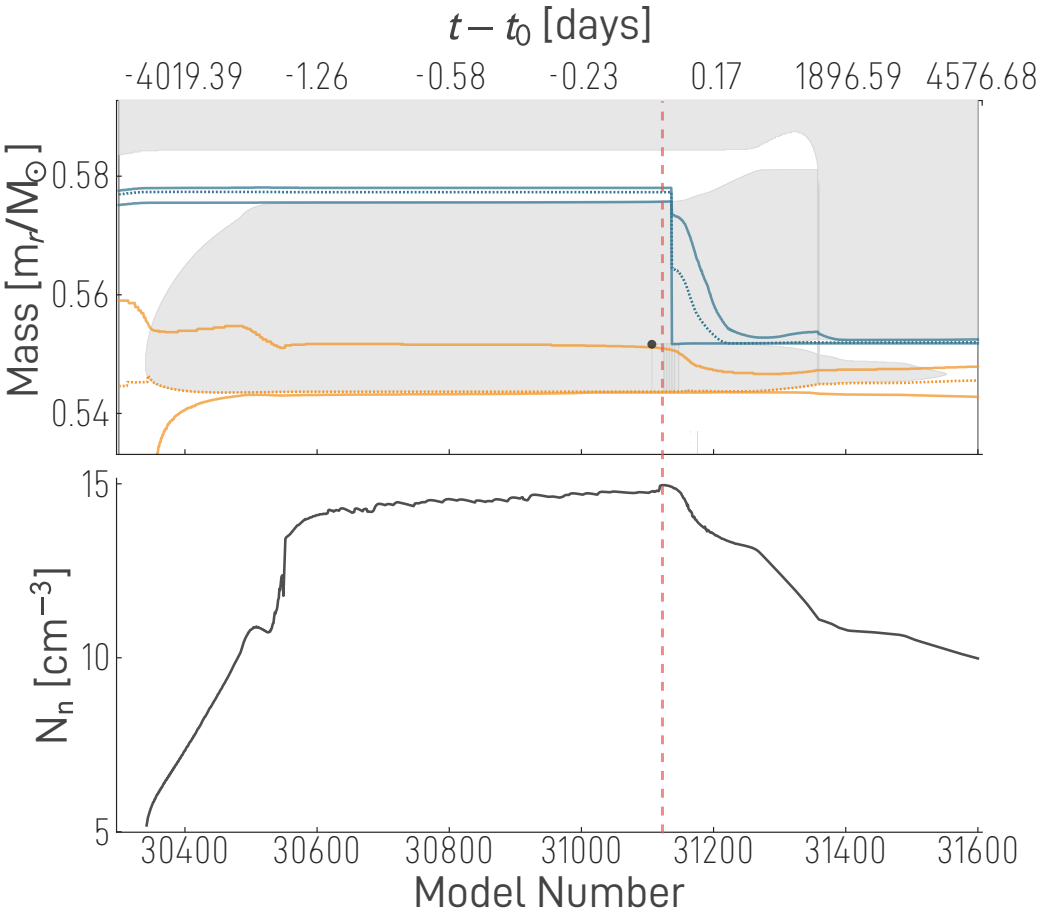

Figure 5.1 Kippenhahn diagram showing the structure of the fiducial model (top) and the maximum neutron density at each time step (bottom). Time is shown as model number on the lower x-axis and as time in days relative to the time of maximum neutron density in the upper x-axis. In the Kippenhahn diagram the top and bottom of the H shell is denoted by the solid blue lines with the dotted blue line following the point of maximum H burning in the shell. The top and the bottom of the He shell is denoted by the solid orange lines with the orange dashed line following the point of maximum He burning in the shell. Formally Convective regions are shown in gray. The time when the neutron density is the largest is denoted by the dashed red line, and the location and time at which the PDCZ splits is denoted by the black circle.

^{13}C reacts after a short time with the abundant α-particles to produce neutrons. 311 years after the pulse began, the neutron density exceeds 10^{11} cm^{-3} marking the beginning of the *i*-process conditions. The following 150.56 days see a steady increase in the neutron densities until the maximum value of 9.15×10^{14} cm^{-3} is reached. Around this time the H luminosity also reaches its maximum of $\log_{10} L_{\mathrm{H}}/\mathrm{L}_\odot = 10.42$. The He luminosity, on the other hand, reached its maximum of $\log_{10} L_{\mathrm{He}}/\mathrm{L}_\odot = 8.18$ somewhat earlier. The run of the luminosity during the PIE can be seen in Figure 5.2.

Before the time when the neutron density reaches its maximum value (time of

maximum neutron density, TOMND), the PDCZ splits in two. The offset between the two events is only 1.14 hours. The neutron density achieves its maximum value in the lower part of the split PDCZ and therefore the bulk of the nucleosynthesis will occur there. Additionally, the upper and lower parts of the split PDCZ do not remerge throughout the remaining evolution. The upper convective zone, which contains some of the nucleosynthetic products of the PIE prior to the split, merges with the CE a few years after the split, and the nucleosynthetic products can make their way to the surface of the star. The splitting of the PDCZ occurs when the timescale for the $^{12}C(p,\gamma)^{13}N$ reaction is approximately equal to the local convective turnover timescale (Cristallo et al. 2009a, Choplin et al. 2021). The influence of numerics on the splitting was tested and will be discussed in Section 5.1.3.

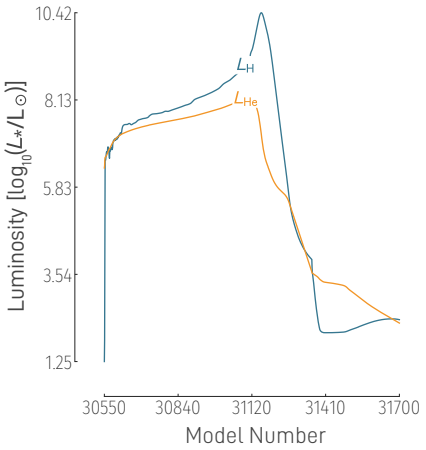

Figure 5.2 Time evolution of the H luminosity (in blue) and the He luminosity (in orange) of the fiducial model during the PIE.

The PIE drastically changes the surface composition of the star. Along with any heavy elements, C is also brought up to the surface in large quantities. The C/O ratio at the surface of the star reaches 19.26. The large C/O ratio triggers intense mass loss rates of up to $\dot{M} \lesssim 1 \times 10^{-5}\,M_\odot\,yr^{-1}$. Despite this, the star is able to survive long enough to undergo three more thermal pulses. The second and third of these pulses are unimportant for the topics of interest in this work, but the first post-PIE pulse is important. The star experiences a rather strong TDU following this first pulse which will have consequences for the final surface abundances as it allows some of the heavy elements which were trapped in the lower part of the split PDCZ to nevertheless reach the surface. This occurs in two steps. First, the PDCZ of the post-PIE pulse will mix the isotopes from the lower part of the split PDCZ throughout the intershell region. Second, the TDU will descend into this intershell region, though not deep enough to reach the same mass coordinate as the lower part of the split PDCZ, and bring some of the mixed material to the surface.

The testing of the numerics has already been mentioned once and was done repeatedly throughout the study as the small spatial and temporal scales involved require that such tests be conducted. For instance, from Figure 5.1 one can see that the time between the PDCZ approaching the base of the H shell and the TOMND is on the order of a year, which is in agreement with Choplin et al. (2021). Thus, the temporal and spatial resolution settings of the code were tested to determine what, if any, impact they had on the occurrence of the PIE. In my tests

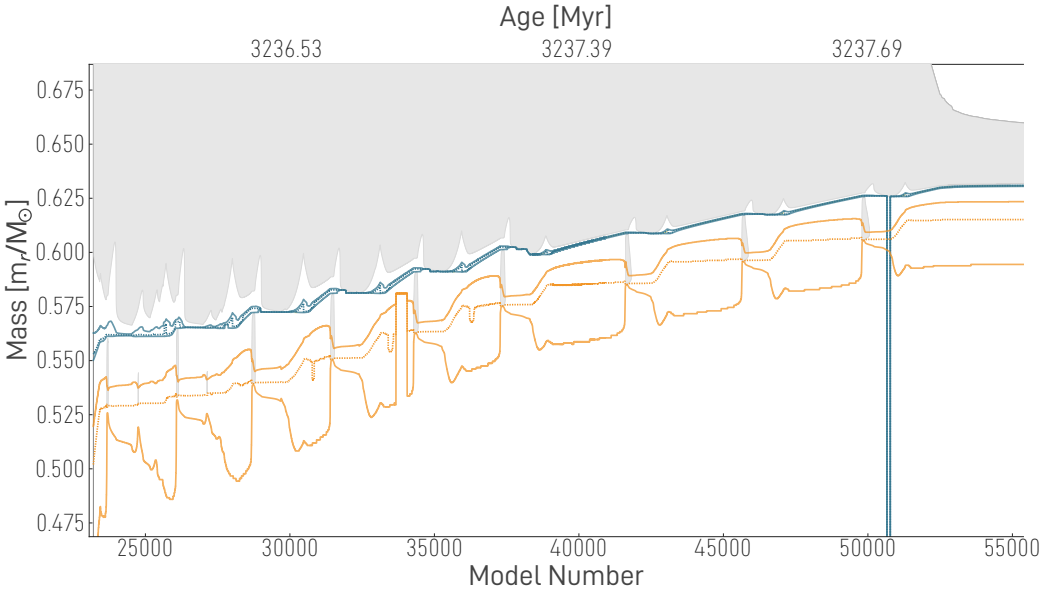

Figure 5.3 Kippenhahn diagram (see Figure 5.1 for an explanation of the plot elements) of the low temporal resolution model. In this case the PIE is missed entirely due to too large of time steps and the model follows a standard AGB evolution.

for this particular model, I find that the occurrence of the PIE is not particularly sensitive to the spatial resolution of our models. It is however sensitive to the temporal resolution. GARSTEC has many ways of controlling the time steps of the models. Apart from setting the minimum and maximum allowed time step, one can also require the time steps to be small enough to restrict the change in certain quantities such as luminosity, effective temperature, etc., to remain below a threshold value. In the end it was found that specifically the size of the allowed changes of the H and He luminosity are key. If larger jumps in the H and He luminosity are allowed between models the PIE will be missed entirely and the star will evolve as a normal AGB star as was also seen in Choplin et al. (2021). The evolution of this low-time-resolution track can be seen in Figure 5.3. In the default case the time step taken by GARSTEC can reach the level of hours and does not exceed 10^{-4} yr at any point during the PIE. In the low-time-resolution case, where the PIE is missed, the smallest time step taken during the pulse where the PIE should occur is about 6.2 days before quickly becoming larger again.

5.1.2 To Ingest or Not to Ingest

The discussion at the end of the previous section begs the questions: “How do you know if you have missed a PIE or if the star should not have one at that pulse?”.

The Entropy Argument

There is currently no consensus in the literature on how to determine whether a PIE should happen for a particular TP. Most of the arguments rely on the idea of an entropy barrier (Fujimoto et al. 1990, Iwamoto et al. 2004, Choplin et al. 2022). Specifically, one calculates the entropy barrier imposed by the H-burning shell across models of different mass and metallicity. Based on the entropy barrier values of the models which experience a PIE or not, one then defines a critical entropy below which a PIE should occur. This is the approach taken in Choplin et al. (2022). While they are able to find a critical entropy barrier value, they stress that this method has a number of important drawbacks. Namely, it only gives a hint as to whether or not a PIE should happen. If the entropy barrier for a particular pulse is near the critical value one would still need to check if using different resolution settings in the code would lead to a PIE. Additionally, the metallicity dependence is not straightforward, and thus one cannot easily extrapolate the critical entropy barrier value to other metallicities. Finally, the exact value is likely to be code dependent.

The Timescale Argument

The method I developed involves using timescale estimates to establish criteria for determining whether a PIE occurs. This approach has been effectively utilized in previous studies to estimate the extent of the PDCZ (Despain & Scalo 1976, Fujimoto 1977) as has already been discussed (see Section 2.2.3 and Section 3.1).

Despain & Scalo (1976) define two key timescales: the timescale for the growth of the instability, τ_{He}, and the timescale for radiative diffusion from the He shell to the H shell, τ_{diff}. As long as $\tau_{\mathrm{He}} < \tau_{\mathrm{diff}}$, the PDCZ will continue to expand, since the instability develops more rapidly than the outer layers can respond to it. However, when $\tau_{\mathrm{He}} \approx \tau_{\mathrm{diff}}$, the outer layers can react to changes in the He shell as quickly as they occur, leading to the cessation of PDCZ growth.

An Update to the Timescale Argument

In the present study the timescales are defined as

$$\tau_{\mathrm{He}} = \frac{\left\langle C_p \right\rangle \langle T \rangle}{L_{\mathrm{He}}/M_{\mathrm{conv}}} \tag{5.1}$$

$$\tau_{\mathrm{diff}} = \frac{C_p \kappa \rho}{s_{\mathrm{rad}} c} H_p^2 \tag{5.2}$$

where the angled brackets denote an average over the PDCZ, C_p is the specific heat capacity, M_{conv} is the mass of the PDCZ, and s_{rad} is a quantity defined in Sugimoto (1970) as

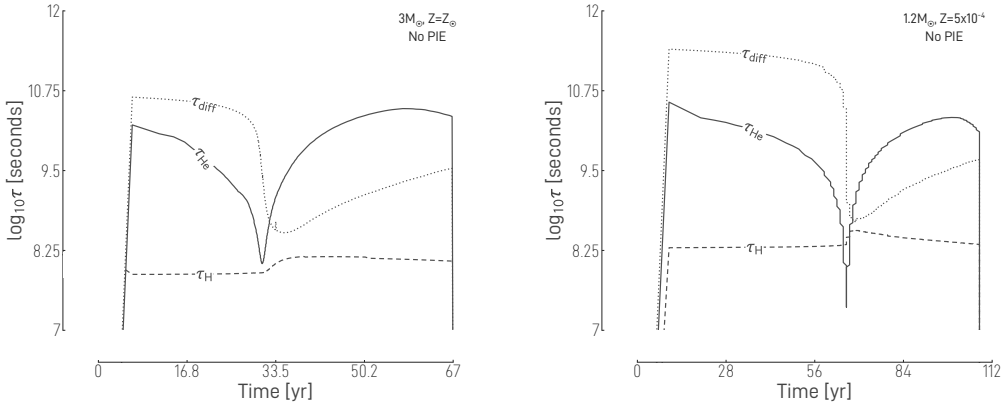

Figure 5.4 Time evolution of the three timescales, $\tau_{\rm He}$, $\tau_{\rm diff}$, and $\tau_{\rm H}$, for the third TP in a $3\,M_\odot$, solar metallicity model (left) and a $1.2\,M_\odot$, $Z=5\times10^{-4}$ model (right). No PIEs are expected for stars with these parameters, and no PIE is seen. The zero point for time on the x-axis is the point when the PDCZ first appears for this pulse.

$$s_{\rm rad} = \frac{4a}{3}\frac{T^3}{\rho}$$

and represents the non-dimensional entropy of radiation. $\tau_{\rm diff}$ is evaluated one grid point beyond the upper boundary of the PDCZ and $\tau_{\rm He}$ is evaluated for the PDCZ. These are almost identical to the definitions used in Fujimoto et al. (1990) with the only difference being that here the specific heat capacity is also averaged over the PDCZ.

To these timescale I also add a third, $\tau_{\rm H}$, that is defined exactly as in Equation (5.2) but evaluated at the base of the H-rich region. This is defined as the point below the H shell where the mass fraction of hydrogen drops below 0.15. The exact value of $\tau_{\rm H}$ is only weakly sensitive to how one defines the base of the H-rich region. Changing the critical value of the hydrogen abundance to 0.1 or 0.2 only results in a change in $\tau_{\rm H}$ of approximately two percent.

Model Investigations of Timescales

I begin by examining the variation of these quantities for pulses where a PIE is not seen and not anticipated to occur. In Figure 5.4, the temporal evolution of the timescales during the third TP is depicted for two models: a $3\,M_\odot$ star with solar metallicity (left panel) and a $1.2\,M_\odot$ star with a metallicity of $Z=5\times10^{-4}$ (right panel), which is ten times higher than that of the fiducial model.

In both cases, $\tau_{\rm He}$ initially decreases as the pulse intensifies. This behavior can be attributed to the increasing luminosity of the He shell. The He luminosity reaches its maximum as $\tau_{\rm He}$ reaches its minimum; subsequently, as the He luminosity declines, $\tau_{\rm He}$ increases again. Shortly after this minimum, the condition

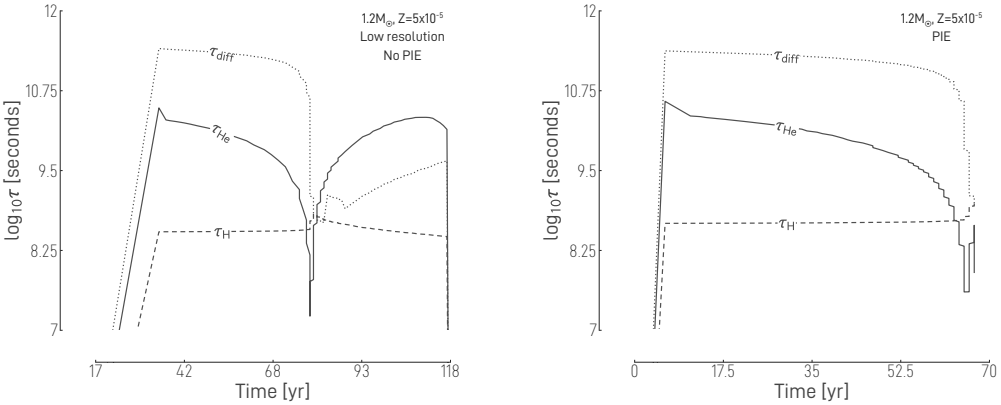

Figure 5.5 Time evolution of the three timescales, τ_{He}, τ_{diff}, and τ_{H}, for the third TP of the low-time-resolution $1.2\,\mathrm{M}_{\odot}$, $\mathrm{Z}=5\times10^{-5}$ model (left) and the fiducial model (right). In the left panel the code missed the PIE due to poor time stepping while in the right panel the PIE was resolved. The zero point for time on the x-axis is the point when the PDCZ first appears for this pulse.

$\tau_{\mathrm{He}} \approx \tau_{\mathrm{diff}}$ is satisfied, marking the point where the PDCZ attains its maximum extent. The evolution of τ_{diff} follows a similar pattern: it initially decreases due to a reduction in density and a rise in temperature just beyond the upper boundary of the PDCZ. After the PDCZ reaches its maximum extent, the layers above it cool, leading to an increase in τ_{diff}. In contrast, τ_{H} remains relatively constant throughout the pulse, with only a slight increase as the PDCZ nears its maximum extent. No PIE occurs in either of these models.

In Figure 5.5, a similar plot to Figure 5.4 is presented, this time illustrating the third TP of a star with $1.2\,\mathrm{M}_{\odot}$ and $\mathrm{Z}=5\times10^{-5}$. The left panel displays the low-time-resolution model where the PIE is not resolved, while the right panel presents the fiducial model in which the PIE is successfully resolved. Comparing these results with those from Figure 5.4 reveals a critical condition that is satisfied in the models of Figure 5.5 but was not met in the previous models: $\tau_{\mathrm{He}} < \tau_{\mathrm{diff}} \simeq \tau_{\mathrm{H}}$. Even in the model where the PIE is unresolved, this condition is briefly met. In the model where the PIE occurs, the onset of the PIE coincides with the condition $\tau_{\mathrm{He}} < \tau_{\mathrm{diff}} \simeq \tau_{\mathrm{H}}$. Additionally, in the low-resolution model where the PIE is missed, this condition is met for TP three through six, but not in any subsequent pulses. This finding aligns with the expectation that PIEs are only possible during the first few TPs (Choplin et al. 2022). It is also noteworthy that even when $\tau_{\mathrm{diff}} = \tau_{\mathrm{H}}$, these quantities are not evaluated at the same grid point, indicating that their equivalence is non-trivial.

By comparing the timescales presented in Figures 5.4 and 5.5, it becomes evident that τ_{H} increases relative to the other timescales as both metallicity and mass decrease. The relationship between these timescales and the star's mass and metallicity can be understood as follows. Starting with τ_{diff}, the key point is

that burning shells exert a strong restorative force against radial perturbations, whereas non-burning mass shells will expand or contract in unison with the rest of the star (Stein 1966). This suggests that the behavior of $\tau_{\rm diff}$ remains relatively consistent across different metallicities and masses, as the intershell region's expansion proceeds in a similar manner in all cases. This consistency is illustrated by comparing Figures 5.4 and 5.5. However, the behavior of $\tau_{\rm H}$ is expected to change because the H-shell luminosity (and consequently the energy generation) is significantly lower during the flash at lower metallicity. This reduction in energy generation means the H shell resists radial changes less effectively, causing the outward expansion of the H shell to begin earlier in the pulse. As a result, the base of the H-rich region is pushed further outward, expanding along with the neighboring layers. At this greater radius, the temperature is lower than it would otherwise be, leading to an increase in $\tau_{\rm H}$.

To verify this, the PIE pulse was re-simulated with the CNO burning rates increased by a factor of ten. This increase in CNO rates increases the H-shell luminosity, thereby enhancing the shell's resistance to radial changes. Consequently, $\tau_{\rm H}$ remains sufficiently low that it never exceeds $\tau_{\rm diff}$, preventing the occurrence of a PIE. It is important to note that increasing the CNO rates also affects the temperature in the shell, making it difficult to disentangle these simultaneous effects and determine which one is primarily responsible for suppressing the PIE. However, the tenfold increase in CNO reaction rates leads to nearly a 100% increase in H-shell luminosity, compared to only a 25% increase in the H-shell temperature near the time when the PIE would have occurred.

The behavior of $\tau_{\rm He}$ is the most straightforward to explain, as it primarily depends on the He luminosity. Therefore, its dependence on mass and metallicity directly follows the trend of He-shell luminosity in AGB stars: $\tau_{\rm He}$ decreases with increasing mass and decreasing metallicity.

The discussion so far has focused on stellar evolution tracks without overshoot from the PDCZ. While the criterion remains applicable to tracks with nonzero `fPDCZ`, a slight modification of the definitions is required. As previously discussed, $\tau_{\rm diff}$ is evaluated just beyond the edge of the PDCZ. When overshoot is considered, $\tau_{\rm diff}$ should be evaluated at the boundary of the overshoot region, defined as the point where the diffusion coefficient drops below $1\,{\rm cm^2\,s^{-1}}$. With this adjustment, the criterion remains valid for tracks including PDCZ overshoot. This is demonstrated in Figure 5.6, where the evolution of timescales is shown for a $1.2\,{\rm M_\odot}$, $Z = 5 \times 10^{-5}$ star with `fPDCZ` $= 0.008$ and `fCE` $= 0.016$. In this case, the criterion $\tau_{\rm He} < \tau_{\rm diff} \simeq \tau_{\rm H}$ is again satisfied as the PIE occurs.

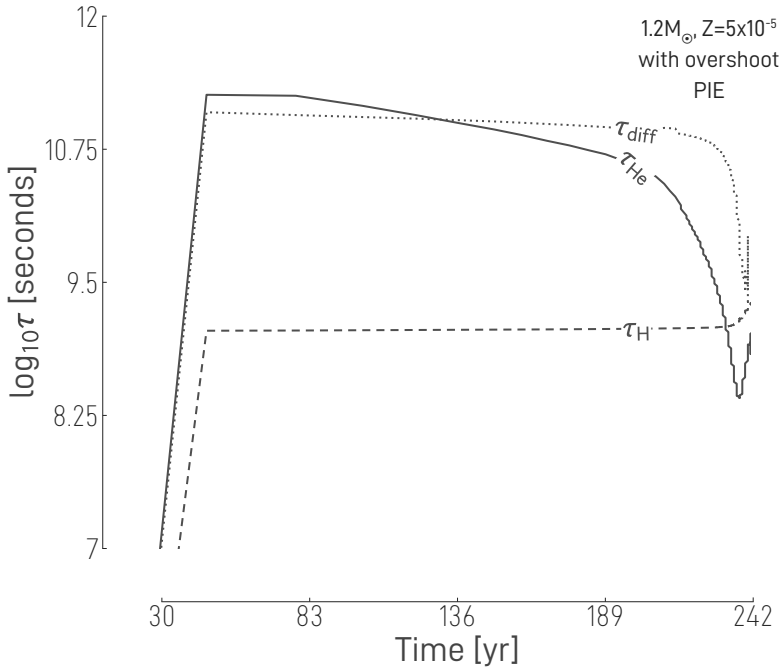

Figure 5.6 Time evolution of the three timescales, $\tau_{\rm He}$, $\tau_{\rm diff}$, and $\tau_{\rm H}$, for the first TP of the $1.2\,M_\odot$, $Z{=}5\times10^{-5}$ star with `fPDCZ` $= 0.008$ and `fCE` $= 0.016$. The zero point for time on the x-axis is the point when the PDCZ first appears for this pulse.

5.1.3 Including Overshoot on the AGB

We will now use the fiducial model as a point of comparison when discussing the models for which overshoot on the AGB was included. Recall that we only vary overshoot parameters on the AGB; all models had overshoot included for core convective zones in earlier phases of the evolution. The key results for all models discussed in this section can be found in Table 5.1.

Overshoot from the CE Only

In an attempt to isolate the impact of overshoot at each convective zone individually, the tracks where overshoot is only applied to one convective zone will be discussed first. Starting with overshoot from the CE, controlled by `fCE`, one can see in Table 5.1 the expected positive correlation between `fCE` and the final C/O ratio. The increase in C/O over the fiducial model is rather minimal, though, and not enough to suppress the post-PIE TPs which were also seen in the fiducial model. Furthermore, all of these tracks experience a rather deep TDU in the TP immediately following the PIE. For the tracks with `fCE` ≥ 0.64 there is a second TDU as well which is not as deep. No track has more than 2 post-PIE TDUs. It is seen in standard AGB evolution that as the end of the AGB phase nears and the

envelope mass becomes small TDU efficiency decreases and can even go to zero. The mass loss in these models is so high that after 2 TPs the envelope mass is quite small. Thus, as with the higher metallicity AGB stars, the TDUs become less and less efficient.

Focusing on the PIE-related quantities, there is a negative correlation between `fCE` and both the maximum neutron density and the neutron exposure. The neutron exposure is here defined as the neutron flux integrated over the time between the beginning of the pulse and the split of the PDCZ. Finally, as with the fiducial model, the PDCZ split always occurs before the TOMND.

Overshoot from PDCZ Only

For those tracks with only PDCZ overshoot, controlled by `fPDCZ`, a new phenomenon appears. While the PDCZ splits before the TOMND for all but one track, the upper and lower parts of the split PDCZ can remerge. This remerging is in some cases temporary, only lasting a couple of time steps, and in some cases is permanent. In all cases the remerging only happens after the peak in the H luminosity has passed and the H burning has begun to decrease. This remerging could allow for the nucleosynthetic product formed in the lower part of the split PDCZ, which would otherwise be trapped there, to make their way to the upper part of the split PDCZ, and eventually to the surface of the star. In the case of tracks with partial or permanent remergings, the neutron exposure reported in Table 5.1 is calculated from the beginning of the pulse to the time when the PDCZ splits for the final time or when the neutron densities fall below 10^{11} cm^{-3}, whichever happens first. It should be noted that the efficiency of the mixing between the formerly split convective zones is not considered when determining if they have remerged or not. Thus, whether substantial mixing occurs between these regions is not considered. An example of a partial remerging can be seen in Figure 5.7 (left panel) around model 23 800, and a permanent remerging is shown in the right panel of Figure 5.7. For these models there is again a negative monotonic relationship between the overshoot and the neutron exposure, with increasing `fPDCZ` the neutron exposure will decrease. Additionally, the final C/O value is much smaller in these tracks than in the previously discussed ones and decreases with increasing `fPDCZ`. This is not surprising as it is well known that overshoot at the base of the PDCZ alters the intershell composition. The larger the overshoot the more He is brought into the PDCZ from below. This leads to stronger flashes with higher temperatures which in turn decreases the C/O ratio (Herwig 2000).

Overshoot at all Boundaries

With overshoot at the isolated boundaries tested, one can move on to the more internally consistent approach of applying overshoot at all convective boundaries.

Table 5.1 Key results of the stellar evolution models for all the tracks discussed in this section.

fPDCZ	fCE	max N_n [cm^{-3}]	τ [mb^{-1}]	Split after TOMND	remerge*	Final C/O	post-PIE Pulses
0.000	0.000	9.15×10^{14}	27.256	n	n	19.256	3
0.000	0.016	8.04×10^{14}	25.50	n	n	20.939	4
0.000	0.064	7.87×10^{14}	28.04	n	n	22.593	4
0.000	0.128	5.99×10^{14}	21.54	n	n	19.804	4
0.008	0.000	8.98×10^{13}	23.17	y	n	8.06	0
0.016	0.000	9.01×10^{13}	20.57	n	t	6.33	0
0.016†	0.000	9.75×10^{13}	22.65	y	t	5.93	0
0.032	0.000	1.24×10^{14}	18.76	n	p	3.976	0
0.008	0.016	1.00×10^{14}	22.71	n	t	7.858	0
0.008†	0.016	8.42×10^{13}	22.65	y	t	7.792	0
0.008	0.128	1.32×10^{14}	20.20	n	t	8.013	0
0.016	0.016	5.6×10^{13}	12.28	n	t	6.436	0
0.016†	0.016	6.24×10^{13}	13.50	y	p	6.651	0
0.016	0.128	4.73×10^{13}	5.04	n	t	7.516	0
0.032	0.016	7.45×10^{13}	10.23	n	t	4.904	0
0.032	0.128	5.40×10^{13}	6.59	n	p	5.294	0

* whether the split PDCZ remerges again: n for no, t for temporarily, p for permanently

† track run without the geometrical cutoff to the overshoot

These tracks will be discussed now. The trends seen in these tracks mirror those seen in the previous sections, implying that their properties can largely be understood as a combination of the properties of the individual convective zone tracks. For instance, none of these tracks have any post-PIE TPs, consistent with the `fPDCZ`-only tracks. There are however some interesting points which must be mentioned. First, in each of these tracks the PDCZ splits before the TOMND, but the PDCZ later remerges either temporarily or permanently. Second, the maximum neutron densities and neutron exposures are smaller for these tracks than for the fiducial model. Finally, in addition to the remerging which has been discussed before, these tracks also experience a sort-of dredge-up-like event. After the TOMND and before the remerging, the upper part of the split PDCZ moves inward in mass engulfing regions below the mass coordinate where the PDCZ split occurred. In this way, the upper part of the split PDCZ is able to partially dredge-up the material from the lower convective zone (see Figure 5.7). The greater `fPDCZ`, the deeper below the PDCZ split point the upper convective zone can reach.

As a final point in this section, it is important to address several numerical

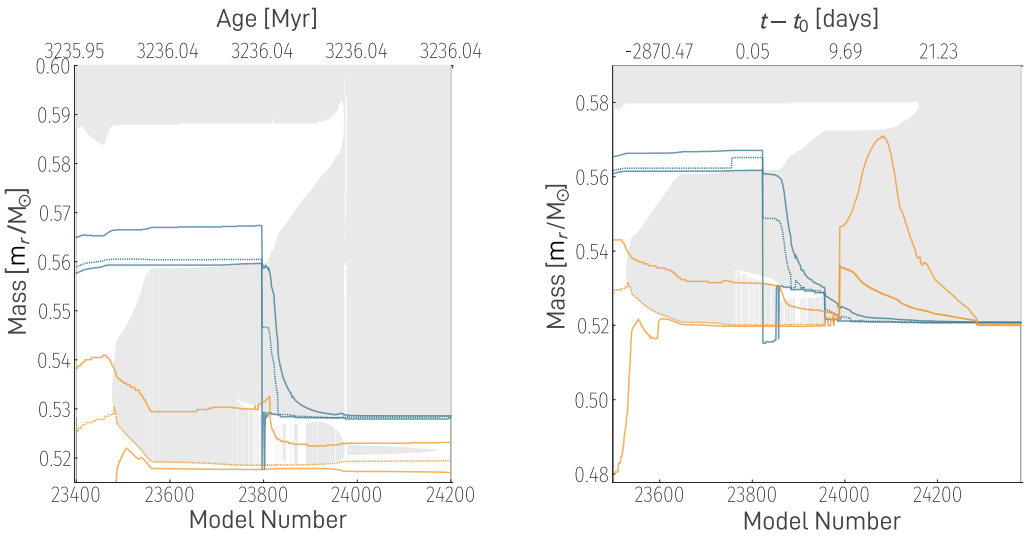

Figure 5.7 Kippenhahn diagrams (see Figure 5.1 for an explanation of the plot elements) of a PIE. Left panel: the `fPDCZ` = 0.016, `fCE` = 0.016 track experiences a partial remerging that occurs around model 23 800. Additionally, one can see the dredge-up-like event that happens when the upper part of the split PDCZ descends into the region below the split point. Right panel: the `fPDCZ` = 0.016, `fCE` = 0.016 track without the geometrical cut-off to the overshoot experiences a permanent remerging.

aspects of the overshooting implementation in `GARSTEC`. First, as mentioned earlier in this section, overshoot was applied exclusively at the base of the CE and at both boundaries of the PDCZ. This strict application of overshoot has a drawback. When the PDCZ splits, the code identifies only one zone as the PDCZ, meaning that overshoot is applied to only one of the resulting zones, while the other remains unaffected.

A second numerical aspect of overshooting in our code is the convective zone cutoff described in Sect. 4.1.1. As discussed in that section, the geometric cutoff is implemented to prevent small convective cores from growing unrealistically large. However, in some models, this cutoff was also being applied to the split convective zones. Therefore, it was necessary to investigate the effects of either removing the geometric cutoff or applying overshoot to both parts of the split PDCZ during the AGB phase. Since both modifications have a similar impact on the models, only one scenario will be discussed: the case where the geometric cutoff is removed. The results for these tracks are presented in Table 5.1, indicated by the † symbol.

The most significant feature of these tracks is that the PDCZ split occurs after the TOMND. Furthermore, the split PDCZ eventually remerges permanently or temporarily. Interestingly, this modification has a minimal impact on the key characteristics of the track. The maximum neutron density and neutron exposure increase by only about 10%. This is because the delay in the PDCZ split caused by removing the geometric cutoff is slight, so the neutron exposure is not significantly

different from the case where the geometric cutoff is retained.

Further Investigations of the Split

As we have seen, the splitting of the PDCZ happens before the TOMND for most models. This is in disagreement with the results from Choplin et al. (2021, 2022) which show that in all cases the split is occurring only after the TOMND, but it is in agreement with Cristallo et al. (2009a). This warrants further investigation. It has already been explained that this split is the result of the competition between the timescale of convection and that of the $^{12}C(p,\gamma)^{13}N$ reaction, with the split occurring once the burning timescale is comparable or exceeds the convective timescale. Because of this, we know how to influence the split. To get the split to occur later one would either increase the mixing velocities or decrease the $^{12}C(p,\gamma)^{13}N$ reaction rate. Both were tested.

Starting with the convective velocities, the PIE was calculated for the fiducial model with the convective velocities artificially increased by a factor of 4. This increases the typical convective velocities from standard values of around $8 \times 10^5\,\mathrm{cm\,s^{-1}}$ to $3 \times 10^6\,\mathrm{cm\,s^{-1}}$. As one can see in Figure 5.8 that alone is enough to push the split of the PDCZ (marked by the black dot) to after the TOMND (denoted by the vertical red dashed line). However, as with the models without the geometrical cutoff, the neutron exposure is only marginally higher (3%) than the fiducial model. This is because the maximum neutron exposure is lower in this model.

The next test was to change the reaction rate of the $^{12}C(p,\gamma)^{13}N$ reaction. `GARSTEC` uses the rate from Xu et al. (2013). Fortuitously, this compilation also provides a "low" rate for all of their reactions which is the rate at the lower edge of their uncertainty. In the case of this reaction, the "low" rate is roughly 25% lower than the standard rate across the temperature range of interest here. This "low" rate was implemented in `GARSTEC` and a similar test as before was done. In this case, as can be seen in the left panel of Figure 5.9, the reduction of the $^{12}C(p,\gamma)^{13}N$ reaction rate pushes the split closer to the TOMND as compared to the fiducial model. The split still happens before than the TOMND, though.

One could of course combine the two effects and a test of this was run as well. The result is shown in the right panel of Figure 5.9. The combination of higher convective velocity and lower $^{12}C(p,\gamma)^{13}N$ reaction rate leads again to the split happening after the TOMND. Also, in this case the mass coordinate of the split is lower than in the standard case. This will have a positive impact on the final surface abundances of the heavy elements as more of the neutron exposed material will make it to the surface.

As a final test, I set all of the physics back to the standard treatment discussed in Chapter 4 and attempted to fine-tune the time-step settings in the code in order to achieve a model which more closely resembles that of Choplin et al.

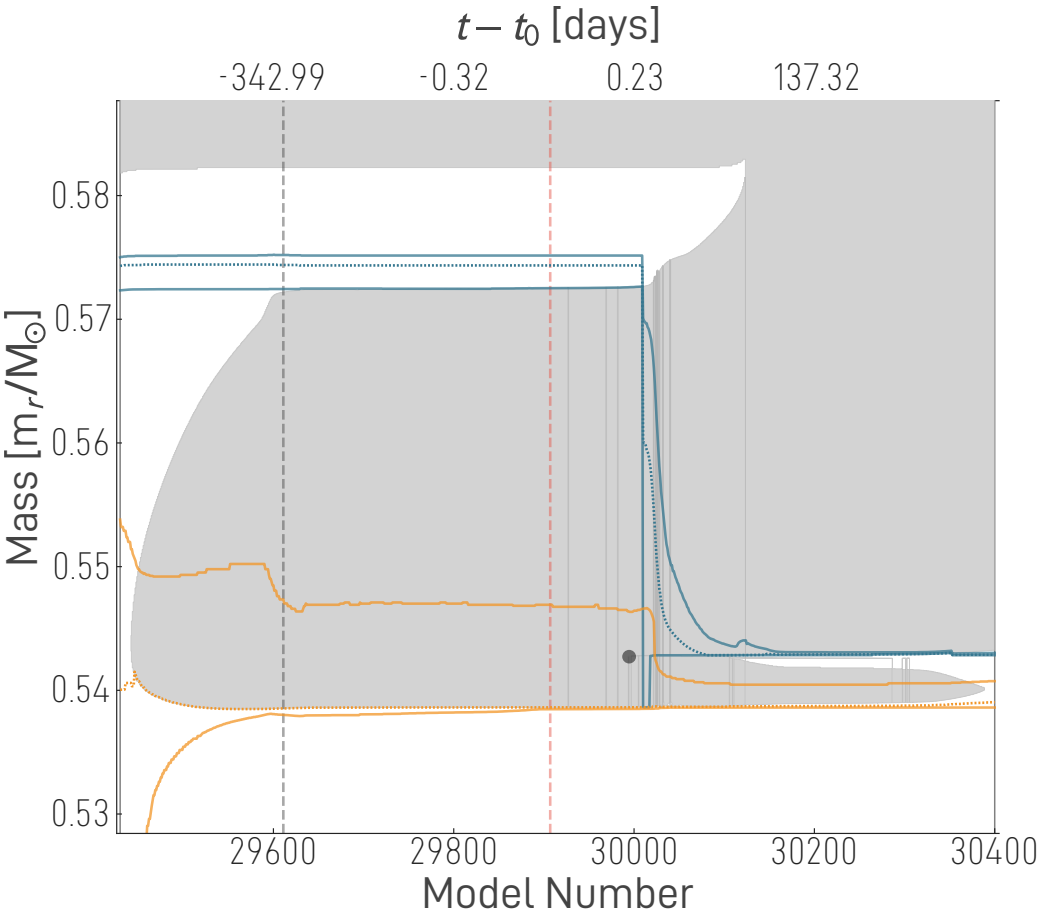

Figure 5.8 Kippenhahn diagram (see Figure 5.1 for an explanation of the plot elements) of a PIE for the fiducial model where the convective velocities have been artificially increased by a factor of 4. The black dashed line marks the time when protons begin being ingested while the red dashed line marks the time when the neutron density achieves its maximum value. The black dot marks the time and location of the splitting of the PDCZ.

(2021). In particular, Fig. 2 of Choplin et al. (2021) shows that the time steps are large enough that less than 200 time steps are needed from the start of the PDCZ to the split. The primary setting which needed to be changed in GARSTEC to achieve something similar was the minimum allowed time step. As a default I had been using 1×10^{-5} yr. If, however, the minimum allowed time step is increased to 3.4×10^{-4} yr, then the results match those of Choplin et al. (2021) better. Specifically, there are slightly over 200 time steps from the start of the PDCZ to the split, and, more importantly, the split of the PDCZ happens after the TOMND. This was tested for all of the models and, in some cases, the maximum allowed change in the H luminosity also had to be increased in order achieve this result.

In Figure 5.10 one can see the result of running this test for the fiducial model. One can clearly see that the PDCZ now splits after the vertical dashed red line which marks the TOMND. Not only that, but the split occurs deeper in the PDCZ

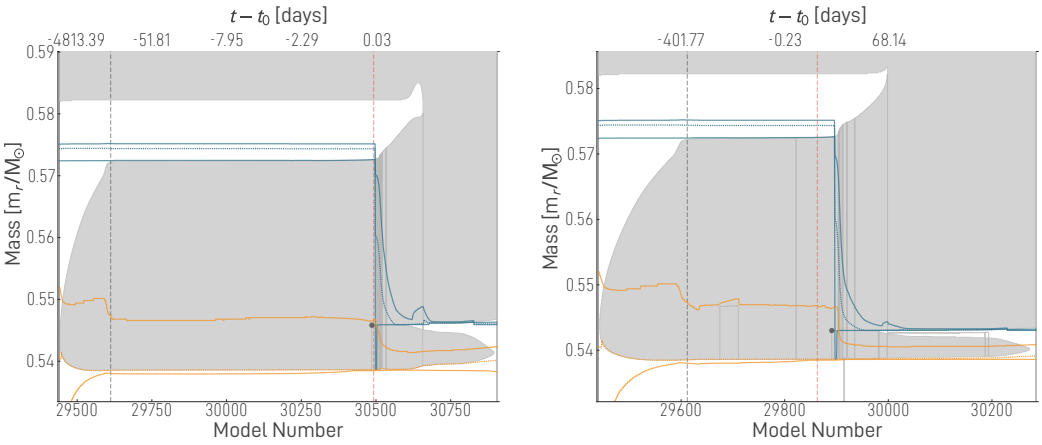

Figure 5.9 Kippenhahn diagram (see Figure 5.8 for an explanation of the plot elements) of a PIE for the fiducial model where the "low" $^{12}C(p,\gamma)^{13}N$ reaction rate from Xu et al. (2013) has been used. The left panel was run with standard convective velocities, and the right panel was run with convective velocities increased by a factor of 4.

than in the standard fiducial model. This will increase the surface abundance enhancements even more.

For the remainder of the work the standard convective velocities and reaction rates will be used, but these tests just serve to further show how even small differences between codes can have very important consequences.

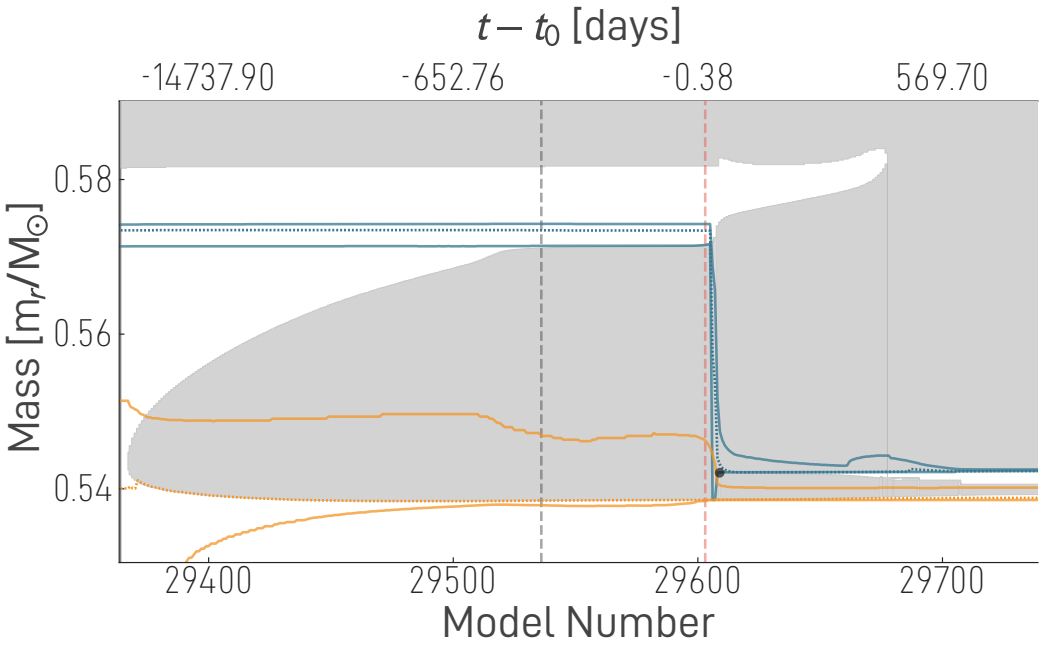

Figure 5.10 Kippenhan diagram (see Figure 5.8 for an explanation of the plot elements) of the fiducial model with fine-tuned time step settings in order to change when the PDCZ splits.

5.1.4 Varying the Mass

At this point the 1.2 $M_\odot$ tracks have been thoroughly covered and the discussion can be extended to tracks of different mass. Stellar tracks with masses of 1 $M_\odot$, 1.5 $M_\odot$, 2 $M_\odot$, and 2.5 $M_\odot$ were run. The results of these simulations can be seen in Table 5.2. Note, that two tracks from Table 5.1 have been included as well for easy comparison. The tracks have been given labels corresponding to the following naming scheme:

$$\underbrace{1\text{M}}_{\text{Mass}}\ \overbrace{\text{P008}}^{\texttt{fPDCZ}}\ \underbrace{\text{C016}}_{\texttt{fCE}}. \tag{5.3}$$

Thus, the label above corresponds to a 1 $M_\odot$ track with values of 0.008 and 0.016 for `fPDCZ` and `fCE`, respectively.

Before discussing the results, it is important to note that one track has been omitted from this table: the 2.5 $M_\odot$ track without overshoot. This is because this track does not experience a PIE meaning that some of the quantities in the table are not defined for this track. Now, one will notice that some trends from Table 5.1 continue here. For instance, regardless of mass, the models without overshoot all have the split of the PDCZ occurring before the TOMND. Additionally, when comparing the models of the same mass with and without overshoot, the model with overshoot generally has a lower value for the maxmimum neutron density and the neutron exposure.

Table 5.2 Key results of the stellar evolution models for tracks of different masses.

Label	max N_n [cm^{-3}]	τ [mb^{-1}]	Split after TOMND	remerge*	Final C/O	post-PIE Pulses
1M P000 C000	4.25×10^{14}	21.821	n	n	19.627	0
1M P008 C016	6.36×10^{13}	13.032	n	t	8.238	0
1.2M P000 C000	9.15×10^{14}	27.256	n	n	19.256	3
1.2M P008 C016	1.00×10^{14}	22.710	n	t	7.858	0
1.5M P000 C000	7.36×10^{14}	20.076	n	n	23.803	13
1.5M P008 C016	1.30×10^{14}	25.087	y	n	8.853	0
2M P000 C000	1.56×10^{15}	25.680	n	n	15.322	10
2M P008 C016	1.64×10^{14}	13.448	y	p	7.584	2
2.5M P008 C016	1.66×10^{14}	63.387	n	t	6.433	5

* whether the split PDCZ remerges again: n for no, t for temporarily, p for permanently

There are however some new results to be gleaned from this table. For example, there is a positive correlation between mass and the maximum neutron density. This is particularly noticeable for the models without overshoot. Furthermore, all models with overshoot either have the split happen after the TOMND or experience some sort of remerging. The 2M P008 C016 and 2.5M P008 C016 tracks also experience TDUs in each post-PIE TP.

Finally, there would appear to be some evidence that the split happens after the TOMND preferentially at higher mass. This was investigated in some detail to try and determine the cause. The results are shown in Table 5.3. A number of quantities were calculated for select tracks at the two extremes of the mass range. max T_{PDCZ} is the maximum temperature in the PDCZ just before the split, max V_{PDCZ} is the same but for the convective velocity, $\overline{\dot{M}_H}$ is the harmonic mean of the proton ingestion rate during the PIE, M_H is the total mass of protons ingested during the PIE, and, finally, Ratio is the ratio of the quantities in the first two columns.

The ingestion rate and total mass ingested were considered because previous studies (Sweigart 1974, Despain 1977, Malaney 1986b) have suggested that, in particular, the ingestion rate may have an impact on the splitting. However, there is no discernible pattern to those models where the split happens before the TOMND (1.5M P008 C016 and 2M P008 C016) and the ingestion rate. The good-split tracks, those whose split occurs after the TOMND, have two unique characteristics. One, they have the highest mass of protons ingested. This along with the fact that the ingestion rates are similar to the other tracks with overshoot implies that the proton ingestion in these tracks takes place over a longer period of time than for the others. Second, one can see that max T_{PDCZ} is lower for tracks

Table 5.3 Quantities which were investigated as possible factors in the splitting of the PDCZ for select *i*-process tracks.

Label	max T_{PDCZ} [MK]	max V_{PDCZ} [cm s^{-1}]	$\overline{\dot{M}_H}$ [proton s^{-1}]	M_H [M$_\odot$]	Ratio [MK/cm s^{-1}]
1M P000 C000	229	9.00×10^{5}	2.89×10^{37}	7.98×10^{-5}	2.54×10^{-4}
1M P008 C016	214	1.69×10^{6}	2.02×10^{42}	9.56×10^{-5}	1.27×10^{-4}
1.5M P008 C016	229	3.30×10^{6}	3.72×10^{41}	1.55×10^{-4}	6.93×10^{-5}
2M P000 C000	263	2.46×10^{6}	9.01×10^{35}	7.09×10^{-5}	1.07×10^{-4}
2M P008 C016	234	2.57×10^{6}	4.47×10^{41}	3.13×10^{-3}	9.11×10^{-5}
2.5M P008 C016	263	2.82×10^{6}	2.07×10^{42}	1.27×10^{-4}	9.32×10^{-5}

with overshoot and increases, though only marginally, with increasing mass. max V_{PDCZ}, on the other hand, is larger for tracks with overshoot and increases more significantly with increasing mass than does max T_{PDCZ}. If one considers the ratio of these quantities, then one will see that the two tracks with good splits have the lowest values for the ratio. This of course makes sense given what has already been discussed about the physical origin of the split.

Timescale Check

As a final word on the structure and evolution of these models, a check of the timescale argument for different masses is in order. Figure 5.11 shows the same kind of plot as in Section 5.1.2 for the 1 M$_\odot$ and 2 M$_\odot$ models with and without overshoot. As one can see the criterion $\tau_{\mathrm{He}} < \tau_{\mathrm{diff}} \simeq \tau_{\mathrm{H}}$ is fulfilled at the start of the PIE for all models regardless of mass and overshoot.

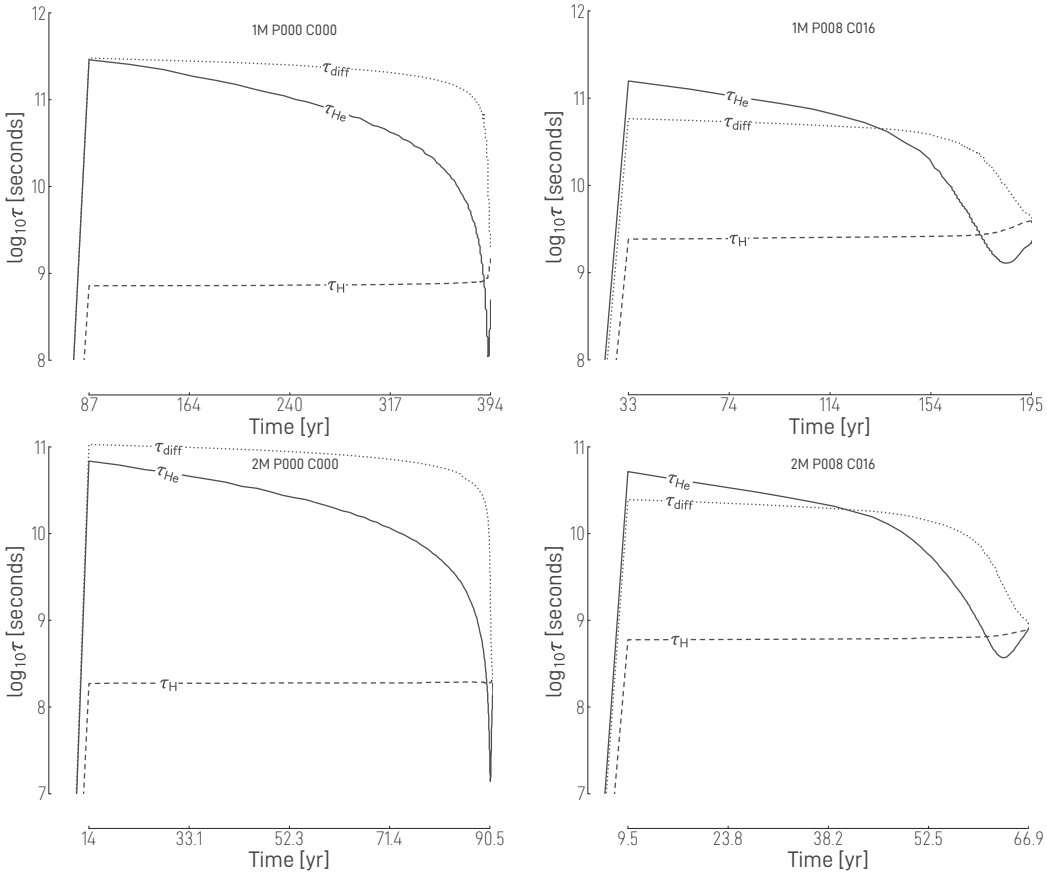

Figure 5.11 Time evolution of the three timescales, τ_{He}, τ_{diff}, and τ_{H}, for 1M Pooo Cooo (upper left), 1M Poo8 Co16 (upper right), 2M Pooo Cooo (lower left), and 2M Poo8 Co16 (lower right). The zero point for time on the x-axis is the point when the PDCZ first appears for this pulse.

5.1.5 The Surface Abundances

Table 5.4 presents the final surface abundances for key light elements across all model tracks, expressed in both mass fraction and $A(X)$[1] notation. The models were computed until wind-driven mass loss nearly depleted the envelope, at which point numerical convergence could not be achieved. While C/O is included in the table for completeness, it has already been discussed in the previous sections and will not discussed further here.

Focusing first on the 1.2 $M_\odot$ tracks with varying overshoot, an examination of the CNO elements reveals that N/O ratios exceeding unity occur exclusively in tracks lacking PDCZ overshoot. The N/O ratio variations are primarily driven by changes in O abundance. As previously noted, higher `fPDCZ` values correlate with elevated helium burning temperatures, resulting in decreased intershell C/O ratios. This shows as enhanced O abundances at the stellar surface, as clearly

demonstrated in the table.

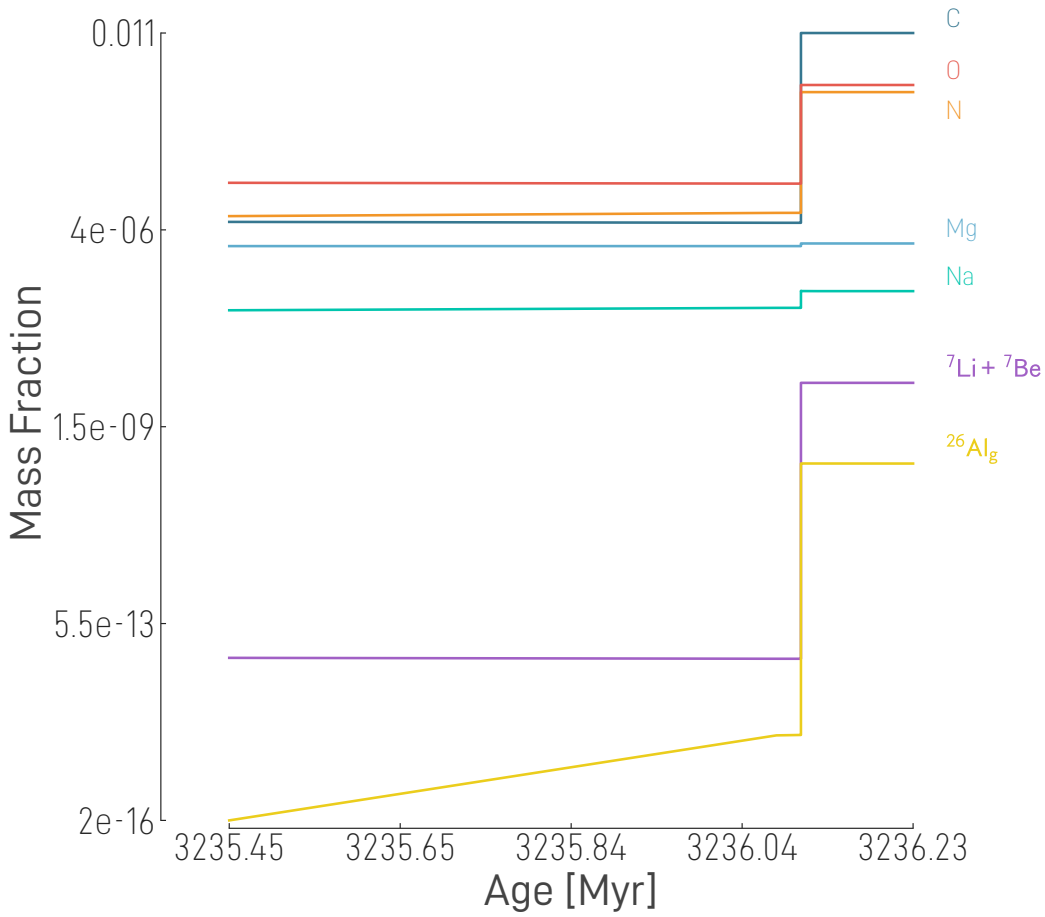

Figure 5.12 Time evolution of the surface abundances (in mass fraction) of certain elements for 1.2M Poo8 Cooo.

^{7}Li also exhibits substantial surface enhancement. Since the reaction network was not applied below a specific temperature threshold, the $^7\mathrm{Be}\,(e^-,\,\nu)^7\mathrm{Li}$ remained inactive in the envelope during late AGB evolution following the PIE. Consequently, Figure 5.12 displays the combined abundance of ^{7}Li and ^{7}Be as a proxy for ^{7}Li, given that all of the ^{7}Be would be expected to decay to ^{7}Li. Test calculations were conducted for one model with a lower temperature cutoff to ensure that this is indeed the case. In Table 5.5 and for the remainder of this chapter it is understood that when we discuss the Li abundances we are in fact discussing the sum of Li and Be abundances. The elevated Li abundance indicates that the Cameron-Fowler mechanism (Cameron 1955, Cameron & Fowler 1971) is at work in these stars. When the upper part of the split-PDCZ region merges with the envelope, the H shell continues burning at the base of the merged convective zones. Initial temperatures of 50 MK post-merging gradually decline,

[1] $A(X)$ is given by $A(X) = \log_{10}(\mathrm{N}_X/\mathrm{N}_\mathrm{H})_* + 12$

creating conditions for brief HBB and a window where ^{7}Be can form and be convectively transported to the surface layers, where electron capture produces ^{7}Li. The surface Li abundance remains stable thereafter, with Li being removed through stellar winds rather than being destroyed.

The PIE's impact on heavier elements is less pronounced. Sodium is enhanced in all tracks, with the `fPDCZ` $= 0$ tracks being the most enhanced. Magnesium and aluminum abundances remain relatively constant across the overshoot parameter space. However, as one can see in Figure 5.12, the envelope does experience a rather large enrichment in the isotope $^{26}\mathrm{Al}_g$. This is a sign of H burning at temperatures above approximately 100 MK (Ventura et al. 2016). Indeed during the PIE the temperatures in the H burning shell exceed 150 MK, enabling $^{26}\mathrm{Al}_g$ synthesis.

Most elements also show a trend in their surface abundances with mass. For C, N, O, and Li the final surface abundances decrease with increasing mass. This is likely a dilution affect. The larger the mass of the star the more massive the envelope and the more diluted any enhancements are as the elements are spread evenly throughout the envelope. Na, Mg, and Al remain rather constant over the mass range with the exception of the 2.5M Po08 Co16 track which shows enhancements in all 3 elements. This is due to the hotter TPs allowing for more processing of the heavier isotopes.

Finally, the 2.5M Pooo Cooo model should be discussed. Recall that this model does not undergo a PIE and instead evolves as a normal AGB star. Because of this, the surface abundance of Li is negligible as expected. The surface abundances of C, N, and O are also all lower than the models with PIEs. In particular N and O are orders of magnitude smaller since less CNO processed material will make its way to the surface in this star. Because of the very low abundance of O, the C/O ratio of this star is the highest of any track. Moreover the $^{12}\mathrm{C}/^{13}\mathrm{C}$ ratio is also the highest of any track. This is not surprising due to the lack of PDCZ overshoot and the low metallicity. For comparison Cristallo et al. (2009b) find that, for a $3\,\mathrm{M}_\odot$, $\mathrm{Z}=1\times10^{-4}$ track with overshoot from the CE, $\mathrm{C/O}=53.0$ and $^{12}\mathrm{C}/^{13}\mathrm{C}=1.72\times10^{4}$. As my model has no overshoot from the CE the values seem reasonable.

Table 5.4 Final surface abundances of the *i*-process tracks. All abundances are given as the decimal log of the mass fraction followed by A(X) in parentheses.

Label	C	N	O	Li	Na	Mg	Al	C/O	$^{12}C/^{13}C$
1M P000 C000	-2.0 (9.25)	-2.39 (8.64)	-3.3 (7.67)	-7.3 (4.03)	-6.29 (4.52)	-5.67 (5.12)	-6.72 (4.02)	19.63	3.22
1M P008 C016	-1.7 (9.52)	-2.74 (8.3)	-2.62 (8.36)	-8.85 (2.49)	-6.36 (4.47)	-5.66 (5.14)	-6.73 (4.03)	8.24	5.35
1.2M P000 C000	-2.02 (9.15)	-3.14 (7.88)	-3.31 (7.65)	-6.93 (4.39)	-5.85 (4.95)	-5.58 (5.2)	-6.71 (4.02)	19.26	7.39
1.2M P000 C016	-2.07 (9.14)	-2.75 (8.27)	-3.38 (7.58)	-6.89 (4.44)	-5.81 (5.0)	-5.57 (5.21)	-6.7 (4.04)	20.18	4.97
1.2M P000 C064	-1.98 (9.2)	-3.09 (7.94)	-3.33 (7.64)	-6.94 (4.39)	-5.43 (5.38)	-5.42 (5.37)	-6.7 (4.04)	22.59	8.68
1.2M P000 C128	-2.0 (9.17)	-3.11 (7.92)	-3.3 (7.67)	-6.87 (4.46)	-5.58 (5.23)	-5.48 (5.31)	-6.68 (4.06)	19.8	8.07
1.2M P008 C000	-1.96 (9.24)	-2.99 (8.03)	-2.87 (8.1)	-8.06 (3.26)	-6.46 (4.34)	-5.63 (5.15)	-6.7 (4.03)	8.06	5.6
1.2M P016 C000	-1.9 (9.28)	-3.04 (7.98)	-2.71 (8.25)	-8.11 (3.21)	-6.48 (4.32)	-5.64 (5.14)	-6.7 (4.03)	6.33	6.23
1.2M P016 C000†	-1.85 (9.34)	-2.99 (8.03)	-2.62 (8.34)	-8.13 (3.2)	-6.46 (4.34)	-5.63 (5.15)	-6.7 (4.03)	5.93	6.32
1.2M P032 C000	-1.74 (9.46)	-2.59 (8.44)	-2.34 (8.63)	-7.95 (3.38)	-6.38 (4.43)	-5.63 (5.15)	-6.69 (4.05)	3.98	6.27
1.2M P008 C016	-1.98 (9.23)	-3.02 (8.0)	-2.88 (8.08)	-8.07 (3.25)	-6.47 (4.34)	-5.64 (5.14)	-6.7 (4.04)	8.06	5.06
1.2M P008 C016†	-1.95 (9.25)	-3.01 (8.01)	-2.84 (8.12)	-8.04 (3.28)	-6.47 (4.34)	-5.63 (5.15)	-6.7 (4.03)	7.79	5.75
1.2M P008 C128	-1.98 (9.22)	-3.02 (8.0)	-2.89 (8.07)	-7.79 (3.53)	-6.48 (4.33)	-5.63 (5.14)	-6.7 (4.03)	8.01	5.38
1.2M P016 C016	-1.93 (9.27)	-3.03 (7.99)	-2.77 (8.19)	-8.08 (3.24)	-6.47 (4.33)	-5.64 (5.14)	-6.7 (4.04)	6.93	5.42
1.2M P016 C016†	-1.81 (9.41)	-2.86 (8.16)	-2.63 (8.34)	-7.9 (3.42)	-6.41 (4.4)	-5.63 (5.15)	-6.69 (4.05)	6.65	5.16
1.2M P016 C128	-1.93 (9.27)	-3.02 (8.0)	-2.81 (8.15)	-7.52 (3.8)	-6.45 (4.36)	-5.65 (5.13)	-6.66 (4.07)	7.52	5.16
1.2M P032 C016	-1.82 (9.37)	-3.03 (7.99)	-2.51 (8.45)	-8.04 (3.28)	-6.46 (4.34)	-5.65 (5.13)	-6.69 (4.05)	4.9	6.12
1.2M P032 C128	-1.85 (9.35)	-3.07 (7.95)	-2.57 (8.39)	-7.53 (3.79)	-6.46 (4.34)	-5.65 (5.13)	-6.68 (4.06)	5.29	6.07
1.5M P000 C000	-2.4 (8.79)	-3.29 (7.71)	-3.78 (7.17)	-7.28 (4.03)	-6.43 (4.36)	-5.7 (5.07)	-6.74 (3.98)	23.8	5.31
1.5M P008 C016	-2.22 (8.96)	-3.22 (7.79)	-3.17 (7.78)	-8.38 (2.93)	-6.54 (4.25)	-5.69 (5.07)	-6.75 (3.97)	8.85	5.52
2M P000 C000	-2.7 (8.48)	-3.42 (7.57)	-3.89 (7.05)	-8.04 (3.25)	-6.42 (4.36)	-5.69 (5.06)	-6.75 (3.96)	15.32	4.86
2M P008 C016	-2.11 (9.05)	-2.92 (8.09)	-2.99 (7.96)	-8.8 (2.5)	-6.19 (4.6)	-5.41 (5.35)	-6.72 (4.0)	7.58	7.9
2.5M P000 C000*	-2.91 (8.14)	-5.04 (5.94)	-4.36 (6.57)	-11.01 (0.28)	-6.59 (4.18)	-5.62 (5.12)	-6.75 (3.95)	28.01	5836.85
2.5M 008 C016	-2.16 (8.92)	-3.8 (7.19)	-2.97 (7.96)	-8.79 (2.51)	-6.01 (4.77)	-5.02 (5.72)	-6.58 (4.13)	6.43	27.45

† track run without the geometrical cutoff to the overshoot

* This track does not experience a PIE.

5.2 Heavy-Element Nucleosynthesis

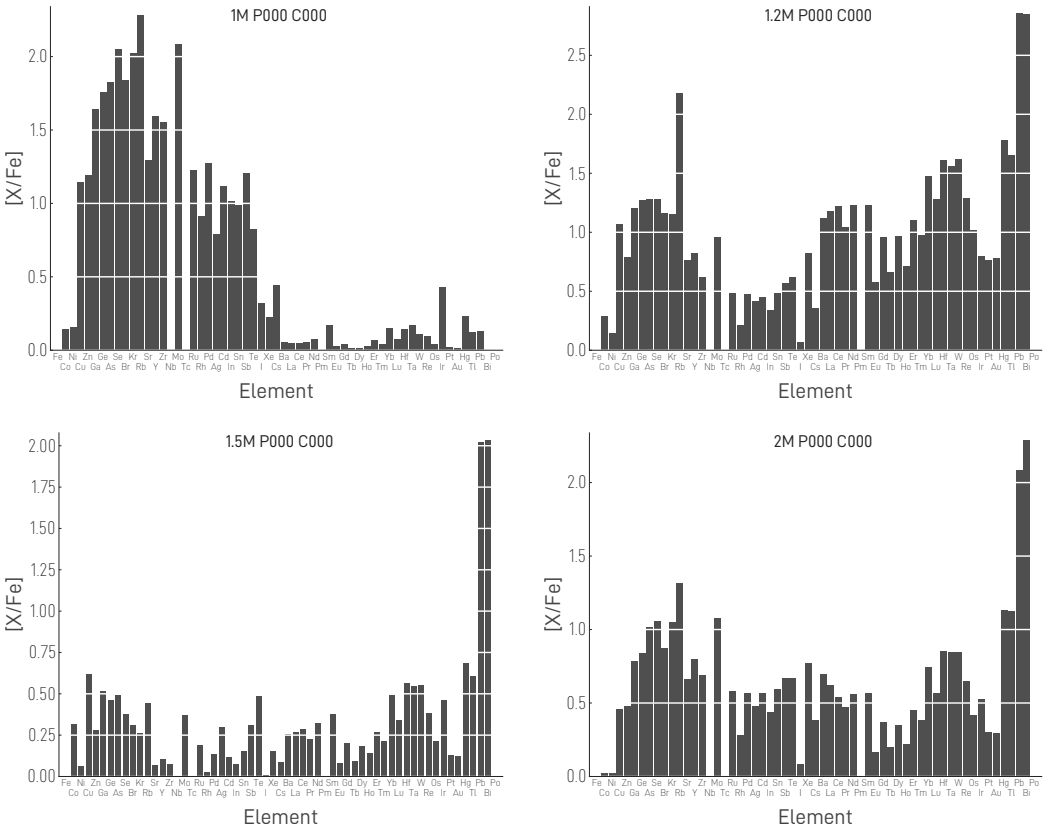

Figure 5.13 Final surface abundances ([X/Fe]) for those models without overshoot. The 2.5M Pooo Cooo model has been omitted due to its lack of a PIE.

Having discussed the stellar models in great detail, I can now move on to discussing the results of the post-processing calculations. As already described, the stellar models were post-processed by the `ANT` code which takes the abundances of ^{1}H, ^{13}C, and ^{14}N, as well as the temperature, density, and diffusion coefficients from `GARSTEC` for every time step and calculates the nucleosynthesis using a network with 1190 isotopes. The focus in this section will be on the surface abundances of the models as this is the material which will be lost from the star and potentially accreted by its binary companion whereby the companion will become the CEMP-r/s star that is observed today. The models that were post-processed correspond to those from Table 5.2.

First, the models without overshoot will be discussed beginning with the 1 $M_{\odot}$ model. The final surface abundances of the heavy elements ($Z \geq 26$) for this track is shown in Figure 5.13 (top left). This is clearly not a typical *i*-process abundance pattern (see Figure 2.20). In fact it looks much more like a convective *s*-process abundance pattern. This could in theory be the result of the activation of the ^{22}Ne neutron source in a pre-PIE TP. However, the neutron densities never reach

appropriate levels for this prior to the PIE. Instead, this abundance pattern is the result of the splitting of the PDCZ. Since the split happens early, the average neutron exposure over the whole PDCZ prior to the split is relatively low. This is a similar situation as one has in the convective *s*-process; a high neutron density for a short time leading to a small neutron exposure. The high Rb abundance relative to Sr, Y, and Zr is a typical signature of this (Wallerstein et al. 1997).

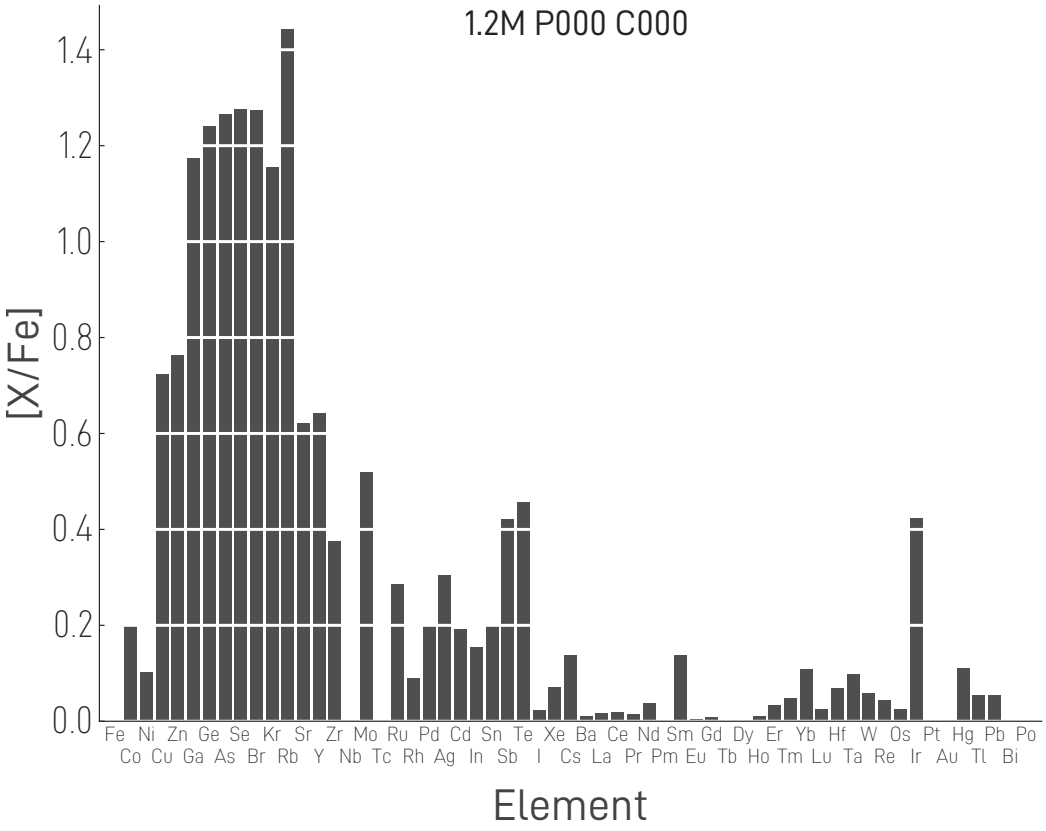

Figure 5.14 The surface abundance ([X/Fe]) following the PIE for the 1.2M Pooo Cooo model.

The 1.2 $M_\odot$ model has surface abundances which are more *i*-process-like. In fact, Figure 5.13 shows that the 1.2 $M_\odot$ (top right), 1.5 $M_\odot$ (bottom left), and 2 $M_\odot$ (bottom right) models all show an abundance pattern which is closer to what is expected for the *i*-process. However, there are some differences between the models including the amount of the surface enhancement as well as some details of the abundance pattern, for instance the relative abundance of the peak elements. The explanation for this is multifaceted so we will take it one model at a time.

First, the 1.2 $M_\odot$ model. Recall that this model, like all models without overshoot, experiences the PDCZ splitting before the TOMND. Therefore, after the PIE the surface abundance pattern is similar to that of the 1 $M_\odot$ model (see Figure 5.14). However, as already discussed, this model experiences a very deep

TDU in the first post-PIE TP. In this way the star is able to bring more of the *i*-process enhanced material to the surface leading to the abundance pattern seen in Figure 5.13 (top right). Perhaps the most striking feature of the final surface abundance distribution is the high Rb abundance. The meaning of a high Rb abundance has already been discussed. However, the magnitude of the Rb abundance in comparison to other first-peak elements for this model is unusual. There is an additional factor which must be discussed here as well. As was seen in the simulations of Choplin et al. (2024) for one particular star, the PIE leaves behind a ^{13}C pocket at its base. The pocket, which in this model spans a mass of around $3 \times 10^{-4}\,M_\odot$, has temperatures between 80 and 100 MK which is exactly what is expected from the traditional ^{13}C pocket in higher metallicity AGB stars. At this temperature the ^{13}C neutron source reaction is active and neutron densities reach 2×10^{7} cm^{-3}. In contrast to the traditional ^{13}C pocket, this pocket lasts much longer, 193 kyr. Therefore, the neutron exposure is correspondingly higher at 8.97 mb^{-1}. This pocket will get engulfed by the following PDCZ and some of its material will then make its way to the surface during the TDU. Thus, the *i*-process abundance pattern will be contaminated by something more *s*-process-like. This deep ^{13}C pocket can be seen in Figure 5.15.

The $1.5\,M_\odot$ track undergoes a very similar evolution to the $1.2\,M_\odot$ track, including the deep ^{13}C pocket forming after the PIE. The reason for its very low enhancement of heavy elements is that the post-PIE TDU it experiences is roughly 1/3 as efficient as that of the $1.2\,M_\odot$ model. Additionally, the neutron exposure of this model during the PIE is approximately 25% less than that of the $1.2\,M_\odot$ model. Together these two aspects explain the low surface enhancements.

The $2\,M_\odot$ model likewise undergoes a PIE with an early split followed by a deep ^{13}C pocket and a TDU after the first post-PIE TP. However, the TDU in this model is twice as efficient as in the $1.5\,M_\odot$ model. Additionally, the temperature in the post-PIE PDCZ reaches 300 MK which is sufficient to activate the ^{22}Ne neutron source reaction and undergo convective *s*-process (Jaeger et al. 2001, Lugaro et al. 2023). This explains the relatively large enhancement of the first-peak elements in this model.

Figure 5.16 shows the final surface abundances of those tracks which have overshoot. As one can see, the final surface abundances for 1M Po08 Co16, 1.2M Po08 Co16, and 1.5M Po08 Co16 look similar to that of 1M Po00 Co00. The reason for this is again the lack of TDU in these models. Even though the 1.5M Po08 Co16 track has a split which occurs after the TOMND, it is so soon after that the neutron exposure is not significantly higher than in other models and so only the first-peak elements arrive at the surface after the PIE. Thus, without a TDU there is no way for the heavier elements to get to the surface. For 2M Po08 Co16 and 2.5M Po08 Co16 the situation is better. These tracks have a TDU for each post-PIE TP and so some of the heavy elements arrive at the surface. The enhancements are still fairly low, though. This is again the dilution affect. These stars have more

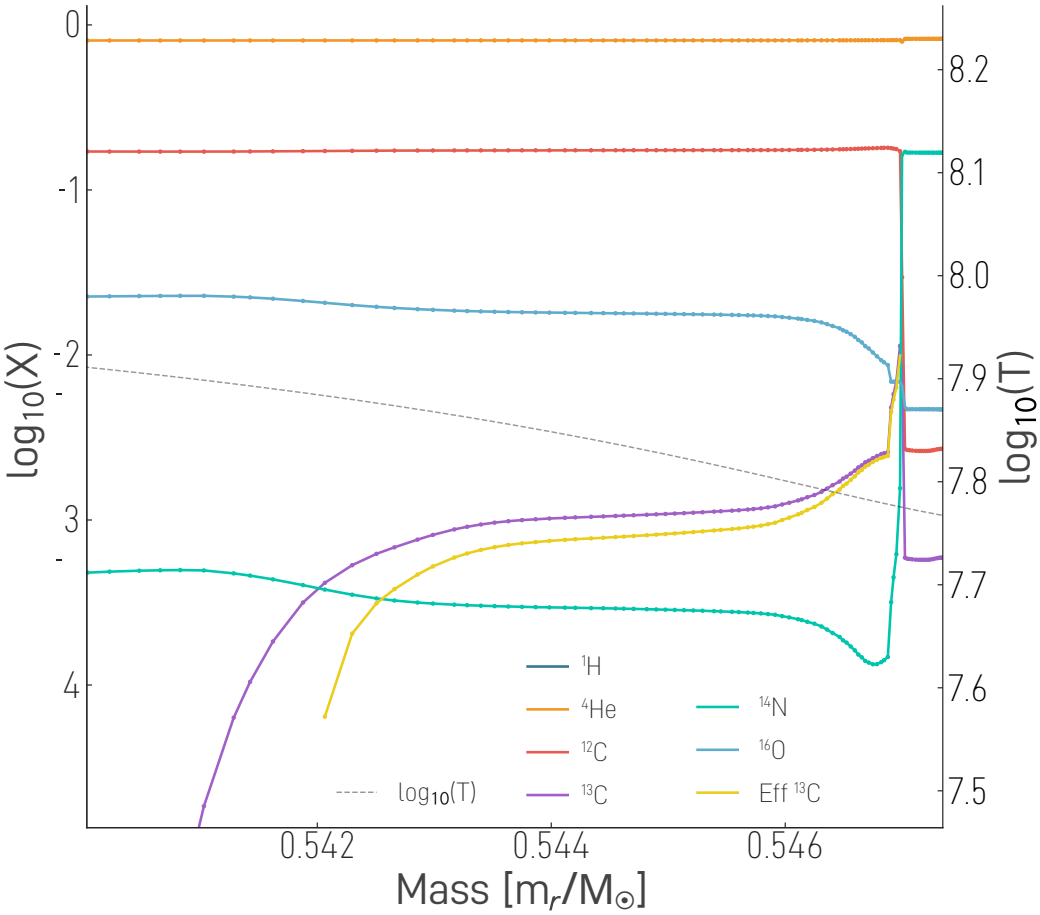

Figure 5.15 The deep ^{13}C pocket. The colored lines show the decimal log of the mass fractions of certain isotopes. The dashed line shows the decimal log of the temperature. The pocket is denoted by the yellow line which traces the $X^{\text{eff}}_{^{13}\text{C}}$. The area to the right of the plot is the diminishing PDCZ.

massive envelopes, but the mass of the PDCZ does not change significantly with stellar mass, thus the heavy elements are spread over a much larger mass and have correspondingly lower surface enhancements. Additionally, in both tracks the ^{22}Ne neutron source reaction is active in the post-PIE TP and so the first peak abundances are high. Finally, there is the 1.2M Pooo C064 track. This is the track whose surface abundances are the most *i*-process-like of any track and the most enhanced. This is because, as was already said, this track has two post-PIE TDUs along with higher neutron exposures owing to the lack of PDCZ overshoot. These tracks all have the deep ^{13}C pocket seen in the models without overshoot as well.

Clearly, the mass and physics of the models affect the final surface abundances greatly. In Figure 5.17 one can see the uncertainty in the final surface mass fraction for each isotope. The uncertainty is given by

$$\delta X_i = \log_{10} X_i^{\min} - \log_{10} X_i^{\max} \tag{5.4}$$

where δX_i is the uncertainty in the mass fraction of isotope i, and $X_i^{\max}$ and $X_i^{\min}$, are the maximum and minimum final surface mass fractions for the isotope across all tracks. Note, that the 2.5M Pooo Cooo has been excluded from this analysis since it does not experience a PIE. The isotopes with the greatest uncertainties are, not surprisingly, the heaviest isotopes. Specifically, ^{176}Lu, ^{198}Hg, ^{207}Pb, ^{208}Pb, and ^{209}Pb have the most uncertain surface mass fractions. Additionally, there is a trend of higher uncertainties for higher mass isotopes. The vast majority of isotopes are uncertain by at least 0.5 dex.

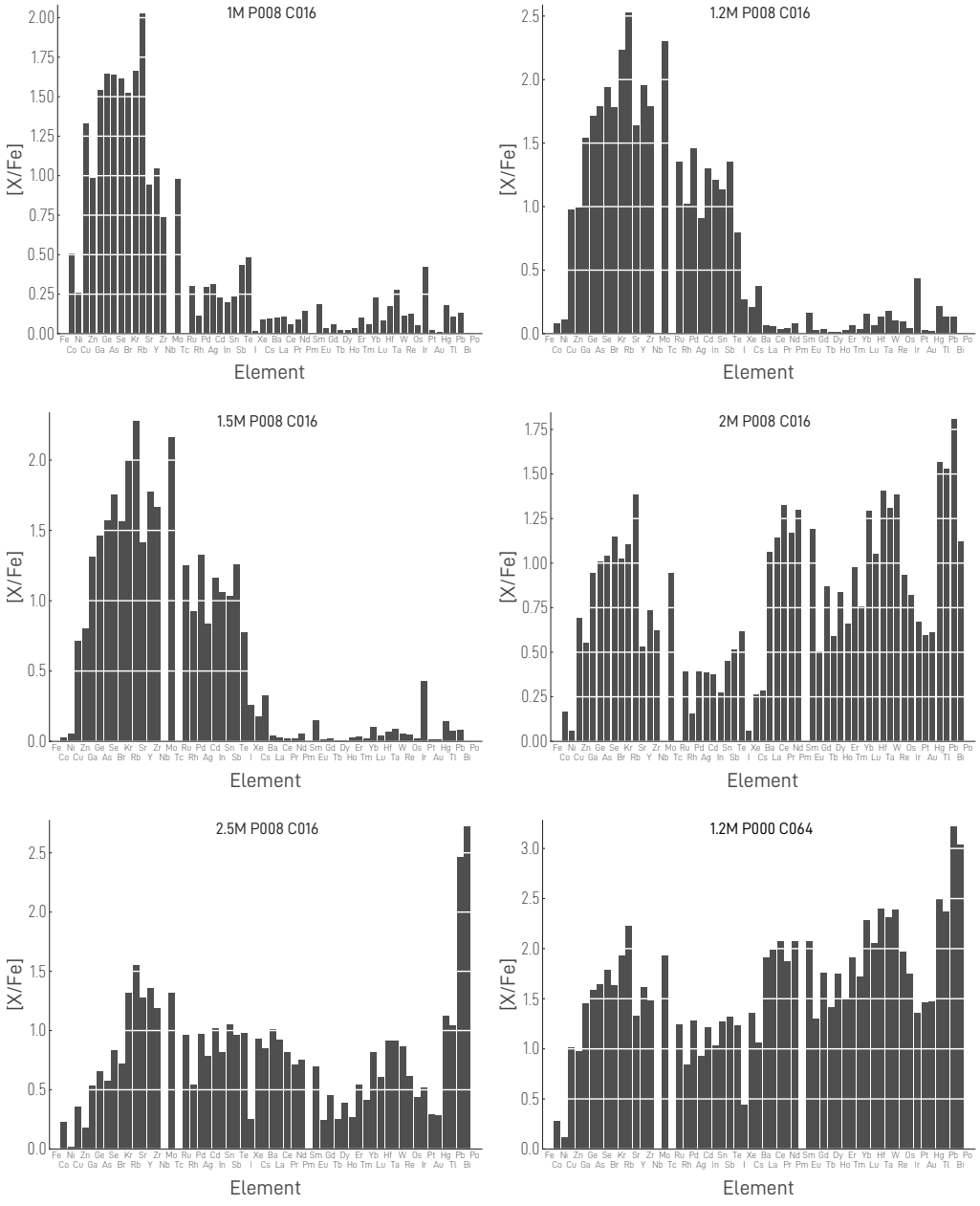

Figure 5.16 Final surface abundance ([X/Fe]) for those models with overshoot.

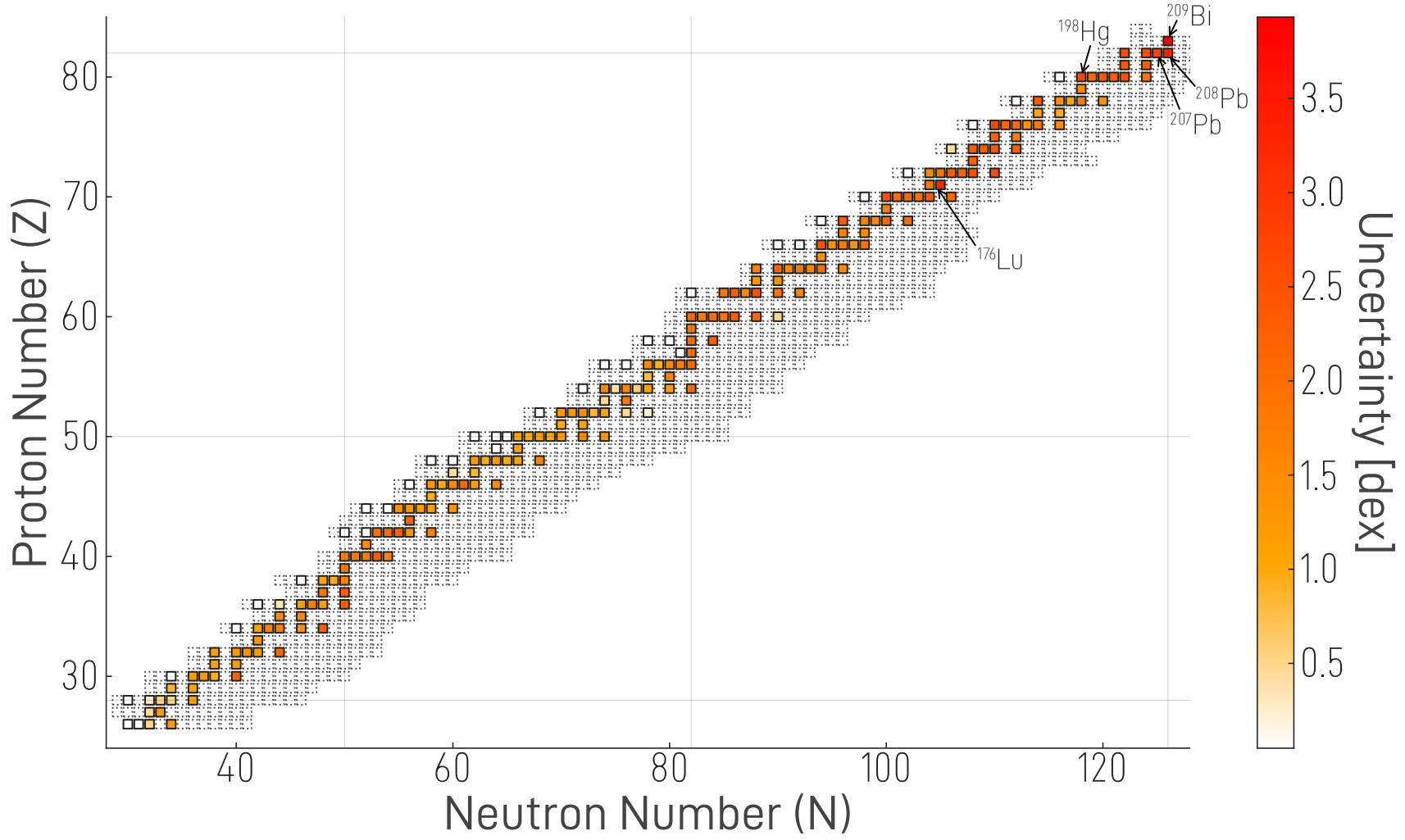

Figure 5.17 Chart of the nuclides showing the uncertainty of the final surface mass fractions for each heavy isotope. Only those isotopes whose mass fraction exceeds 1×10^{-15} are included. Those isotopes whose mass fraction is less are marked by the empty squares with dotted edges. The saturation of the red color for each isotope denotes how uncertain the mass yields are. The light gray lines mark magic numbers. The five isotopes with the largest uncertainties are labeled.

5.3 Discussion

5.3.1 Comparison with Observations

The final surface abundances of our models can also be compared to the growing number of observations of CEMP-r/s stars. Following Karinkuzhi et al. (2021), CEMP-r/s stars are classified as such based on their abundance distribution's distance to an *r*-process distribution (see Section 2.3.1). All the objects used for comparison in this study are those that were defined as CEMP-r/s by Karinkuzhi et al. (2021) as well as a number of additional objects identified by Choplin et al. (2021). All objects have [Fe/H] between -2 and -3 and are CEMP-r/s stars based on the Karinkuzhi et al. (2021) classification system. The basic properties of these objects can be seen in Table 5.5.

The comparisons of the light element abundances of the models to the observations can be seen in Figures 5.18 and 5.19. The top line of plots show only data for the 1.2 $M_\odot$ tracks, whereas the bottom row of plots shows the data for the tracks in Table 5.2. Thus, 1.2M Pooo Cooo and 1.2M Poo8 Co16 are in all plots in both rows. In all panels there is an additional set of points that are in blue and are the so-called diluted abundances. As previously discussed, these CEMP-r/s stars are thought to owe their abundances not only to the environment they were born in, but also to a mass transfer phase with a companion star which is where the *i*-process actually occurred. To account for this, when comparing abundances, one does not compare the observations directly to the abundance of the *i*-process star model. Rather, one dilutes the abundances of the *i*-process star with material of the star's initial composition which the CEMP-r/s star is assumed to also have prior to the mass transfer phase. In that case the abundance of the diluted material can be calculated as

$$X_{\text{diluted}} = (1-f)X_* + f X_{\text{initial}}, \tag{5.5}$$

where X_* is the surface mass fraction of isotope X of the *i*-process star, X_{initial} is the initial mass fraction, and f is the dilution factor, a free parameter ranging in value from 0 to 1. The f value used in Figure 5.18 is 0.80 which was chosen as it provides a good match to the observations. This high value of f is consistent with the findings of Choplin et al. (2021), who argue that it is advantageous because it requires less extreme amounts of accreted material and significantly reduces the implied accretion efficiency (see erratum for Choplin et al. 2021). In another study focusing on the *s*-process abundance enhancement in Ba stars, Cseh et al. (2022) found that the average best-fitting f was approximately 0.7 for longer period systems, while shorter period systems required a lower f. Focusing first on the top row of panels, the elements N and O in our models shows a good agreement with the observations. However, models that include large

Table 5.5 Key characteristics of the observed CEMP-r/s stars used in this study. Errors are provided where available.

Star	$T_{\rm eff}$	$\log_{10}(g)$	[Fe/H]	[C/H]	[N/H]	[O/H]	Reference
CS 22891-171	5215 ± 68.0	1.24 ± 0.09	−2.50 ± 0.10	−0.43 ± 0.08	−0.83 ± 0.08		1
HD 5223	4650 ± 120.0	1.03 ± 0.30	−2.00 ± 0.08	−0.53 ± 0.03	−0.73 ± 0.05	−1.39 ± 0.10	1
HD 76396	4750 ± 100.0	2.00 ± 0.30	−2.27 ± 0.10	−0.43 ± 0.05	−1.43 ± 0.05	−0.99 ± 0.10	1
HD 145777	4443 ± 57.0	0.50 ± 0.10	−2.32 ± 0.10	−0.93 ± 0.10	−0.63 ± 0.05	−1.69 ± 0.10	1
HD 187861	5000 ± 100.0	1.50 ± 0.25	−2.60 ± 0.10	−0.13 ± 0.09	0.02 ± 0.03	−1.29 ± 0.10	1
HD 196944	5168 ± 48.0	1.28 ± 0.16	−2.50 ± 0.09	−1.28 ± 0.06	−1.13 ± 0.08	−1.69 ± 0.10	1
HD 209621	4740 ± 55.0	1.75 ± 0.25	−2.00 ± 0.09	−0.43 ± 0.06	−0.03 ± 0.08	−0.89 ± 0.10	1
HD 224959	4969 ± 64.0	1.26 ± 0.29	−2.36 ± 0.09	−0.13 ± 0.05	0.12 ± 0.06	−1.19 ± 0.05	1
HE 0151-0341	4820 ± 112.0	1.15 ± 0.08	−2.89 ± 0.08	−0.53 ± 0.04	−0.23 ± 0.03	−1.39 ± 0.10	1
HE 0319-0215	4738 ± 100.0	0.66 ± 0.40	−2.90 ± 0.10	−0.43 ± 0.08	−0.43 ± 0.09	−0.99 ± 0.10	1
HE 1120-2122	4500 ± 100.0	0.50 ± 0.50	−2.00 ± 0.10	−0.83 ± 0.08	−0.53 ± 0.04	−1.19 ± 0.10	1
CS 22948-027	5000	1.90	−2.23 ± 0.16	−0.13 ± 0.20			2
CS 29497-030	7000 ± 44.0	4.00 ± 0.39	−2.52 ± 0.16	0.03 ± 0.10	−0.23 ± 0.35	−0.85 ± 0.11	3,4
CS 31062-050	5500	2.7	−2.33 ± 0.16	−0.19 ± 0.24	−0.97 ± 0.37		5,6
HE 0243-3044	5400 ± 100.0	3.20 ± 0.30	−2.58 ± 0.20	−0.15 ± 0.27	−1.10 ± 0.28	−0.68	7
HE 0338-3945	6160 ± 100.0	4.13 ± 0.33	−2.42 ± 0.05	−0.19		−1.03 ± 0.09	8,9
HE 2148-1247	6380 ± 100	3.90 ± 0.25	−2.3 ± 0.15	−0.35 ± 0.20			10,11
HE 2258-6358	4900 ± 150.0	1.60 ± 0.50	−2.65 ± 0.03	−0.25 ± 0.09	−1.23 ± 0.25	−0.82 ± 0.10	12

(1) Karinkuzhi et al. (2021), (2) Aoki et al. (2007), (3) Ivans et al. (2005), (4) Roederer et al. (2014), (5) Aoki et al. (2002b), (6) Aoki et al. (2006), (7) Hansen et al. (2015), (8) Jonsell et al. (2006), (9) Zhang et al. (2011), (10) Cohen et al. (2003), (11) Cohen et al. (2013), (12) Placco et al. (2013)

amounts of overshoot from the PDCZ may have too much O, depending on the chosen value of f. For C, the models predict too large of abundances even after dilution. In the bottom row one can see that the agreement to observations is improved for masses of 1.5 and 2 $M_\odot$. Additionally, the 2.5M Pooo Cooo track, which does not experience the PIE, falls below the observed values for O and N.

Figure 5.19 presents abundance ratios plotted against each other. As before the top row of panels are for the 1.2 $M_\odot$ models, while the bottom row shows the data for the tracks in Table 5.2. For the 1.2 $M_\odot$ models the tracks all match the observations well for [N/O]. All model points in this plot are shifted to the right by the C abundances which are too high as already discussed. For the [Na/O] vs. [Mg/O] plot most of the models seem to match the observations well except those with `fPDCZ` $= 0$. When looking at the models with different mass the conclusions are similar. The trend of models without overshoot being outside the observations continues. Finally, the 2.5M Pooo Cooo track which does not have a PIE is clearly outside the data. Overall, some amount of overshoot from the PDCZ seems necessary, however, even values of 0.016 push the model abundances to the most extreme end of the observations for O and N. Moreover, overshoot from the CE improves the agreement to the observed [Na/O] and [Mg/O]. As before, models with masses of 1.5 and 2 $M_\odot$ fit the observations the best. It is also interesting to note that only when looking at [N/H] would one say that the 2.5M Pooo Cooo data point is a clear outlier after dilution. This is in agreement with Fujimoto et al. (2000) who claimed that stars which experience a PIE will be N-rich C stars. Thus, it may not be easy to distinguish, from the light-element abundances, from which kind of star a CEMP-r/s star accreted its mass from: a star with a PIE or a standard AGB star. However, N is a good element to focus on for this task.

Lastly, we discuss Li in this section. Due to the limited number of Li abundance observations in CEMP-r/s stars, a different sample of stars was used as compared to the previous plots. These stars are listed in Table 5.6. All stars are CEMP-r/s stars with [Fe/H] between −2 and −3 and have observed Li abundances. For consistency the dilution factor was kept the same as before ($f = 0.8$).

As can be seen in Figure 5.20, the Li abundances of our models tend to be high even after dilution, though many are still within the observational constraints. The models without PDCZ overshoot, including the fiducial model, are more Li-rich than the most Li-rich stars in our sample even after dilution. The situation is similar for the stars of different masses, however, at higher masses ($> 1.5\,M_\odot$) even the tracks without overshoot fall within the observations.

A comparison of the heavy isotope abundances to observations can also be done. Liu et al. (2014) analyze stardust grains and find two which are unable to be matched by *s*-process models. They propose that these two stardust grains come from an *i*-process source. The main difference between these grains and those of normal *s*-process models is that the grains exhibit a negative value

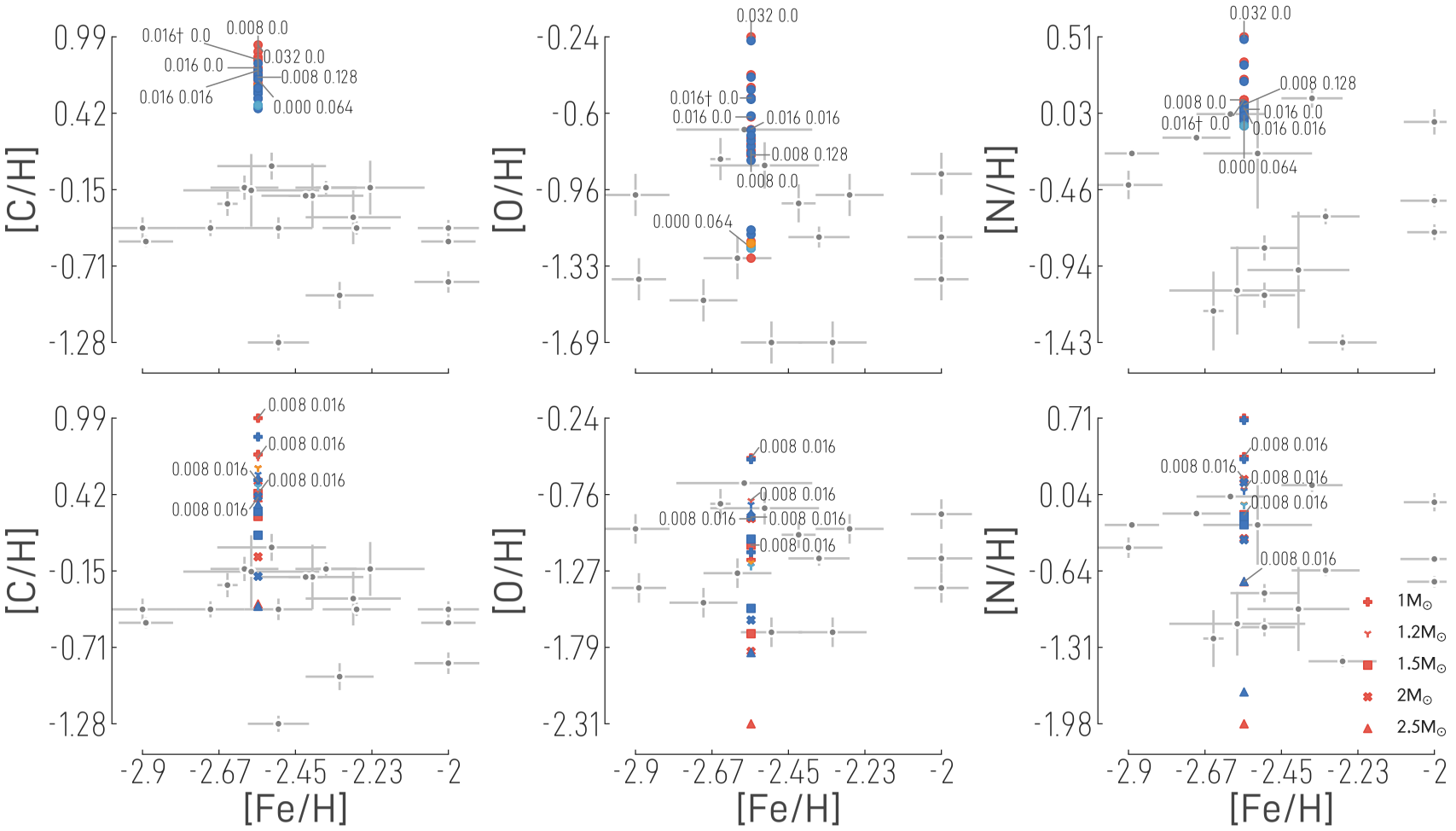

Figure 5.18 Abundance of [C/H] (Left), [O/H] (middle), and [N/H] (Right) vs. [Fe/H] for models and observations. The top row of plots show only data for the 1.2 $M_\odot$ tracks, whereas the bottom row of plots shows the data for the tracks in Table 5.2. Thus, 1.2M Pooo Cooo and 1.2M Poo8 Co16 are in all plots in both rows. The gray points are the observations including errors where available. The red points are the model abundances, while the blue points are the abundances after the dilution factor ($f = 0.80$) has been applied. The points corresponding to the fiducial model abundance and diluted abundance are in orange and light blue, respectively. Some of the non-diluted points are labeled by the `fPDCZ` and `fCE` values for reference.

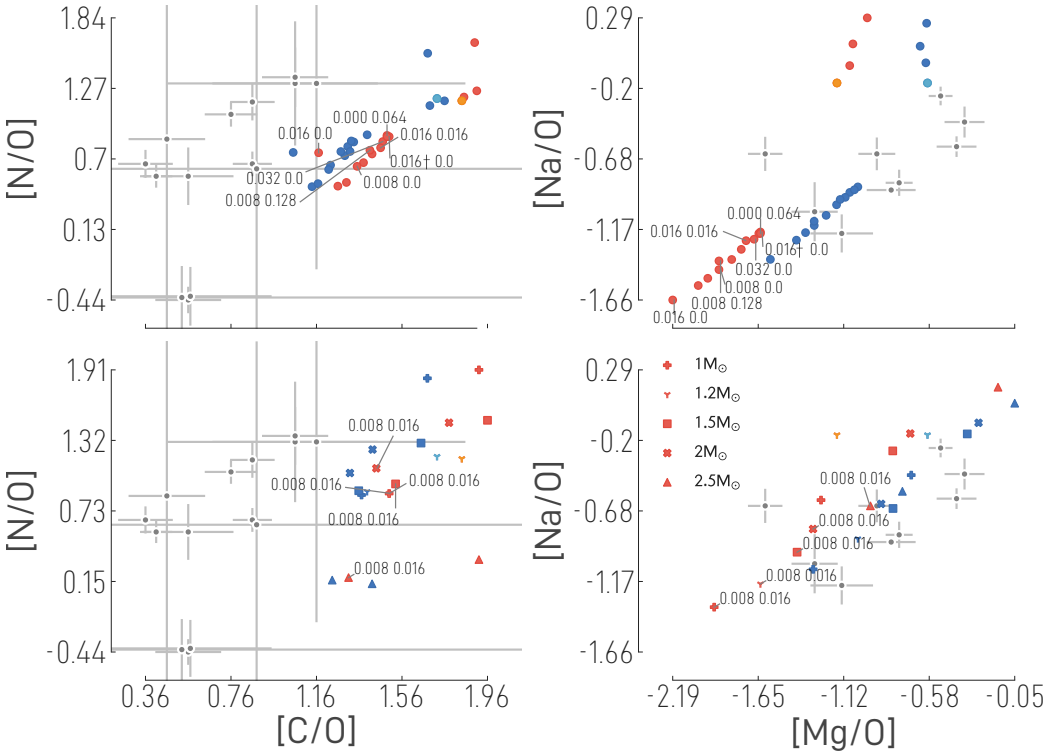

Figure 5.19 Abundance ratios of [N/O] vs. [C/O] (left) and [Na/O] vs. [Mg/O] (right) from models and observations. The top row of plots show only data for the 1.2 $M_\odot$ tracks, whereas the bottom row of plots shows the data for the tracks in Table 5.2. Thus, 1.2M Pooo Cooo and 1.2M Poo8 Co16 are in all plots in both rows. The plot elements and dilution factor are the same as in Figure 5.18.

Table 5.6 Key characteristics of the observed CEMP-r/s stars used in the Li analysis. Errors are provided where available.

Star	[Fe/H]	[Li/H]	Ref.
CS 22183-015	-2.82 ± 0.15	<-2.65	1
CS 22898-027	-2.44 ± 0.17	-1.08 ± 0.01	1
CS 22948-027	-2.23 ± 0.16	<-2.26	2
CS 22949-008a	-2.09 ± 0.04	<-2.26	1
CS 29497-030	-2.52 ± 0.16	<-2.16	3
CS 29526-110	-2.06 ± 0.30	<-0.96	4
LP 706-7	-2.53 ± 0.30	-0.96 ± 0.02	4
SDSS 1707+58	-2.52 ± 0.30	<-0.76	4
HD 5223	-2.10 ± 0.20	0.00 ± 0.03	5
HE 1418+0150	-2.00 ± 0.20	-0.05 ± 0.03	5
HD 187216	-2.50 ± 0.20	0.00 ± 0.03	5
HE 0017+0055	-2.60 ± 0.20	-0.10 ± 0.03	5

(1) Masseron et al. (2012), (2) Aoki et al. (2002a),
(3) Sivarani et al. (2004), (4) Aoki et al. (2008),
(5) Susmitha et al. (2021)

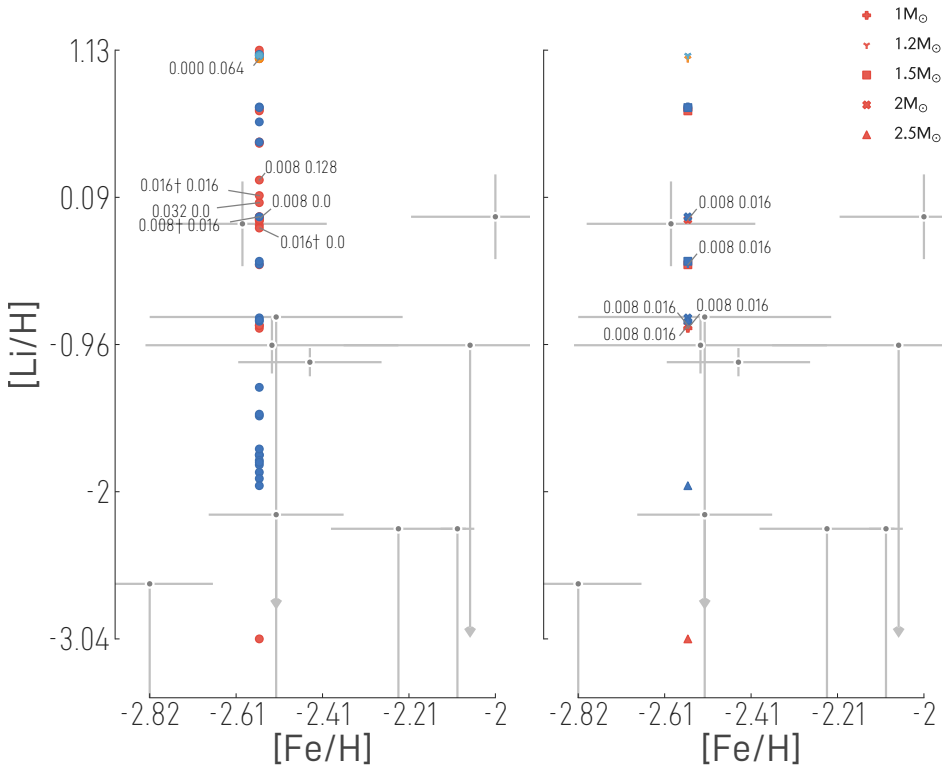

Figure 5.20 Surface abundance of [Li/H] vs. [Fe/H] for models and observations. The plot elements and dilution factor are the same as in Figure 5.18. The left panel shows only data for the 1.2 $M_\odot$ tracks, whereas the right panel shows the data for the tracks in Table 5.2. Thus, 1.2M Pooo Cooo and 1.2M Poo8 Co16 are in both panels. Those observations for which only a maximum Li abundance is provided have a downward facing arrow as an error bar for their Li abundances.

for $\delta\left(^{134}\mathrm{Ba}/^{136}\mathrm{Ba}\right)$. If one compares the measured $\delta\left(^{134}\mathrm{Ba}/^{136}\mathrm{Ba}\right)$ and $^{12}\mathrm{C}/^{13}\mathrm{C}$ values to those at the surface of my models, one finds the values in Table 5.7. While the model values for $\delta\left(^{134}\mathrm{Ba}/^{136}\mathrm{Ba}\right)$ are almost all negative, agreeing with the conclusion of Liu et al. (2014), some are not as negative as the measured value even when factoring in the uncertainties. The tracks without PDCZ overshoot have more negative values than those with. Furthermore, the $^{12}\mathrm{C}/^{13}\mathrm{C}$ ratio is much too small in the models. To investigate this in more detail, the value of these quantities at different locations and at different times in the 1.2M Pooo Co64 model are also listed in the table. For example, the row marked "post-PIE" shows the value of these quantities in the lower part of the split PDCZ after the *i*-process nucleosynthesis is done. "Deep Pocket" refers to the values in the deep $^{13}\mathrm{C}$ pocket at the end of its lifetime and "post-PDCZ" refers to the values in the former PDCZ region after the first post-PIE TP and before the TDU. These values cannot be directly compared to the observed values since this material would need to make its way to the surface of the star and would thus be diluted by the envelope composition. Nevertheless, it can help us to understand how these

Table 5.7 Isotopic measurements for two stardust grains (G232 and G244) associated with an *i*-process source from Liu et al. (2014) compared to values from my models. For 1.2M Pooo Co64, values at different locations and times in the evolution are also given. See text for more details.

Source	$^{12}C/^{13}C$	$\delta(^{134}Ba/^{136}Ba)$
G232	94±1.0	−606±388
G244	68±1.0	−433±328
1M P000 C000 (surface)	3	−22
1M P008 C016 (surface)	5	−29
1.2M P000 C000 (surface)	7	−173
1.2M P008 C016 (surface)	5	−20
1.2M P000 C064 (surface)	9	−63
1.2M P000 C064 (post-PIE)	417	−827
1.2M P000 C064 (deep pocket)	15 135 612	373
1.2M P000 C064 (post-PDCZ)	69 183 097	85
1.5M P000 C000 (surface)	5	−57
1.5M P008 C016 (surface)	6	−8
2M P000 C000 (surface)	5	−175
2M P008 C016 (surface)	8	−61
2.5M P000 C000 (surface)	5836	1
2.5M P008 C016 (surface)	27	90

values are affected by different events.

As one can see the post-PIE values are in better agreement with the observations, in particular for $\delta(^{134}Ba/^{136}Ba)$. However, this material is then also subjected to the neutron exposure of the deep ^{13}C pocket. This drastically changes the values. The $^{12}C/^{13}C$ value increases dramatically as the ^{13}C is burned to produce neutrons for the *s*-process. Moreover, $\delta(^{134}Ba/^{136}Ba)$ becomes quite large reflecting the *s*-process neutron densities. Finally, this material is spread out over the intershell by the subsequent PDCZ and, prior to the TDU, has the values in the "post-PDCZ" row of the table. These values are again more what one would expect for the *s*-process.

This analysis has shown that the contamination of the *i*-process material by the *s*-process occuring in the deep ^{13}C pocket can have a significant impact on the final surface abundaces of heavy isotopes. Additionally, the high measured $^{12}C/^{13}C$ is informative as well. As has already been discussed in connection with Table 5.4, a standard, low-metallicity AGB star would be expected to have a $^{12}C/^{13}C$ greater than 1000. Models with a PIE and no TDUs have $^{12}C/^{13}C$ values near the CNO cycle equilibrium values. The measured value is somewhere in between. The way for a model to do this would be a PIE followed by many TDUs. This can be seen in the models of Cristallo et al. (2009a) where a PIE occurs followed by many TDUs and yields a surface $^{12}C/^{13}C$ value of nearly 80. For my models with a PIE,

the highest $^{12}C/^{13}C$ value is 27.45 for 2.5M Poo8 Co16, which is also the model with the most post-PIE TDUs with 5. Unfortunately, this model also has the ^{22}Ne neutron source active in the TPs which causes it to have a positive $\delta\left(^{134}Ba/^{136}Ba\right)$. This would suggest that in order for my models to have enough TDUs to match the measured $^{12}C/^{13}C$ values, the mass loss rate would have to be significantly reduced. This could occur if either the surface C/O were reduced or if the mass loss prescription were altered. Additionally, the mass of the star which generates the stardust grain should be less than 2.5 $M_\odot$ to avoid activating the ^{22}Ne source.

Now a comparison of surface abundaces ([X/Fe]) to observations will be conducted. Since many models in this work have abundances which are not typical for the *i*-process, I will also compare the surface abundances of the models to some CEMP-s stars with metallicities of $-2 \leq [Fe/H] \leq -3$. To determine how good the fit of the models to the observations is a reduced χ^2, χ^2_{red}, calculation is performed. For each observed star the χ^2_{red} for each model is calculated as

$$\chi^2_{red} = \frac{1}{N}\sum_{i=1}^{N}\frac{\left([X/Fe]_i^{model} - [X/Fe]_i^{observed}\right)^2}{\sigma_i^2}, \tag{5.6}$$

where N is the total number of observed elements used, $[X/Fe]_i^{model}$ is the model's surface value for [X/Fe] for isotope i, $[X/Fe]_i^{observed}$ is the observed value for [X/Fe] for isotope i, and σ_i is the observational error for isotope i. Following Choplin et al. (2021) a minimum value of 0.2 for σ_i is assumed. The dilution factor, f, is allowed to freely vary in order to get the best fit. In Table 5.8 one can see, for each observed star, the best fitting model as well as the χ^2_{red} and dilution factor for that fit. The stars in the upper part of the table are CEMP-r/s stars, while those in the bottom part are CEMP-s stars.

As one can see, the best fitting model for all but one CEMP-r/s star is 1.2M Pooo Co64. Given that this model also has the most typical *i*-process abundance pattern, that was to be expected. The χ^2_{red} for many of the CEMP-r/s stars is not satisfactory. Additionally, one must also eliminate any case where $f = 0$. This would imply an unrealistic mass transfer efficiency. This leaves only 1 of the CEMP-r/s stars which is fit reasonably well. Figure 5.21 provides an overview of the model and observational data. The colored markers in the upper panel of the figure show the observational data with errors. The gray region is the span of abundances covered by the models and the gray line is the mean of the model abundance data. The residuals (model–observation) of the best fitting model to the corresponding observations for each observed star are shown in the lower panel. Additionally, the mean of the residuals for each element is marked by the red rectangles. Some elements have also been labeled. In Figure B.1 one can find a similar plot for each observed CEMP-r/s star and best fitting model separately, along with the χ^2_{red} and dilution factor. The χ^2_{red} does not tell the whole story, though. There are some stars where only one element is not fit well and all others are (see HE1120-2122 in

Figure B.1 as an example). In this case the model may still represent a good fit to the observations. The residuals for most elements are good across all best fitting tracks. The vast majority of points lie within the dashed lines marking values of −0.4 and +0.4 dex. Anything between these lines represents a reasonable fit to the data considering that the uncertainty on the observations is on the order of 0.2–0.4 dex.

Nevertheless, there are two isotopes whose abundances are measured in most of the stars and whose average residuals are well outside the dotted lines: Y and Eu. For Y the final surface abundance is primarily determined by the material which reaches the surface immediately after the PIE — the subsequent TDUs do not change the surface abundance of this element significantly. This is true of all first-peak elements. The high Y abundance results from material exposed to a very high neutron density for short times. If the duration of the neutron flux were increased, then more of the material would make it past the first peak. That being said, the Y abundances for some stars have also posed problems for other studies. This will be discussed more in Section 5.3.2. The Eu abundance deviations are likely explained by the *s*-process nucleosynthesis which happens in the deep ^{13}C pockets. This contaminates the *i*-process enhanced material with a more *s*-process-like abundance signature. This leads to lower Eu enhancement, especially relative to the Ba enhancements. The impact of *s*-process contamination was already seen when comparing the models to meteorite measurements.

The fact that the first-peak element surface abundances are almost exclusively the results of the enrichment which occurs when the upper part of the split PDCZ merges with the CE, provides a way to test observationally if the early split is realistic or not. Given that the observed first peak element abundances are generally not well matched by the models this suggests that the split occurs too soon in the models. Alternatively, if one assumes the models are correct, then this would suggest that the CEMP-r/s stars are polluted by something other than AGB stars. If one omits the first-peak elements from the comparison and recalculates the $\chi^2_{\rm red}$, then the results improve significantly. This is shown for select stars as the number in parentheses in the $\chi^2_{\rm red}$ column of Table 5.8.

Figure 5.22 shows the same type of plot as Figure 5.21 but for the CEMP-s star data. In Figure B.2 one can find a similar plot for each observed CEMP-s star and best fitting model separately, along with the reduced χ^2 and dilution factor. In this case there is no element whose mean residual is outside the dotted lines, however, as with the CEMP-r/s stars, there is a tendency for the residuals to be below zero. This means the models have a tendency to be less enriched in these elements than the observed stars. Here we can also see that Eu is fit better than for the CEMP-r/s stars supporting the argument that contamination by the *s*-process is part of the reason for the lower Eu abundances. Overall, the quality of the fits for the CEMP-s stars is better than for the CEMP-r/s stars with the exception of CS 22942-019. For this star the abundance pattern of the 2.5M P008 C016 star is a

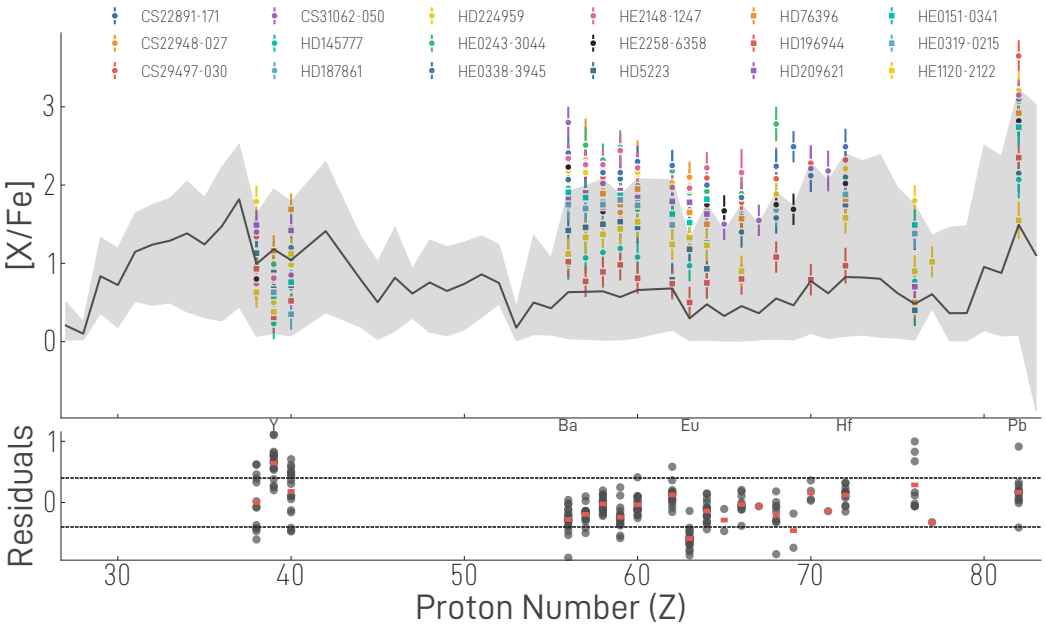

Figure 5.21 Overview of the model data and observations for the CEMP-r/s stars. In the upper panel the gray region denotes the spread of abundances of the model data, the gray line is the mean value for the abundances of the isotopes for all model data, and the points are the observations with errors. In the lower panel are the residuals (model–observations) of the best fitting track and the corresponding observed star for each star. The dashed gray lines mark the values of −0.4 and +0.4. The red rectangles mark the mean of the values of the residuals for each element. Some elements have also been labeled.

good fit, but the magnitude of the model surface abundance is too small to match the observations.

The fact that the models presented here experience a PIE and an *s*-process event and can potentially explain both some CEMP-r/s and some CEMP-s stars brings up an interesting prospect. Namely, that PIEs may be responsible for both some CEMP-r/s and some CEMP-s stars. The deciding factor between whether the final surface abundances are more *s*-process- or *i*-process-like is when the split occurs and whether TDUs occur afterwards. The later the split and the more post-PIE TDUs, the more *i*-process-like the surface abundances will be and vice versa. This channel of "failed *i*-process stars", i.e. stars with early splits and a deep ^{13}C pocket with surface abundances that are more *s*-process-like, would in fact be necessary to explain the CEMP-s stars at low metallicity given these models. This is because the models show that any amount of PDCZ overshoot up to at least a mass of 2.5 $M_\odot$ will lead to a PIE and no standard ^{13}C pocket will be produced at any point. Thus, none of the models undergo the typical *s*-process synthesis channel of the ^{13}C pocket. Furthermore, at higher masses one would expect that the *s*-process happens under convective conditions during the TPs. Therefore, it seems there is a problem in producing ^{13}C pockets at low metallicity. A problem which would be solved by the deep ^{13}C pockets seen after the PIEs

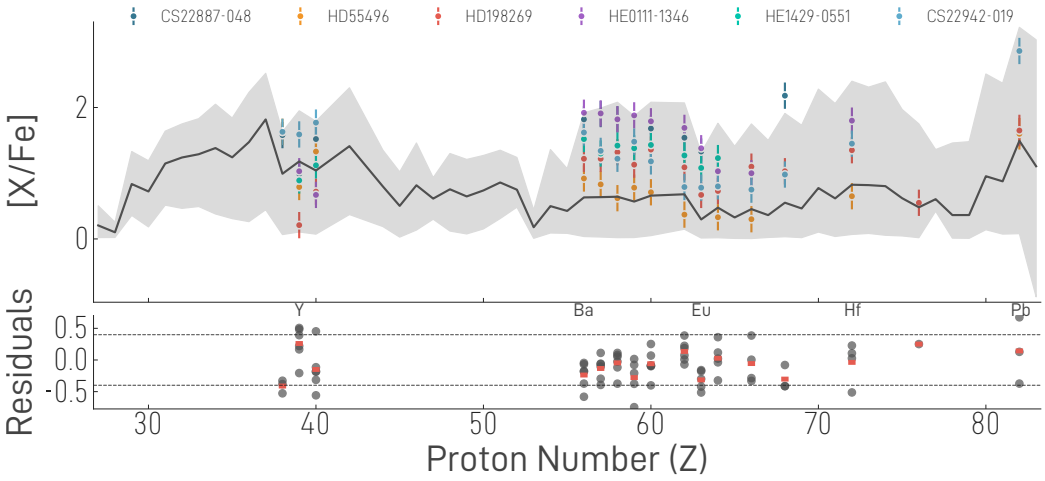

Figure 5.22 Overview of the model data and observations for the CEMP-s stars. All plot elements have the same meaning as in Figure 5.21.

in these models. It should be noted that other studies see standard ^{13}C pockets after PIEs so this argument may not be necessary. Nevertheless, it is an interesting prospect which deserves attention.

In order for this scenario to work one would have to understand what physical conditions impact when the split happens and whether this could vary from star to star. So far most studies seem to find the split always happening before the TOMND or always happening after. Though, there is still a dearth of comprehensive and robust studies across many codes in this area.

Overall, there are a few general conclusions which can be drawn from these results. First, models with `fPDCZ` higher than 0.008 and equal to 0.0 are often in tension with the observations of light element abundances. Second, `fCE` should be high enough to allow for post-PIE TDUs in order to increase the heavy-element surface abundance enhancements, though 0.128 is likely too large. Third, tracks with a mass of 1.5 and 2 $M_\odot$ match the observations of light elements the best. Finally, the heavy-element abundances are best matched by a track with no PDCZ overshoot and `fCE` > 0.016. Overall, there is a difficulty for my models to match both the light and heavy element abundances simultaneously and certain elements like C and Y are overproduced across all models.

5.3.2 Comparison with Previous Works

In this section the results of this study will be compared to other studies. The focus will be on a comparison to the studies of the Brussels group (Choplin et al. 2021, 2022, 2024) and to those of Cristallo et al. (2009a).

In Cristallo et al. (2009a) they simulate a 1.5 $M_\odot$, $Z=5\times10^{-5}$ star. The PIE and subsequent splitting of the PDCZ occur in the same way in their models as in mine, including the fact that the split happens before the TOMND. The H-free

core mass in their model at the PIE is 0.565 $M_\odot$ as compared to my 0.59 $M_\odot$. This difference is the result of my model including overshoot in the pre-AGB evolution. The maximum neutron density in their model, 1×10^{15} cm^{-3}, is slightly larger than my 1.5M Pooo Cooo. The split convective zones then never merge again and the upper convective zone merges with the envelope in what they refer to as "deep TDU." In contrast to our model, their model goes on to have many more TPs and many additional TDUs, whereas 1.5M Pooo Cooo experiences many more TPs but only one post-PIE TDU. This causes more of the material in the lower part of the split PDCZ in their model to nevertheless make its way to the surface of the star. Again, this occurs because each subsequent PDCZ overlaps with the region where the lower part of the PDCZ was and, thus, mixes the material from the lower part of the PDCZ throughout the intershell. The TDU can then dredge this material up to the surface.

In terms of the nucleosynthesis there are some similarities and some discrepancies. First, they also find that initially after the TDU only first peak elements get to the surface. It is only due to the post-PIE TDUs that the heavier elements also get to the surface. Furthermore, the first-peak element abundances in their models are also not largely affected by the TDUs. The pattern of the first-peak abundances is similar to my models and quite different from those of the Brussels group. Specifically, Rb, Kr, and Y show higher abundances in the models with an early split. This is a sign of high neutron densities for short periods of time (Wallerstein et al. 1997, Busso et al. 2001). However, because their model goes through more than 20 TDUs the final surface abundances of the heavier elements are higher than in my models. Furthermore, they do not mention a deep ^{13}C pocket after the PIE, however, they do find standard ^{13}C pockets after each TDU.

In the first part of a series of papers from the Brussels group they simulate a 1.0 $M_\odot$, Z=4.3×10^{-5} star. The largest difference between our models and theirs is that theirs experiences the PDCZ split only after the TOMND. The H-free core mass at the PIE for their model is 0.551 $M_\odot$ while for my model it is 0.557 $M_\odot$. This is due to the fact that the models from the Brussels group do include overshoot prior to the AGB. In terms of abundances their model post-PIE has $^{12}C/^{13}C = 4.98$ in mass as well as C/O= 3.46 as opposed to 3.22 and 19.627, respectively, for 1M Pooo Cooo.

The exact value of these ratios ultimately depend on a number of factors including, but not limited to:

- The competition between the triple-α reaction rate, the CNO cycle rates, and the ^{13}C neutron-source reaction rate
- The ingestion by the PDCZ of material that has been processed by the H shell and, thus, has CNO-like values for these ratios
- The depth at which the PDCZ splits

- When during the pulse the PDCZ splits
- The composition of the envelope prior to the PIE

That being said, we can draw some conclusions simply by looking at how the value of these ratios change in the upper part of the split PDCZ after the split. After the PDCZ splits, the $^{12}C/^{13}C$ ratio continues to decrease. This is the result of the combined effect of the continued CNO cycle burning that is still occurring in the convective zone since temperatures there are up to 80 MK and the continued expansion of the upper boundary of the convective zone into regions with lower $^{12}C/^{13}C$ ratio values. It has already been shown that my models overproduce C and so the value of C/O from the Brussels group is likely more realistic.

As part of this study they also test the time stepping and spatial resolution of their code on the PIE. They find, as do I, that too large of time steps can cause the PIE to be missed. They also find that the split of the PDCZ is not impacted by the time step or resolution — it always happens after the TOMND. In my models I find that by increasing the time step sufficiently the split of the PDCZ can be pushed to later in the PIE. These results are not necessarily inconsistent as I varied the time step by a factor of 10 whereas they only vary it by at most a factor of 2–3.

The nucleosynthesis of their model is of course quite different owing to the later split. They find that the heavy element abundances reach the surface immediately following the PIE with no need for additional TDUs. Indeed they report no TDUs for this model. The final surface abundance pattern is similar to that of my 1.2M Pooo C064 model but with approximately 10 times larger enhancements for elements past the first peak. They also do a comparison of their abundances after dilution to observed CEMP-r/s stars, all of which I have included in this work as well. On average the model of the Brussels group has better χ^2_{red} values than my models. However, they also have trouble fitting the first-peak elements for a number of the observed stars.

Their analysis was extended to different masses and metallicities in Choplin et al. (2022). Here they also find that the $2\,M_\odot$ model without overshoot has a PIE and the $3\,M_\odot$ model does not. This is consistent with what is seen in my $2\,M_\odot$ and $2.5\,M_\odot$ models. They find, however, that the $1\,M_\odot$ model has higher neutron exposure and neutron densities than the $2\,M_\odot$. This is the opposite of what is seen in my models. Furthermore, they continue to find the split of the PDCZ to happen after the TOMND regardless of mass or metallicity. Because of this, there are large discrepancies between my models and theirs when it comes to the surface abundances.

In this paper they also test the effect of changing the convective velocities on the splitting of one of their models. Their results agree with mine. Namely, that a lower convective velocity leads to a larger mass coordinate of the split. I find that the convective velocity can also cause the split to occur later or earlier. They make no mention of this suggesting that they see no impact.

In Choplin et al. (2024) the same 1.0 $M_\odot$, Z=4.3 × 10^{-5} star is run with varying overshoot parameters. Note, that the models still do not consider overshoot prior to the AGB phase. They focus mainly on the impact of overshoot on the heavy element abundances and, importantly, only calculate the models up until the split point. They then employ what they call a dilution procedure to approximate what the surface abundances would be. Nevertheless, there are a few things that can be compared between my study and theirs:

- As before, they find that the split of the convection zone occurs after the TOMND.
- I also see that the evolution of neutron density proceeds more smoothly when overshoot is applied to the PDCZ.
- The duration of the PIE was also found to decrease with $f_{\rm PDCZ}$ in our models.
- I also find that increasing the overshoot reduces the neutron exposure.
- Here they also find the deep ^{13}C pocket. However, they only see it at high metallicity ([Fe/H] = −1). Furthermore, their pocket is larger (2×10^{-3} $M_\odot$ vs 3×10^{-4} $M_\odot$ in my model), has lower neutron densities (2.3×10^{6} cm^{-3} vs 2×10^{7} cm^{-3}), and lives longer (500 kyr vs 193 kyr).

The differences in the pocket quantities may well be the result of the very different metallicities. Because of the split, the heavy element abundances of my models and theirs are different as was the case with the previous studies. Unfortunately, since they do not evolve the models past the splitting of the PDCZ, there is no information regarding post-PIE TDUs for this study. None of the models from the Brussels group include overshoot prior to the AGB. As such the H-free core mass at the start of the AGB is likely underestimated. This could be why our models are different. Core mass is a critical property of AGB stars, and it is known to influence many aspects of the standard AGB evolution.

Table 5.8 The name and metallicity of the observed star as well the best fitting model with its $\chi^2_{\rm red}$ and dilution factor, f. The numbers in parentheses are the result of the $\chi^2_{\rm red}$ calculation after omitting first peak elements. CEMP-r/s stars are in the upper part of the table and CEMP-s stars are in the lower part.

Star	[Fe/H]	Best Model	$\chi^2_{\rm red}$	f	Reference
CS 22891-171	-2.50 ± 0.10	1.2M P000 C064	3.53	0.34	1
HD 5223	-2.00 ± 0.08	1.2M P000 C064	2.97	0.82	1
HD 76396	-2.27 ± 0.10	1.2M P000 C064	3.32	0.49	1
HD 145777	-2.32 ± 0.10	1.2M P000 C064	2.45 (1.07)	0.89	1
HD 187861	-2.60 ± 0.10	1.2M P000 C064	3.67	0.55	1
HD 196944	-2.50 ± 0.09	1.2M P000 C000	1.13	0.58	1, 4
HD 209621	-2.00 ± 0.09	1.2M P000 C064	4.27	0.45	1
HD 224959	-2.36 ± 0.09	1.2M P000 C064	3.90 (1.26)	0.09	1
HE 0151-0341	-2.89 ± 0.08	1.2M P000 C064	2.80 (1.07)	0.52	1
HE 0319-0215	-2.90 ± 0.10	1.2M P000 C064	2.67 (0.81)	0.67	1
HE 1120-2122	-2.00 ± 0.10	2M P008 C016	2.25	0.00	1
CS 22948-027	-2.23 ± 0.16	1.2M P000 C064	3.43	0.00	2, 13
CS 29497-030	-2.52 ± 0.16	1.2M P000 C064	2.46	0.00	3, 4
CS 31062-050	-2.33 ± 0.16	1.2M P000 C064	3.89	0.10	5, 6, 15
HE 0243-3044	-2.58 ± 0.20	1.2M P000 C064	3.89	0.00	7
HE 0338-3945	-2.42 ± 0.05	1.2M P000 C064	3.94	0.00	8, 9
HE 2148-1247	-2.30 ± 0.15	1.2M P000 C064	4.38	0.00	10, 11
HE 2258-6358	-2.65 ± 0.03	1.2M P000 C064	2.84 (1.60)	0.44	12
CS22887-048	-2.10 ± 0.09	1.2M P000 C064	2.10	0.33	1
HD55496	-2.10 ± 0.09	2.5M P008 C016	1.84	0.39	1
HD198269	-2.10 ± 0.10	2M P008 C016	0.90	0.12	1
HE0111-1346	-2.10 ± 0.09	1.2M P000 C064	2.40	0.61	1
HE1429-0551	-2.70 ± 0.10	1.2M P000 C064	0.66	0.76	1
CS 22942-019	-2.50 ± 0.09	2.5M P008 C016	4.78	0.00	1, 14

(1) Karinkuzhi et al. (2021), (2) Aoki et al. (2007), (3) Ivans et al. (2005), (4) Roederer et al. (2014), (5) Aoki et al. (2002b), (6) Aoki et al. (2006), (7) Hansen et al. (2015), (8) Jonsell et al. (2006), (9) Zhang et al. (2011), (10) Cohen et al. (2003), (11) Cohen et al. (2013), (12) Placco et al. (2013), (13) Hill et al. (2000), (14) Masseron et al. (2010), (15) Lai et al. (2007)

5.4 Conclusion

In this chapter, a grid of stellar models with masses between $1\,M_\odot$–$2.5\,M_\odot$ and a metallicity of $Z = 5 \times 10^{-5}$ were run. In addition to varying the mass, also the overshoot parameters for various convective boundaries were varied. The primary conclusions of the current investigation are

- A new timescale argument was developed to check whether a PIE should occur at a particular TP. The criterion for a PIE is $\tau_{\mathrm{He}} < \tau_{\mathrm{diff}} \simeq \tau_{\mathrm{H}}$.
- It was found that those stars which have a PIE also have a deep ^{13}C pocket which forms at the base of the PDCZ and burns under radiative conditions in the following interpulse period.
- Models with PIEs may be able to explain both some CEMP-r/s and CEMP-s stars.
- The splitting of the PDCZ is critical in determining the final surface abundances and is sensitive to the code settings and physics choices. However, even if the split occurs before the TOMND, TDUs can still bring heavy elements to the surface.

For the fiducial model ($M = 1.2\,M_\odot$, $Z = 5 \times 10^{-5}$, no overshoot) it was found that a PIE does occur with neutron densities approaching $1 \times 10^{15}\,\mathrm{cm}^{-3}$. The H burning in the PDCZ causes the PDCZ to split as seen in other studies. In my models, the splitting of the PDCZ happens before the TOMND. Because of this, the surface is enriched only with first-peak elements when the upper part of the PDCZ merges with the envelope. However, in the TP after the PIE there is an efficient TDU which serves to also bring the second- and third-peak elements to the surface. This model also develops a deep ^{13}C pocket at the base of the PDCZ after the PIE. This pocket is engulfed by the following PDCZ and contaminates the surface abundances with an *s*-process signature.

This same model was run with varying overshoot parameters which have an impact on the model. It was found that overshoot tends to decrease the maximum neutron exposure and does not delay the splitting of the PDCZ significantly in most cases. Furthermore, the PIE happens at an earlier pulse and the AGB phase ends before any further TPs can occur except for stars with masses greater than $1.5\,M_\odot$.

To test the robustness of the PIE in the models, the fiducial model was run with various time step and spatial resolution settings. It was found that if the time step is allowed to be too large then the PIE is missed. A timescale argument was then presented which allows for a test of whether a PIE should occur at a particular pulse or not. The timescale argument was then checked for accuracy against models with and without overshoot. In a similar manner, the robustness

of when the PDCZ splits was tested. It was found that lowering the proton capture on ^{12}C rate does not affect when the split happens. On the other hand, increasing the convective velocities by a factor of 4 and increasing the time step both pushed the splitting of the PDCZ past the TOMND.

Because the split happens before or very shortly after the maximum neutron density occurs, the surface abundances after the PIE only show signs of first-peak element enhancements. If the model experiences a post-PIE TDU then the second and third peak elements are able to be brought to the surface. This means that the only models which have a surface abundance pattern close to what is expected for the *i*-process are those models with either no PDCZ overshoot or with masses above 1.5 $M_\odot$.

The surface abundances were compared against observations of CEMP-r/s and CEMP-s stars. It was found that the models are generally in agreement with observations for the light elements with the exception of C which is overabundant in the models. Additionally, some models have Li abundances which are higher than observed. In general, the results seem to favor models with low but nonzero values for `fPDCZ`. For the heavy element abundances the conclusions are less definitive. Overall, the heavy-element abundances favor models with no PDCZ overshoot and `fCE` > 0.016. The models fit the CEMP-s stars better than the CEMP-r/s stars. However, if the first-peak elements are ignored then the models can also fit a number of the CEMP-r/s stars well. Since the first-peak abundances are largely determined by the material which reaches the surface immediately after the PIE, these results suggest that either the split occurs too early in my models or that CEMP-r/s star were not polluted by AGB stars. Additionally, the fact that these "failed *i*-process" stars are able to match the CEMP-s stars provides a possible new channel for explaining their origin. Considering the results here along with those of the Brussels group one could potentially explain both the CEMP-r/s and low-metallicity CEMP-s stars via AGB stars which undergo PIEs.

In the future this analysis would need to be extended to additional metallicities. The most critical task, though, is to get a better understanding of what impacts the split of the PDCZ, both physically as well as numerically. This single aspect has the largest impact on the final surface abundances.

Chapter 6

Investigations of the *s*-process

> Es ist nicht [das Ziel der Wissenschaft], der unendlichen Weisheit eine Tür zu öffnen, sondern eine Grenze zu setzen dem unendlichen Irrtum.
>
> Bertolt Brecht, *Leben des Galilei*

The discussion of the *s*-process until now was primarily driven by two ideas: There is a lot that we qualitatively understand about how the *s*-process occurs in AGB stars, and there is a lot that remains quantitatively uncertain. One of the goals of this investigation is to test how the uncertainties in how we model physics in 1D stellar evolution models, e.g. atmosphere boundary conditions or convection, impacts the quantitative results of our models. In what follows, I will run a grid of stellar models for a particular mass and metallicity while varying the physics choices. The results of these computations will then be compared to previous studies as well as to observations.

6.1 A First Look

As a first step in this investigation it was prudent to determine which physics and/or which parameters have a noticeable impact on the models in order to determine which are worth varying. The computation time of AGB models is not as prohibitive as it once was, but it still is a computationally expensive task. Therefore, it remains a worthwhile exercise to determine which parameters can be held fixed in order to reduce the size of the grid of models which needs to be run.

6.1.1 The Boundary Conditions

First, the effect of the different boundary conditions (BCs) was tested. As a reminder there are two options for the atmosphere model: the Lucy spherical atmosphere model and the Eddington gray atmosphere model. There are also two different opacity descriptions which can be used for the outer layers: the standard RM opacities and the PM opacities. This gives four possible boundary conditions to be tested. These four boundary conditions will be abbreviated as such for the remainder of this work:

- Eddington gray atmosphere with RM opacities: EddR
- Eddington gray atmosphere with PM opacities: EddP
- Lucy spherical atmosphere with RM opacities: LucyR
- Lucy spherical atmosphere with PM opacities: LucyP

Stellar tracks with each of the four boundary conditions were run from the ZAMS until the AGB. The HRD diagram for these tracks up until the tip of the RGB is shown in Figure 6.1. When viewing Figure 6.1 it is clear that the primary effect of the switch to PM opacities is the shifting of the stellar tracks to lower effective temperatures. This, however, only occurs after the tracks have left the MS. Furthermore, this effect is independent of the atmosphere model used. Despite the Eddington grey atmosphere being a poor approximation for the atmosphere of an giant star, switching to a Lucy spherical atmosphere does not appear to affect the stellar track much at all. This is in agreement with what was already shown in Wagstaff & Weiss (2018). The opacities have a much more significant impact on the evolution of the star.

When these stars get to the AGB there are some differences noticeable in all of the tracks. Looking at Figure 6.2 one can see that there is now a small difference between the LucyP and EddP tracks which were indistinguishable on the RGB, and there is a noticeable difference between the EddR and LucyR tracks. It should be mentioned that the LucyR track faced some computational difficulties in this phase which were not seen in the LucyP or EddR tracks.

Based on these tests it was decided to only run tracks with the EddR and LucyP BCs for the remainder of the grid. In this way we cover both the standard BC which is used in almost all other simulations as well as the BC which is the most physically motivated for AGB stars.

6.1.2 The Overshoot Parameters

Recall that in this version of `GARSTEC` there are 3 overshoot parameters relevant on the AGB: `fCE` controls overshoot from the CE, `fPDCZt` controls overshoot from

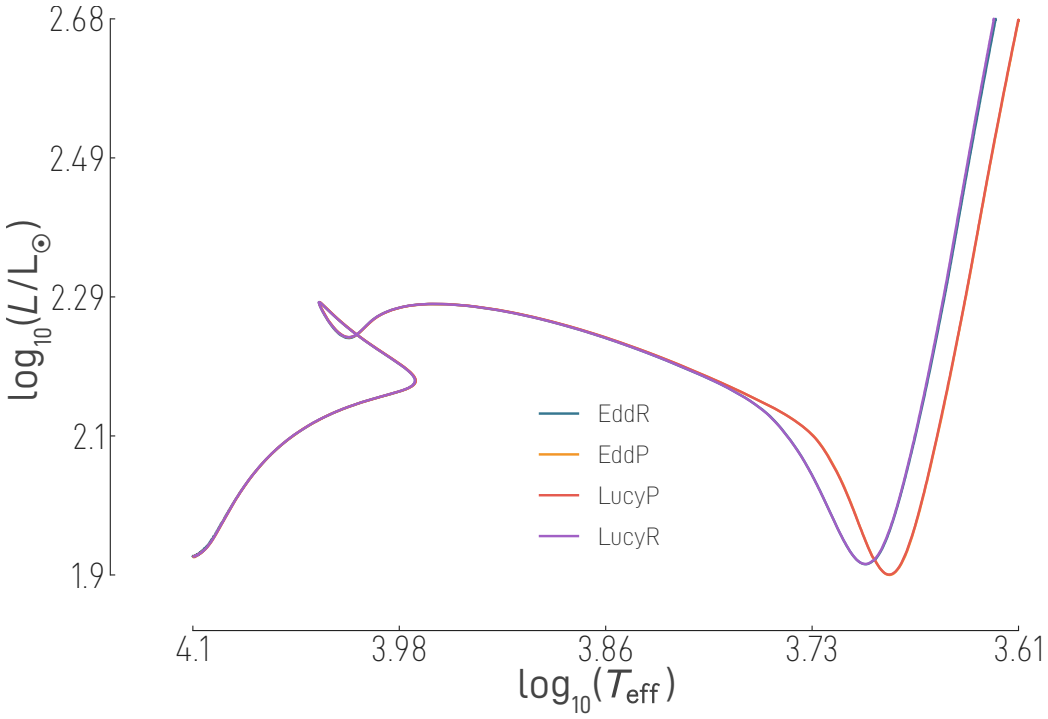

Figure 6.1 HRD of models with various BCs: EddR (Blue), EddP (Orange), LucyR (Purple), LucyP (Red). The models are run from the ZAMS to the RGB. The EddR and LucyR almost perfectly overlap for the entirety of the evolution shown. The same is true of the EddP and LucyP models.

the upper boundary of the PDCZ, and `fPDCZb` which controls overshoot from the lower boundary of the PDCZ. It is clear from many studies (Herwig et al. (1997), Lugaro et al. (2003), Weiss & Ferguson (2009), and Wagstaff et al. (2020), and references therein) that overshoot from the CE and from the bottom of the PDCZ are important for AGB evolution. It is less clear if the overshoot from the top of the PDCZ is important. A few test tracks were run with the same `fCE` and `fPDCZb` but differing values for `fPDCZt`. The results of our tests reflect what was already discussed in Wagstaff (2018), namely, that `fPDCZt` does not have much of an impact on the evolution of the tracks (assuming one does not increase it to such unrealistically high levels that one triggers a PIE). Based on this there is no need to vary `fPDCZb` and `fPDCZt` independently, but rather one can use one overshoot value for both boundaries of the PDCZ which will be called `fPDCZ`. One could of course argue that `fPDCZt` could be set to zero, but the more internally consistent thing to do is to let there be overshoot even if it does not have a great affect on the models.

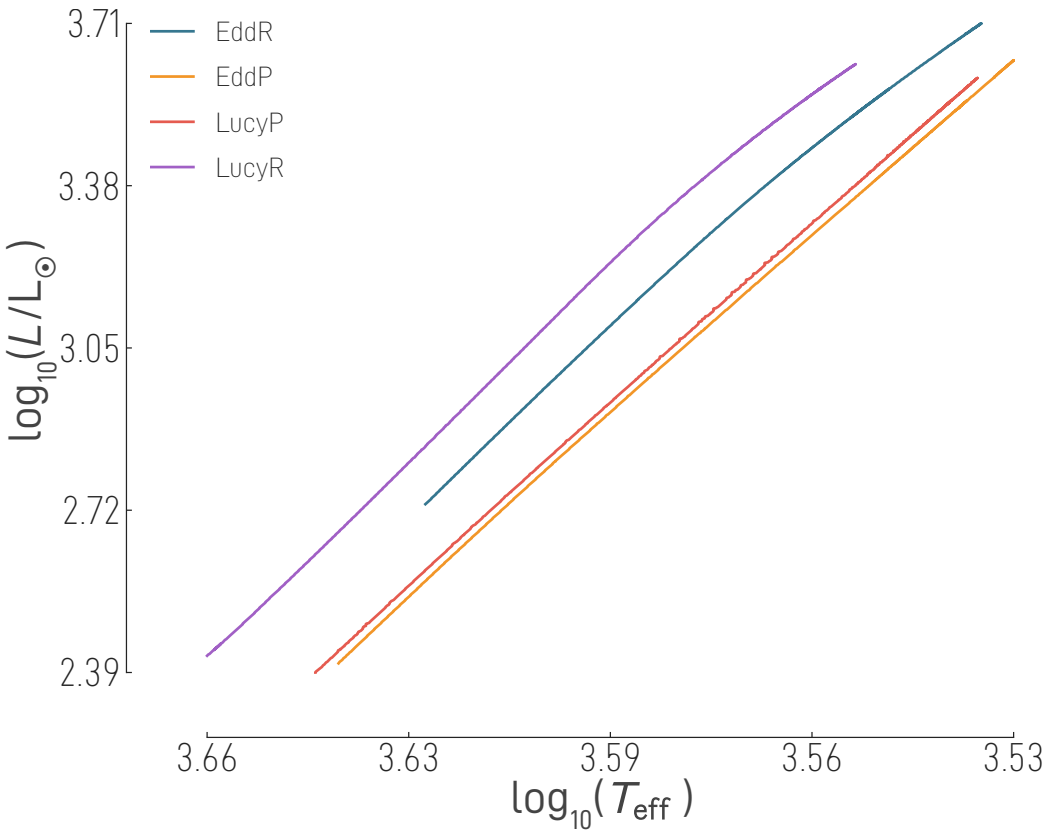

Figure 6.2 HRD of models on the AGB with various BCs: EddR (Blue), EddP (Orange), LucyR (Purple), LucyP (Red).

6.2 Models of a $3\,M_\odot$, $Z_\odot$ Star

The focus of this study is on the varying of the physics not on the varying of the stellar parameters themselves. To that end I only considered one star of a particular mass and metallicity ($M = 3\,M_\odot$ and $Z = Z_\odot$) and varied the physics for this one star. This included overshoot, opacities, atmosphere treatment, equation of state, atomic diffusion, and mass loss. For the purposes of disambiguation the following naming convection will be applied to the models discussed in this chapter. The label for each track will have at least four parts which are best explained with an example:

$$\overbrace{\text{Edd}}^{\text{atmosphere model}}\ \underbrace{\text{P}}_{\text{Opacity}}\ \overbrace{\text{Poo8}}^{\texttt{fPDCZ}}\ \underbrace{\text{Co16}}_{\texttt{fCE}}, \tag{6.1}$$

where the atmosphere model can either be “Edd” for Eddington gray atmosphere or “Lucy” for a spherical atmosphere, opacities can either be “P” for PM opacities or “R” for RM opacities, and the overshoot values are given without the leading “0.”.

Thus, the example above would be the label for a track which uses the Eddington gray atmosphere model with PM opacities in the outer layers and has an overshoot parameter value of 0.008 for the PDCZ and 0.016 for the CE. In addition to these four parts, extra information may be given about each track if another aspect of the physics differs from the standard treatment. These include "FEoS" for those tracks which use the FreeEoS instead of the standard OPAL EoS, "VW" for those tracks which use the Vassiliadis & Wood (1993) wind description, and "Diff" for those tracks which include atomic diffusion in radiative layers.

The pre-AGB evolution of these stars were all calculated with a consistent outer BC, mass loss prescription, and EoS. The overshoot parameter for the convective cores and CE prior to the AGB was 0.016 in all tracks. The pre-AGB tracks were stopped after the end of core He burning and this final model was used as the starting model for the AGB tracks. Thus, for example, all EddR+OPAL EoS tracks were run from the same post-HB starting model.

The pre-AGB evolution proceeds in the standard way and so will not be discussed in detail. There are two important points, though. First, The pre-AGB mass loss of all models was at most 1%; ergo, is not an important distinction between the models. Second, The H-free core mass at the start of the AGB differs between models with different physics. This could be important as the H-free core mass is one of the defining characteristics of AGB stars. For EddR+OPAL EoS the H-free core mass is $0.607\,M_\odot$, for EddR+FreeEoS it is $0.587\,M_\odot$, and for LucyP+OPAL EoS it is $0.604\,M_\odot$.

Table 6.1 shows key global quantities for the *s*-process tracks run in this study. The headers of the table have the following meanings

- Label: The label of the track
- $N_{\rm TP}$: The number of TPs the track undergoes
- $N_{\rm TDU}$: The number of TDUs that occur
- $\Delta t_{\rm AGB}$: The AGB lifetime
- Final C/O: The Final C/O ratio
- Final $M_{\rm env}$: The final envelope mass
- $\overline{\Delta t_{\rm interpulse}}$: The mean duration of the interpulse phases
- $\overline{M_{\rm pocket}}$: The mean maximum mass of the ^{13}C pockets
- $\overline{\Delta t_{\rm pocket}}$: The mean lifetime of the ^{13}C pockets
- $\overline{\tau_{\rm pocket}}$: The mean neutron exposure of the ^{13}C pockets.

Table 6.1 Key global results of the stellar evolution models for all the tracks discussed in this chapter.

Label	N_{TP}	N_{TDU}	Δt_{AGB} [kyr]	Final C/O	Final M_{env} [$\mathrm{M}_\odot$]	$\overline{\Delta t_{\mathrm{interpulse}}}$ [kyr]	$\overline{M_{\mathrm{pocket}}}$ [$\mathrm{M}_\odot$]	$\overline{\Delta t_{\mathrm{pocket}}}$ [kyr]	$\overline{\tau_{\mathrm{pocket}}}$ [mb^{-1}]
EddR P008 C016	13	10	877.4	1.48	1.39	67.45	3.2×10^{-6}	45.28	0.517
EddR P008 C016 Diff	14	10	871.1	1.44	1.79	62.18	1.5×10^{-5}	26.85	0.0003
LucyP P008 C016	14	10	921.8	1.49	1.45	65.80	4.5×10^{-6}	47.23	0.481
EddR P008 C064	10	7	748.2	1.80	1.61	74.78	7.5×10^{-6}	61.11	0.442
EddR P008 C064 FEoS	7	6	596.6	1.70	1.73	85.16	7.7×10^{-6}	63.45	0.378
EddR P008 C064 Diff	12	7	1067.5	1.64	1.62	88.91	1.9×10^{-5}	30.84	0.0008
LucyP P008 C064 Diff	12	7	828.4	1.62	1.55	75.26	2.2×10^{-5}	34.74	0.0007
LucyP P008 C064	11	7	789.0	1.59	1.60	71.69	7.7×10^{-6}	67.33	0.429
EddR P008 C128	10	7	732.1	1.79	1.59	73.17	1.4×10^{-5}	52.14	0.075
EddR P016 C016	13	9	861.9	1.41	1.50	66.24	6.4×10^{-6}	56.65	0.413
EddR P016 C016 FEoS	9	8	642.4	1.49	1.49	71.32	3.0×10^{-6}	53.85	0.509
EddR P016 C064	9	7	711.9	1.73	1.67	79.03	7.5×10^{-6}	61.23	0.245
EddR P016 C064 FEoS	7	6	576.0	1.64	1.84	82.21	5.3×10^{-6}	62.11	0.353
EddR P016 C064 Diff	11	7	963.6	1.58	1.62	87.53	2.1×10^{-5}	33.78	0.001
EddR P016 C064 VW	12	9	955.2	1.90	2.29	79.53	5.1×10^{-6}	68.05	0.372
LucyP P016 C064	10	6	737.8	1.50	1.77	73.71	7.1×10^{-6}	57.99	0.186
EddR P016 C128	9	6	689.3	1.64	1.71	76.52	1.6×10^{-5}	61.14	0.108

Additionally, Appendix C contains, for each track, a table of quantities for each pulse cycle in that track.

Before discussing the results, there is an important point which must be addressed. One will notice that the final envelope mass is rather large, but the AGB phase ends only when the envelope is gone. The reason the computations have not been run to the end of the AGB is due to convergence issues. There are a number of well-known convergence issues which can affect AGB calculations. Perhaps the most well known, due to its ubiquity in stellar codes, is the Fe peak opacity instability. This instability, caused by a peak in the opacity of Fe, results in the local luminosity of a stellar model just below the CE to exceed the Eddington luminosity (Lau et al. 2012). This is not seen in my models when the convergence issue occurs. The instability at work here is another. Since the late 1960's it has been theorized that the envelopes of luminous giant stars may become dynamically unstable due to hydrogen recombination (Lucy 1967, Paczyński & Ziółkowski 1968). Normally H is fully ionized in stars, however, in the extended envelopes of AGB stars temperatures can drop low enough that H recombines. This recombination in the outermost part of the envelope injects enough energy to lead to very large envelope ejection. This is known as the hydrogen recombination instability (HRI), and the first identification of this instability in a stellar model was in a model run with GARSTEC (Wagenhuber & Weiss 1994). The HRI is the cause of the convergence issues seen in our models. This can be seen in Figure 6.3 where the luminosity of the star is plotted as a function of model number and the rate of gravothermal energy release, ϵ_g, is plotted as a function of relative mass coordinate for 4 different model numbers. The peak in ϵ_g at around $m_r/M_* = 0.98$ is due to the energy release of recombination. Furthermore, the negative ϵ_g at larger mass coordinates is where recombination has already occurred and expansion is being driven.

The HRI prevents one from carrying out the calculations until the end of the AGB. In tests it was seen that by increasing the mixing length parameter to values > 1.85 one is able to calculate additional pulses. This is because increasing the mixing length parameter will increase the effective temperature enough to avoid this instability. In this study, this was not done because of the effect this would have on the TDU and thus likely on the characteristics of the ^{13}C pockets. Therefore, our calculations stop earlier than those of other studies. Furthermore, the AGB lifetime is then only the time the star is on the AGB up to when the convergence issues arise; no attempt at extrapolating the quantities to the true end of the AGB is done. In all cases the HRI occurred when the models reached an effective temperature between 2400 K and 2550 K and a luminosity between $3.97 \leq \log_{10} L_*/L_\odot \leq 4.09$. Generally speaking, the higher the effective temperature the higher the luminosity needed to be to trigger the instability. It should be noted that it remains to be seen whether the HRI really occurs in stars. Additionally, since the HRI can be avoided with a relatively modest increase in the

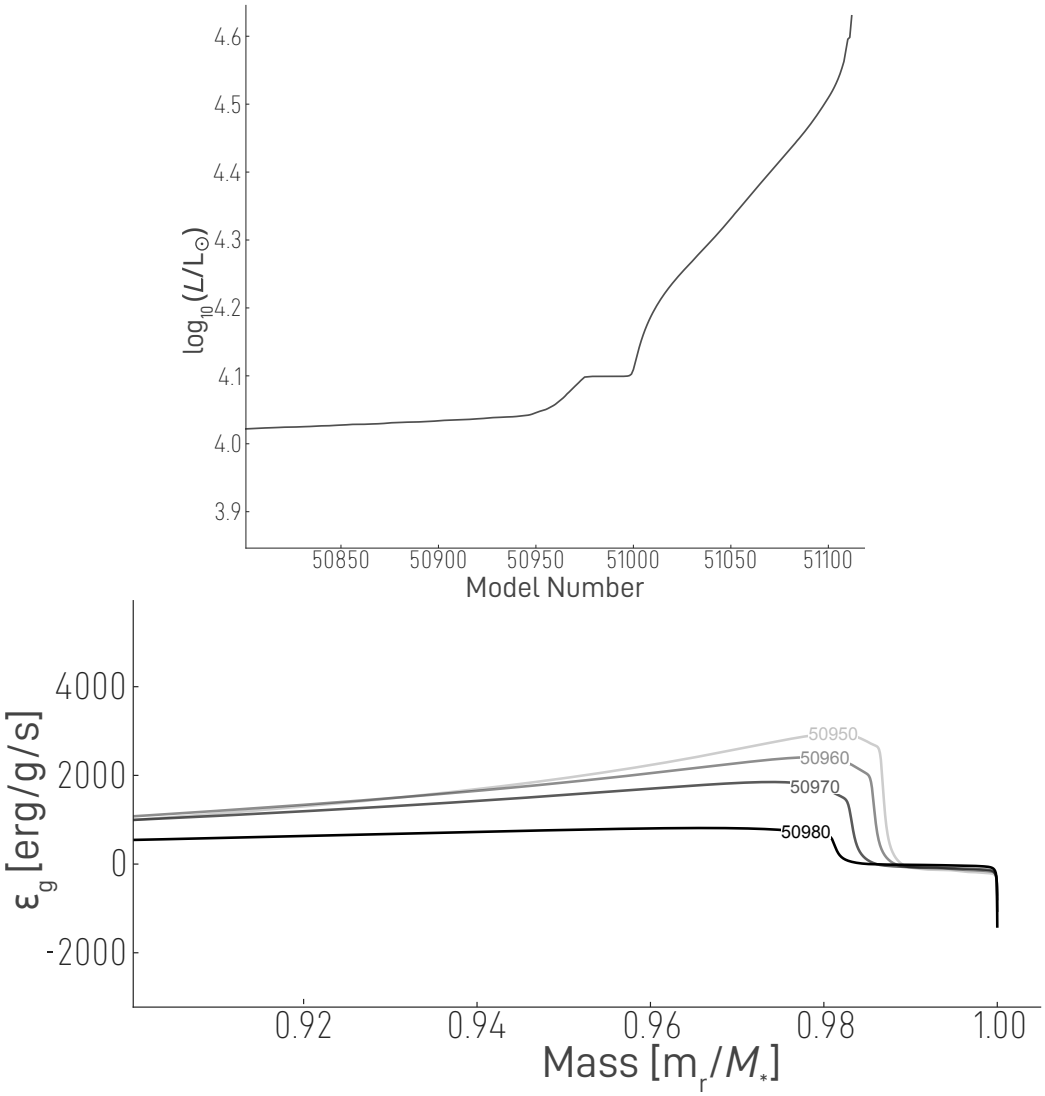

Figure 6.3 $\log_{10} L_*/\mathrm{L}_\odot$ versus model number (top). The physical time plotted here is approximately 40 yr. ϵ_g in the outermost region of the star at 4 different time steps (bottom). Each line is labeled with its corresponding model number.

mixing length parameter, the occurrence of the HRI may simply be an indication that the mixing length parameter is too small.

Moving on to the other quantities. The trend of N_{TP} and N_{TDU} follows what would be expected a priori. Namely, higher values of `fCE` lead to fewer total TPs because the TDU efficiency is higher, and thus the C/O ratio increases faster and the mass loss is correspondingly stronger earlier. This is also reflected in the AGB lifetimes. It is interesting that regardless of `fCE` the TDU does not happen for the first few TPs. The exception to this are the tracks run with FreeEoS which have TDUs from the second pulse onward. The FreeEoS tracks also have the longest interpulse phases and shortest AGB lifetimes. These characteristics can

be explained by the fact that the FreeEoS tracks have more violent flashes than the OPAL EoS tracks. The maximum He luminosity in the flash is on average more than 0.3 dex higher in the FreeEoS tracks. This will lead preferentially to more efficient TDUs and longer interpulse times. The more efficient TDUs, along with the TDUs starting at an earlier pulse, will cause the track to lose mass faster and reduce its AGB lifetime. In general, the interpulse duration varies significantly between tracks with different physics. Within a track there is a tendency for the interpulse period to first increase and eventually decrease again, though some tracks end due to the HRI before the decrease begins. This trend of the interpulse duration first increasing and then decreasing is seen in models from other studies as well (Karakas & Lattanzio 2007, Cristallo et al. 2009b).

The track with one of the longest lifetimes is EddR P016 C064 VW. The mass loss of this track is much less than our standard mass loss treatment and as such this track undergoes three more TPs and two more TDUs and has a longer AGB lifetime than EddR P016 C064. It also ends with an envelope which is 0.6 $M_\odot$ more massive. The main differences between my standard mass loss descriptions and the VW mass loss is that the mass loss rates in my models explicity depend on the effective temperature and are derived specifically for O- and C-rich AGB stars. This is an important result because many other studies use the VW mass loss. Thus, the mass loss rate for my models is significantly larger than that of many other studies. The outer BC also has some impact on the AGB lifetime. If we compare the final envelope mass and number of TPs of the EddR and LucyP models one will notice that the LucyP models have perhaps 1 additional pulse while having similar or higher final envelope masses. This is surprising since the reduced effective temperature of the LucyP models should lead to higher mass loss rates. A closer look reveals that this is the case, but it is complicated by other factors. For example, the P016 C064 tracks show that the EddR model has an extra TDU, hence a higher C/O. This also increases mass loss and, in this case, causes the EddR track to lose more mass than the LucyP model. For the P008 C064 models, the TDU efficiency of the LucyP track is lower than for the EddR track and, thus, the EddR track has a higher C/O. Despite this, the final envelope mass of the two tracks is comparable. Therefore, if these tracks were able to be run to the end of the AGB, one would likely see that the LucyP tracks end the AGB with fewer TDUs and fewer pockets. The final C/O ratio largely follows the expected trends. Namely, that lower values of `fPDCZ` and higher values of `fCE` will lead to higher C/O ratio values. Additionally, the use of the LucyP outer boundary conditions also results in a lower final surface C/O value for some models. This is due to the LucyP model having one less TDU than the EddR model as discussed above.

This leaves the quantities associated with the ^{13}C pocket to be discussed. First, it may be useful to discuss what values one might expect for these quantities. The ^{13}C pocket is expected to have neutron densities up to $N_n \leq 1 \times 10^7$ cm^{-3}. In order to match observations of [hs/ls], the neutron exposure should be in the

range of $\tau_{\text{pocket}} \approx 0.2\,\text{mb}^{-1}$–$0.5\,\text{mb}^{-1}$ with $M_{\text{pocket}} \geq 7 \times 10^{-5}\,\text{M}_{\odot}$ (Herwig et al. 2003). As one can see in Table 6.1, $\overline{M_{\text{pocket}}}$ and $\overline{\tau_{\text{pocket}}}$ vary significantly between the models. The tracks with the lowest $\overline{\tau_{\text{pocket}}}$ are those with the highest `fCE` (and those with atomic diffusion which will be discussed later). This is because these models mix too many protons into the intershell region and thereby produce ^{14}N which acts as a neutron poison. On the other hand, this large amount of mixing causes these models to have among the highest values for $\overline{M_{\text{pocket}}}$. Thus, there is a competition between these two effects which must be kept in mind when modeling AGB stars. It should also be noted that the size of the ^{13}C pocket in these models also decreases over the pocket's lifetime as ^{13}C is processed into ^{14}N. Other than the two models with the highest `fCE`, the rest have neutron exposures which are in or very near the required range. There appears to be a negative correlation between the amount of overshoot from the PDCZ and the neutron exposure. This is likely due to this overshoot being positively correlated with TDU efficiency and more protons being mixed into the intershell leading to lower effective ^{13}C in the pocket. In theory overshoot from the base of the PDCZ could actually increase the neutron exposure as it raises the amount of ^{12}C in the intershell which can later become the ^{13}C needed for the neutron-source reaction (Lugaro et al. 2003). These results show, however, that the impact this has on the TDU efficiency erases any potential benefit from the increased amount of intershell ^{12}C.

The values for M_{pocket} are unfortunately all much smaller than the value needed to match observations. As discussed in Section 3.2, this is a common problem among codes using a diffusive mixing scheme. Nevertheless, it is still useful to look at how M_{pocket} changes across the tracks. First, as expected, the size of the pocket increases with increasing `fCE`. `fPDCZ`, on the other hand, seems to have a negligible affect on the size of the pocket. The implication of this is interesting. This suggests that TDU efficiency has no impact on the size of the ^{13}C pocket and that the only thing which matters is the CBM of the protons. The EoS also has no impact on the pocket size. In addition, neither the mass loss prescription nor the outer BC show signs of influencing the size of the pocket. One could have expected the outer BC to play a role since the properties of envelope are more sensitive to the outer BCs when the envelope is convective (Kippenhahn et al. 2013, Ch. 11.3.3). Other than `fCE`, the factor which has the largest impact on the size of the pocket is atomic diffusion which can increase the pocket size by a factor of 2–3. These pockets are however short-lived and do not produce significant neutron exposures. This point will be discussed in more detail in Section 6.4.1.

6.3 The Nucleosynthesis

One of the primary points of interest for AGB stars is their nucleosynthesis and yields to which we now turn our attention. Unfortunately, as seen in the previous

section, the ^{13}C-pocket sizes are far from what is predicted to be necessary to reproduce observations and are so small that one would expect little surface abundance enhancements. Nevertheless, a select number of tracks have been post-processed and analyzed. Furthermore, we will look at the light element nucleosynthesis for all tracks.

The models which have been post-processed have [hs/ls] between −0.01 for EddR P016 C064 and 0.14 for EddR P008 C064 irwin. This puts these models beyond or at the highest end of what is allowed observationally for solar metallicity stars. Recall that $-0.5 \leq [\text{hs/ls}] < 0.0$ at solar metallicity. The reason for this is discussed in Busso et al. (2001), where they find that [hs/ls] tends to zero at solar metallicity and as the pocket size decreases (see their Fig. 4). This is primarily the result of the limited surface enhancements of the *s*-process elements causing [hs/Fe] and [ls/Fe] to be nearly 0.0. Indeed when looking at [hs/Fe] and [ls/Fe] for the models they range from 0.02–0.16 and 0.004–0.04, respectively. Figure 6.4 shows the final surface abundance of the EddR P008 C064 model and clearly demonstrates the small surface abundance enhancements of the models.

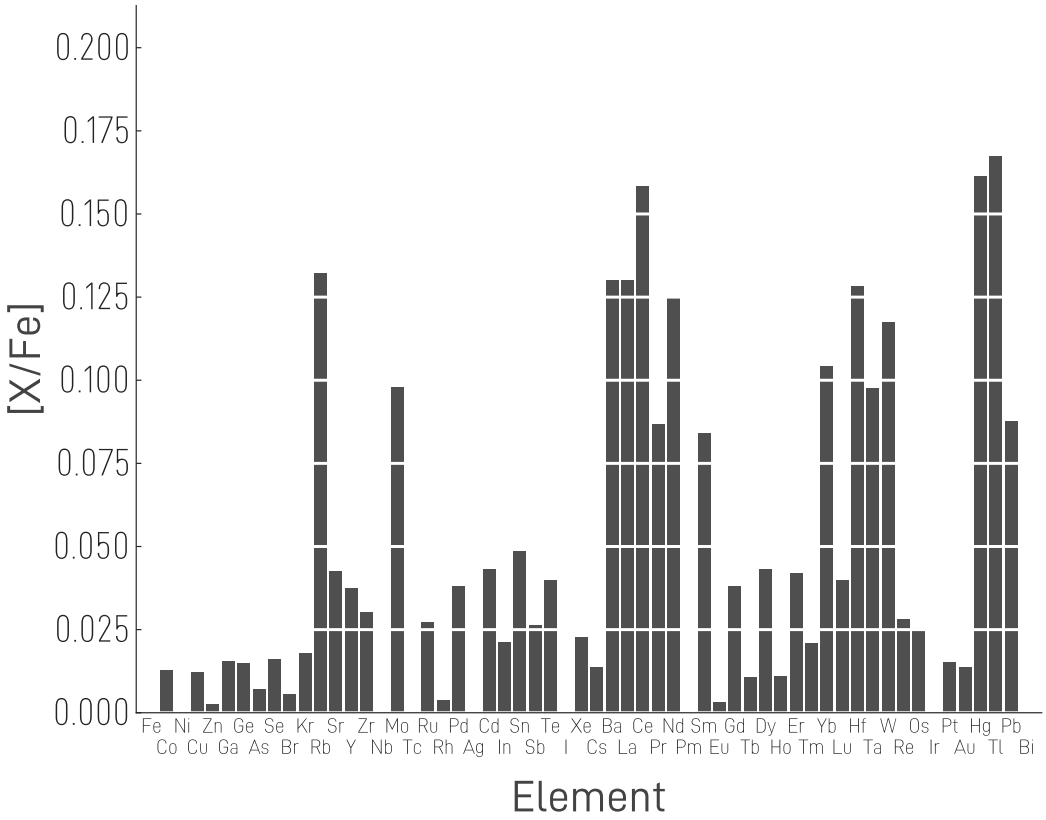

Figure 6.4 The final surface abundances ([X/Fe]) of the EddR P008 C064 track.

Figure 6.4 also shows that the model has a high Rb abundance relative to the other first-peak elements. A high Rb abundance relative to Sr, Y, or Zr usually implies high neutron densities (Käppeler et al. 2011). In the case of my models

it means that the ^{22}Ne neutron source is marginally active in the TP. This, along with the positive [hs/ls] from the small ^{13}C pockets, means that the abundance pattern for the first-peak elements is dominated by the convective *s*-process. The Mo abundance is also explained in this way. Indeed neutron densities in the final 4 pulses for this model exceed 1×10^9 cm^{-3} as a result of the partial activation of the ^{22}Ne neutron-source reaction.

The yields for isotopes that are included in `GARSTEC` (see Section 4.1.4) are calculated from the output of `GARSTEC`. The yields for heavier isotopes come from the output of `ANT`. Table 6.2 shows the mass yields of select light isotopes ($Z < 26$) for every track. Appendix C.2 contains similar tables with the net yields and overproduction factors. Table 6.3 shows the mass yields of select heavy ($Z \geq 26$) isotopes for every post-processed track. The first row in Table 6.2 also shows the light yields of EddR Poo8 Co16 as calculated from the output of `ANT`. The results are in very good agreement with the largest deviations occurring for ^{19}F and ^{22}Ne, where the yields in `GARSTEC` are larger by a factor of 1.86 (0.27 dex) and 3.68 (0.58 dex), respectively. This is likely explained by the usage of different reaction rates and different sized network between the codes.

Table 6.2 Mass yields for select light isotopes for all *s*-process tracks. All yields have units of solar mass. For comparison, the first row shows the mass yield for EddR Poo8 Co16 as calculated from `ANT`.

Label	^{7}Li	^{12}C	^{13}C	^{14}N	^{16}O	^{17}O	^{19}F	^{22}Ne	^{23}Na	^{24}Mg	^{26}Mg	^{27}Al
EddR P008 C016[a]	3.21E-10	2.26E-2	2.03E-4	6.48E-3	2.12E-2	4.29E-5	8.24E-7	3.80E-4	1.45E-4	1.20E-3	1.81E-4	1.41E-4
EddR P008 C016	2.54E-10	2.16E-2	2.05E-4	6.51E-3	2.09E-2	4.42E-5	1.53E-6	1.40E-3	1.52E-4	1.21E-3	1.96E-4	1.44E-4
EddR P008 C016 Diff	2.55E-10	2.18E-2	2.05E-4	6.53E-3	2.08E-2	4.43E-5	1.47E-6	1.30E-3	1.53E-4	1.21E-3	1.95E-4	1.42E-4
LucyP P008 C016	2.54E-10	2.14E-2	2.05E-4	6.52E-3	2.08E-2	4.43E-5	1.54E-6	1.38E-3	1.54E-4	1.21E-3	1.96E-4	1.44E-4
EddR P008 C064	2.35E-10	2.78E-2	2.06E-4	6.60E-3	2.15E-2	4.30E-5	2.13E-6	1.86E-3	1.60E-4	1.23E-3	1.96E-4	1.45E-4
EddR P008 C064 FEoS	2.23E-10	2.75E-2	2.10E-4	6.75E-3	2.32E-2	4.82E-5	2.00E-6	1.83E-3	1.65E-4	1.25E-3	1.99E-4	1.47E-4
EddR P008 C064 Diff	2.35E-10	2.44E-2	2.08E-4	6.61E-3	2.12E-2	4.48E-5	1.78E-6	1.61E-3	1.57E-4	1.23E-3	1.95E-4	1.44E-4
LucyP P008 C064 Diff	2.34E-10	2.44E-2	2.07E-4	6.58E-3	2.18E-2	4.47E-5	1.65E-6	1.50E-3	1.56E-4	1.22E-3	1.94E-4	1.43E-4
LucyP P008 C064	2.36E-10	2.45E-2	2.08E-4	6.61E-3	2.17E-2	4.49E-5	1.70E-6	1.51E-3	1.57E-4	1.23E-3	1.95E-4	1.44E-4
EddR P008 C128	2.36E-10	2.67E-2	2.07E-4	6.62E-3	2.16E-2	4.49E-5	1.95E-6	1.77E-3	1.59E-4	1.23E-3	1.97E-4	1.46E-4
EddR P016 C016	2.53E-10	2.43E-2	2.06E-4	6.56E-3	2.51E-2	4.45E-5	1.41E-6	1.47E-3	1.56E-4	1.22E-3	2.05E-4	1.43E-4
EddR P016 C016 FEoS	2.31E-10	2.50E-2	2.10E-4	6.70E-3	2.31E-2	4.78E-5	1.57E-6	1.53E-3	1.60E-4	1.24E-3	2.02E-4	1.46E-4
EddR P016 C064	2.35E-10	3.27E-2	2.07E-4	6.63E-3	2.52E-2	4.31E-5	1.89E-6	2.00E-3	1.63E-4	1.23E-3	2.06E-4	1.46E-4
EddR P016 C064 FEoS	3.11E-10	2.76E-2	2.11E-4	6.79E-3	2.32E-2	4.84E-5	1.82E-6	1.66E-3	1.64E-4	1.26E-3	2.01E-4	1.48E-4
EddR P016 C064 Diff	2.34E-10	3.07E-2	2.06E-4	6.60E-3	2.74E-2	4.48E-5	1.65E-6	1.81E-3	1.61E-4	1.23E-3	2.12E-4	1.46E-4
EddR P016 C064 VW	2.38E-10	4.00E-2	2.05E-4	6.43E-3	2.84E-2	4.28E-5	3.29E-6	3.30E-3	1.80E-4	1.24E-3	2.21E-4	1.50E-4
LucyP P016 C064	2.34E-10	2.70E-2	2.09E-4	6.65E-3	2.56E-2	4.51E-5	1.44E-6	1.56E-3	1.58E-4	1.23E-3	2.03E-4	1.45E-4
EddR P016 C128	2.32E-10	2.93E-2	2.07E-4	6.66E-3	2.56E-2	4.52E-5	1.64E-6	1.74E-3	1.61E-4	1.24E-3	2.01E-4	1.45E-4

a Yields calculated from `ANT` instead of `GARSTEC`

Table 6.3 Mass yields for select heavy isotopes for all post-processed *s*-process tracks. All yields have units of solar mass.

Label	^{70}Zn	^{70}Ge	^{80}Kr	^{88}Sr	^{89}Y	^{136}Ba	^{138}Ba	^{139}La	^{208}Pb
EddR P008 C016	3.03E-08	9.53E-08	4.65E-09	9.61E-08	2.33E-08	2.85E-09	2.65E-08	3.65E-09	2.17E-08
LucyP P008 C016	3.03E-08	9.54E-08	4.68E-09	1.00E-07	2.42E-08	3.17E-09	2.99E-08	4.07E-09	2.27E-08
EddR P008 C064	3.06E-08	9.99E-08	5.06E-09	1.04E-07	2.51E-08	3.46E-09	3.39E-08	4.57E-09	2.39E-08
EddR P008 C064 FEoS	3.10E-08	9.98E-08	4.97E-09	1.02E-07	2.48E-08	3.70E-09	4.09E-08	5.24E-09	2.43E-08
LucyP P008 C064	3.06E-08	9.91E-08	4.99E-09	1.04E-07	2.49E-08	3.51E-09	3.39E-08	4.54E-09	2.50E-08
EddR P016 C064	3.08E-08	9.99E-08	5.13E-09	1.06E-07	2.52E-08	2.91E-09	2.66E-08	3.68E-09	2.22E-08

6.4 Discussion

6.4.1 Diffusion

As was already discussed, atomic diffusion is capable of increasing the size of the ^{13}C pocket by a factor of 2–3. The idea of atomic diffusion impacting the *s*-process in AGB stars is not new. Prialnik et al. (1981) ran an AGB model of a 6 $M_\odot$ star with atomic diffusion and found that the TPs have been completely suppressed. They explain this by arguing that atomic diffusion takes the normally very sharp composition border of the burning shells and spreads it out. This effectively widens the shell so the thin-shell instability never occurs.

Iben (1982) addresses this result and claims it cannot be correct. He argues that the timescale over which atomic diffusion can distort the H profile during H burning at least two orders of magnitude larger than the timescale for H shell to move a distance equal to its width as a consequence of H burning. He does acknowledge that H diffusion could play a role in spreading the H profile below the CE during the post-flash phase when the envelope is moving inward in mass coordinate.

In response to this rebuttal of their paper, the original others of Prialnik et al. (1981) wrote a second paper, Kovetz et al. (1984). They begin by admitting that their first paper had some issues: pressure and thermal diffusion were ignored and the effect of atomic diffusion was amplified by a poor zoning technique. They find that having fixed these issues atomic diffusion does not inhibit the shell instability. Furthermore, they find that pressure and thermal diffusion are always opposite in sign to concentration diffusion during the post-flash dip with the pressure diffusion being the larger of the two opposers. They conclude that atomic diffusion cannot play an important role in the at-the-time accepted picture of the *s*-process. After this paper, there is little mention of atomic diffusion in AGB stars. Busso et al. (1992) claim that the mass affected through purely diffusive processes cannot exceed $1 \times 10^{-4}\,M_\odot$ which is lower than for the overshoot and semiconvection models of Hollowell & Iben (1988) (see discussion in Section 3.1), so they do not consider it important.

The idea of atomic diffusion is worth looking into again now, as much has changed in our understanding of the *s*-process in AGB stars since these papers. For one, these papers were all assuming the old *s*-process scenario where a carbon layer is formed below the CE and has to survive long enough to be engulfed by the ensuing PDCZ where the *s*-process actually happens. Kovetz et al. (1984) found that atomic diffusion helps create this carbon layer, but that the layer would not survive until the PDCZ engulfs it. This is of course sufficient in the current understanding of the *s*-process. Moreover, it is now thought that semiconvection is not important and that overshoot alone is only capable of large enough pockets when adopting rather extreme overshoot parameters. Finally, atomic diffusion is

often neglected in stellar models due to the long times necessary for it to change chemical gradients over a large distance. However, the ^{13}C pocket is on the order of 100 km wide meaning that atomic diffusion needs only be fast enough to affect composition gradients over rather small distances to have an impact on the pocket.

Unfortunately, the results presented here show that while diffusion does lead to larger pockets, it also leads to those pockets being smoothed out and producing insignificant neutron exposures. This is because the ^{14}N settles faster than the lighter ^{13}C and so the ^{14}N pocket slowly encroaches on the ^{13}C pocket during the pocket's lifetime, effectively choking off the *s*-process. This is a very similar behavior as was seen in Langer et al. (1999) and Herwig & Langer (2001) with the effect of rotational mixing on the ^{13}C pocket. As with rotational mixing, atomic diffusion is a mixing process which acts throughout the life of the pocket as opposed to overshoot which only affects the formation and has no further impact as the CE recedes to higher mass coordinates. It should also be noted that since atomic diffusion is a very slow process any other physical process acting in the opposite direction, for example radiative levitation which is not included in our simulations, could negate the effect of atomic diffusion.

6.4.2 Comparison to Other Studies

Unfortunately, the HRI renders comparisons to other studies difficult since other studies do not report seeing the HRI in their models. This means the models from other studies have far more pulses, pockets, and TDUs. Nevertheless, a comparison will be attempted. I will start with Weiss & Ferguson (2009) as they also used `GARSTEC` and much of the same physics as used here.

The models of Weiss & Ferguson (2009) use the same C/O opacities, the same mass loss prescription, the FreeEoS, and an overshoot of 0.016 at every convective boundary. Thus, their 3 $M_\odot$ model is most comparable to EddR P016 C016 FEoS. Their model begins the AGB with a core mass of 0.596 $M_\odot$, only 0.008 $M_\odot$ larger than my model. The model goes on to have 12 TPs and 11 TDUs ending the AGB after 693 kyr with a core mass of 0.617 $M_\odot$ and a C/O ratio of 1.407. EddR P016 C016 FEoS, on the other hand, experiences 9 TPs and 8 TDUs but has a similar AGB lifetime at 642 kyr. The final C/O ratio for this model is 1.49, which, together with the fewer TDUs, implies a higher TDU efficiency. The growth of the core mass for the two models is 0.021 and 0.013 for their model and mine, respectively. Furthermore, they do not find the HRI in their models. However, convergence issues due to the Fe peak opacity do occur for their models at a total mass which is similar to my models but much higher than the models of Cristallo et al. (2011) and Pignatari et al. (2016), for example. The differences between my models and theirs would be explained by a higher energy release during the pulse in the current models. This would lead to more violent pulses, more efficient TDUs, and less core growth. This could be due to the old

network not including all of the isotopes that the extended network does, thus underestimating the energy generation.

The NuGrid model (Pignatari et al. 2016, P16) closest in mass and metallicity to one of my models is the 3 $M_\odot$, $Z = 0.02$ model. This model begins the AGB with a core mass of 0.596 $M_\odot$, in good agreement with my models, and undergoes a total of 23 TPs and 20 TDUs, far more than any model in this study due to the HRI and the use of the VW wind description in P16. The AGB lifetime for this model is correspondingly higher at 1270 kyr. However, the final C/O ratio is around 1.6 which is in agreement with most of the models in Table 6.1. The average interpulse duration for their models is 57.7 kyr which is smaller than any of the models here. This is the result of the decreasing interpulse duration of the later pulses. The pocket sizes in their models tend to be between 2×10^{-5} $M_\odot$–3×10^{-5} $M_\odot$ which is also larger than any of the pockets in this study. This is due to their approach of increasing the overshoot from the CE during the TDU from 0.016 to 0.128. This was done specifically to yield larger pocket sizes. Nevertheless, their models have lower TDU efficiencies for the initial pulses until the TDU efficiency peaks and both codes agree on the efficiency again. This is strange since my tracks with $\texttt{fCE} = 0.128$ have much higher TDU efficiencies. Perhaps P16 only increased the overshoot parameter at the deepest extent of the TDU and not for the entirety of the TDU. Unfortunately, no further details are given in the paper. That being said, it is known that different codes have very different predictions for TDU efficiencies (Marigo et al. 2013).

Next, a comparison to the 3 $M_\odot$, $Z = 0.02$ model of Karakas & Lattanzio (2007) (K07) will be done. This model begins the AGB with a core mass of 0.576 $M_\odot$. The small core mass is due to the lack of consideration of overshoot in these models. The model ends the AGB after 25 TPs and 16 TDUs with a core mass 0.680 $M_\odot$. This is a rather large increase in the core mass which is aided in part by the lack of overshoot. It is known that overshoot at the bottom of the PDCZ leads to lower core growth along the AGB (Weiss & Ferguson 2009). Despite the lack of overshoot, the TDU efficiency of their model is very similar to that of EddR P008 C016. No overshoot is also the reason why the TDUs only begin after 9 TPs in the K09 model. Without overshoot the minimum core mass necessary for TDU increases, and since these models have small core masses to begin with it takes a number of TPs for the core to reach sufficient size for TDUs. The model becomes C rich after 18 TPs and 9 TDUs, only 2 more TDUs than is necessary for EddR P008 C016 to be C rich. Furthermore, the final C/O abundances are very similar with 1.43 and 1.48 for K07 and EddR P008 C016, respectively. The ^{13}C pocket related quantities cannot be compared for these models as K07 do not resolve the pocket. One additional interesting point on this study is the convergence issue they encounter. They find that their models fail to converge while they still have very massive envelopes. The Fe peak instability is determined not to be the cause. Given that their 3 $M_\odot$ model ends with a very similar final mass to mine and that

the Fe peak instability is not responsible, it is quite possible that their models also experienced the HRI. In Karakas (2010) (K10) they update the models from K07. The primary difference between the studies is the inclusion of an artificial pocket. This can have some impact on the light element nucleosynthesis, as we will see in Figure 6.5. Additionally, the convergence issues of K07 seem to have been overcome.

Finally, the 3 $M_\odot$, $Z = 0.02$ model of Cristallo et al. (2011) (C11) will be analyzed. This model again has no overshoot prior to the AGB and so the initial core mass, 0.550 $M_\odot$, is lower than my models. Once on the AGB, overshoot is applied to all boundaries, though their implementation of overshoot naturally leads to no overshoot at the base of the PDCZ as already explained (see Section 3.2). The small core mass again leads to much longer average interpulse times (130.588 kyr), but because overshoot is used, the model begins dredging up material after only 3 TPs as opposed to 9 in K07. The model has 17 TPs and 14 TDUs and ends with a core mass of 0.635 $M_\odot$ and C/O = 1.59. The TDU efficiency is rather low in this model only peaking at 0.607. Thus, it takes 10 TDUs before the model becomes a carbon star. This model most closely matches EddR P016 C016 albeit with lower TDU efficiencies due to the lack of overshoot at the base of the PDCZ. As already discussed the advective mixing formalism used in C11 study leads to much larger pocket sizes than with diffusive mixing.

Turning to the nucleosynthesis, in Figure 6.5 one can see a comparison of my light-isotope yields to those of K07, K10, C11, and P16. The plots are split into two since different studies provide their yields in the form of different quantities. As one can see, there is overall good agreement between my models and those of the other studies. There are however some exceptions, the most notable of which is ^{16}O. For P16 the agreement is quite good, but for K07, K10, and C11 the result disagrees more than it does for any other isotope. The explanation for this is simple. This is the result of using (or not using as is the case for K07, K10, and C11) overshoot at the base of the PDCZ. My models and those of P16 both have overshoot and the ^{16}O yields agree. ^{14}N is another isotope where my model's yields are similar to some studies' yields (K10, C11, and P16) but not all (K07). Given that my yields are close to three of the four studies, I do not consider this a problem. Finally, ^{19}F and ^{24}Mg also show strong deviations from other studies. ^{24}Mg is produced in small quantities via neutron captures in ^{13}C pockets and marginally destroyed in TPs (Cristallo et al. 2011). Given that my models agree quite well with P16 and disagree significantly with K07, K10, and C11, the most likely explanation is again overshoot at the base of the PDCZ. This overshoot will lead to more violent TPs with higher temperatures in the PDCZ and, consequently, to more destruction of ^{24}Mg. For ^{19}F, the primary factors impacting its abundance are the temperature in the PDCZ and the TDU (Lugaro et al. 2004). The temperatures in the PDCZ of my models fall within the range of 220 MK–260 MK which is required for ^{19}F synthesis. Thus, the underproduction

of ^{19}F in my models is likely due to the fewer TPs and TDUs which my models experience.

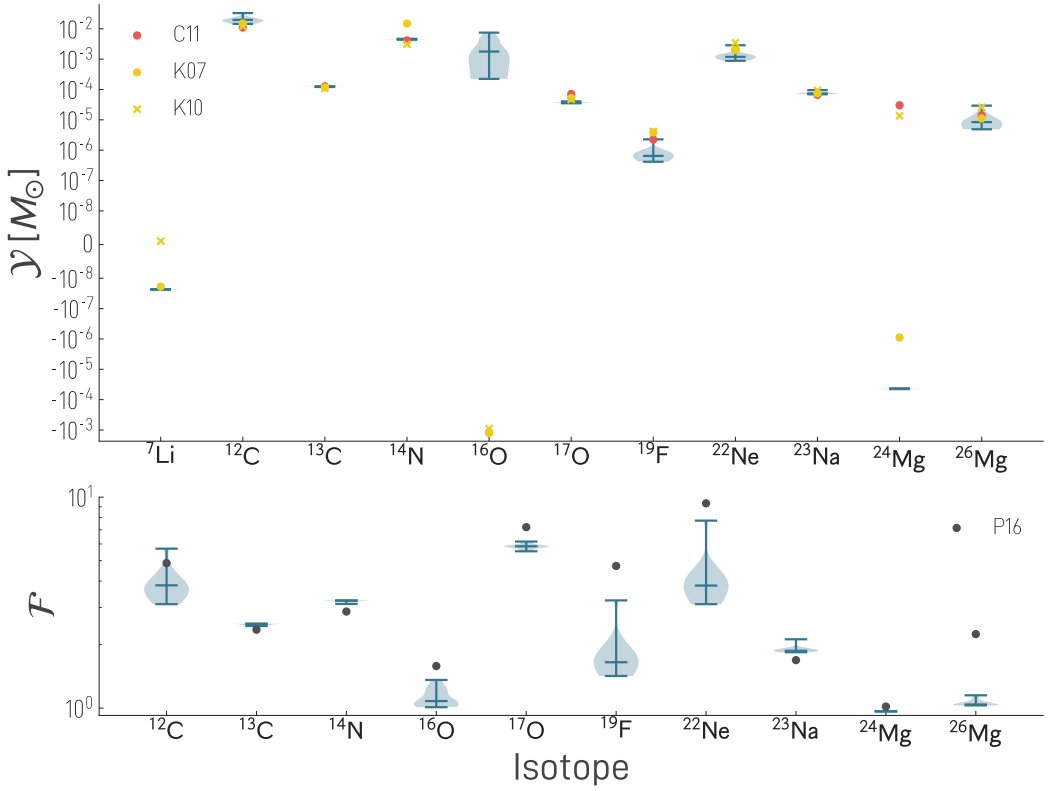

Figure 6.5 Comparison of light-isotope yields across studies. The yields of all tracks in this work are shown in the blue distributions. The yields of Karakas & Lattanzio (2007) and Karakas (2010) are shown as yellow circles and x's, respectively. The yields of Cristallo et al. (2011) are in red, and the yields of Pignatari et al. (2016) are in black.

Figure 6.6 shows the same type of plot as Figure 6.5 for select heavy isotopes. The yields of K07 and K10 have been omitted here as they are not provided in K07 and only provided for elements and not for isotopes in K10. As expected, due to the small ^{13}C pockets and fewer TDUs of my models, the yields are very small in comparison to other studies. Nevertheless, it is encouraging that, in particular for C11, the yields of my models follow the same pattern. For the overproduction factors there is enough uncertainty in the models that it is hard to say if the pattern matches that of P16, but the mean values seem to agree with the pattern except for ^{80}Kr.

6.4.3 Comparison to Observations

There are a number of observations which can serve as useful benchmarks for these models. First, we will look at the initial-final mass relationship (IFMR), which provides a useful constraint on the final core masses of our AGB models. When

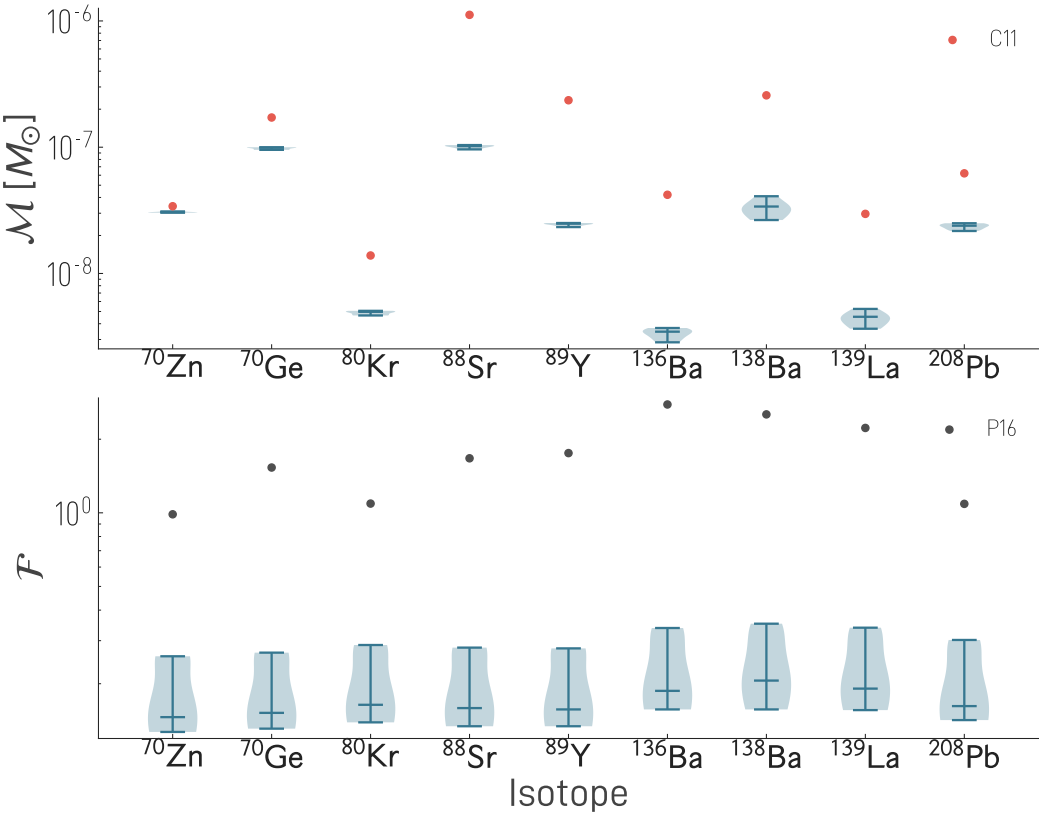

Figure 6.6 Comparison of heavy-isotope yields across studies. The yields of all tracks in this work are shown in the blue distributions. The C11 yields are in red, and the yields of P16 are in black.

developing the relationship between initial and final stellar masses, one typically focuses on isolated white dwarfs found within stellar clusters. These white dwarfs should have evolved from single stars rather than binary systems. Observers analyze the spectra of these stars to determine key properties of their atmospheres, including the surface gravity and effective temperature. By combining these measurements with theoretical white-dwarf cooling models the white dwarf's mass, how long it has been cooling, and other characteristics can be derived. The progenitor star's initial mass can then be determined by taking the cluster's age and subtracting the time the white dwarf has spent cooling and comparing this age to stellar models of different masses. Interesting recent work in this field includes El-Badry et al. (2018), Cummings et al. (2018), Marigo et al. (2020, 2021). It should be clear that this relationship is only semi-empirical and relies on various modeling assumptions.

In Cummings et al. (2018) analytical formulae for the final mass are given which, for a star with an initial mass of 3 $M_\odot$, can be written as

$$\frac{M_{\text{final}}}{M_\odot} = (0.187 \pm 0.061)\frac{M_{\text{initial}}}{M_\odot} + (0.194 \pm 0.199). \tag{6.2}$$

If one assumes Gaussian errors and uses a Monte Carlo method to propagate the errors on the coefficients through to the final mass then one finds that, for $M_{\text{initial}} = 3\,\text{M}_\odot$, $M_{\text{final}} = 0.746 \pm 0.269\,\text{M}_\odot$. In El-Badry et al. (2018), a different IFMR is given based on a piecewise linear fit. For a $3\,\text{M}_\odot$ model the data points on either side to be fit through are $(M_{\text{initial}}, M_{\text{final}}) = (2.75^{+0.36}_{-0.31}\,\text{M}_\odot, 0.67 \pm 0.02\,\text{M}_\odot)$ and $(3.54^{+0.55}_{-0.43}\,\text{M}_\odot, 0.81 \pm 0.03\,\text{M}_\odot)$. One can then again use a Monte Carlo approach to sample the data points to fit through, perform a linear fit on the data, and then determine what the final mass would be based on the fit and an initial mass of $3\,\text{M}_\odot$. Doing this, one finds that $M_{\text{final}} = 0.727 \pm 0.176\,\text{M}_\odot$. The results of the Monte Carlo experiment can be seen in Figure 6.7 along with the data from this work.

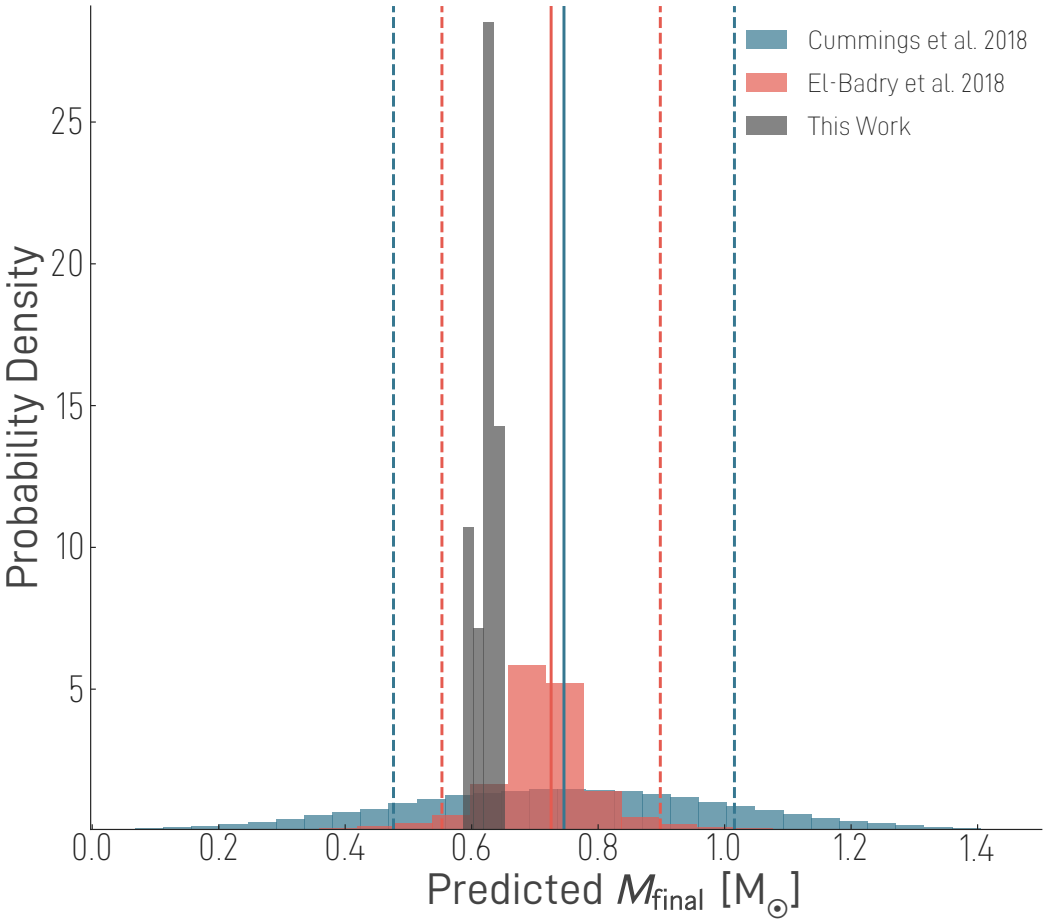

Figure 6.7 The semi-empirical IFMRs of Cummings et al. (2018) (blue) and El-Badry et al. (2018) (red). Solid lines indicate mean values while dashed lines indicate the 68% confidence interval. The data for the models presented in this work are in black. The height of the various distributions relative to one another has no practical meaning.

Comparing these IFMRs to the final core masses of my models one can see that the models systematically under predict the final core mass — all models are below the means of the two IFMRs. This is a known problem for models in this mass range

(see Pastorelli et al. 2019, Wagstaff et al. 2020). The disagreement increases for higher `fCE` and to a lesser extent higher `fPDCZ`. However, the uncertainty on the IFMR is still quite large and the model data is fully within the 68% confidence intervals of both IFMRs.

One can also look at the luminosity of the model at the first TDU. Based on observations of 23 S stars (star which have experienced at least one TDU), Shetye et al. (2021) found that, for a $M_{\rm initial} = 3\,\mathrm{M}_\odot$ star at solar metallicity, the lowest observed luminosity was between $3.66 \leq \log_{10}(L_*/\mathrm{L}_\odot) \leq 3.68$. Comparison of this to models is not without complication. The luminosity of the model over one TP cycle can vary over 0.4 dex. Additionally, since the sample size is quite low, it is quite likely that the true minimum luminosity is actually smaller than what is given above. For EddR Poo8 Co16, for example, the minimum luminosity post-TDU is $\log_{10}(L_*/\mathrm{L}_\odot) = 3.55$ which would be in tension with the observations, but during the subsequent interpulse phase the luminosity is $\log_{10}(L_*/\mathrm{L}_\odot) = 3.8$, which is in agreement with the observations. For this model the time between the first TDU and the second which the star spends at a luminosity below the limit of $\log_{10}(L_*/\mathrm{L}_\odot) = 3.68$ is 8760 yr, which is just over 10% of the total time between TDUs. Regardless of physics chosen, all models have similar values for minimum and interpulse luminosity after the first TDU. This either means that the lowest luminosity star in Shetye et al. (2021) is not at the true minimum luminosity, which is plausible given the small sample size and the short duration of the power down phase where this true minimum would occur, or that the models are under-luminous during the TDU. This would imply that the models are in general under-luminous. The luminosity of a star on the AGB in the interpulse follows a core mass-luminosity relationship (see Boothroyd & Sackmann (1988a) for a review of results from various authors). In Boothroyd & Sackmann (1988a), this relationship is given as

$$L_*/\mathrm{L}_\odot = \begin{cases} 38\,000\left(\frac{M_{\rm core}}{\mathrm{M}_\odot} - 0.447\right), & \text{if } 0.52\,\mathrm{M}_\odot < M_{\rm core} < 0.6\,\mathrm{M}_\odot \\ 50\,000\left(\frac{M_{\rm core}}{\mathrm{M}_\odot} - 0.484\right), & \text{if } 0.60\,\mathrm{M}_\odot < M_{\rm core} < 0.72\,\mathrm{M}_\odot \end{cases} \tag{6.3}$$

If one assumes that the difference between the minimum luminosity and the interpulse luminosity for real stars is the same as seen in EddR Poo8 Co16 and, additionally, require that the model is never allowed to drop below the observed minimum luminosity, then this would imply an interpulse luminosity of $\log_{10}(L_*/\mathrm{L}_\odot) = 3.93$. Using Equation (6.3) and a luminosity of $\log_{10}(L_*/\mathrm{L}_\odot) = 3.93$, one finds that this star would be expected to have a core mass of $0.654\,\mathrm{M}_\odot$ This is higher than even the final core mass of my EddR Poo8 Co16 model. This high core mass could potentially be achieved if the core overshoot value were increased in the pre-AGB evolution. The higher core mass would also be in better agreement with the IFMR. Ultimately, a much larger sample of stars is needed in order to determine how

robust this lower luminosity limit truly is.

The final comparison done was to the observations of PG1159 stars. PG1159 is a spectral classification for post-AGB stars at the center of planetary nebulae. The surface of PG1159 stars used to be at the mass coordinate of the top of the intershell region of the former AGB star. Thus, the surface abundances of PG1159 stars provide constraints on the intershell abundances of AGB stellar models. For example, it is well established that the observed O abundance of PG1159 stars cannot be explained without some form of CBM at the base of the PDCZ (Werner & Herwig 2006, Wagstaff & Weiss 2018). In Figure 6.8, one can see the comparison of the final intershell abundances of all the tracks to the observed PG1159 data from Werner & Herwig (2006), Löbling et al. (2019), and Werner et al. (2024). The O/He data is well matched by the tracks, though

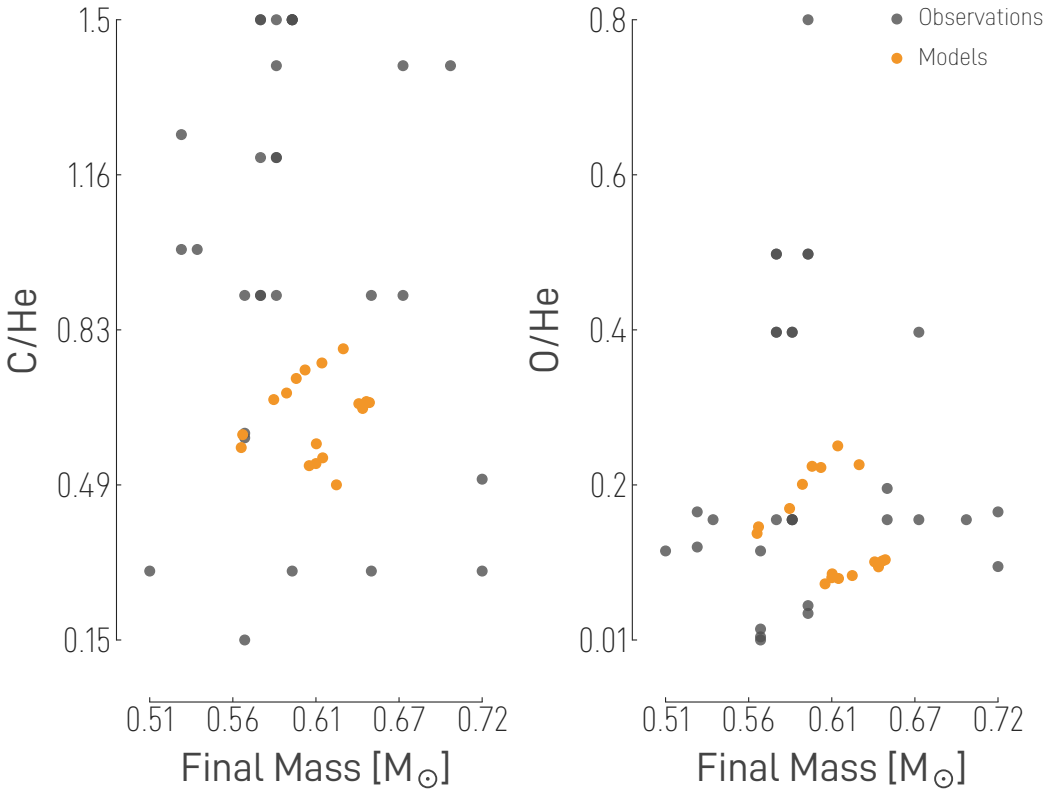

Figure 6.8 Comparison of the final intershell abundances for my models (orange) to observed PG1159 stars (black). The left panel shows the ratio of the mass fractions of C and He versus final mass, while the right panel shows the ratio of the mass fractions of O and He versus final mass. For the track data the final mass was taken to be the core mass of the final model.

the spread of the data cannot be matched — an issue also seen in the C/He plot. While the tracks are well within the spread of the data for C/He, they do seem to occupy a region which is largely devoid of data. The inability of models to explain the spread of C/He and O/He was also noted by Wagstaff et al. (2020). Perhaps

extending the grid to include multiple metallicities would allow for the spread to be matched.

6.4.4 Uncertainties

Finally, a discussion of the uncertainties of the results based on the choice of physics is in order. First, it is important to note that, due to the HRI, the models end before the true end of the AGB. Hence, the difference between quantities for two tracks is only a lower limit. If the tracks could be evolved further, the differences would likely get larger. The impact of the outer boundary condition is largely negligible. The structure and evolution of the LucyP models differs insignificantly with those of the EddR models. This is in agreement with Wagstaff & Weiss (2018) who also found that the outer boundary condition has neither an impact on the structure of the star nor an impact on the observable predictions of the model. However, it is expected that the increased mass loss of the LucyP models would lead to fewer TDUs if the models were able to be evolved to the end of the AGB. Ultimately, the BC only matters insofar as it may impact the mass loss. While mass loss was only altered in this study for one model, one can nevertheless quantify the differences. The spread in the number of TPs due to mass loss is 3 and for TDUs it is 2. This correlates to a difference in AGB lifetime of 140 kyr. The EoS causes little to no spread in the number of TDUs but the number of TPs can differ by 3. This is because with the FreeEoS the TDUs start to happen at an earlier pulse number. None of these physical processes affect the ^{13}C-pocket size. Atomic diffusion, on the other hand does. It increases the size of the pocket by a factor of 2–3, but it also leads to an early quenching of the pocket and effectively chokes off any *s*-process enhancements. Finally, the greatest difference in the models is seen when varying the overshoot. It affects almost every quantity in Table 6.1. As expected, increased `fCE` increases the size of the pocket. However, it also causes a decrease in the neutron exposure of the pocket. At the highest values of `fCE` the neutron exposures are even below what is required for the *s*-process. The other quantities change as expected due of the overshoot: higher overshoot means fewer TPs, TDUs that start earlier and are more efficient, higher C/O, and longer interpulse times due to smaller core mass growth.

Finally, the uncertainty in the yields must be addressed. Each isotope has a unique uncertainty associated with its yield. In Figure 6.9, one can see the light isotopes (those included in the `GARSTEC` nuclear network) plotted on a chart of nuclides. The color shows the uncertainty in dex for the net yield of that isotope. The more red the more uncertain the yield. The uncertainty was calculated via

$$\delta\mathscr{Y}_i = \log_{10}|\mathscr{Y}_i^{\min}| - \log_{10}|\mathscr{Y}_i^{\max}| \tag{6.4}$$

where $\delta\mathscr{Y}_i$ is the uncertainty in the net yield of isotope i, and $\mathscr{Y}_i^{\max}$ and $\mathscr{Y}_i^{\min}$,

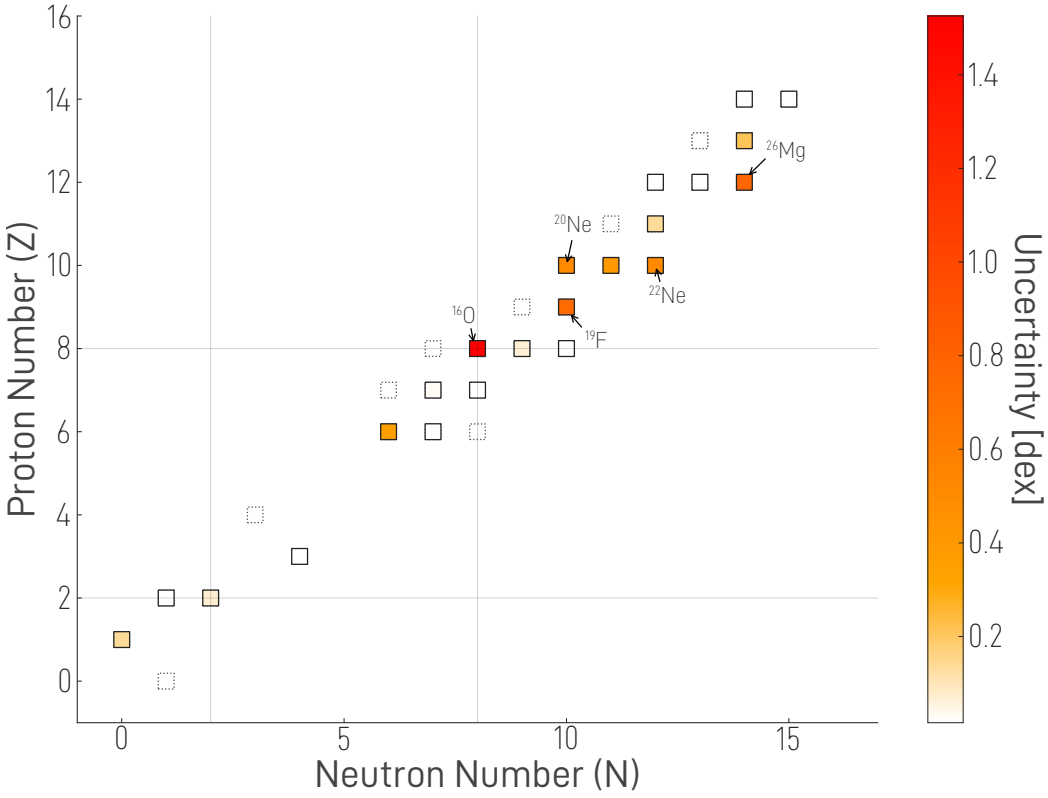

Figure 6.9 Chart of the nuclides showing the uncertainty of the net yields for each light isotope. Only those isotopes whose net yield exceeds 1×10^{-15} $M_\odot$ are included. Those isotopes whose net yield is less are marked by the empty squares with dotted edges. The saturation of the red color for each isotope denotes how uncertain the mass yields are. The light gray lines mark magic numbers. The five isotopes with the largest uncertainties are labeled.

are the maximum and minimum net yields for the isotope across all tracks. The five isotopes with the largest uncertainties are labeled: ^{16}O, ^{19}F, ^{20}Ne, ^{22}Ne, and ^{26}Mg. The uncertainties in these isotopes originate in the number of TDUs a model experiences as well as the overshoot at the base of the PDCZ. Each of these isotope yields are sensitive to the temperature in the He shell. For ^{16}O this has been discussed many times. ^{19}F requires a very specific temperature range in the PDCZ to be produced (220 MK–260 MK). Therefore, changing the overshoot at the base of the PDCZ will affect its yields (Lugaro et al. 2004). The story is similar for the remaining isotopes.

Figure 6.10 shows the same type of plot as Figure 6.9 but for isotopes from ^{56}Fe and heavier. In this case, the isotopes with the largest uncertainties are ^{152}Gd, ^{176}Lu, ^{186}Os, ^{198}Hg, and ^{209}Bi. The tracks with the larger `fCE` values have higher net yields for these isotopes. Additionally, EddR P008 C064 FEoS has marginally higher net yields for these isotopes than the other P008 C064 tracks. There is clearly a trend of greater uncertainty at greater atomic mass. However, many of the isotopes have yield uncertainties below a factor of 2 meaning their yields are

quite reliable.

In conclusion, the physics one chooses can have an important impact. However, the yields for many isotopes seem to be quite robust against the choice of physics with many having uncertainties under a factor of 2. The low uncertainties for the heavy isotopes is a reflection of the fact that the yields primarily depend on the characteristics of the ^{13}C pocket which are fairly similar across the models which have been post-processed. For the light isotopes, uncertainties can be as large as a factor of 10 even for key isotopes like ^{16}O and other isotopes of interest in AGB stars like ^{19}F. It should also be noted that these uncertainties are only due to the choice of physics in the models and do not consider the uncertainties in nuclear rates at all. Because of this, one should consider these lower limits on the true model uncertainties for the yields.

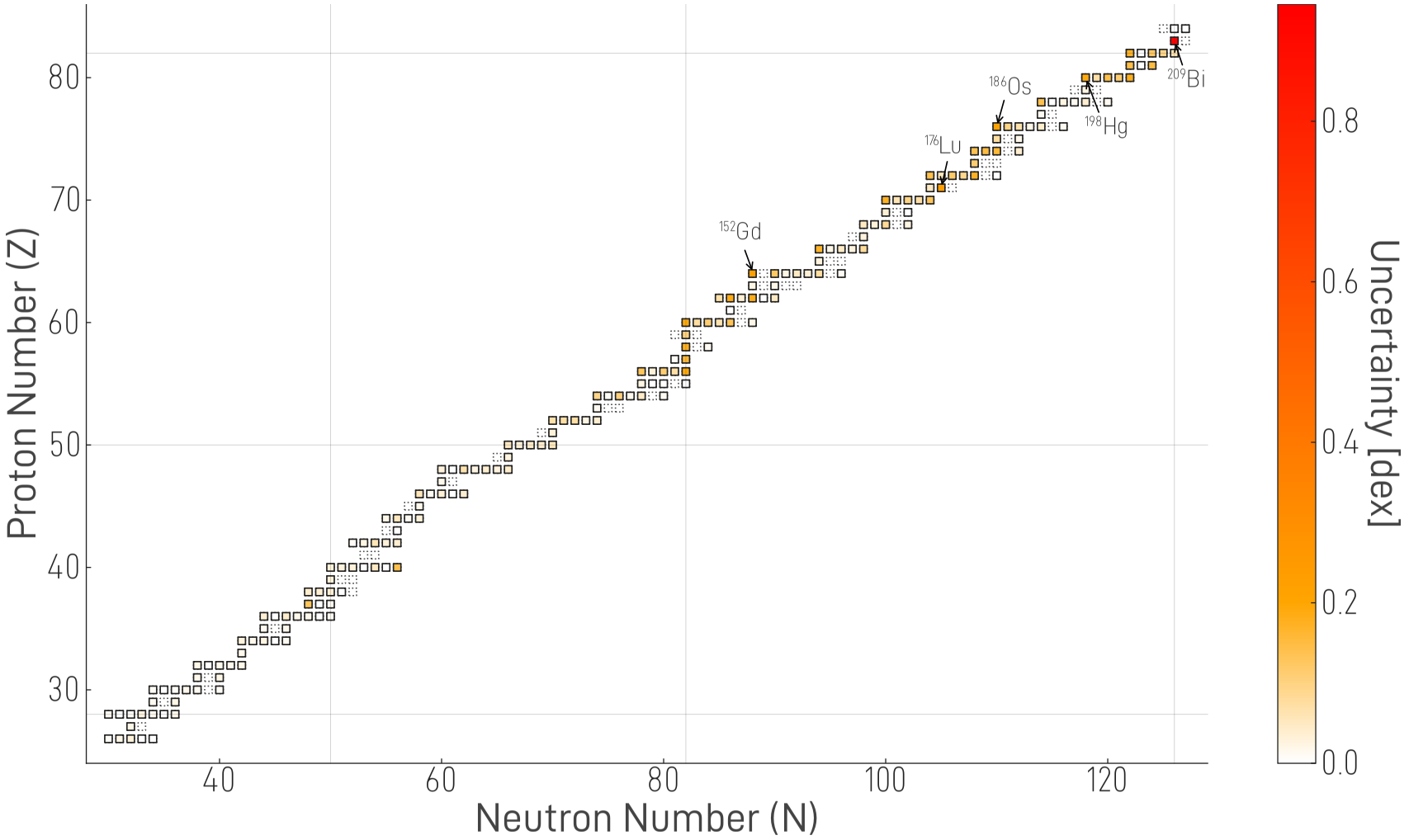

Figure 6.10 Chart of the nuclides showing the uncertainty of the net yields for each heavy isotope. Only those isotopes whose net yield exceeds $1 \times 10^{-15}\,M_\odot$ are included. Those isotopes whose net yield is less are marked by the empty squares with dotted edges. The saturation of the red color for each isotope denotes how uncertain the mass yields are. The light gray lines mark magic numbers. The five isotopes with the largest uncertainties are labeled.

6.5 Conclusions

In this work, a grid of models for a $3\,M_{\odot}$, solar metallicity star with varying choices of physics was run. The atmosphere model, the opacities of the outer layers, the overshoot values, the EoS, the mass loss prescription, and the use of atomic diffusion were all varied. The primary conclusions of this investigation are:

- The HRI is seen in all models and prevents a calculation of the models to the true end of the AGB.
- Convective overshoot, atomic diffusion, mass loss, and the EoS have the largest impacts on the characteristics of the ^{13}C pockets and the AGB evolution.
- The ^{13}C pockets in the models are too small to match observations or the results of other studies.
- The yields of heavy elements are largely robust with most yields varying by less than a factor of 2 across all models. The light elements have larger uncertainties, up to a factor of 10.

The models for this investigation were run from the ZAMS to the point in the AGB evolution when convergence issues were reached. These convergence issues resulted from the HRI and forced an early end to the AGB calculations for all models presented here. The results of the calculations were compared to observations and previous works. The final core masses of the models agree with the IFMR within uncertainties but seem to be systematically too small. The comparison of the luminosity of the models after the first TDU with observations of S stars is inconclusive. There are reasons to think that our models do agree with the observations, however, this would depend on the stars not having been observed in a restricted phase of the TP cycle. Given the small sample of stars in the study, this is not unreasonable. If one assumes that the observations were done in this phase then there is a large tension between the models and the observations, which would be rectified by larger core masses in the models. However, the core mass implied by the observed luminosity would be larger than the core mass after the first TDU seen in models by any group, though it would improve the agreement to the IFMR. The intershell abundances of the models were compared against the surface abundances of PG1159 stars and show good agreement to the data. Nevertheless, the models cannot explain the spread in the observed data perhaps due to only one metallicity being considered in this study.

Comparing the models to other studies, one finds that my models have fewer TPs and TDUs, largely due to the HRI. The mass loss prescription used in my models

also leads to significantly higher mass loss than the VW prescription commonly used in other studies. Direct comparison across studies is complicated by the fact that the physics varies rather significantly across studies. The nuclear yields of heavy isotopes in my models are smaller than those of other studies because of the small ^{13}C pockets in my models. This also causes the [hs/ls] of my models to be beyond or at the highest limits allowed by observations. However, relative yields agree for many isotopes. The yields of light isotopes are in agreement with those of P16 with some exceptions (e.g. ^{19}F).

Finally, the uncertainties in various quantities as a result of the physics choices were calculated. It was found that the yield uncertainties are below a factor of 2 for many isotopes with a clear trend of higher uncertainty for isotopes at the second peak and beyond. For the light isotopes the yields are actually more uncertain with ^{16}O yields uncertain by over an order of magnitude depending on the value of `fPDCZ`. Ultimately, it was determined that overshoot, mass loss, and, to a lesser degree, EoS are the modeling physics which affect the models the most. Future work in this area should extend this analysis to further masses and metallicities. Only the overshoot, mass loss, and EoS would need to be varied for future studies. Moreover, the nuclear uncertainties should also be accounted for in the yield uncertainties. Finally, it may be worth investigating the impact of atomic diffusion on the ^{13}C pocket at different masses and metallicities.

Chapter 7

Conclusion

> It is reasonable to hope that in the not too distant future we shall be competent to understand so simple a thing as a star.
>
> Arthur Eddington, *The Internal Constitution of the Stars*

This thesis has investigated two important nucleosynthesis processes that can occur in AGB stars: the intermediate neutron-capture process (*i*-process) and the slow neutron-capture process (*s*-process). Through detailed stellar evolution modeling coupled with post-processing nucleosynthesis calculations utilizing a new mixing scheme developed for this work, I have explored how various physical processes and numerical treatments affect these nucleosynthetic processes and their resulting abundance patterns.

7.1 The *i*-process

The investigation of the *i*-process yielded several important results regarding both the conditions necessary for proton ingestion events (PIEs) and the nucleosynthesis that occurs during them. I developed and validated a novel timescale-based criterion for determining when PIEs should occur in stellar models. This criterion involves comparing three characteristic timescales: τ_{He}, τ_{diff}, and τ_{H}. When $\tau_{\mathrm{He}} < \tau_{\mathrm{diff}} \simeq \tau_{\mathrm{H}}$, a PIE occurs. This criterion was found to be robust across different masses and metallicities. The timing of the split in the pulse-driven convection zone (PDCZ) during a PIE was found to be crucial in determining the final surface abundances. Our models generally showed the split occurring before the time of maximum neutron density (TOMND). This is in agreement with Cristallo et al. (2009a), but in contrast to Choplin et al. (2021). Test calculations showed that the timing of the split can be influenced by the convective velocities in the PDCZ

and the time step settings used in the calculations. In theory, the $^{12}C(p,\gamma)^{13}N$ rate is also influential, but reducing it to the lowest values allowed by experimental uncertainties showed no meaningful change in the split. The use of convective boundary mixing through diffusive overshooting was found to have significant effects on both the occurrence and characteristics of PIEs. Specifically, higher overshooting parameters led to PIEs occurring at earlier thermal pulses and with smaller neutron exposures. Models with overshooting also showed the possibility for the split PDCZ to remerge.

Comparison of surface abundances of observed stars revealed a complex picture. Most models showed good agreement with observations for N and O abundances while C abundances were systematically too high even after dilution. Li abundances showed significant variation with mass and overshooting but were generally in agreement with observations. For the heavy elements, it was found that the models struggle to match the first-peak element abundances. This suggests the PDCZ split occurs too early in our models. Tracks with overshoot from the PDCZ showed systematically lower heavy element enhancements. This is because these models tend not to have a post-PIE TDU. This is a requirement for getting heavy elements to the surface when the split happens early in the PIE. Additionally, it was found that deep ^{13}C pockets formed after PIEs, contaminating the surface abundances with an *s*-process signature. Overall, the stars with an early splitting of the PDCZ, which I have called "failed *i*-process" stars, are able to match the surface abundances of some CEMP-r/s as well as most of the low-metallicity CEMP-s stars. This may be a hint that a wide range of CEMP stars could be explained via AGB stars which experience a PIE, but which have splits occurring at different points in the PIE. That being said, one has to also bring up the alternate explanation which is that the CEMP-r/s stars are polluted by a source other than AGB stars, such as rapidly-accreting white dwarf stars.

7.2 The *s*-process

For the *s*-process investigation, $3\,M_\odot$, solar metallicity models were run with various different physics choices. In total, the atmosphere model, the opacities of the outer layers, the equation of state (EoS), the mass loss prescription, the use of atomic diffusion, and the overshoot parameters were varied. Varying the input physics revealed that the size and characteristics of the ^{13}C pocket are primarily influenced by the overshooting parameter at the convective envelope (`fCE`), atomic diffusion, which can increase pocket size but leads to negligible neutron exposures, and the EoS, which affects the timing and efficiency of the third dredge-ups (TDU). Additionally, the mass loss prescription is important, though it is less impactful for my models since the hydrogen recombination instability (HRI) ends the AGB evolution prematurely. The outer boundary condition is only

important in that it reduces the effective temperature of the model which would impact the mass loss.

Despite the fact that the ^{13}C pockets in this study are smaller than predicted to match observations, the uncertainties in nucleosynthetic yields were quantified across different choices of input physics. Heavy element yields show relatively small uncertainties (generally below a factor of 2) while light element yields exhibit much larger uncertainties, particularly for key isotopes like ^{16}O and ^{19}F. There is a clear trend among the heavy elements of increasing uncertainty with increasing atomic mass.

7.3 Status and Future Work

Our findings have several important implications for our understanding of stellar nucleosynthesis and galactic chemical evolution. First, a new advective mixing scheme was developed which allows for a much better agreement in the mixing between advective and diffusive mixing schemes, in particular when overshoot is used. This can easily be implemented in other codes and used for future post-processing applications. Second, the identification of a robust criterion for PIE occurrence provides a valuable tool for future stellar evolution calculations and could help explain the origin of CEMP-r/s stars. Third, the demonstration that failed *i*-process events can produce *s*-process-like abundance patterns suggests a possible new channel for explaining CEMP-s stars at low metallicity. Finally, the quantification of uncertainties in nucleosynthetic yields for the *s*-process and final surface abundances for the *i*-process provides important results for galactic chemical evolution models and interpretations of observed abundance patterns.

There are a number of important directions for future research based on this work.

1. Extension of the *i*-process investigation to different masses and metallicities to better understand the parameter space where PIEs occur.

2. Likewise, the quantification of yield uncertainties in the *s*-process models should be extended to different masses and metallicities.

3. Further investigation of the HRI. Primarily, it would be important to investigate if it truly occurs in stars and determine potential observational signatures.

4. Expansion of the uncertainty analysis for both the *s*-process and the *i*-process to include nuclear reaction rate uncertainties.

5. Investigation of the interplay between atomic diffusion and other mixing processes in AGB stars, particularly regarding their effect on the ^{13}C pocket formation and evolution.

6. Development of improved treatments for convective boundary mixing that can better reproduce observed abundance patterns while maintaining physical consistency.

These investigations would provide essential fundamental contributions as researchers work toward a more complete understanding of the origin of heavy elements in the universe.

Appendix A

List of Acronyms

Below is a list of all of the acronyms used in this study along with their meaning. All acronyms are defined in the text as well.

AGB Asymptotic giant branch

CAIs Calcium-aluminum-rich inclusions

CBM Convective boundary mixing

CE Convective envelope

CEMP Carbon enhanced extremely metal poor

CEMP-s Carbon-enhanced extremely metal-poor with signs of *s*-process enhancement

CEMP-r Carbon-enhanced extremely metal-poor with signs of *r*-process enhancement

CEMP-r/s Carbon-enhanced extremely metal-poor with signs of both *r*-*s*-process enhancement

CEMP-no Carbon-enhanced extremely metal-poor with signs of neither *r*-*s*-process enhancement

CMD Color-magnitude diagram

E-AGB Early asymptotic giant branch

EoS Equation of state

fCHB The overshoot parameter for the core convective zone during H burning

fCHeB The overshoot parameter for the core convective zone during He burning

fCE The overshoot parameter for the base of the convective envelope

fPDCZt The overshoot parameter for the top of the pulse-driven convection zone

fPDCZb The overshoot parameter for the bottom of the pulse-driven convection zone

FDU First dredge-up

HBB Hot-bottom burning

HB Horizontal branch

HRD Hertzsprung-Russell diagram

HRI Hydrogen recombination instability

IFMR Initial-final mass relation

IGW Internal gravity wave

ISM Interstellar medium

KADoNiS Karlsruhe Astrophysical Database of Nucleosynthesis in Stars

LPV Long-period variable star

LTE Local thermodynamic equilibrium

MLT Mixing length theory

MS Main sequence

PDCZ Pulse-driven convection zone

PIE Proton ingestion event

PM Planck mean

RAWD Rapidly accreting white dwarf

RGB Red giant branch

RM Rosseland mean

SDU Second dredge-up

TOMND Time of maximum neutron density

TDU Third dredge-up

TPs Thermal pulses

TP-AGB Thermally pulsing asymptotic giant branch

ZAMS Zero-age main sequence

Appendix B

l-process Figures

In this appendix one can find individual plots for each CEMP-r/s (Figure B.1) and CEMP-s star (Figure B.2), showing both the observational data and its corresponding best-fit model. Each plot includes the name of the observed star as well as the χ^2_{red} value and dilution factor, f, for the best-fit model.

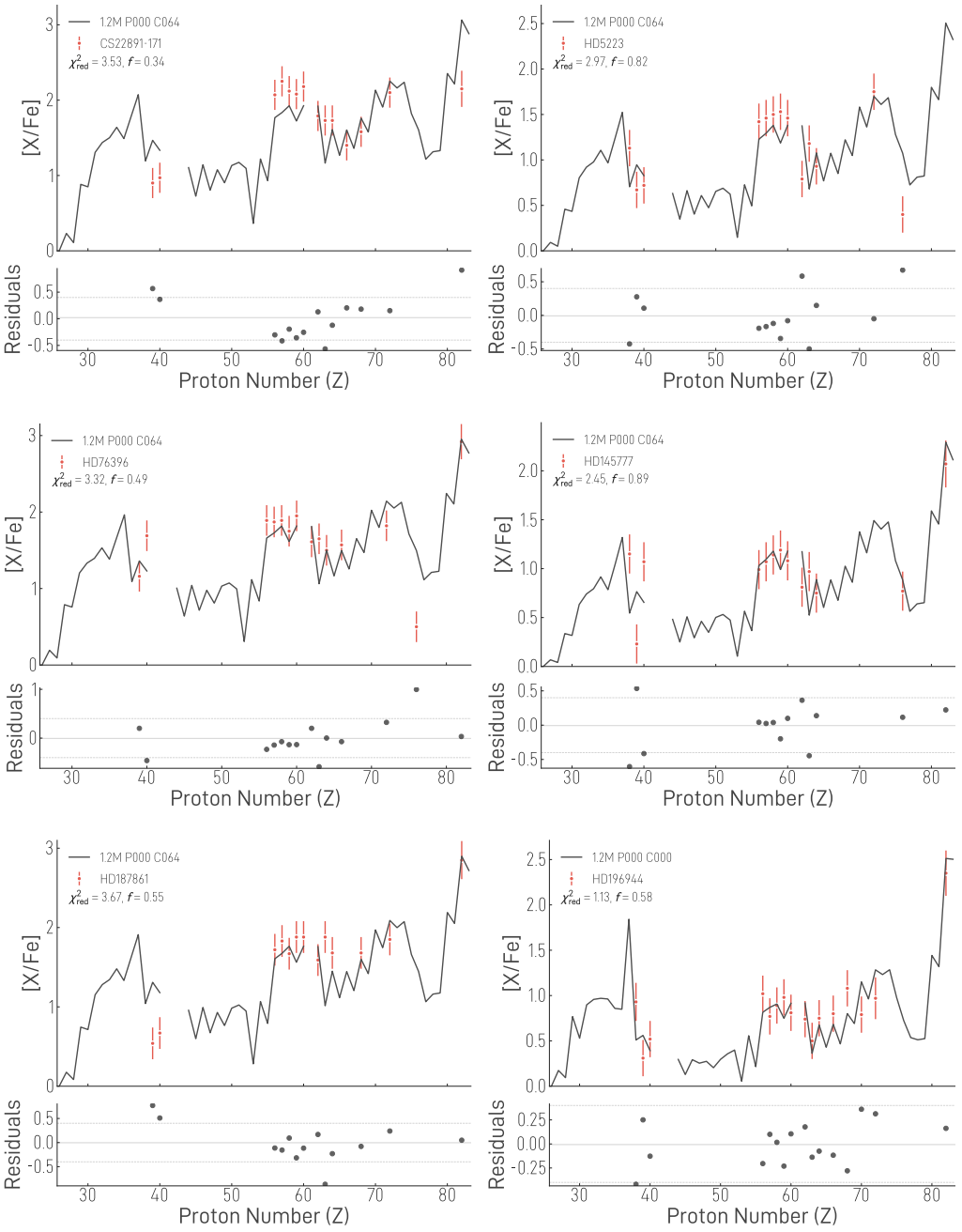

Figure B.1 The best fitting model for each observed CEMP-r/s star. In the upper panel the data points are the observations with errors, the black line is the diluted abundance of the model. The reduced χ^2 and dilution factor are given in the legend. In the lower panel are the residuals (model–observation) of the fit. The dashed lines mark the values of −0.4 and +0.4. The solid line marks the mean of the residuals.

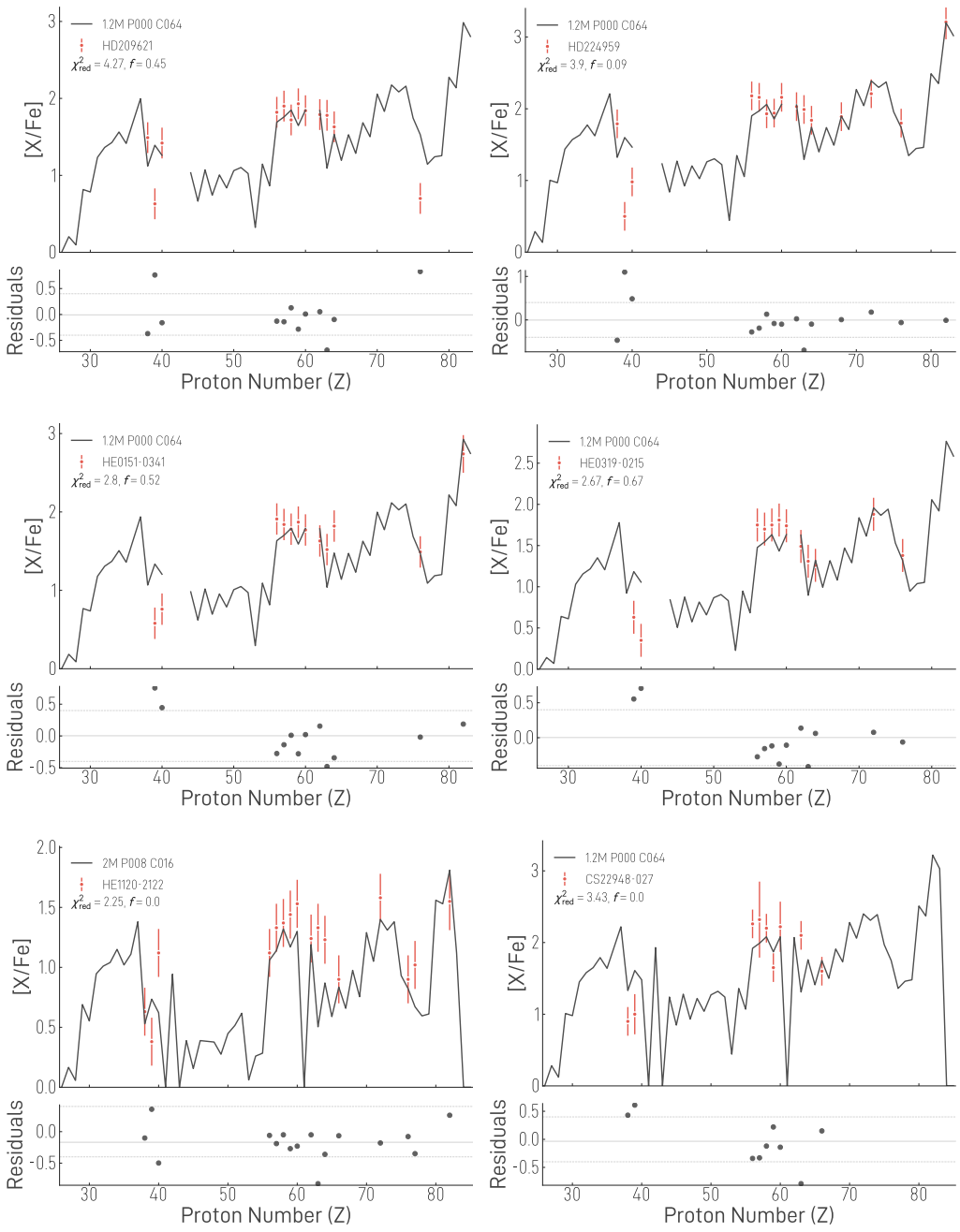

Figure B.1 (cont.)

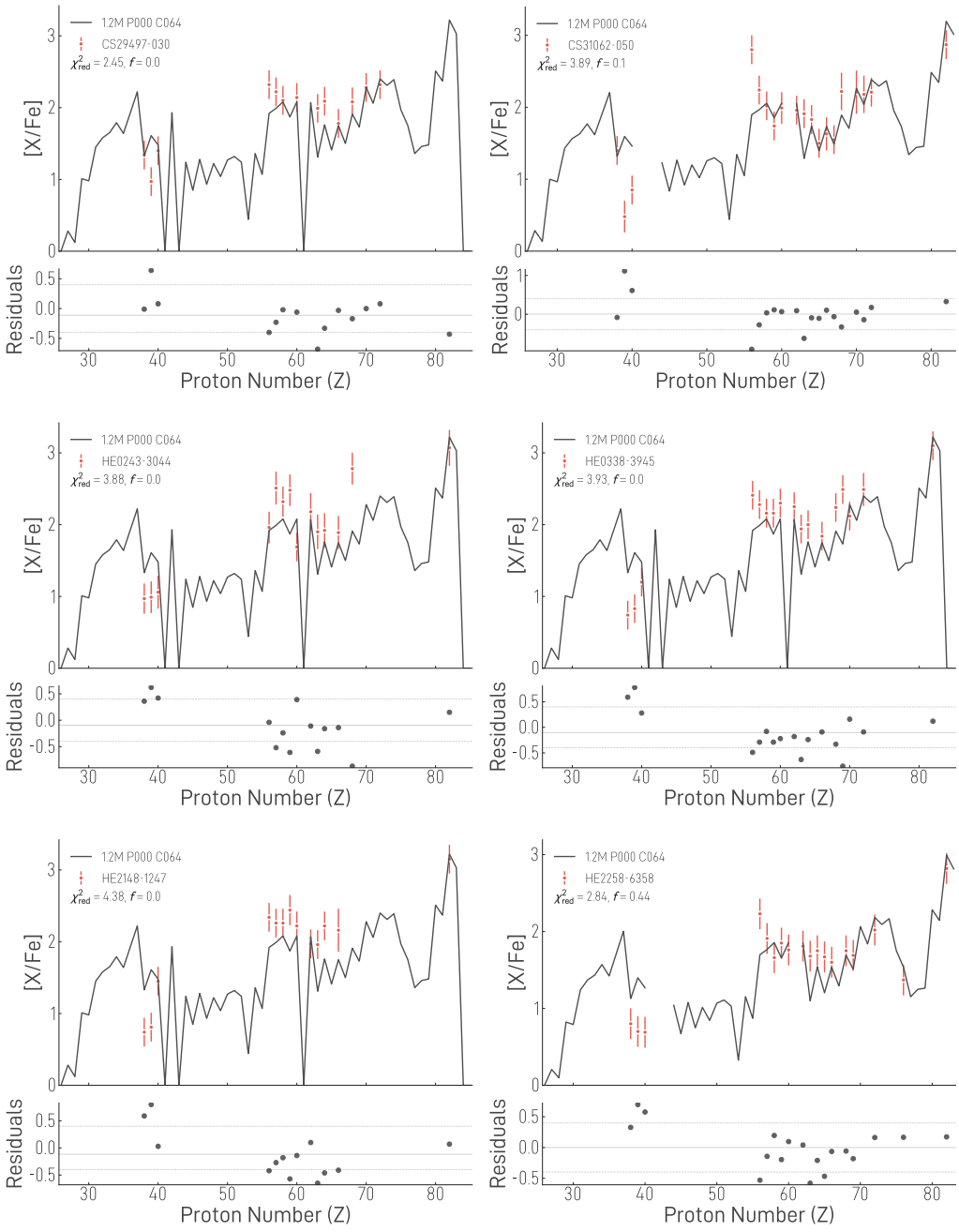

Figure B.1 (cont.)

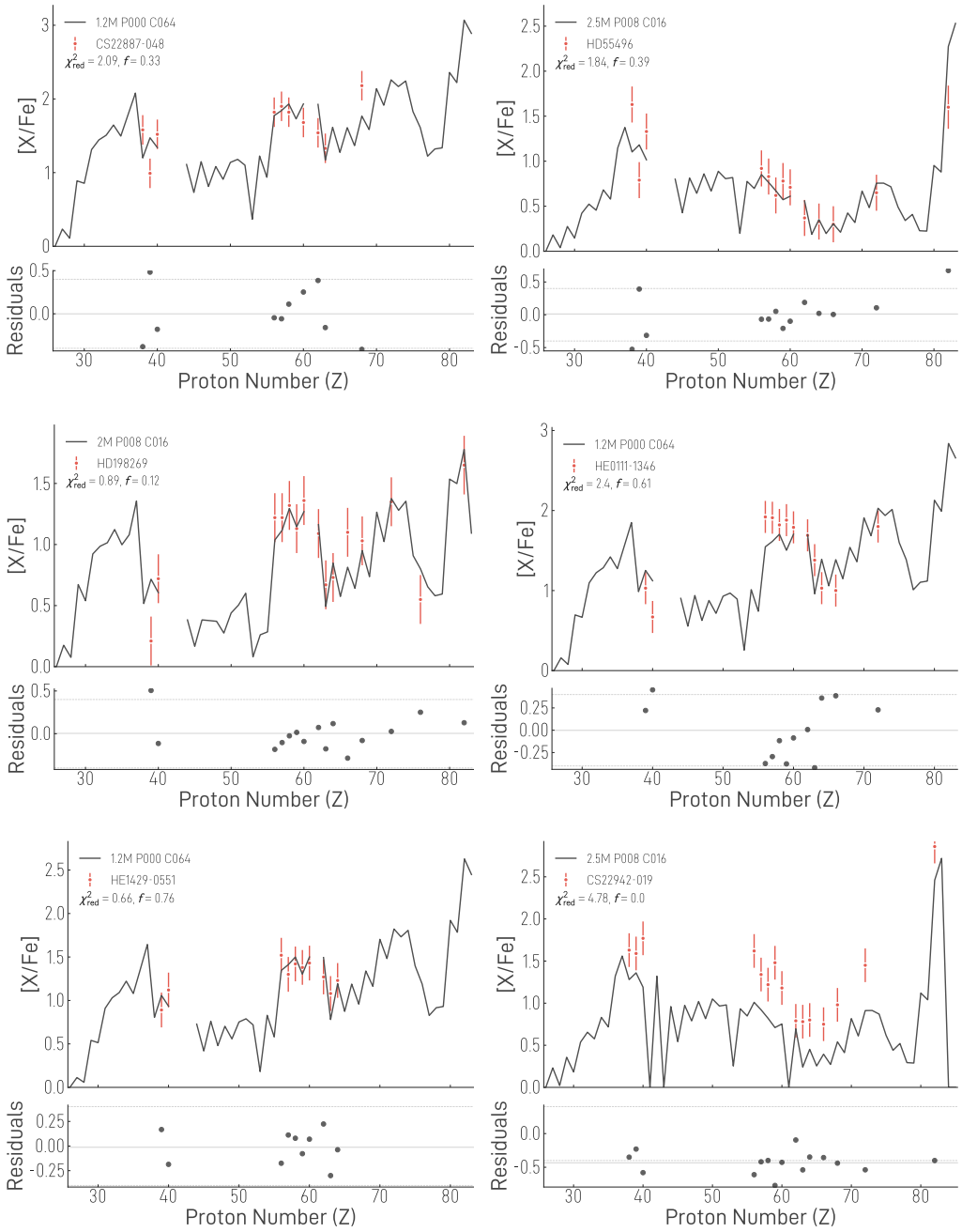

Figure B.2 The best fitting model for each observed CEMP-s star. The plot elements are the same as for Figure B.1.

Appendix C

s-process Tables

C.1 Pulse-by-Pulse Tables

Below one can find, for each *s*-process model, a table of important quantities for each TP cycle. The table headers are defined as follows:

- TP: A running count of the number of TPs
- M: The total mass at the start of the TP
- M_{core}: The mass of the H-free core at thte start of the TP
- M_{PDCZ}: The maximum extent (in solar massed) of the PDCZ for that TP
- TDU: The number of TDUs which have occured
- λ: The TDU efficiency for that TDU
- C/O: The C/O ratio following that TDU
- $\Delta t_{\text{interpulse}}$: The duration of the interpulse phase for that TP
- M_{pocket}: The mass of the ^{13}C pocket
- τ_{pocket}: The neutron exposure of the ^{13}C pocket.

Table C.1 Key results for the EddR Poo8 Co16 (see Section 6.2) track for each pulse cycle.

	Pulse				Interpulse					
TP	M [$M_\odot$]	M_{core} [$M_\odot$]	M_{PDCZ} [$M_\odot$]	T_{PDCZ} [K]	TDU	λ	C/O	$\Delta t_{interpulse}$ [kyr]	M_{pocket} [$M_\odot$]	τ_{pocket} [mb^{-1}]
1	2.96	0.608	0.029	8.37	0	0.0	0.31	59.84	0.0	0.0
2	2.96	0.611	0.028	8.38	0	0.0	0.31	65.10	0.0	0.0
3	2.95	0.614	0.029	8.41	0	0.0	0.31	68.31	0.0	0.0
4	2.95	0.619	0.029	8.43	1	0.227	0.32	69.01	0.0	0.0
5	2.94	0.623	0.029	8.44	2	0.359	0.38	70.33	0.0	0.0
6	2.93	0.628	0.028	8.45	3	0.458	0.46	70.95	0.0	0.0
7	2.93	0.632	0.028	8.46	4	0.522	0.57	70.58	0.0	0.0
8	2.91	0.635	0.027	8.47	5	0.608	0.70	70.26	0.0	0.0
9	2.90	0.6390	0.026	8.47	6	0.674	0.85	69.82	0.0	0.0
10	2.89	0.642	0.025	8.48	7	0.766	1.0	70.22	4.0×10^{-6}	0.544
11	2.83	0.644	0.025	8.48	8	0.747	1.15	69.57	3.6×10^{-6}	0.517
12	2.70	0.6470	0.024	8.48	9	0.750	1.31	68.12	2.7×10^{-6}	0.518
13	2.46	0.649	0.024	8.49	10	0.771	1.48	54.84	2.4×10^{-6}	0.491

Table C.2 Key results for the EddR Poo8 Co16 Diff (see Section 6.2) track for each pulse cycle.

	Pulse				Interpulse					
TP	M [$M_\odot$]	M_{core} [$M_\odot$]	M_{PDCZ} [$M_\odot$]	T_{PDCZ} [K]	TDU	λ	C/O	$\Delta t_{interpulse}$ [kyr]	M_{pocket} [$M_\odot$]	τ_{pocket} [mb^{-1}]
1	2.96	0.609	0.030	8.38	0	0.0	0.31	60.20	0.0	0.0
2	2.96	0.611	0.027	8.38	0	0.0	0.31	63.66	0.0	0.0
3	2.95	0.615	0.029	8.41	0	0.0	0.31	66.99	0.0	0.0
4	2.95	0.619	0.029	8.43	1	0.233	0.32	67.61	2.5×10^{-5}	0.0001
5	2.94	0.624	0.028	8.44	2	0.371	0.38	69.02	2.1×10^{-5}	0.0001
6	2.93	0.628	0.028	8.45	3	0.462	0.47	69.54	1.8×10^{-5}	0.009
7	2.93	0.632	0.027	8.46	4	0.520	0.58	69.03	1.5×10^{-5}	0.0001
8	2.91	0.636	0.027	8.47	5	0.596	0.70	68.50	1.6×10^{-5}	0.005
9	2.90	0.639	0.026	8.47	6	0.673	0.84	68.17	1.3×10^{-5}	0.006
10	2.89	0.642	0.025	8.48	7	0.770	1.00	68.68	1.3×10^{-5}	0.006
11	2.88	0.645	0.025	8.48	8	0.751	1.15	67.87	1.2×10^{-5}	0.006
12	2.86	0.647	0.024	8.48	9	0.745	1.30	66.36	1.1×10^{-5}	0.005
13	2.71	0.650	0.023	8.49	10	0.756	1.44	64.69	1.0×10^{-5}	0.004
14	2.44	0.652	0.023	8.49	10*	0.0	1.44	0.00	0.0	0.0

Table C.3 Key results for the LucyP Poo8 Co16 (see Section 6.2) track for each pulse cycle.

	Pulse				Interpulse					
TP	M [$M_\odot$]	M_{core} [$M_\odot$]	M_{PDCZ} [$M_\odot$]	T_{PDCZ} [K]	TDU	λ	C/O	$\Delta t_{interpulse}$ [kyr]	M_{pocket} [$M_\odot$]	τ_{pocket} [mb^{-1}]
1	2.96	0.606	0.027	8.34	0	0.0	0.31	54.18	0.0	0.0
2	2.96	0.607	0.029	8.37	0	0.0	0.31	64.53	0.0	0.0
3	2.95	0.610	0.030	8.40	0	0.0	0.31	68.92	0.0	0.0
4	2.95	0.615	0.030	8.42	0	0.0	0.31	69.85	0.0	0.0
5	2.94	0.619	0.029	8.43	1	0.235	0.33	70.29	0.0	0.0
6	2.94	0.624	0.029	8.45	2	0.375	0.39	71.16	0.0	0.0
7	2.93	0.628	0.028	8.45	3	0.448	0.48	71.02	0.0	0.0
8	2.92	0.633	0.027	8.46	4	0.540	0.59	70.59	8.4×10^{-6}	0.513
9	2.91	0.636	0.027	8.47	5	0.614	0.72	70.16	0.0	0.0
10	2.89	0.640	0.026	8.47	6	0.679	0.86	69.76	4.5×10^{-6}	0.532
11	2.88	0.643	0.025	8.48	7	0.725	1.01	69.33	5.2×10^{-6}	0.534
12	2.79	0.645	0.024	8.48	8	0.746	1.16	68.71	2.7×10^{-6}	0.522
13	2.64	0.648	0.024	8.48	9	0.750	1.32	67.51	3.3×10^{-6}	0.507
14	2.36	0.650	0.023	8.49	10	0.779	1.50	35.26	2.7×10^{-6}	0.276

Table C.4 Key results for the EddR Poo8 Co64 (see Section 6.2) track for each pulse cycle.

	Pulse				Interpulse					
TP	M [$M_\odot$]	M_{core} [$M_\odot$]	M_{PDCZ} [$M_\odot$]	T_{PDCZ} [K]	TDU	λ	C/O	$\Delta t_{interpulse}$ [kyr]	M_{pocket} [$M_\odot$]	τ_{pocket} [mb^{-1}]
1	2.96	0.609	0.029	8.37	0	0.0	0.31	60.9	0.0	0.0
2	2.96	0.611	0.027	8.38	0	0.0	0.31	65.26	0.0	0.0
3	2.95	0.615	0.029	8.41	0	0.0	0.31	68.32	0.0	0.0
4	2.95	0.619	0.029	8.43	1	0.533	0.38	72.16	0.0	0.0
5	2.94	0.623	0.029	8.45	2	0.818	0.54	78.43	1.2×10^{-5}	0.583
6	2.93	0.625	0.030	8.46	3	0.984	0.77	84.51	1.0×10^{-5}	0.439
7	2.92	0.627	0.030	8.47	4	1.065	1.03	90.62	9.7×10^{-6}	0.566
8	2.86	0.628	0.030	8.48	5	1.058	1.29	95.16	4.1×10^{-6}	0.515
9	2.70	0.628	0.029	8.48	6	1.037	1.54	96.76	5.4×10^{-6}	0.490
10	2.39	0.628	0.029	8.49	7	1.005	1.80	35.71	3.8×10^{-6}	0.061

Table C.5 Key results for the EddR Poo8 Co64 FEoS (see Section 6.2) track for each pulse cycle.

	Pulse				Interpulse					
TP	M [$M_\odot$]	M_{core} [$M_\odot$]	M_{PDCZ} [$M_\odot$]	T_{PDCZ} [K]	TDU	λ	C/O	$\Delta t_{interpulse}$ [kyr]	M_{pocket} [$M_\odot$]	τ_{pocket} [mb^{-1}]
1	2.96	0.588	0.029	8.40	1	0.0	0.36	70.22	1.3×10^{-5}	0.060
2	2.96	0.589	0.029	8.43	2	1.233	0.52	78.69	5.5×10^{-6}	0.094
3	2.95	0.590	0.032	8.46	3	1.353	0.79	93.09	1.3×10^{-5}	0.587
4	2.94	0.591	0.034	8.48	4	1.355	1.12	108.15	6.8×10^{-6}	0.549
5	2.85	0.590	0.036	8.49	5	1.280	1.43	118.67	4.7×10^{-6}	0.512
6	2.68	0.588	0.036	8.49	6	1.233	1.71	127.11	3.7×10^{-6}	0.469
7	2.30	0.586	0.038	8.50	6*	0.0	1.71	0.00	0.0	0.0

* Track ends before TDU can occur

Table C.6 Key results for the EddR Poo8 Co64 Diff (see Section 6.2) track for each pulse cycle.

	Pulse				Interpulse					
TP	M [$M_\odot$]	M_{core} [$M_\odot$]	M_{PDCZ} [$M_\odot$]	T_{PDCZ} [K]	TDU	λ	C/O	$\Delta t_{interpulse}$ [kyr]	M_{pocket} [$M_\odot$]	τ_{pocket} [mb^{-1}]
1	2.97	0.603	0.044	8.36	0	0.0	0.31	61.32	0.0	0.0
2	2.96	0.612	0.031	8.37	0	0.0	0.31	57.12	0.0	0.0
3	2.96	0.614	0.029	8.38	0	0.0	0.31	59.74	0.0	0.0
4	2.95	0.617	0.030	8.41	0	0.0	0.31	63.58	0.0	0.0
5	2.95	0.621	0.030	8.42	0	0.0	0.31	64.52	0.0	0.0
6	2.94	0.626	0.029	8.44	1	0.473	0.37	67.11	3.2×10^{-5}	0.0015
7	2.93	0.630	0.029	8.45	2	0.768	0.53	71.72	2.8×10^{-5}	0.0019
8	2.93	0.633	0.029	8.46	3	0.977	0.75	77.15	2.1×10^{-5}	0.0009
9	2.91	0.634	0.029	8.47	4	1.086	0.99	82.70	2.1×10^{-5}	0.0005
10	2.90	0.635	0.029	8.48	5	1.079	1.23	87.29	1.2×10^{-5}	0.0002
11	2.88	0.635	0.028	8.48	6	1.059	1.46	89.40	1.3×10^{-5}	0.0002
12	2.68	0.635	0.028	8.49	7	1.035	1.68	85.30	1.0×10^{-5}	0.0001

Table C.7 Key results for the LucyP Poo8 Co64 Diff (see Section 6.2) track for each pulse cycle.

	Pulse				Interpulse					
TP	M [$M_\odot$]	M_{core} [$M_\odot$]	M_{PDCZ} [$M_\odot$]	T_{PDCZ} [K]	TDU	λ	C/O	$\Delta t_{interpulse}$ [kyr]	M_{pocket} [$M_\odot$]	τ_{pocket} [mb^{-1}]
1	2.96	0.605	0.029	8.34	0	0.0	0.31	54.18	0.0	0.0
2	2.96	0.606	0.020	8.30	0	0.0	0.31	54.87	0.0	0.0
3	2.96	0.609	0.031	8.39	0	0.0	0.31	65.45	0.0	0.0
4	2.95	0.612	0.029	8.40	0	0.0	0.31	67.03	0.0	0.0
5	2.95	0.616	0.030	8.42	1	0.299	0.33	69.15	3.7×10^{-5}	0.0018
6	2.94	0.621	0.030	8.44	2	0.600	0.43	73.38	2.2×10^{-5}	0.0001
7	2.93	0.624	0.030	8.45	3	0.917	0.63	79.43	2.3×10^{-5}	0.0019
8	2.92	0.626	0.030	8.46	4	1.01	0.87	85.20	2.9×10^{-5}	0.0006
9	2.91	0.627	0.030	8.47	5	1.066	1.12	90.55	1.7×10^{-5}	0.0005
10	2.81	0.628	0.030	8.48	6	1.049	1.37	93.74	1.4×10^{-5}	0.0002
11	2.61	0.628	0.029	8.48	7	1.031	1.62	94.91	1.1×10^{-5}	0.0001

* Track ends before TDU can occur

Table C.8 Key results for the LucyP Poo8 Co64 (see Section 6.2) track for each pulse cycle.

	Pulse				Interpulse					
TP	M [$M_\odot$]	M_{core} [$M_\odot$]	M_{PDCZ} [$M_\odot$]	T_{PDCZ} [K]	TDU	λ	C/O	$\Delta t_{interpulse}$ [kyr]	M_{pocket} [$M_\odot$]	τ_{pocket} [mb^{-1}]
1	2.96	0.606	0.028	8.34	0	0.0	0.31	54.64	0.0	0.0
2	2.96	0.607	0.029	8.37	0	0.0	0.31	64.46	0.0	0.0
3	2.95	0.610	0.030	8.40	0	0.0	0.31	68.94	0.0	0.0
4	2.95	0.615	0.030	8.42	1	0.237	0.32	70.49	1.1×10^{-5}	0.086
5	2.94	0.619	0.030	8.44	2	0.578	0.41	74.85	7.6×10^{-6}	0.212
6	2.94	0.623	0.030	8.45	3	0.904	0.61	81.19	1.2×10^{-5}	0.531
7	2.93	0.625	0.030	8.46	4	1.015	0.85	87.25	9.7×10^{-6}	0.636
8	2.91	0.626	0.030	8.47	5	1.053	1.10	92.64	6.0×10^{-6}	0.537
9	2.82	0.627	0.030	8.48	6	1.053	1.35	96.20	4.4×10^{-6}	0.521
10	2.63	0.627	0.029	8.48	7	1.034	1.59	97.70	3.5×10^{-6}	0.479
11	2.22	0.627	0.029	8.49	7*	0.0	1.59	0.00	0.0	0.0

* Track ends before TDU can occur

Table C.9 Key results for the EddR P008 C128 (see Section 6.2) track for each pulse cycle.

	Pulse				Interpulse					
TP	M [$M_\odot$]	$M_{\rm core}$ [$M_\odot$]	$M_{\rm PDCZ}$ [$M_\odot$]	$T_{\rm PDCZ}$ [K]	TDU	λ	C/O	$\Delta t_{\rm interpulse}$ [kyr]	$M_{\rm pocket}$ [$M_\odot$]	$\tau_{\rm pocket}$ [mb^{-1}]
1	2.96	0.608	0.028	8.36	0	0.0	0.31	56.75	0.0	0.0
2	2.96	0.610	0.028	8.38	0	0.0	0.31	63.99	0.0	0.0
3	2.96	0.614	0.029	8.41	0	0.0	0.31	67.57	0.0	0.0
4	2.95	0.618	0.029	8.43	1	0.623	0.39	72.80	5.0×10^{-6}	0.0
5	2.94	0.621	0.030	8.44	2	0.892	0.57	80.24	1.6×10^{-5}	0.144
6	2.93	0.623	0.030	8.46	3	1.083	0.83	88.48	2.0×10^{-5}	0.188
7	2.92	0.624	0.030	8.47	4	1.128	1.12	96.33	1.8×10^{-5}	0.053
8	2.83	0.625	0.030	8.48	5	1.108	1.40	101.58	1.2×10^{-5}	0.042
9	2.63	0.625	0.030	8.48	6	1.077	1.67	103.71	1.1×10^{-5}	0.023
10	2.20	0.625	0.030	8.49	7*	0.000	1.78	0.00	0.0	0.0

* Track ends before TDU can occur

Table C.10 Key results for the EddR P016 C016 (see Section 6.2) track for each pulse cycle.

	Pulse				Interpulse					
TP	M [$M_\odot$]	$M_{\rm core}$ [$M_\odot$]	$M_{\rm PDCZ}$ [$M_\odot$]	$T_{\rm PDCZ}$ [K]	TDU	λ	C/O	$\Delta t_{\rm interpulse}$ [kyr]	$M_{\rm pocket}$ [$M_\odot$]	$\tau_{\rm pocket}$ [mb^{-1}]
1	2.96	0.608	0.034	8.37	0	0.0	0.31	63.28	0.0	0.0
2	2.96	0.611	0.032	8.38	0	0.0	0.31	66.05	0.0	0.0
3	2.95	0.614	0.034	8.42	0	0.0	0.31	68.62	0.0	0.0
4	2.95	0.618	0.035	8.43	1	0.343	0.35	70.91	0.0	0.0
5	2.94	0.623	0.035	8.45	2	0.445	0.42	72.40	0.0	0.0
6	2.93	0.627	0.034	8.46	3	0.551	0.53	72.69	0.0	0.0
7	2.92	0.630	0.034	8.47	4	0.676	0.66	72.84	0.0	0.0
8	2.91	0.633	0.033	8.47	5	0.778	0.81	73.19	0.0	0.0
9	2.90	0.635	0.032	8.48	6	0.865	0.96	73.99	0.0	0.0
10	2.89	0.637	0.032	8.48	7	0.919	1.11	75.32	4.4×10^{-6}	0.517
11	2.78	0.638	0.032	8.49	8	0.921	1.26	75.65	4.2×10^{-6}	0.519
12	2.58	0.639	0.031	8.49	9	0.942	1.42	76.03	2.6×10^{-6}	0.541
13	2.14	0.640	0.031	8.49	9*	0.0	1.42	0.00	0.0	0.0

* Track ends before TDU can occur

Table C.11 Key results for the EddR Po16 Co16 FEoS (see Section 6.2) track for each pulse cycle.

	Pulse				Interpulse					
TP	M [$M_\odot$]	M_{core} [$M_\odot$]	M_{PDCZ} [$M_\odot$]	T_{PDCZ} [K]	TDU	λ	C/O	$\Delta t_{interpulse}$ [kyr]	M_{pocket} [$M_\odot$]	τ_{pocket} [mb^{-1}]
1	2.96	0.588	0.028	8.39	1	0.0	0.32	66.29	0.0	0.0
2	2.96	0.590	0.028	8.42	2	0.738	0.39	68.71	0.0	0.0
3	2.95	0.593	0.030	8.45	3	0.756	0.52	73.45	0.0	0.0
4	2.94	0.595	0.030	8.46	4	0.856	0.69	78.09	0.0	0.0
5	2.93	0.597	0.030	8.48	5	0.958	0.89	82.60	0.0	0.0
6	2.92	0.599	0.031	8.48	6	1.030	1.10	87.99	2.6×10^{-6}	0.535
7	2.84	0.600	0.031	8.49	7	1.017	1.30	91.09	3.4×10^{-6}	0.498
8	2.69	0.600	0.031	8.49	8	1.029	1.49	93.39	3.0×10^{-6}	0.494
9	2.41	0.601	0.032	8.5	8*	0.0	1.49	0.00	0.0	0.0

* Track ends before TDU can occur

Table C.12 Key results for the EddR Po16 Co64 (see Section 6.2) track for each pulse cycle.

	Pulse				Interpulse					
TP	M [$M_\odot$]	M_{core} [$M_\odot$]	M_{PDCZ} [$M_\odot$]	T_{PDCZ} [K]	TDU	λ	C/O	$\Delta t_{interpulse}$ [kyr]	M_{pocket} [$M_\odot$]	τ_{pocket} [mb^{-1}]
1	2.96	0.609	0.034	8.37	0	0.0	0.31	63.86	0.0	0.0
2	2.96	0.611	0.031	8.38	0	0.0	0.31	66.16	0.0	0.0
3	2.95	0.615	0.034	8.42	1	0.565	0.37	71.03	9.9×10^{-6}	0.022
4	2.95	0.618	0.036	8.44	2	0.844	0.51	77.78	0.0	0.0
5	2.94	0.620	0.037	8.46	3	1.057	0.74	84.99	8.0×10^{-6}	0.225
6	2.93	0.621	0.037	8.47	4	1.217	1.01	92.91	9.5×10^{-6}	0.137
7	2.88	0.621	0.038	8.48	5	1.250	1.27	100.85	5.9×10^{-6}	0.464
8	2.74	0.620	0.038	8.48	6	1.214	1.51	106.47	7.6×10^{-6}	0.506
9	2.47	0.619	0.038	8.49	7	1.173	1.74	47.23	4.0×10^{-6}	0.116

Table C.13 Key results for the EddR Po16 Co64 FEoS (see Section 6.2) track for each pulse cycle.

	Pulse				Interpulse					
TP	M [$M_\odot$]	M_{core} [$M_\odot$]	M_{PDCZ} [$M_\odot$]	T_{PDCZ} [K]	TDU	λ	C/O	$\Delta t_{interpulse}$ [kyr]	M_{pocket} [$M_\odot$]	τ_{pocket} [mb^{-1}]
1	2.96	0.588	0.028	8.39	1	0.0	0.34	67.42	8.4×10^{-8}	0.009
2	2.96	0.590	0.029	8.42	2	1.174	0.47	75.11	6.1×10^{-6}	0.081
3	2.95	0.591	0.031	8.45	3	1.333	0.73	89.05	7.7×10^{-6}	0.448
4	2.94	0.591	0.033	8.47	4	1.367	1.06	104.31	9.0×10^{-6}	0.573
5	2.88	0.590	0.035	8.49	5	1.276	1.36	115.40	4.7×10^{-6}	0.523
6	2.72	0.589	0.036	8.49	6	1.242	1.64	123.95	4.5×10^{-6}	0.484
7	2.41	0.588	0.037	8.50	6*	0.0	1.64	0.00	0.0	0.0

* Track ends before TDU can occur

Table C.14 Key results for the EddR Po16 Co64 Diff (see Section 6.2) track for each pulse cycle.

	Pulse				Interpulse					
TP	M [$M_\odot$]	M_{core} [$M_\odot$]	M_{PDCZ} [$M_\odot$]	T_{PDCZ} [K]	TDU	λ	C/O	$\Delta t_{interpulse}$ [kyr]	M_{pocket} [$M_\odot$]	τ_{pocket} [mb^{-1}]
1	2.96	0.604	0.049	8.38	0	0.0	0.31	52.12	0.0	0.0
2	2.96	0.612	0.033	8.36	0	0.0	0.31	59.17	0.0	0.0
3	2.96	0.614	0.034	8.39	0	0.0	0.31	62.69	0.0	0.0
4	2.95	0.617	0.036	8.42	0	0.0	0.31	66.14	0.0	0.0
5	2.95	0.622	0.036	8.43	1	0.451	0.36	68.84	3.0×10^{-5}	0.0016
6	2.94	0.625	0.036	8.45	2	0.748	0.50	73.07	2.8×10^{-5}	0.0034
7	2.93	0.628	0.036	8.46	3	1.025	0.71	78.15	2.5×10^{-5}	0.0025
8	2.92	0.629	0.036	8.47	4	1.199	0.94	84.09	1.8×10^{-5}	0.0001
9	2.91	0.629	0.036	8.48	5	1.255	1.17	91.22	1.6×10^{-5}	0.0001
10	2.79	0.628	0.036	8.49	6	1.224	1.38	96.43	1.6×10^{-5}	0.0001
11	2.54	0.626	0.036	8.49	7	1.178	1.58	60.95	1.4×10^{-5}	0.0001

Table C.15 Key results for the EddR Po16 Co64 VW (see Section 6.2) track for each pulse cycle.

	Pulse				Interpulse					
TP	M [$M_\odot$]	M_{core} [$M_\odot$]	M_{PDCZ} [$M_\odot$]	T_{PDCZ} [K]	TDU	λ	C/O	$\Delta t_{interpulse}$ [kyr]	M_{pocket} [$M_\odot$]	τ_{pocket} [mb^{-1}]
1	2.98	0.607	0.03	8.34	0	0.0	0.31	57.26	0.0	0.0
2	2.98	0.608	0.032	8.37	0	0.0	0.31	65.17	0.0	0.0
3	2.98	0.612	0.035	8.41	0	0.0	0.31	68.73	0.0	0.0
4	2.98	0.616	0.035	8.43	1	0.545	0.37	72.72	0.0	0.0
5	2.98	0.619	0.036	8.45	2	0.857	0.53	78.95	0.0	0.0
6	2.98	0.621	0.036	8.46	3	1.043	0.75	85.14	0.0	0.0
7	2.98	0.622	0.037	8.47	4	1.222	1.01	92.96	4.6×10^{-6}	0.232
8	2.98	0.622	0.037	8.48	5	1.251	1.25	100.90	6.2×10^{-6}	0.193
9	2.97	0.621	0.037	8.48	6	1.226	1.45	106.93	5.3×10^{-6}	0.515
10	2.97	0.620	0.038	8.49	7	1.195	1.64	111.32	4.5×10^{-6}	0.470
11	2.96	0.618	0.038	8.49	8	1.175	1.80	113.99	4.8×10^{-6}	0.447
12	2.88	0.616	0.038	8.49	9*	0.0	1.80	0.0	0.0	0.0

* Track ends before TDU can occur

Table C.16 Key results for the LcyP Po16 Co64 (see Section 6.2) track for each pulse cycle.

	Pulse				Interpulse					
TP	M [$M_\odot$]	M_{core} [$M_\odot$]	M_{PDCZ} [$M_\odot$]	T_{PDCZ} [K]	TDU	λ	C/O	$\Delta t_{interpulse}$ [kyr]	M_{pocket} [$M_\odot$]	τ_{pocket} [mb^{-1}]
1	2.96	0.606	0.030	8.34	0	0.0	0.31	58.48	0.0	0.0
2	2.96	0.607	0.032	8.38	0	0.0	0.31	66.10	0.0	0.0
3	2.95	0.61	0.035	8.41	0	0.0	0.31	69.63	0.0	0.0
4	2.95	0.615	0.036	8.43	1	0.546	0.37	73.53	0.0	0.0
5	2.94	0.618	0.036	8.45	2	0.814	0.53	79.59	7.5×10^{-6}	0.0
6	2.93	0.621	0.037	8.46	3	1.085	0.76	86.46	6.8×10^{-6}	0.010
7	2.92	0.621	0.037	8.47	4	1.213	1.02	94.42	1.0×10^{-5}	0.241
8	2.85	0.621	0.038	8.48	5	1.229	1.27	101.38	5.8×10^{-6}	0.178
9	2.70	0.620	0.038	8.48	6	1.227	1.50	107.23	4.9×10^{-6}	0.502
10	2.38	0.619	0.038	8.49	6*	0.0	1.50	0.00	0.0	0.0

* Track ends before TDU can occur

Table C.17 Key results for the EddR P016 C128 (see Section 6.2) track for each pulse cycle.

	Pulse				Interpulse					
TP	M [$M_\odot$]	M_{core} [$M_\odot$]	M_{PDCZ} [$M_\odot$]	T_{PDCZ} [K]	TDU	λ	C/O	$\Delta t_{\text{interpulse}}$ [kyr]	M_{pocket} [$M_\odot$]	τ_{pocket} [mb^{-1}]
1	2.96	0.608	0.031	8.36	0	0.0	0.31	59.03	0.0	0.0
2	2.96	0.610	0.032	8.38	0	0.0	0.31	65.23	0.0	0.0
3	2.95	0.614	0.034	8.41	1	0.712	0.38	71.12	1.4×10^{-5}	0.070
4	2.95	0.616	0.036	8.44	2	0.983	0.55	79.91	1.3×10^{-5}	0.172
5	2.94	0.618	0.037	8.46	3	1.189	0.82	89.36	1.8×10^{-5}	0.221
6	2.93	0.619	0.038	8.47	4	1.298	1.11	98.95	2.5×10^{-5}	0.123
7	2.85	0.618	0.039	8.48	5	1.309	1.39	108.71	1.3×10^{-5}	0.041
8	2.69	0.616	0.039	8.48	6	1.277	1.65	116.11	1.2×10^{-5}	0.020
9	2.31	0.614	0.039	8.49	6*	0.0	1.65	0.00	0.0	0.0

* Track ends before TDU can occur

C.2 *s*-process Yield Tables

Table C.18 and Table C.19 show the net yields and overproduction factors for select light isotopes for each *s*-process model.

Table C.18 The net yields for select light isotopes for all *s*-process tracks. The yields all have untis of solar mass.

Label	^{7}Li	^{12}C	^{13}C	^{14}N	^{16}O	^{17}O	^{19}F	^{22}Ne	^{23}Na	^{24}Mg	^{26}Mg	^{27}Al
EddR P008 C016	-2.29E-8	1.47E-2	1.23E-4	4.50E-3	3.47E-4	3.66E-5	5.41E-7	9.79E-4	6.94E-5	-4.29E-5	8.73E-6	-6.42E-7
EddR P008 C016 Diff	-2.29E-8	1.49E-2	1.23E-4	4.51E-3	2.23E-4	3.67E-5	4.79E-7	8.81E-4	7.00E-5	-4.30E-5	7.43E-6	-2.39E-6
LucyP P008 C016	-2.29E-8	1.45E-2	1.24E-4	4.51E-3	3.05E-4	3.67E-5	5.44E-7	9.60E-4	7.11E-5	-4.30E-5	8.42E-6	-6.94E-7
EddR P008 C064	-2.32E-8	2.08E-2	1.23E-4	4.56E-3	7.49E-4	3.53E-5	1.13E-6	1.44E-3	7.61E-5	-4.35E-5	6.55E-6	-6.63E-7
EddR P008 C064 FEoS	-2.37E-8	2.04E-2	1.25E-4	4.67E-3	1.98E-3	4.04E-5	9.69E-7	1.39E-3	7.91E-5	-4.45E-5	5.21E-6	-2.50E-6
EddR P008 C064 Diff	-2.32E-8	1.74E-2	1.25E-4	4.57E-3	4.08E-4	3.72E-5	7.76E-7	1.19E-3	7.28E-5	-4.35E-5	4.88E-6	-2.43E-6
LucyP P008 C064 Diff	-2.31E-8	1.74E-2	1.24E-4	4.54E-3	1.05E-3	3.70E-5	6.48E-7	1.08E-3	7.25E-5	-4.33E-5	5.03E-6	-2.48E-6
LucyP P008 C064	-2.32E-8	1.75E-2	1.25E-4	4.57E-3	8.58E-4	3.72E-5	6.97E-7	1.09E-3	7.29E-5	-4.36E-5	4.90E-6	-2.48E-6
EddR P008 C128	-2.33E-8	1.97E-2	1.24E-4	4.57E-3	7.83E-4	3.72E-5	9.41E-7	1.34E-3	7.46E-5	-4.36E-5	6.55E-6	-8.84E-7
EddR P016 C016	-2.30E-8	1.74E-2	1.24E-4	4.53E-3	4.45E-3	3.69E-5	4.15E-7	1.05E-3	7.21E-5	-4.32E-5	1.59E-5	-2.39E-6
EddR P016 C016 FEoS	-2.35E-8	1.80E-2	1.27E-4	4.63E-3	2.01E-3	4.00E-5	5.51E-7	1.10E-3	7.42E-5	-4.41E-5	9.74E-6	-2.49E-6
EddR P016 C064	-2.33E-8	2.57E-2	1.23E-4	4.58E-3	4.37E-3	3.54E-5	8.78E-7	1.57E-3	7.89E-5	-4.37E-5	1.49E-5	-5.69E-7
EddR P016 C064	-2.38E-8	2.04E-2	1.26E-4	4.69E-3	1.78E-3	4.06E-5	7.79E-7	1.23E-3	7.73E-5	-4.49E-5	5.27E-6	-2.51E-6
EddR P016 C064 Diff	-2.32E-8	2.37E-2	1.23E-4	4.56E-3	6.67E-3	3.71E-5	6.48E-7	1.38E-3	7.67E-5	-4.35E-5	2.20E-5	-4.72E-7
EddR P016 C064 VW	-2.34E-8	3.30E-2	1.21E-4	4.37E-3	7.48E-3	3.51E-5	2.27E-6	2.87E-3	9.53E-5	-4.39E-5	2.94E-5	2.30E-6
LucyP P016 C064	-2.34E-8	2.00E-2	1.26E-4	4.59E-3	4.63E-3	3.74E-5	4.32E-7	1.13E-3	7.35E-5	-4.38E-5	1.18E-5	-2.46E-6
EddR P016 C128	-2.34E-8	2.23E-2	1.24E-4	4.60E-3	4.61E-3	3.75E-5	6.28E-7	1.31E-3	7.57E-5	-4.39E-5	9.48E-6	-2.46E-6

Table C.19 The overproduction factors for select light isotopes for all *s*-process tracks.

Label	^{7}Li	^{12}C	^{13}C	^{14}N	^{16}O	^{17}O	^{19}F	^{22}Ne	^{23}Na	^{24}Mg	^{26}Mg	^{27}Al
EddR P008 C016	1.10E-2	3.14	2.51	3.23	1.02	5.85	1.55	3.35	1.84	9.66E-1	1.05	9.95E-1
EddR P008 C016 Diff	1.10E-2	3.16	2.51	3.23	1.01	5.85	1.48	3.11	1.84	9.66E-1	1.04	9.83E-1
LucyP P008 C016	1.10E-2	3.11	2.51	3.23	1.01	5.85	1.55	3.30	1.85	9.66E-1	1.04	9.95E-1
EddR P008 C064	1.00E-2	3.99	2.49	3.23	1.04	5.62	2.12	4.41	1.90	9.66E-1	1.03	9.95E-1
EddR P008 C064 FEoS	9.32E-3	3.87	2.48	3.24	1.09	6.16	1.94	4.23	1.92	9.66E-1	1.03	9.83E-1
EddR P008 C064 Diff	1.00E-2	3.49	2.51	3.23	1.02	5.85	1.77	3.81	1.86	9.66E-1	1.03	9.83E-1
LucyP P008 C064 Diff	1.00E-2	3.51	2.51	3.23	1.05	5.85	1.65	3.56	1.86	9.66E-1	1.03	9.83E-1
LucyP P008 C064	1.00E-2	3.51	2.51	3.23	1.04	5.85	1.69	3.57	1.86	9.66E-1	1.03	9.83E-1
EddR P008 C128	1.00E-2	3.82	2.49	3.23	1.04	5.85	1.93	4.17	1.88	9.66E-1	1.03	9.94E-1
EddR P016 C016	1.09E-2	3.51	2.51	3.23	1.22	5.85	1.42	3.51	1.86	9.66E-1	1.08	9.84E-1
EddR P016 C016 FEoS	9.71E-3	3.54	2.51	3.24	1.10	6.16	1.54	3.57	1.87	9.66E-1	1.05	9.83E-1
EddR P016 C064	1.00E-2	4.67	2.49	3.23	1.21	5.61	1.87	4.70	1.93	9.66E-1	1.08	9.96E-1
EddR P016 C064	1.29E-2	3.84	2.48	3.23	1.08	6.13	1.75	3.81	1.89	9.66E-1	1.03	9.83E-1
EddR P016 C064 Diff	1.00E-2	4.40	2.48	3.23	1.32	5.85	1.64	4.28	1.91	9.66E-1	1.12	9.97E-1
EddR P016 C064 VW	1.01E-2	5.70	2.45	3.12	1.36	5.54	3.24	7.74	2.12	9.66E-1	1.15	1.02
LucyP P016 C064	9.93E-3	3.85	2.51	3.23	1.22	5.85	1.43	3.66	1.87	9.66E-1	1.06	9.83E-1
EddR P016 C128	9.83E-3	4.17	2.48	3.23	1.22	5.85	1.62	4.07	1.89	9.66E-1	1.05	9.83E-1

Bibliography

Abia, C., & Wallerstein, G. 1998. Heavy-Element Abundances in Seven SC Stars and Several Related Stars. *Monthly Notices of the Royal Astronomical Society*, **293**(Jan.), 89–106.

Abia, C., Busso, M., Gallino, R., Domínguez, I., Straniero, O., & Isern, J. 2001. The 85Kr S-Process Branching and the Mass of Carbon Stars. *The Astrophysical Journal*, **559**(Oct.), 1117–1134.

Alpher, R. A., Bethe, H., & Gamow, G. 1948. The Origin of Chemical Elements. *Physical Review*, **73**(7), 803–804.

Althaus, Leandro G., Camisassa, María E., Miller Bertolami, Marcelo M., Córsico, Alejandro H., & García-Berro, Enrique. 2015. White Dwarf Evolutionary Sequences for Low-Metallicity Progenitors: The Impact of Third Dredge-Up. *Astronomy & Astrophysics*, **576**(Apr.), A9.

Anders, Evan H., & Pedersen, May G. 2023. Convective Boundary Mixing in Main-Sequence Stars: Theory and Empirical Constraints. *Galaxies*, **11**(Apr.), 56.

Angelou, George C, Bellinger, Earl P, Hekker, Saskia, Mints, Alexey, Elsworth, Yvonne, Basu, Sarbani, & Weiss, Achim. 2020. Convective Boundary Mixing in Low- and Intermediate-Mass Stars – I. Core Properties from Pressure-Mode Asteroseismology. *Monthly Notices of the Royal Astronomical Society*, **493**(4), 4987–5004.

Angulo, C., Arnould, M., Rayet, M., Descouvemont, P., Baye, D., Leclercq-Willain, C., Coc, A., Barhoumi, S., Aguer, P., Rolfs, C., Kunz, R., Hammer, J. W., Mayer, A., Paradellis, T., Kossionides, S., Chronidou, C., Spyrou, K., degl'Innocenti, S., Fiorentini, G., Ricci, B., Zavatarelli, S., Providencia, C., Wolters, H., Soares, J., Grama, C., Rahighi, J., Shotter, A., & Lamehi Rachti, M. 1999. A Compilation of Charged-Particle Induced Thermonuclear Reaction Rates. *Nuclear Physics A*, **656**(Aug.), 3–183.

Aoki, Wako, Norris, John E., Ryan, Sean G., Beers, Timothy C., & Ando, Hiroyasu. 2002a. The Chemical Composition of Carbon-rich, Very Metal Poor Stars: A

New Class of Mildly Carbon Rich Objects without Excess of Neutron-Capture Elements. *The Astrophysical Journal*, **567**(Mar.), 1166–1182.

Aoki, Wako, Ryan, Sean G., Norris, John E., Beers, Timothy C., Ando, Hiroyasu, & Tsangarides, Stelios. 2002b. A Subaru/High Dispersion Spectrograph Study of Lead (Pb) Abundances in Eight s-Process Element-rich, Metal-poor Stars. *The Astrophysical Journal*, **580**(Dec.), 1149–1158.

Aoki, Wako, Bisterzo, Sara, Gallino, Roberto, Beers, Timothy C., Norris, John E., Ryan, Sean G., & Tsangarides, Stelios. 2006. Carbon-Enhanced Metal-poor Stars: Osmium and Iridium Abundances in the Neutron-Capture-enhanced Subgiants CS 31062-050 and LP 625-44. *The Astrophysical Journal*, **650**(Oct.), L127–L130.

Aoki, Wako, Beers, Timothy C., Christlieb, Norbert, Norris, John E., Ryan, Sean G., & Tsangarides, Stelios. 2007. Carbon-Enhanced Metal-poor Stars. I. Chemical Compositions of 26 Stars. *The Astrophysical Journal*, **655**(Jan.), 492–521.

Aoki, Wako, Beers, Timothy C., Sivarani, Thirupathi, Marsteller, Brian, Lee, Young Sun, Honda, Satoshi, Norris, John E., Ryan, Sean G., & Carollo, Daniela. 2008. Carbon-Enhanced Metal-Poor Stars. III. Main-Sequence Turnoff Stars from the SDSS SEGUE Sample. *The Astrophysical Journal*, **678**(May), 1351–1371.

Arlandini, Claudio, Käppeler, Franz, Wisshak, Klaus, Gallino, Roberto, Lugaro, Maria, Busso, Maurizio, & Straniero, Oscar. 1999. Neutron Capture in Low-Mass Asymptotic Giant Branch Stars: Cross Sections and Abundance Signatures. *The Astrophysical Journal*, **525**(Nov.), 886–900.

Arnett, W. D., & Truran, J. W. 1969. Carbon-Burning Nucleosynthesis at Constant Temperature. *The Astrophysical Journal*, **157**(July), 339.

Arp, Halton C., Baum, William A., & Sandage, Allan R. 1953. The Color-Magnitude Diagram of the Globular Cluster M 92. *The Astronomical Journal*, **58**(Feb.), 4.

Aston, F. W. 1919. The Constitution of the Elements. **104**(2616), 393.

Aston, F. W. 1920a. The Constitution of the Elements. **105**(2627), 8.

Aston, F. W. 1920b. The Constitution of the Elements. **105**(2644), 547.

Aston, F. W. 1920c. The Constitution of the Elements. **106**(2667), 468.

Aston, F. W. 1921. Isotopes and Atomic Weights. **107**(2689), 334–338.

Aston, F. W. 1922. The Atoms of Matter; Their Size, Number, and Construction. **110**(2769), 702–705.

Aston, F. W. 1924. Atomic Species and Their Abundance on the Earth. *Nature*, **113**(Mar.), 393–395.

Atkinson, R. D. E., & Houtermans, F. G. 1929. Zur Frage Der Aufbaumöglichkeit Der Elemente in Sternen. *Zeitschrift fur Physik*, **54**(Sept.), 656–665.

Bader, Georg, & Deuflhard, Peter. 1983. A Semi-Implicit Mid-Point Rule for Stiff Systems of Ordinary Differential Equations. *Numerische Mathematik*, **41**(3), 373–398.

Baker, C. P., & Holloway, M.G. 1947. *Note on the Origin of the Term "Barn"*. Tech. rept. 523. Los Alamos Scientific Laboratory.

Bao, Z. Y., & Käppeler, F. 1987. Neutron Capture Cross Sections for S-Process Studies. *Atomic Data and Nuclear Data Tables*, **36**(Jan.), 411.

Bao, Z. Y., Beer, H., Käppeler, F., Voss, F., Wisshak, K., & Rauscher, T. 2000. Neutron Cross Sections for Nucleosynthesis Studies. *Atomic Data and Nuclear Data Tables*, **76**(Sept.), 70–154.

Bartlett, James H. 1932. Nuclear Structure. *Nature*, **130**(July), 165.

Battich, T., Miller Bertolami, M. M., Serenelli, A. M., Justham, S., & Weiss, A. 2023. A Self-Synthesized Origin for Heavy Metals in Hot Subdwarf Stars. *Astronomy & Astrophysics*, **680**(Dec.), L13.

Battino, U., Pignatari, M., Ritter, C., Herwig, F., Denisenkov, P., Den Hartogh, J. W., Trappitsch, R., Hirschi, R., Freytag, B., Thielemann, F., & Paxton, B. 2016. Application of a Theory and Simulation-based Convective Boundary Mixing Model for AGB Star Evolution and Nucleosynthesis. *The Astrophysical Journal*, **827**(Aug.), 30.

Beer, H., Käppeler, F., & Arcoragi, J. P. 1989. *Maxwellian-Averaged (n,γ) Cross-Section for kT = 30 keV.* Proceedings of the 5th Workshop on Nuclear Astrophysics.

Beers, T. C., Preston, G. W., & Shectman, S. A. 1985. A Search for Stars of Very Low Metal Abundance. I. *The Astronomical Journal*, **90**(Oct.), 2089–2102.

Beers, Timothy C. 1999 (Jan.). Low-Metallicity and Horizontal-Branch Stars in the Halo of the Galaxy. *Page 202 of:* Gibson, Brad K., Axelrod, Rim S., & Putman, Mary E. (eds), *The Third Stromlo Symposium: The Galactic Halo*. Astronomical Society of the Pacific Conference Series, vol. 165.

Beers, Timothy C., & Christlieb, Norbert. 2005. The Discovery and Analysis of Very Metal-Poor Stars in the Galaxy. *Annual Review of Astronomy and Astrophysics*, **43**(Sept.), 531–580.

Beers, Timothy C., Preston, George W., & Shectman, Stephen A. 1992. A Search for Stars of Very Low Metal Abundance. II. *The Astronomical Journal*, **103**(June), 1987.

Bethe, H. A. 1939a. Energy Production in Stars. *Physical Review*, **55**(1), 103–103.

Bethe, H. A. 1939b. Energy Production in Stars. *Physical Review*, **55**(5), 434–456.

Bethe, H. A., & Critchfield, C. L. 1938. The Formation of Deuterons by Proton Combination. *Physical Review*, **54**(Aug.), 248–254.

Bidelman, William P., & Keenan, Philip C. 1951. The Ba II Stars. *The Astrophysical Journal*, **114**(Nov.), 473.

Biermann, L. 1951. Kometenschweife Und Solare Korpuskularstrahlung. **29**(Jan.), 274.

Birge, R. T., & Menzel, D. H. 1931. The Relative Abundance of the Oxygen Isotopes, and the Basis of the Atomic Weight System. *Physical Review*, **37**(June), 1669–1671.

Black, DC, & Pepin, RO. 1969. Trapped Neon in Meteorites—II. *Earth and Planetary Science Letters*, **6**(5), 395–405.

Bladh, S., Liljegren, S., Höfner, S., Aringer, B., & Marigo, P. 2019. An Extensive Grid of DARWIN Models for M-type AGB Stars. I. Mass-loss Rates and Other Properties of Dust-Driven Winds. *Astronomy and Astrophysics*, **626**(June), A100.

Blanco, V. M., McCarthy, M. F., & Blanco, B. M. 1980. Carbon and Late M-type Stars in the Magellanic Clouds. *The Astrophysical Journal*, **242**(Dec.), 938–964.

Bloecker, T. 1995. Stellar Evolution of Low and Intermediate-Mass Stars. I. Mass Loss on the AGB and Its Consequences for Stellar Evolution. *Astronomy and Astrophysics*, **297**(May), 727.

Bohr, Aage, & Mottelson, Ben R. 1953a. Interpretation of Isomeric Transitions of Electric Quadrupole Type. *Physical Review*, **89**(1), 316–317.

Bohr, Aage, & Mottelson, Ben R. 1953b. Rotational States in Even-Even Nuclei. *Physical Review*, **90**(4), 717–719.

Bohr, N. 1909. Determination of the Surface-Tension of Water by the Method of Jet Vibration. *Philosophical Transactions of the Royal Society of London Series A*, **209**(Jan.), 281–317.

Bohr, N, & Kalckar, F. 1937. *Kgl. Danske Vid. Selskab, Math. Phys. Medd., 14*.

Bohr, Niels. 1913. On the Constitutions of Atoms and Molecules. Pt. I. *Philosophical Magazine*, **26**(Dec.), 1–25.

Bohr, Niels. 1936. Neutron Capture and Nuclear Constitution. *Nature*, **137**(Feb.), 344–348.

Boothroyd, Arnold I., & Sackmann, I. Juliana. 1988a. Low-Mass Stars. II. The Core Mass–Luminosity Relations for Low-Mass Stars. *The Astrophysical Journal*, **328**(May), 641.

Boothroyd, Arnold I., & Sackmann, I. Juliana. 1988b. Low-Mass Stars. III. Low-Mass Stars with Steady Mass Loss: Up to the Asymptotic Giant Branch and through the Final Thermal Pulses. *The Astrophysical Journal*, **328**(May), 653.

Boothroyd, Arnold I., & Sackmann, I. Juliana. 1988c. Low-Mass Stars. IV. The Production of Carbon Stars. *The Astrophysical Journal*, **328**(May), 671.

Bossini, D., Miglio, A., Salaris, M., Vrard, M., Cassisi, S., Mosser, B., Montalbán, J., Girardi, L., Noels, A., Bressan, A., Pietrinferni, A., & Tayar, J. 2017. Kepler Red-Clump Stars in the Field and in Open Clusters: Constraints on Core Mixing. *Monthly Notices of the Royal Astronomical Society*, **469**(Aug.), 4718–4725.

Brahe, T. 1573. De Nova et Nullius Aevi Memoria Prius Visa Stella, Iam Pridem Anno a Nato Christo 1572, Mense Novembri Primum Conspecta, Contemplatio Mathematica. *Hafniae, Laurentius.(Kopenhagen)*.

Brecht, Bertolt. 2013. *Leben Des Galilei: Schauspiel*. Suhrkamp Verlag.

Brogaard, K., Arentoft, T., Miglio, A., Casali, G., Thomsen, J. S., Tailo, M., Montalbán, J., Grisoni, V., Willett, E., Stokholm, A., Grundahl, F., Stello, D., & Sandquist, E. L. 2023 (Aug.). *An Asteroseismic Age Estimate of the Open Cluster NGC 6866 Using Kepler and Gaia*.

Burbidge, E. Margaret, Burbidge, G. R., Fowler, William A., & Hoyle, F. 1957. Synthesis of the Elements in Stars. *Reviews of Modern Physics*, **29**(Jan.), 547–650.

Busso, M., Gallino, R., Lambert, D. L., Raiteri, C. M., & Smith, V. V. 1992. Nucleosynthesis and Mixing on the Asymptotic Giant Branch. I. MS and S Stars with and without TC. *The Astrophysical Journal*, **399**(Nov.), 218.

Busso, M., Lambert, D. L., Beglio, L., Gallino, R., Raiteri, C. M., & Smith, V. V. 1995. Nucleosynthesis and Mixing on the Asymptotic Giant Branch. II. Carbon and Barium Stars in the Galactic Disk. *The Astrophysical Journal*, **446**(June), 775.

Busso, M., Gallino, R., & Wasserburg, G. J. 1999. Nucleosynthesis in Asymptotic Giant Branch Stars: Relevance for Galactic Enrichment and Solar System Formation. *Annual Review of Astronomy and Astrophysics*, **37**, 239–309.

Busso, Maurizio, Gallino, Roberto, Lambert, David L., Travaglio, Claudia, & Smith, Verne V. 2001. Nucleosynthesis and Mixing on the Asymptotic Giant Branch. III. Predicted and Observed s-Process Abundances. *The Astrophysical Journal*, **557**(Aug.), 802–821.

Cameron, A. G. W. 1955. Origin of Anomalous Abundances of the Elements in Giant Stars. *The Astrophysical Journal*, **121**(Jan.), 144.

Cameron, A. G. W. 1960. New Neutron Sources of Possible Astrophysical Importance. *The Astronomical Journal*, **65**(Jan.), 485.

Cameron, A. G. W., & Fowler, W. A. 1971. Lithium and the S-PROCESS in Red-Giant Stars. *The Astrophysical Journal*, **164**(Feb.), 111.

Campbell, S. W., & Lattanzio, J. C. 2008. Evolution and Nucleosynthesis of Extremely Metal-Poor and Metal-Free Low- and Intermediate-Mass Stars. I. Stellar Yield Tables and the CEMPs. *Astronomy and Astrophysics*, **490**(2), 769–776.

Campbell, S. W., Lugaro, M., & Karakas, A. I. 2010. Evolution and Nucleosynthesis of Extremely Metal-Poor and Metal-Free Low- and Intermediate-Mass Stars. II. s-Process Nucleosynthesis during the Core He Flash. *Astronomy and Astrophysics*, **522**(Nov.), L6.

Chadwick, J. 1932. The Existence of a Neutron. *Proceedings of the Royal Society of London Series A*, **136**(June), 692–708.

Chieffi, Alessandro, Domínguez, Inma, Limongi, Marco, & Straniero, Oscar. 2001. Evolution and Nucleosynthesis of Zero-Metal Intermediate-Mass Stars. *The Astrophysical Journal*, **554**(June), 1159–1174.

Chladni, Ernst Florens Friedrich. 1794. *Ueber Den Ursprung Der von Pallas Gefundenen Und Anderer Ihr Ähnlicher Eisenmassen Und Über Einige Damit in Verbindung Stehende Naturerscheinungen*. bey Johann Friedrich Hartknoch.

Choplin, A., Siess, L., & Goriely, S. 2021. The Intermediate Neutron Capture Process. I. Development of the i-Process in Low-Metallicity Low-Mass AGB Stars. *Astronomy & Astrophysics, Volume 648, id.A119, <NUMPAGES>16</NUMPAGES> pp.*, **648**(Apr.), A119.

Choplin, A., Siess, L., & Goriely, S. 2022. The Intermediate Neutron Capture Process. III. The i-Process in AGB Stars of Different Masses and Metallicities without Overshoot. *Astronomy and Astrophysics*, **667**(Nov.), A155.

Choplin, A., Siess, L., Goriely, S., & Martinet, S. 2024 (Feb.). *The Intermediate Neutron Capture Process. V. The i-Process in AGB Stars with Overshoot*.

Christy-Sackmann, I. Juliana, Smith, Richard L., & Despain, Keith H. 1974. Surface Abundances Resulting from Deep Mixing. **66**(Jan.), 123.

Ciani, G. F., Csedreki, L., Rapagnani, D., Aliotta, M., Balibrea-Correa, J., Barile, F., Bemmerer, D., Best, A., Boeltzig, A., Broggini, C., Bruno, C. G., Caciolli, A., Cavanna, F., Chillery, T., Colombetti, P., Corvisiero, P., Cristallo, S., Davinson, T., Depalo, R., Di Leva, A., Elekes, Z., Ferraro, F., Fiore, E., Formicola, A., Fülöp, Zs., Gervino, G., Guglielmetti, A., Gustavino, C., Gyürky, Gy., Imbriani, G., Junker, M., Lugaro, M., Marigo, P., Masha, E., Menegazzo, R., Mossa, V., Pantaleo, F. R., Paticchio, V., Perrino, R., Piatti, D., Prati, P., Schiavulli, L., Stöckel, K., Straniero, O., Szücs, T., Takács, M. P., Terrasi, F., Vescovi, D., Zavatarelli, S., & LUNA Collaboration. 2021. Direct Measurement of the C 13 (α ,n)O 16 Cross Section into the s -Process Gamow Peak. *Physical Review Letters*, **127**(Oct.), 152701.

Clayton, D. D., Fowler, W. A., Hull, T. E., & Zimmerman, B. A. 1961. Neutron Capture Chains in Heavy Element Synthesis. *Annals of Physics*, **12**(Mar.), 331–408.

Clayton, Donald D. 1983. *Principles of Stellar Evolution and Nucleosynthesis*.

Clayton, Donald D., & Rassbach, M. E. 1967. Termination of the S-PROCESS. *The Astrophysical Journal*, **148**(Apr.), 69.

Clayton, Donald D., & Ward, Richard A. 1974. S-Process Studies: Exact Evaluation of an Exponential Distribution of Exposures. *The Astrophysical Journal*, **193**(Oct.), 397–400.

Clegg, R. E. S., Lambert, D. L., & Bell, R. A. 1979. Isotopes of Titanium in Cool Stars. *The Astrophysical Journal*, **234**(Nov.), 188–199.

Cohen, Judith G., Christlieb, Norbert, Qian, Y. Z., & Wasserburg, G. J. 2003. Abundance Analysis of HE 2148-1247, A Star with Extremely Enhanced Neutron Capture Elements. *The Astrophysical Journal*, **588**(May), 1082–1098.

Cohen, Judith G., Christlieb, Norbert, Thompson, Ian, McWilliam, Andrew, Shectman, Stephen, Reimers, Dieter, Wisotzki, Lutz, & Kirby, Evan. 2013. Normal and Outlying Populations of the Milky Way Stellar Halo at [Fe/H] <-2. *The Astrophysical Journal*, **778**(Nov.), 56.

Condon, Edward. 1925. The Age of the Stars. *Proceedings of the National Academy of Science*, **11**(Feb.), 125–130.

Couch, Richard G., Schmiedekamp, Ann B., & Arnett, W. David. 1974. S-PROCESS Nucleosynthesis in Massive Stars: Core Helium Burning. *The Astrophysical Journal*, **190**(May), 95–100.

Cowan, J. J., & Rose, W. K. 1977. Production of 14C and Neutrons in Red Giants. *The Astrophysical Journal*, **212**(Feb.), 149–158.

Cristallo, S., Straniero, O., Gallino, R., Herwig, F., Chieffi, A., Limongi, M., & Busso, M. 2001. The Formation of the 13C Pocket in Asymptotic Giant Branch Stars and Related Nucleosynthesis. *Nuclear Physics A*, **688**(May), 217–220.

Cristallo, S., Piersanti, L., Straniero, O., Gallino, R., Domínguez, I., & Käppeler, F. 2009a. Asymptotic-Giant-Branch Models at Very Low Metallicity. *Publications of the Astronomical Society of Australia*, **26**(Aug.), 139–144.

Cristallo, S., Straniero, O., Gallino, R., Piersanti, L., Domínguez, I., & Lederer, M. T. 2009b. EVOLUTION, NUCLEOSYNTHESIS, AND YIELDS OF LOW-MASS ASYMPTOTIC GIANT BRANCH STARS AT DIFFERENT METALLICITIES. *The Astrophysical Journal*, **696**(1), 797–820.

Cristallo, S., Piersanti, L., Straniero, O., Gallino, R., Domínguez, I., Abia, C., Di Rico, G., Quintini, M., & Bisterzo, S. 2011. Evolution, Nucleosynthesis, and Yields of Low-mass Asymptotic Giant Branch Stars at Different Metallicities. II. The FRUITY Database. *The Astrophysical Journal Supplement Series*, **197**(Dec.), 17.

Cristallo, S., Straniero, O., Piersanti, L., & Gobrecht, D. 2015. Evolution, Nucleosynthesis, and Yields of AGB Stars at Different Metallicities. III. Intermediate-mass Models, Revised Low-mass Models, and the Ph-FRUITY Interface. *The Astrophysical Journal Supplement Series*, **219**(Aug.), 40.

Cristallo, S., Karinkuzhi, D., Goswami, A., Piersanti, L., & Gobrecht, D. 2016. Constraints of the Physics of Low-mass AGB Stars from CH and CEMP Stars. *The Astrophysical Journal*, **833**(Dec.), 181.

Cruz, M. A., Serenelli, A., & Weiss, A. 2013. S-Process in Extremely Metal-Poor, Low-Mass Stars. *Astronomy & Astrophysics*, **559**(Nov.), A4.

Cseh, B., Világos, B., Roriz, M. P., Pereira, C. B., D'Orazi, V., Karakas, A. I., Soós, B., Drake, N. A., Junqueira, S., & Lugaro, M. 2022. Barium Stars as Tracers of S-Process Nucleosynthesis in AGB Stars. I. 28 Stars with Independently Derived AGB Mass. *Astronomy and Astrophysics*, **660**(Apr.), A128.

Cummings, Jeffrey D., Kalirai, Jason S., Tremblay, P. E., Ramirez-Ruiz, Enrico, & Choi, Jieun. 2018. The White Dwarf Initial-Final Mass Relation for Progenitor Stars from 0.85 to 7.5 M ⊙. *The Astrophysical Journal*, **866**(Oct.), 21.

Curie, Irène, & Joliot, F. 1932. New Evidence for the Neutron. *Nature*, **130**(July), 57.

Cyburt, Richard H., Amthor, A. Matthew, Ferguson, Ryan, Meisel, Zach, Smith, Karl, Warren, Scott, Heger, Alexander, Hoffman, R. D., Rauscher, Thomas, Sakharuk, Alexander, Schatz, Hendrik, Thielemann, F. K., & Wiescher, Michael. 2010. THE JINA REACLIB DATABASE: ITS RECENT UPDATES AND IMPACT ON TYPE-I X-RAY BURSTS. *The Astrophysical Journal Supplement Series*, **189**(1), 240.

Dardelet, L., Ritter, C., Prado, P., Heringer, E., Higgs, C., Sandalski, S., Jones, S., Denisenkov, P., Venn, K., Bertolli, M., Pignatari, M., Woodward, P., & Herwig, F. 2014 (Jan.). I Process and CEMP-s+r Stars. *Page 145 of: XIII Nuclei in the Cosmos (NIC XIII)*.

Denissenkov, Pavel A., & Tout, Christopher A. 2003. Partial Mixing and Formation of the 13C Pocket by Internal Gravity Waves in Asymptotic Giant Branch Stars. *Monthly Notices of the Royal Astronomical Society*, **340**(Apr.), 722–732.

Denissenkov, Pavel A., Herwig, Falk, Battino, Umberto, Ritter, Christian, Pignatari, Marco, Jones, Samuel, & Paxton, Bill. 2017. I-Process Nucleosynthesis and Mass Retention Efficiency in He-shell Flash Evolution of Rapidly Accreting White Dwarfs. *The Astrophysical Journal*, **834**(Jan.), L10.

Denissenkov, Pavel A., Herwig, Falk, Woodward, Paul, Andrassy, Robert, Pignatari, Marco, & Jones, Samuel. 2019. The I-Process Yields of Rapidly Accreting White Dwarfs from Multicycle He-shell Flash Stellar Evolution Models with Mixing Parametrizations from 3D Hydrodynamics Simulations. *Monthly Notices of the Royal Astronomical Society*, **488**(Sept.), 4258–4270.

d'Escourt Atkinson, R. 1931a. Atomic Synthesis and Stellar Energy. *The Astrophysical Journal*, **73**(May), 250.

d'Escourt Atkinson, R. 1931b. Atomic Synthesis and Stellar Energy. II. *The Astrophysical Journal*, **73**(June), 308.

d'Escourt Atkinson, R. 1936. Atomic Synthesis and Stellar Energy. III. *The Astrophysical Journal*, **84**(July), 73.

Despain, K. H. 1977. Convective Neutron and S-Process Element Production in Deeply Mixed Envelopes. *The Astrophysical Journal*, **212**(Mar.), 774–790.

Despain, K. H., & Scalo, J. M. 1976. A Criterion for the Maximum Extent of Flash-Driven Convection. *The Astrophysical Journal*, **208**(Sept.), 789–796.

Deutsch, Armin J. 1956. The Circumstellar Envelope of Alpha Herculis. **123**(Mar.), 210.

Dillmann, I, Heil, M, Käppeler, F, Plag, R, Rauscher, T, & Thielemann, F-K. 2006. KADoNiS-The Karlsruhe Astrophysical Database of Nucleosynthesis in Stars. *Pages 123–127 of: AIP Conference Proceedings*, vol. 819. American Institute of Physics.

Dillmann, Iris, Plag, Ralf, Heil, Michael, Käppeler, Franz, & Rauscher, Thomas. 2008. Present Status of the KADoNiS Database. *arXiv preprint arXiv:0806.2016*.

Dillmann, Iris, Plag, Ralf, Käppeler, Franz, Mengoni, Alberto, Heinz, Christian, & Pignatari, Marco. 2014. The New KADoNiS v1. 0 and Its Influence on the Weak s-Process Nucleosynthesis. *In: PoS (NIC XIII Conf.)*, vol. 57.

Dunbar, D. N., Pixley, R. E., Wenzel, W. A., & Whaling, W. 1953. The 7.68-Mev State in C12. *Physical Review*, **92**(Nov.), 649–650.

Eddington, A. S. 1916. On the Radiative Equilibrium of the Stars. *Monthly Notices of the Royal Astronomical Society*, **77**(Nov.), 16–35.

Eddington, A. S. 1920. The Internal Constitution of the Stars. *The Observatory*, **43**(Oct.), 341–358.

Eddington, A. S. 1921. Das Strahlungsgleichgewicht Der Sterne. *Zeitschrift fur Physik*, **7**(Dec.), 351–397.

Eddington, Arthur Stanley. 1927. *Stars and Atoms*. Clarendon Press.

Eddington, Arthur Stanley. 1959. *The Internal Constitution of the Stars*. Dover Publication.

Einstein, A. 1905a. Ist Die Trägheit Eines Körpers von Seinem Energieinhalt Abhängig? *Annalen der Physik*, **323**(Jan.), 639–641.

Einstein, A. 1905b. Über Die von Der Molekularkinetischen Theorie Der Wärme Geforderte Bewegung von in Ruhenden Flüssigkeiten Suspendierten Teilchen. *Annalen der Physik*, **322**(Jan.), 549–560.

El-Badry, Kareem, Rix, Hans-Walter, & Weisz, Daniel R. 2018. An Empirical Measurement of the Initial-Final Mass Relation with Gaia White Dwarfs. *The Astrophysical Journal*, **860**(June), L17.

Elsasser, Walter M. 1934. Sur Le Principe de Pauli Dans Les Noyaux-II. *J. phys. radium*, **5**(8), 389–397.

Encrenaz, Therese, Bibring, J. P., & Blanc, M. 2004. *The Solar System*. Springer Berlin.

Eriksson, K., Nowotny, W., Höfner, S., Aringer, B., & Wachter, A. 2014. Synthetic Photometry for Carbon-Rich Giants. IV. An Extensive Grid of Dynamic Atmosphere and Wind Models. *Astronomy and Astrophysics*, **566**(June), A95.

Ferguson, Jason W., Alexander, David R., Allard, France, Barman, Travis, Bodnarik, Julia G., Hauschildt, Peter H., Heffner-Wong, Amanda, & Tamanai, Akemi. 2005. Low-Temperature Opacities. *The Astrophysical Journal*, **623**(1), 585–596.

Fowler, W. A., Burbidge, G. R., & Burbidge, E. Margaret. 1955. Stellar Evolution and the Synthesis of the Elements. *The Astrophysical Journal*, **122**(Sept.), 271.

Freytag, B., Ludwig, H. G., & Steffen, M. 1996. Hydrodynamical Models of Stellar Convection. The Role of Overshoot in DA White Dwarfs, A-type Stars, and the Sun. *Astronomy & Astrophysics*, **313**(Sept.), 497–516.

Fujimoto, M. Y. 1977. On the Origin of R-Type Carbon Stars: Possibility of Hydrogen Mixing during Helium Flicker. *Publications of the Astronomical Society of Japan*, **29**(Jan.), 331–350.

Fujimoto, M. Y., Iben, Jr., I., Chieffi, A., & Tornambe, A. 1984. Hydrogen and Helium Burning in Zero-Metal Asymptotic Giant Branch Stars and the Existence of Thresholds (in Core Mass and CNO Abundance) for the Occurrence of Helium Shell Flashes. *The Astrophysical Journal*, **287**(Dec.), 749–760.

Fujimoto, Masayuki Y., Iben, Jr., Icko, & Hollowell, David. 1990. Helium Flashes and Hydrogen Mixing in Low-Mass Population III Stars. *The Astrophysical Journal*, **349**(Feb.), 580.

Fujimoto, Masayuki Y., Ikeda, Yasufumi, & Iben, Jr., Icko. 2000. The Origin of Extremely Metal-poor Carbon Stars and the Search for Population III. *The Astrophysical Journal*, **529**(Jan.), L25–L28.

Gallino, R., Busso, M., Picchio, G., & Raiteri, C. M. 1990. On the Astrophysical Interpretation of Isotope Anomalies in Meteoritic SiC Grains. *Nature*, **348**(Nov.), 298–302.

Gallino, Roberto, Arlandini, Claudio, Busso, Maurizio, Lugaro, Maria, Travaglio, Claudia, Straniero, Oscar, Chieffi, Alessandro, & Limongi, Marco. 1998. Evolution and Nucleosynthesis in Low-Mass Asymptotic Giant Branch Stars. II. Neutron Capture and the S-Process. *The Astrophysical Journal*, **497**(Apr.), 388–403.

Gamow, G. 1928. Zur Quantentheorie Des Atomkernes. *Zeitschrift fur Physik*, **51**(Mar.), 204–212.

Gamow, G. 1930. Mass Defect Curve and Nuclear Constitution. *Proceedings of the Royal Society of London. Series A, Containing Papers of a Mathematical and Physical Character*, **126**(803), 632–644.

Gamow, George. 1961. *The Creation of the Universe.* Viking Press.

Girardi, L., Bertelli, G., Bressan, A., Chiosi, C., & Vallenari, A. 1999. Testing Stellar Structure and Evolution with GAIA. *Baltic Astronomy*, **8**(Jan.), 265–269.

Goldschmidt, V. M. 1930. Geochemische Verteilungsgesetze Und Kosmische Häufigkeit Der Elemente. *Naturwissenschaften*, **18**(Nov.), 999–1013.

Goldschmidt, Victor Moritz. 1937. The Principles of Distribution of Chemical Elements in Minerals and Rocks. The Seventh Hugo Müller Lecture, Delivered before the Chemical Society on March 17th, 1937. *Journal of the Chemical Society (Resumed)*, 655–673.

Goriely, S., & Mowlavi, N. 2000. Neutron-Capture Nucleosynthesis in AGB Stars. *Astronomy and Astrophysics*, **362**(Oct.), 599–614.

Goriely, S., & Siess, L. 2018. Sensitivity of the S-Process Nucleosynthesis in AGB Stars to the Overshoot Model. *Astronomy and Astrophysics*, **609**(Jan.), A29.

Goriely, S., Siess, L., & Choplin, A. 2021. The Intermediate Neutron Capture Process. II. Nuclear Uncertainties. *Astronomy and Astrophysics*, **654**(Oct.), A129.

Greenstein, J. L. 1954 (Jan.). Nuclear Reactions Affecting the Abundance of the Elements : General Survey. *Page 307 of: Liege International Astrophysical Colloquia*. Liege International Astrophysical Colloquia, vol. 5.

Grevesse, N., & Sauval, A. J. 1998. Standard Solar Composition. *Space Science Reviews*, **85**(May), 161–174.

Gurney, R. W., & Condon, E. U. 1929. Quantum Mechanics and Radioactive Disintegration. *Physical Review*, **33**(Feb.), 127–140.

Haas, Arthur Erich. 1910. Uber Die Elektrodynamische Bedeutung Des Planckschen Strahlungsgesetzes Und Uber Eine Neue Bestimmung Des Elektrischen Elementarquantums Und Der Dimension Des Wasserstoffatoms. *Sitzungsberichte der kaiserlichen Akademie der Wissenschaft Wien*, 119–144.

Habing, Harm J., & Olofsson, Hans. 2004. *Asymptotic Giant Branch Stars*. Springer.

Hampel, Melanie, Stancliffe, Richard J., Lugaro, Maria, & Meyer, Bradley S. 2016. The Intermediate Neutron-capture Process and Carbon-enhanced Metal-poor Stars. *The Astrophysical Journal*, **831**(Nov.), 171.

Hansen, T., Hansen, C. J., Christlieb, N., Beers, T. C., Yong, D., Bessell, M. S., Frebel, A., García Pérez, A. E., Placco, V. M., Norris, J. E., & Asplund, M. 2015. An Elemental Assay of Very, Extremely, and Ultra-metal-poor Stars. *The Astrophysical Journal*, **807**(July), 173.

Harkins, William D. 1917. The Structure of Atoms and the Evolution of the Elements as Related to the Composition of the Nuclei of Atoms. *Science*, **46**(Nov.), 443–448.

Harris, M. J., Fowler, W. A., Caughlan, G. R., & Zimmerman, B. A. 1983. Thermonuclear Reaction Rates, III. *Annual Review of Astronomy and Astrophysics*, **21**(Jan.), 165–176.

Haxel, Otto, Jensen, J. Hans, & Suess, Hans E. 1949. On the "Magic Numbers" in Nuclear Structure. *Physical Review*, **75**(June), 1766–1766.

Heil, M., Detwiler, R., Azuma, R. E., Couture, A., Daly, J., Görres, J., Käppeler, F., Reifarth, R., Tischhauser, P., Ugalde, C., & Wiescher, M. 2008. The 13C(α,n) Reaction and Its Role as a Neutron Source for the s Process. *Physical Review C*, **78**(Aug.), 025803.

Heisenberg, W. 2007. *Physics and Philosophy: The Revolution in Modern Science*. Harper Perennial Modern Thought. HarperCollins.

Henyey, L. G., Wilets, L., Böhm, K. H., Lelevier, R., & Levee, R. D. 1959. A Method for Automatic Computation of Stellar Evolution. *The Astrophysical Journal*, **129**(May), 628.

Henyey, L. G., Forbes, J. E., & Gould, N. L. 1964. A New Method of Automatic Computation of Stellar Evolution. *The Astrophysical Journal*, **139**(Jan.), 306.

Hertzsprung, E. 1911. Number 63. Zweiundzwanzigsten Bandes Erstes Stuck. Uber Die Verwendung Photographischer Effecktiver Wellenlangen Zur Bestimmung von Farbenaquivalenten. *Publikationen des Astrophysikalischen Observatoriums zu Potsdam*, **22**(Jan.), A1–A40.1.

Herwig, F. 2000. The Evolution of AGB Stars with Convective Overshoot. *Astronomy and Astrophysics*, **360**(Aug.), 952–968.

Herwig, F., Bloecker, T., Schoenberner, D., & El Eid, M. 1997. Stellar Evolution of Low and Intermediate-Mass Stars. IV. Hydrodynamically-based Overshoot and Nucleosynthesis in AGB Stars. *Astronomy and Astrophysics*, **324**(Aug.), L81–L84.

Herwig, Falk, & Austin, Sam M. 2004. Nuclear Reaction Rates and Carbon Star Formation. *The Astrophysical Journal*, **613**(Sept.), L73–L76.

Herwig, Falk, & Langer, Norbert. 2001. Formation of the Neutron Donor 13C in AGB Stars by Overshoot and Rotation. *Memorie della Societa Astronomica Italiana*, **72**(Jan.), 277–287.

Herwig, Falk, Langer, Norbert, & Lugaro, Maria. 2003. The S-Process in Rotating Asymptotic Giant Branch Stars. *The Astrophysical Journal*, **593**(Aug.), 1056–1073.

Hill, V., Barbuy, B., Spite, M., Spite, F., Cayrel, R., Plez, B., Beers, T. C., Nordström, B., & Nissen, P. E. 2000. Heavy-Element Abundances in the CH/CN-strong Very Metal-Poor Stars CS 22948-27 and CS 29497-34. *Astronomy and Astrophysics*, **353**(Jan.), 557–568.

Hix, W. Raphael, & Meyer, Bradley S. 2006. Thermonuclear Kinetics in Astrophysics. *Nuclear Physics A*, **777**(Oct.), 188–207.

Hoffleit, Dorrit. 1997. History of the Discovery of Mira Stars. *Journal of the American Association of Variable Star Observers (JAAVSO)*, **25**(Jan.), 115–136.

Hollowell, David, & Iben, Jr., Icko. 1988. Nucleosynthesis of Solar System Material in a Low-Mass, Low-Metallicity Asymptotic Giant Branch Star. *The Astrophysical Journal*, **333**(Oct.), L25.

Hoppe, Peter. 2010. Stardust In Primitive Solar System Materials. *AIP Conference Proceedings*, **1213**(1), 84–94.

Hoyle, F. 1946. The Synthesis of the Elements from Hydrogen ⋆. *Monthly Notices of the Royal Astronomical Society*, **106**(5), 343–383.

Hoyle, F. 1954. On Nuclear Reactions Occuring in Very Hot STARS.I. the Synthesis of Elements from Carbon to Nickel. *The Astrophysical Journal Supplement Series*, **1**(Sept.), 121.

HSL. 2013. *A Collection of Fortran Codes for Large Scale Scientific Computation*.

Iben, I., & Renzini, A. 1983. Asymptotic Giant Branch Evolution and Beyond. *Annual Review of Astronomy and Astrophysics*, **21**, 271–342.

Iben, Jr., I. 1975a. Neon-22 as a Neutron Source, Light Elements as Modulators, and s-Process Nucleosynthesis in a Thermally Pulsing Star. *The Astrophysical Journal*, **196**(Mar.), 549–558.

Iben, Jr., I. 1975b. Thermal Pulses: P-Capture, Alpha -Capture, s-Process Nucleosynthesis; and Convective Mixing in a Star of Intermediate Mass. *The Astrophysical Journal*, **196**(Mar.), 525–547.

Iben, Jr., I. 1976. Further Adventures of a Thermally Pulsating Star. *The Astrophysical Journal*, **208**(Aug.), 165–176.

Iben, Jr., I. 1977. Thermal Pulse and Interpulse Properties of Intermediate-Mass Stellar Models with Carbon-Oxygen Cores of Mass 0.96, 1.16, and 1.36 M Sun. *The Astrophysical Journal*, **217**(Nov.), 788–798.

Iben, Jr., I. 1982. Low Mass Asymptotic Giant Branch Evolution. I. *The Astrophysical Journal*, **260**(Sept.), 821–837.

Iben, Jr., I., & Renzini, A. 1982. On the Formation of Carbon Star Characteristics and the Production of Neutron-Rich Isotopes in Asymptotic Giant Branch Stars of Small Core Mass. *The Astrophysical Journal*, **263**(Dec.), L23–L27.

Iben, Jr., Icko, & Rood, Robert T. 1970. Metal-Poor Stars. III. on the Evolution of Horizontal-Branch Stars. *The Astrophysical Journal*, **161**(Aug.), 587.

Iglesias, Carlos A., & Rogers, Forrest J. 1996. Updated Opal Opacities. *Astrophysics Journal*, **464**(June), 943.

Iliadis, Christian. 2007. *Nuclear Physics of Stars*. Wiley-VCH Verlag.

Irwin, Alan W. 2012. FreeEOS: Equation of State for Stellar Interiors Calculations. *Astrophysics Source Code Library*, Nov., ascl:1211.002.

Ivans, Inese I., Sneden, Chris, Gallino, Roberto, Cowan, John J., Preston, George W., & Bisterzo, Sara. 2005 (Jan.). CS29497-030 Abundance Constraints on Neutron-Capture Nucleosynthesis. *Pages 467–472 of:* Hill, Vanessa, Francois, Patrick, & Primas, Francesca (eds), *From Lithium to Uranium: Elemental Tracers of Early Cosmic Evolution*. IAU Symposium Proceedings of the International Astronomical Union 228, vol. 228.

Iwamoto, Nobuyuki. 2009. Evolution and Nucleosynthesis in Extremely Metal-Poor, Asymptotic Giant Branch Stars. *Publications of the Astronomical Society of Australia*, **26**(Aug.), 145–152.

Iwamoto, Nobuyuki, Kajino, Toshitaka, Mathews, Grant J., Fujimoto, Masayuki Y., & Aoki, Wako. 2004. Flash-Driven Convective Mixing in Low-Mass, Metal-deficient Asymptotic Giant Branch Stars: A New Paradigm for Lithium Enrichment and a Possible s-Process. *The Astrophysical Journal*, **602**(Feb.), 377–388.

Jadhav, M., Pignatari, M., Herwig, F., Zinner, E., Gallino, R., & Huss, G. R. 2013. Relics of Ancient Post-AGB Stars in a Primitive Meteorite. *The Astrophysical Journal*, **777**(Nov.), L27.

Jaeger, M., Kunz, R., Mayer, A., Hammer, J. W., Staudt, G., Kratz, K. L., & Pfeiffer, B. 2001. 22Ne(α,n)25Mg: The Key Neutron Source in Massive Stars. *Physical Review Letters*, **87**(Nov.), 202501.

Jeans, J. H. 1924. The Ages and Masses of the Stars. *Nature*, **114**(Dec.), 828–829.

Jeans, J. H. 1925a. The Ages and Masses of the Stars. *Nature*, **115**(Feb.), 297–298.

Jeans, J. H. 1925b. A Theory of Stellar Evolution. *Monthly Notices of the Royal Astronomical Society*, **85**(June), 914–933.

Jensen, J Hans D. 1965. The History of the Theory of Structure of the Atomic Nucleus. *Science*, **147**(3664), 1419–1423.

Jensen, J. Hans D., Sueß, Hans E., & Haxel, Otto. 1949. Modellmäßige Deutung Der Ansgezeichneten Nucleonenzahlen Im Kernbau. *Naturwissenschaften*, **36**(May), 155–156.

Jones, S., Ritter, C., Herwig, F., Fryer, C., Pignatari, M., Bertolli, M. G., & Paxton, B. 2016. H Ingestion into He-burning Convection Zones in Super-AGB Stellar Models as a Potential Site for Intermediate Neutron-Density Nucleosynthesis. *Monthly Notices of the Royal Astronomical Society*, **455**(Feb.), 3848–3863.

Jonsell, K., Barklem, P. S., Gustafsson, B., Christlieb, N., Hill, V., Beers, T. C., & Holmberg, J. 2006. The Hamburg/ESO R-process Enhanced Star Survey (HERES). III. HE 0338-3945 and the Formation of the r + s Stars. *Astronomy and Astrophysics*, **451**(May), 651–670.

Kaeppeler, F., Wiescher, M., Giesen, U., Goerres, J., Baraffe, I., El Eid, M., Raiteri, C. M., Busso, M., Gallino, R., Limongi, M., & Chieffi, A. 1994. Reaction Rates for 18O(Alpha , Gamma) 22Ne, 22Ne(Alpha , Gamma) 26Mg, and 22Ne(Alpha , n) 25Mg in Stellar Helium Burning and s-Process Nucleosynthesis in Massive Stars. *The Astrophysical Journal*, **437**(Dec.), 396.

Kappeler, F., Beer, H., & Wisshak, K. 1989. S-Process Nucleosynthesis-Nuclear Physics and the Classical Model. *Reports on Progress in Physics*, **52**(Aug.), 945–1013.

Käppeler, F., Gallino, R., Bisterzo, S., & Aoki, Wako. 2011. The s Process: Nuclear Physics, Stellar Models, and Observations. *Reviews of Modern Physics*, **83**(Jan.), 157–194.

Karakas, A. I. 2010. Updated Stellar Yields from Asymptotic Giant Branch Models. *Monthly Notices of the Royal Astronomical Society*, **403**(Apr.), 1413–1425.

Karakas, A. I., Lattanzio, J. C., & Pols, O. R. 2002. Parameterising the Third Dredge-up in Asymptotic Giant Branch Stars. *Publications of the Astronomical Society of Australia*, **19**(Jan.), 515–526.

Karakas, Amanda, & Lattanzio, John C. 2007. Stellar Models and Yields of Asymptotic Giant Branch Stars. *Publications of the Astronomical Society of Australia*, **24**(Oct.), 103–117.

Karakas, Amanda I., & Lugaro, Maria. 2016. Stellar Yields from Metal-rich Asymptotic Giant Branch Models. *The Astrophysical Journal*, **825**(July), 26.

Karinkuzhi, D., Van Eck, S., Goriely, S., Siess, L., Jorissen, A., Merle, T., Escorza, A., & Masseron, T. 2021. Low-Mass Low-Metallicity AGB Stars as an Efficient i-Process Site Explaining CEMP-rs Stars. *Astronomy and Astrophysics*, **645**(Jan.), A61.

Keenan, Philip C. 1942. The Spectra of CH Stars. *The Astrophysical Journal*, **96**(July), 101.

Kippenhahn, Rudolf, Weigert, Alfred, & Weiss, Achim. 2013. *Stellar Structure and Evolution*. Astronomy and Astrophysics Library. Springer Berlin, Heidelberg.

Kirchhoff, G., & Bunsen, R. 1860. Chemische Analyse Durch Spectralbeobachtungen. *Annalen der Physik*, **186**(Jan.), 161–189.

Kitsikis, A. 2008 (Apr.). *Theoretical AGB and Post-AGB Models for Synthetic Population Studies*. Ph.D. thesis, Ludwig-Maximilians-Universitaet Muenchen.

Kitsikis, A., & Weiss, A. 2007 (Nov.). AGB and Post-AGB Stellar Evolution: Theoretical Models for Synthetic Population Studies. *Page 99 of:* Kerschbaum, F., Charbonnel, C., & Wing, R. F. (eds), *Why Galaxies Care about AGB Stars: Their Importance as Actors and Probes*. Astronomical Society of the Pacific Conference Series, vol. 378.

Kobayashi, Chiaki, Karakas, Amanda I., & Lugaro, Maria. 2020. The Origin of Elements from Carbon to Uranium. *The Astrophysical Journal*, **900**(Sept.), 179.

Kovetz, A., Prialnik, D., & Shaviv, G. 1984. Diffusion in a Thermally Pulsating Star. *The Astrophysical Journal*, **282**(July), 584–590.

Kragh, Helge. 2013. Big Bang: The Etymology of a Name. *Astronomy and Geophysics*, **54**(Apr.), 2.28–2.30.

Krane, K.S., & Halliday, D. 1987. *Introductory Nuclear Physics*. Wiley.

Kunz, R., Fey, M., Jaeger, M., Mayer, A., Hammer, J. W., Staudt, G., Harissopulos, S., & Paradellis, T. 2002. Astrophysical Reaction Rate of 12C(α, γ)16O. *The Astrophysical Journal*, **567**(Mar.), 643–650.

Lai, David K., Johnson, Jennifer A., Bolte, Michael, & Lucatello, Sara. 2007. Carbon and Strontium Abundances of Metal-poor Stars*. *The Astrophysical Journal*, **667**(2), 1185.

Lambert, David L., Smith, Verne V., Busso, Maurizio, Gallino, Roberto, & Straniero, Oscar. 1995. The Chemical Composition of Red Giants. IV. The Neutron Density at the s-Process Site. *The Astrophysical Journal*, **450**(Sept.), 302.

Langer, N., Heger, A., Wellstein, S., & Herwig, F. 1999. Mixing and Nucleosynthesis in Rotating TP-AGB Stars. *Astronomy and Astrophysics*, **346**(June), L37–L40.

Lattanzio, John C. 1987. The Formation of a 1.5 Msun Carbon Star with M Bol = -4.4. *The Astrophysical Journal*, **313**(Feb.), L15.

Lattanzio, John C. 1989. Carbon Dredge-up in Low-Mass Stars and Solar Metallicity Stars. *The Astrophysical Journal*, **344**(Sept.), L25.

Lau, H. H. B., Gil-Pons, P., Doherty, C., & Lattanzio, J. 2012. The End of Super AGB and Massive AGB Stars. I. The Instabilities That Determine the Final Mass of AGB Stars. *Astronomy and Astrophysics*, **542**(June), A1.

Lau, Herbert H. B., Stancliffe, Richard J., & Tout, Christopher A. 2009. The Evolution of Low-Metallicity Asymptotic Giant Branch Stars and the Formation of Carbon-Enhanced Metal-Poor Stars. *Monthly Notices of the Royal Astronomical Society*, **396**(June), 1046–1057.

Liu, Nan, Savina, Michael R., Davis, Andrew M., Gallino, Roberto, Straniero, Oscar, Gyngard, Frank, Pellin, Michael J., Willingham, David G., Dauphas, Nicolas, Pignatari, Marco, Bisterzo, Sara, Cristallo, Sergio, & Herwig, Falk. 2014. Barium Isotopic Composition of Mainstream Silicon Carbides from Murchison: Constraints for s-Process Nucleosynthesis in Asymptotic Giant Branch Stars. *The Astrophysical Journal*, **786**(May), 66.

Löbling, L., Rauch, T., Miller Bertolami, M. M., Todt, H., Friederich, F., Ziegler, M., Werner, K., & Kruk, J. W. 2019. Spectral Analysis of the Hybrid PG 1159-Type Central Stars of the Planetary Nebulae Abell 43 and NGC 7094. *Monthly Notices of the Royal Astronomical Society*, **489**(Oct.), 1054–1071.

Lodders, Katharina. 2021. Relative Atomic Solar System Abundances, Mass Fractions, and Atomic Masses of the Elements and Their Isotopes, Composition of the Solar Photosphere, and Compositions of the Major Chondritic Meteorite Groups. *Space Science Reviews*, **217**(Apr.), 44.

Luck, R. E., & Bond, Howard E. 1991. Subgiant CH Stars. II. Chemical Compositions and the Evolutionary Connection with Barium Stars. *The Astrophysical Journal Supplement Series*, **77**(Dec.), 515.

Lucy, L. B. 1976. Mass Loss by Cool Carbon Stars. *The Astrophysical Journal*, **205**(Apr.), 482–491.

Lucy, Leon B. 1967. Formation of Planetary Nebulae. *The Astronomical Journal*, **72**(Jan.), 813.

Lugaro, M., Ott, U., & Kereszturi, Á. 2018. Radioactive Nuclei from Cosmochronology to Habitability. *Progress in Particle and Nuclear Physics*, **102**(Sept.), 1–47.

Lugaro, Maria, Herwig, Falk, Lattanzio, John C., Gallino, Roberto, & Straniero, Oscar. 2003. S-Process Nucleosynthesis in Asymptotic Giant Branch Stars: A Test for Stellar Evolution. *The Astrophysical Journal*, **586**(Apr.), 1305–1319.

Lugaro, Maria, Ugalde, Claudio, Karakas, Amanda I., Görres, Joachim, Wiescher, Michael, Lattanzio, John C., & Cannon, Robert C. 2004. Reaction Rate Uncertainties and the Production of 19F in Asymptotic Giant Branch Stars. *The Astrophysical Journal*, **615**(Nov.), 934–946.

Lugaro, Maria, Karakas, Amanda I., Stancliffe, Richard J., & Rijs, Carlos. 2012. The S-Process in Asymptotic Giant Branch Stars of Low Metallicity and the Composition of Carbon-enhanced Metal-poor Stars. *The Astrophysical Journal*, **747**(Mar.), 2.

Lugaro, Maria, Pignatari, Marco, Reifarth, René, & Wiescher, Michael. 2023. The s Process and Beyond. *Annual Review of Nuclear and Particle Science*, **73**(Sept.), 315–340.

Maeder, A., & Meynet, G. 1991. Tables of Isochrones Computed from Stellar Models with Mass Loss and Overshooting. *Astronomy and Astrophysics Supplement Series*, **89**(Sept.), 451.

Magic, Z., Serenelli, A., Weiss, A., & Chaboyer, B. 2010. On Using the Color-Magnitude Diagram Morphology of M67 to Test Solar Abundances. *The Astrophysical Journal*, **718**(Aug.), 1378–1387.

Malaney, R. A. 1986a. Heavy-Element Synthesis in AGB and Post-AGB Stars of Low Mass. *Monthly Notices of the Royal Astronomical Society*, **223**(Dec.), 709–725.

Malaney, R. A. 1986b. Neutron Synthesis in AGB and Post-AGB Stars of Low Mass. *Monthly Notices of the Royal Astronomical Society*, **223**(Dec.), 683–707.

Malaney, Robert A. 1987. The S-Process Nucleosynthesis of Barium Stars. *The Astrophysical Journal*, **321**(Oct.), 832.

Marigo, P. 2002. Asymptotic Giant Branch Evolution at Varying Surface C/O Ratio: Effects of Changes in Molecular Opacities. *Astronomy and Astrophysics*, **387**(May), 507–519.

Marigo, P., Bressan, A., Girardi, L., Aringer, B., Gullieuszik, M., & Groenewegen, M. A. T. 2011 (Sept.). Evolutionary Models for AGB Stars in the Magellanic Clouds. *Page 431 of:* Kerschbaum, F., Lebzelter, T., & Wing, R. F. (eds), *Why Galaxies Care about AGB Stars II: Shining Examples and Common Inhabitants*. Astronomical Society of the Pacific Conference Series, vol. 445.

Marigo, Paola, Bressan, Alessandro, Nanni, Ambra, Girardi, Léo, & Pumo, Maria Letizia. 2013. Evolution of Thermally Pulsing Asymptotic Giant Branch Stars - I. The COLIBRI Code. *Monthly Notices of the Royal Astronomical Society*, **434**(Sept.), 488–526.

Marigo, Paola, Cummings, Jeffrey D., Curtis, Jason Lee, Kalirai, Jason, Chen, Yang, Tremblay, Pier-Emmanuel, Ramirez-Ruiz, Enrico, Bergeron, Pierre, Bladh, Sara, Bressan, Alessandro, Girardi, Léo, Pastorelli, Giada, Trabucchi, Michele, Cheng, Sihao, Aringer, Bernhard, & Tio, Piero Dal. 2020. Carbon Star Formation as Seen through the Non-Monotonic Initial–Final Mass Relation. *Nature Astronomy*, **4**(11), 1102–1110.

Marigo, Paola, Bossini, Diego, Trabucchi, Michele, Addari, Francesco, Girardi, Léo, Cummings, Jeffrey, Pastorelli, Giada, Dal Tio, Piero, Costa, Guglielmo, & Bressan, Alessandro. 2021 (Nov.). *A Fresh Look at AGB Stars in Galactic Open Clusters with Gaia: Impact on Stellar Models and the Initial-Final Mass Relation*.

Masseron, T., Johnson, J. A., Plez, B., van Eck, S., Primas, F., Goriely, S., & Jorissen, A. 2010. A Holistic Approach to Carbon-Enhanced Metal-Poor Stars. *Astronomy and Astrophysics*, **509**(Jan.), A93.

Masseron, Thomas, Johnson, Jennifer A., Lucatello, Sara, Karakas, Amanda, Plez, Bertrand, Beers, Timothy C., & Christlieb, Norbert. 2012. Lithium Abundances in Carbon-enhanced Metal-poor Stars. *The Astrophysical Journal*, **751**(May), 14.

Mattsson, L., Wahlin, R., & Höfner, S. 2010. Dust Driven Mass Loss from Carbon Stars as a Function of Stellar Parameters . I. A Grid of Solar-Metallicity Wind Models. *Astronomy and Astrophysics*, **509**(Jan.), A14.

Maury, Antonia C., & Pickering, Edward C. 1897. Spectra of Bright Stars Photographed with the 11-Inch Draper Telescope as Part of the Henry Draper Memorial. *Annals of Harvard College Observatory*, **28**(Jan.), 1–128.

Mayer, Maria G. 1948. On Closed Shells in Nuclei. *Physical Review*, **74**(Aug.), 235–239.

Mayer, Maria Goeppert. 1949. On Closed Shells in Nuclei. II. *Physical Review*, **75**(June), 1969–1970.

Mayer, Maria Goeppert. 1964. The Shell Model. *Science*, **145**(3636), 999–1006.

McClure, R. D., Fletcher, J. M., & Nemec, J. M. 1980. The Binary Nature of the Barium Stars. *The Astrophysical Journal*, **238**(May), L35–L38.

Merrill, Paul W. 1952. Spectroscopic Observations of Stars of Class S. *The Astrophysical Journal*, **116**(July), 21.

Miller Bertolami, Marcelo M. 2022. A Red Giants' Toy Story. *The Astrophysical Journal*, **941**(Dec.), 149.

Miller Bertolami, Marcelo Miguel. 2016. New Models for the Evolution of Post-Asymptotic Giant Branch Stars and Central Stars of Planetary Nebulae. *Astronomy & Astrophysics*, **588**(Apr.), A25.

Moseley, H.G.J. 1913. XCIII. The High-Frequency Spectra of the Elements. *The London, Edinburgh, and Dublin Philosophical Magazine and Journal of Science*, **26**(156), 1024–1034.

Moseley, H.G.J. 1914. LXXX. The High-Frequency Spectra of the Elements. Part II. *The London, Edinburgh, and Dublin Philosophical Magazine and Journal of Science*, **27**(160), 703–713.

Nagaoka, H. 1904. On a Dynamical System Illustrating the Spectrum Lines and the Phenomena of Radio-activity. *Nature*, **69**(Feb.), 392–393.

Nicholson, J. W. 1912a. The Constitution of the Solar Corona. III. *Monthly Notices of the Royal Astronomical Society*, **72**(9), 729–740.

Nicholson, J. W. 1912b. The Constitution of the Solar Corona. IL. *Monthly Notices of the Royal Astronomical Society*, **72**(8), 677–693.

Nilsson, Sven Gösta. 1955. Binding States of Individual Nucleons in Strongly Deformed Nuclei. **29**(CERN-55-30), 1–69.

Noddack, I., & Noddack, W. 1930. Die Häufigkeit Der Chemischen Elemente. *Die Naturwissenschaften*, **18**(35), 757–764.

Norris, John E., Ryan, Sean G., & Beers, Timothy C. 1997a. Extremely Metal-poor Stars. IV. The Carbon-rich Objects. *The Astrophysical Journal*, **488**(Oct.), 350–363.

Norris, John E., Ryan, Sean G., & Beers, Timothy C. 1997b. Extremely Metal-poor Stars. The Carbon-rich, Neutron Capture Element–poor Object CS 22957-027. *The Astrophysical Journal*, **489**(Nov.), L169.

Olofsson, H., Carlstrom, U., Eriksson, K., Gustafsson, B., & Willson, L. A. 1990. Bright Carbon Stars with Detached Circumstellar Envelopes - A Naturalconsequence of Helium Shell Flashes ? *Astronomy and Astrophysics*, **230**(Apr.), L13–L16.

Ostlie, Dale A., & Cox, Arthur N. 1986. A Linear Survey of the Mira Variable Star Instability Region of the Hertzsprung-Russell Diagram. *The Astrophysical Journal*, **311**(Dec.), 864.

Paczyński, B., & Ziółkowski, J. 1968. On the Origin of Planetary Nebulae and Mira Variables. *Acta Astronomica*, **18**(Jan.), 255.

Pastorelli, Giada, Marigo, Paola, Girardi, Léo, Chen, Yang, Rubele, Stefano, Trabucchi, Michele, Aringer, Bernhard, Bladh, Sara, Bressan, Alessandro, Montalbán, Josefina, Boyer, Martha L., Dalcanton, Julianne J., Eriksson, Kjell, Groenewegen, Martin A. T., Höfner, Susanne, Lebzelter, Thomas, Nanni, Ambra, Rosenfield, Philip, Wood, Peter R., & Cioni, Maria-Rosa L. 2019. Constraining the Thermally Pulsing Asymptotic Giant Branch Phase with Resolved Stellar Populations in the Small Magellanic Cloud. *Monthly Notices of the Royal Astronomical Society*, **485**(June), 5666–5692.

Payne, Cecilia H. 1925a. Astrophysical Data Bearing on the Relative Abundance of the Elements. *Proceedings of the National Academy of Science*, **11**(Mar.), 192–198.

Payne, Cecilia Helena. 1925b (Jan.). *Stellar Atmospheres; a Contribution to the Observational Study of High Temperature in the Reversing Layers of Stars.* Ph.D. thesis.

Peters, James G. 1968. Nucleosynthesis by the S-PROCESS in Stars of 9 and 15 Solar Masses. *The Astrophysical Journal*, **154**(Oct.), 225.

Peters, James G., Fowler, William A., & Clayton, Donald D. 1972. Weak S-PROCESS Irradiations. *The Astrophysical Journal*, **173**(May), 637.

Petkovesk, Marko, Wilf, Herbert, & Zeilberger, Doron. 1996. *A=B*. 1 edn. A K Peters/CRC Press.

Pignatari, M., Herwig, F., Hirschi, R., Bennett, M., Rockefeller, G., Fryer, C., Timmes, F. X., Ritter, C., Heger, A., Jones, S., Battino, U., Dotter, A., Trappitsch, R., Diehl, S., Frischknecht, U., Hungerford, A., Magkotsios, G., Travaglio, C., & Young, P. 2016. NuGrid Stellar Data Set. I.Stellar Yields from H to Bi for Stars

with Metallicities Z = 0.02 and Z = 0.01. *The Astrophysical Journal Supplement Series*, **225**(Aug.), 24.

Placco, Vinicius M., Frebel, Anna, Beers, Timothy C., Karakas, Amanda I., Kennedy, Catherine R., Rossi, Silvia, Christlieb, Norbert, & Stancliffe, Richard J. 2013. Metal-Poor Stars Observed with the Magellan Telescope. I. Constraints on Progenitor Mass and Metallicity of AGB Stars Undergoing s-Process Nucleosynthesis. *The Astrophysical Journal*, **770**(June), 104.

Pols, Onno R., Tout, Christopher A., Lattanzio, John C., & Karakas, Amanda I. 2001 (Jan.). Thermal Pulses and Dredge-up in AGB Stars. *Page 31 of:* Podsiadlowski, Ph., Rappaport, S., King, A. R., D'Antona, F., & Burderi, L. (eds), *Evolution of Binary and Multiple Star Systems*. Astronomical Society of the Pacific Conference Series, vol. 229.

Prialnik, D., Kovetz, A., & Shaviv, G. 1981. The Effect of Diffusion on Asymptotic Branch Evolution. *The Astrophysical Journal*, **247**(July), 225–235.

Professor Sir E. Rutherford F.R.S. 1919. LIV. Collision of α Particles with Light Atoms. IV. An Anomalous Effect in Nitrogen. *The London, Edinburgh, and Dublin Philosophical Magazine and Journal of Science*, **37**(222), 581–587.

Reimers, D. 1975. Circumstellar Absorption Lines and Mass Loss from Red Giants. *Memoires of the Societe Royale des Sciences de Liege*, **8**(Jan.), 369–382.

Remple, B. A., Battich, T., & Weiss, A. 2024. The Impact of Overshoot on the I-Process in AGB Stars. *Astronomy and Astrophysics*, **687**(July), A260.

Remple, Bryce A., Angelou, George C., & Weiss, Achim. 2021. Determining Fundamental Parameters of Detached Double-Lined Eclipsing Binary Systems via a Statistically Robust Machine Learning Method. *Monthly Notices of the Royal Astronomical Society*, **507**(Oct.), 1795–1813.

Renzini, A. 1981. Red Giants as Precursors of Planetary Nebulae. **88**(Jan.), 431–446.

Reynolds, JH, & Turner, G. 1964. Rare Gases in the Chondrite Renazzo. *Journal of Geophysical Research*, **69**(15), 3263–3281.

Rhodes, R. 2012. *The Making of the Atomic Bomb*. Simon & Schuster.

Roederer, Ian U., Preston, George W., Thompson, Ian B., Shectman, Stephen A., Sneden, Christopher, Burley, Gregory S., & Kelson, Daniel D. 2014. A Search for Stars of Very Low Metal Abundance. VI. Detailed Abundances of 313 Metal-poor Stars. *The Astronomical Journal*, **147**(June), 136.

Rogers, F. J., & Nayfonov, A. 2002. Updated and Expanded OPAL Equation-of-State Tables: Implications for Helioseismology. *The Astrophysical Journal*, **576**(2), 1064–1074.

Rose, William K., & Smith, Richard L. 1972. Final Evolution of a Low-Mass Star. II. *The Astrophysical Journal*, **173**(Apr.), 385.

Rosenberg, H. 1910. Über Den Zusammenhang von Helligkeit Und Spektraltypus in Den Plejaden. *Astronomische Nachrichten*, **186**(Oct.), 71.

Rosseland, S. 1924. Electrical State of a Star. *Monthly Notices of the Royal Astronomical Society*, **84**(June), 720–728.

Rossi, Silvia, Beers, Timothy C., & Sneden, Chris. 1999 (Jan.). Carbon Abundances for Metal-Poor Stars Based on Medium-Resolution Spectra. *Page 264 of:* Gibson, Brad K., Axelrod, Rim S., & Putman, Mary E. (eds), *The Third Stromlo Symposium: The Galactic Halo*. Astronomical Society of the Pacific Conference Series, vol. 165.

Russell, H. N. 1925. The Problem of Stellar Evolution. *Nature*, **116**(Aug.), 209–212.

Russell, Henry Norris. 1914. Relations Between the Spectra and Other Characteristics of the Stars. *Popular Astronomy*, **22**(May), 275–294.

Russell, Henry Norris. 1929. On the Composition of the Sun's Atmosphere. *The Astrophysical Journal*, **70**(July), 11.

Russell, Henry Norris. 1934. Molecules in the Sun and Stars. *The Astrophysical Journal*, **79**(Apr.), 317.

Rutherford, E., & Soddy, F. 1903. LX. Radioactive Change. *The London, Edinburgh, and Dublin Philosophical Magazine and Journal of Science*, **5**(29), 576–591.

Rutherford, Ernest. 1911. LXXIX. The Scattering of α and β Particles by Matter and the Structure of the Atom. *The London, Edinburgh, and Dublin Philosophical Magazine and Journal of Science*, **21**(125), 669–688.

Rutherford, Ernest, & Chadwick, James. 1925. XCIX. Scattering of α-Particles by Atomic Nuclei and the Law of Force. *The London, Edinburgh, and Dublin Philosophical Magazine and Journal of Science*, **50**(299), 889–913.

Sackmann, I. J. 1977. What Quenches the Helium Shell Flashes? *The Astrophysical Journal*, **212**(Feb.), 159–170.

Sackmann, I. J. 1980. A New Flash Mixing. *The Astrophysical Journal*, **241**(Oct.), L37–L40.

Sackmann, I. J., & Boothroyd, A. I. 1991 (Jan.). On Low Mass AGB Stars. *Page 275 of:* Michaud, Georges, & Tutukov, A. V. (eds), *Evolution of Stars: The Photospheric Abundance Connection*. Proceedings of the 145th Symposium of the International Astronomical Union, vol. 145.

Sackmann, I. J., Smith, R. L., & Despain, K. H. 1974. Carbon and Eruptive Stars: Surface Enrichment of Lithium, Carbon, Nitrogen, and 13C by Deep Mixing. *The Astrophysical Journal*, **187**(Feb.), 555–574.

Salpeter, E. E. 1954. Electrons Screening and Thermonuclear Reactions. *Australian Journal of Physics*, **7**(Sept.), 373.

Sandage, A., & Walker, M. F. 1966. Three-Color Photometry of the Bright Stars in the Globular Cluster M 92. *The Astrophysical Journal*, **143**(Feb.), 313–326.

Sandage, A. R. 1953. The Color-Magnitude Diagram for the Globular Cluster M 3. *The Astronomical Journal*, **58**(Jan.), 61–75.

Sanders, Robert H. 1967. S-Process Nucleosynthesis in Thermal Relaxation Cycles. *The Astrophysical Journal*, **150**(Dec.), 971.

Sandin, C., Mattsson, L., Chubb, K. L., Ergon, M., & Weilbacher, P. M. 2023. Three-Component Modelling of O-rich AGB Star Winds. I. Effects of Drift Using Forsterite. *Astronomy and Astrophysics*, **677**(Sept.), A27.

Scalo, J. M. 1981 (Jan.). Observations and Theories of Mixing in Red Giants. *Pages 77–114 of:* Iben, I., Jr., & Renzini, A. (eds), *Physical Processes in Red Giants*. Astrophysics and Space Science Library, vol. 88.

Scalo, J. M., & Ulrich, R. K. 1973. Studies of Evolved Stars. I. Plume Mixing in S and N Stars. *The Astrophysical Journal*, **183**(July), 151.

Scalo, J. M., Despain, K. H., & Ulrich, R. K. 1975. Studies of Evolved Stars. V. Nucleosynthesis in Hot-Bottom Convective Envelopes. *The Astrophysical Journal*, **196**(Mar.), 805–817.

Schoenberner, D. 1979. Asymptotic Giant Branch Evolution with Steady Mass Loss. *Astronomy and Astrophysics*, **79**(Oct.), 108–114.

Schumann, T. 1925. The Ages and Masses of the Stars. *Nature*, **115**(Jan.), 120.

Schwarzschild, K. 1906. On the Equilibrium of the Sun's Atmosphere. *Nachrichten von der Königlichen Gesellschaft der Wissenschaften zu Göttingen. Math.-phys. Klasse*, **195**(Jan.), 41–53.

Schwarzschild, M., & Härm, R. 1965. Thermal Instability in Non-Degenerate Stars. *The Astrophysical Journal*, **142**(Oct.), 855.

Schwarzschild, M., & Härm, R. 1967. Hydrogen Mixing by Helium-Shell Flashes. *The Astrophysical Journal*, **150**(Dec.), 961.

Schwarzschild, Martin. 1958. *Structure and Evolution of the Stars*. Princeton University Press.

Secchi, A. 1868. A Catalogue of Spectra of Red Stars. *Monthly Notices of the Royal Astronomical Society*, **28**(May), 196.

Seeger, Philip A., Fowler, William A., & Clayton, Donald D. 1965. Nucleosynthesis of Heavy Elements by Neutron Capture. *The Astrophysical Journal Supplement Series*, **11**(Feb.), 121.

Shakespeare, William. 2001. *Love's Labour's Lost*. Dover Publications.

Shaviv, Giora. 2012. The Synthesis of the Elements. *Astrophysics and Space Science Library*, **387**(Jan.).

Shetye, Shreeya, Van Eck, Sophie, Jorissen, Alain, Goriely, Stephane, Siess, Lionel, Van Winckel, Hans, Plez, Bertrand, Godefroid, Michel, & Wallerstein, George. 2021. S Stars and S-Process in the Gaia Era. II. Constraining the Luminosity of the Third Dredge-up with Tc-rich S Stars. *Astronomy and Astrophysics*, **650**(June), A118.

Shklovskii, I. S. 1957. Once More on the Distances to Planetary Nebulae and the Evolution of Their Nuclei. *Soviet Astronomy*, **1**(June), 397.

Shorin, V. S., Gribunin, V. M., Kononov, V. N., & Sidorova, I. I. 1971. Nucleosynthesis of Elements: S-process. *Astrophysics*, **7**(July), 286–293.

Siess, L. 2007. Evolution of Massive AGB Stars. II. Model Properties at Non-Solar Metallicity and the Fate of Super-AGB Stars. *Astronomy and Astrophysics*, **476**(Dec.), 893–909.

Siess, L., Homan, W., Toupin, S., & Price, D. J. 2022. 3D Simulations of AGB Stellar Winds. I. Steady Winds and Dust Formation. *Astronomy and Astrophysics*, **667**(Nov.), A75.

Sivarani, T., Bonifacio, P., Molaro, P., Cayrel, R., Spite, M., Spite, F., Plez, B., Andersen, J., Barbuy, B., Beers, T. C., Depagne, E., Hill, V., François, P., Nordström, B., & Primas, F. 2004. First Stars IV. CS 29497-030: Evidence for Operation of the s-Process at Very Low Metallicity. *Astronomy and Astrophysics*, **413**(Jan.), 1073–1085.

Smith, Verne V., & Lambert, David L. 1986. The Chemical Composition of Red Giants. II. Helium Burning and the s-Process in the MS and S Stars. *The Astrophysical Journal*, **311**(Dec.), 843.

Smith, Verne V., & Lambert, David L. 1990. The Chemical Composition of Red Giants. III. Further CNO Isotopic and s-Process Abundances in Thermally Pulsing Asymptotic Giant Branch Stars. *The Astrophysical Journal Supplement Series*, **72**(Feb.), 387.

Sneden, Christopher, McWilliam, Andrew, Preston, George W., Cowan, John J., Burris, Debra L., & Armosky, Bradley J. 1996. The Ultra–Metal-poor, Neutron-Capture–rich Giant Star CS 22892-052. *The Astrophysical Journal*, **467**(Aug.), 819.

Society, Royal. 1802. *Philosophical Transactions of the Royal Society of London*. W. Bowyer and J. Nichols for Lockyer Davis, printer to the Royal Society.

Soddy, Frederick. 1913. Intra-Atomic Charge. **92**(2301), 399–400.

Sparks, W. M., & Endal, A. S. 1980. Theoretical Studies of Massive Stars. II - Evolution of a 15 Solar-Mass Star from Carbon Shell Burning to Iron Core Collapse. *The Astrophysical Journal*, **237**(Apr.), 130–141.

Stein, Robert F. 1966. *Stellar Evolution: A Survey with Analytic Models*. Plenum Press.

Stothers, Richard B., & Chin, Chao-Wen. 1992. Stellar Evolution in Blue Populous Clusters of the Small Magellanic Cloud and the Problems of Envelope Semiconvection and Convective Core Overshooting. *The Astrophysical Journal*, **390**(May), 136.

Straniero, O., Gallino, R., Busso, M., Chiefei, A., Raiteri, C. M., Limongi, M., & Salaris, M. 1995. Radiative 13C Burning in Asymptotic Giant Branch Stars and S-Processing. *The Astrophysical Journal*, **440**(Feb.), L85.

Straniero, Oscar, Chieffi, Alessandro, Limongi, Marco, Busso, Maurizio, Gallino, Roberto, & Arlandini, Claudio. 1997. Evolution and Nucleosynthesis in Low-Mass Asymptotic Giant Branch Stars. I. Formation of Population I Carbon Stars. *The Astrophysical Journal*, **478**(Mar.), 332–339.

Straniero, Oscar, Gallino, Roberto, & Cristallo, Sergio. 2006. S Process in Low-Mass Asymptotic Giant Branch Stars. *Nuclear Physics A*, **777**(Oct.), 311–339.

Strömgren, Bengt. 1933. On the Interpretation of the Hertzsprung-Russell-Diagram. Mit 4 Abbildungen. *Zeitschrift fur Astrophysik*, **7**(Jan.), 222.

Suda, T., & Fujimoto, M. Y. 2010. Evolution of Low- and Intermediate-Mass Stars with [Fe/H] <= - 2.5. *Monthly Notices of the Royal Astronomical Society*, **405**(June), 177–193.

Suda, Takuma, Yamada, Shimako, Katsuta, Yutaka, Komiya, Yutaka, Ishizuka, Chikako, Aoki, Wako, & Fujimoto, Masayuki Y. 2011. The Stellar Abundances for Galactic Archaeology (SAGA) Data Base - II. Implications for Mixing and Nucleosynthesis in Extremely Metal-Poor Stars and Chemical Enrichment of the Galaxy. *Monthly Notices of the Royal Astronomical Society*, **412**(Apr.), 843–874.

Suess, Hans E., & Urey, Harold C. 1956. Abundances of the Elements. *Reviews of Modern Physics*, **28**(Jan.), 53–74.

Sugimoto, D. 1970. Mixing between Stellar Envelope and Core in Advanced Phases of Evolution. I —General Treatment and Brief Summary of Results—. *Progress of Theoretical Physics*, **44**(Aug.), 375–388.

Sugimoto, D., & Nomoto, K. 1975. Thermal Instability of Helium-Burning Shell in Stars Evolving toward Carbon-Detonation Supernovae. *Publications of the Astronomical Society of Japan*, **27**(Jan.), 197–213.

Suh, Kyung-Won. 2021. A New Catalog of Asymptotic Giant Branch Stars in Our Galaxy. *The Astrophysical Journal Supplement Series*, **256**(Oct.), 43.

Susmitha, A., Ojha, D. K., Sivarani, T., Ninan, J. P., Bandyopadhyay, A., Surya, Arun, & Unni, Athira. 2021. Optical and NIR Spectroscopy of Cool CEMP Stars to Probe the Nucleosynthesis in Low-Mass AGB Binary System. *Monthly Notices of the Royal Astronomical Society*, **506**(Sept.), 1962–1977.

Sweigart, A. V. 1973. Initial Asymptotic Branch Evolution of Population II Stars. *Astronomy and Astrophysics*, **24**(May), 459.

Sweigart, Allen V. 1974. Do Helium-Shell Flashes Cause Extensive Mixing in Low-Mass Stars? *The Astrophysical Journal*, **189**(Apr.), 289–292.

Thomson, Joseph John. 1904. XXIV. On the Structure of the Atom: An Investigation of the Stability and Periods of Oscillation of a Number of Corpuscles Arranged at Equal Intervals around the Circumference of a Circle; with Application of the Results to the Theory of Atomic Structure. *The London, Edinburgh, and Dublin Philosophical Magazine and Journal of Science*, **7**(39), 237–265.

Thoul, Anne A., Bahcall, John N., & Loeb, Abraham. 1994. Element Diffusion in the Solar Interior. *The Astrophysical Journal*, **421**(Feb.), 828.

Timmes, F. X. 1999. Integration of Nuclear Reaction Networks for Stellar Hydrodynamics. *The Astrophysical Journal Supplement Series*, **124**(Sept.), 241–263.

Truran, J. W., & Iben, Jr., I. 1977. On S-Process Nucleosynthesis in Thermally Pulsing Stars. *The Astrophysical Journal*, **216**(Sept.), 797–810.

Truran, J. W., Hansen, C. J., Cameron, A. G. W., & Gilbert, A. 1966. Thermonuclear Reactions in Medium and Heavy Nuclei. *Canadian Journal of Physics*, **44**(Jan.), 151.

Ulrich, Roger K. 1973 (Jan.). The S-Process in Stars. *Page 139 of:* Schramm, David N., & Arnett, W. David (eds), *Explosive Nucleosynthesis*.

[unknown]. 1932. *Faust. Eine Historie*.

Unsöld, Albrecht. 1928. Über Die Struktur Der Fraunhofersehen Linien Und Die Quantitative Spektralanalyse Der Sonnenatmosphäre. *Zeitschrift fur Physik*, **46**(Nov.), 765–781.

Urey, Harold C., Brickwedde, F. G., & Murphy, G. M. 1932. A Hydrogen Isotope of Mass 2. *Physical Review*, **39**(Jan.), 164–165.

Van Den Broek, A. 1911. The Number of Possible Elements and Mendeléff's "Cubic" Periodic System. *Nature*, **87**(2177), 78–78.

van Loon, J. Th, Cioni, M.-R. L., Zijlstra, A. A., & Loup, C. 2005. An Empirical Formula for the Mass-Loss Rates of Dust-Enshrouded Red Supergiants and Oxygen-Rich Asymptotic Giant Branch Stars. *Astronomy and Astrophysics*, **438**(1), 273–289.

Vanture, Andrew D. 1992. The CH Stars. III. Heavy Element Abundances. *The Astronomical Journal*, **104**(Nov.), 1997–2004.

Vassiliadis, E., & Wood, P. R. 1993. Evolution of Low- and Intermediate-Mass Stars to the End of the Asymptotic Giant Branch with Mass Loss. *The Astrophysical Journal*, **413**(Aug.), 641.

Ventura, P., García-Hernández, D. A., Dell'Agli, F., D'Antona, F., Mészáros, Sz., Lucatello, S., Di Criscienzo, M., Shetrone, M., Tailo, M., Tang, Baitian, & Zamora, O. 2016. Evidence of AGB Pollution in Galactic Globular Clusters from the Mg-al Anticorrelations Observed by the APOGEE Survey. **831**(L17), L17.

von Fraunhofer, J. 1817. *Denkschriften Der Königlichen Akademie Der Wissenschaften Zu München*. Die Akademie.

von Weizsäcker, Carl Friedrich Freiherr. 1938. *Über Elementumwandlungen Im Inneren Der Sterne. II*. S. Hirzel.

von Weizsäcker, CF. 1937. Über Elementumwandlungen Im Innern Der Sterne. I. *I (On*, **38**, 176–191.

Wachter, A., Schröder, K.-P., Winters, J. M., Arndt, T. U., & Sedlmayr, E. 2002. An Improved Mass-Loss Description for Dust-Driven Superwinds and Tip-AGB Evolution Models. *Astronomy and Astrophysics*, **384**(Mar.), 452–459.

Wagenhuber, J., & Weiss, A. 1994. Termination of AGB-evolution by Hydrogen Recombination. *Astronomy and Astrophysics*, **290**(Oct.), 807–814.

Wagoner, Robert V. 1969. Synthesis of the Elements Within Objects Exploding from Very High Temperatures. *The Astrophysical Journal Supplement Series*, **18**(June), 247.

Wagstaff, G., & Weiss, A. 2018. Influence of the Outer Boundary Condition on Models of AGB Stars. *Monthly Notices of the Royal Astronomical Society*, **477**(July), 4824–4837.

Wagstaff, G., Miller Bertolami, M. M., & Weiss, A. 2020. Impact of Convective Boundary Mixing on the TP-AGB. *Monthly Notices of the Royal Astronomical Society*, **493**(Apr.), 4748–4762.

Wagstaff, Graham. 2018 (Jan.). *Convective and Atmospheric Boundaries of Asymptotic Giant Branch Stars*. Ph.D. thesis, Ludwig-Maximilians-Universitaet Muenchen.

Wallerstein, George, Iben, Jr., Icko, Parker, Peter, Boesgaard, Ann Merchant, Hale, Gerald M., Champagne, Arthur E., Barnes, Charles A., Käppeler, Franz, Smith, Verne V., Hoffman, Robert D., Timmes, Frank X., Sneden, Chris, Boyd, Richard N., Meyer, Bradley S., & Lambert, David L. 1997. Synthesis of the Elements in Stars: Forty Years of Progress. *Reviews of Modern Physics*, **69**(Oct.), 995–1084.

Weigert, A. 1966. Sternentwicklung VI: Entwicklung Mit Neutrinoverlusten Und Thermische Pulse Der Helium-Schalenquelle Bei Einem Stern von 5 Sonnenmassen. *Zeitschrift fur Astrophysik*, **64**(Jan.), 395.

Weiss, A., & Ferguson, J. W. 2009. New Asymptotic Giant Branch Models for a Range of Metallicities. *Astronomy and Astrophysics*, **508**(Dec.), 1343–1358.

Weiss, A., Hillebrandt, W., Thomas, H. C., & Ritter, H. 2004. *Cox and Giuli's Principles of Stellar Structure*. Cambridge Scientific Publishers Ltd.

Weiss, Achim, & Schlattl, Helmut. 2008. GARSTEC—the Garching Stellar Evolution Code. The Direct Descendant of the Legendary Kippenhahn Code. *Astrophysics and Space Science*, **316**(1-4), 99–106.

Werner, Klaus, & Herwig, Falk. 2006. The Elemental Abundances in Bare Planetary Nebula Central Stars and the Shell Burning in AGB Stars. *Publications of the Astronomical Society of the Pacific*, **118**(Feb.), 183–204.

Werner, Klaus, Todt, Helge, Bond, Howard E., & Zeimann, Gregory R. 2024. Spectroscopic Survey of Faint Planetary-Nebula Nuclei. III. A [WC] Central Star and Two New PG1159 Nuclei. *Astronomy and Astrophysics*, **686**(June), A29.

Wollaston, William Hyde. 1802. XII. A Method of Examining Refractive and Dispersive Powers, by Prismatic Reflection. *Philosophical Transactions of the Royal Society of London*, 365–380.

Xu, Y., Takahashi, K., Goriely, S., Arnould, M., Ohta, M., & Utsunomiya, H. 2013. NACRE II: An Update of the NACRE Compilation of Charged-Particle-Induced Thermonuclear Reaction Rates for Nuclei with Mass Number A<16. *Nuclear Physics A*, **918**(Nov.), 61–169.

Yagüe López, A., García-Hernández, D. A., Ventura, P., Doherty, C. L., den Hartogh, J. W., Jones, S. W., & Lugaro, M. 2022. First Models of the s Process in AGB Stars of Solar Metallicity for the Stellar Evolutionary Code ATON with a Novel Stable Explicit Numerical Solver. *Astronomy & Astrophysics, Volume 657, id.A28, 18 pp.*, **657**(Jan.), A28.

Zhang, L., Karlsson, T., Christlieb, N., Korn, A. J., Barklem, P. S., & Zhao, G. 2011. The Hamburg/ESO R-process Enhanced Star Survey (HERES). VI. The Galactic Chemical Evolution of Silicon. *Astronomy and Astrophysics*, **528**(Apr.), A92.

Zinner, Ernst, Nittler, Larry R., Gallino, Roberto, Karakas, Amanda I., Lugaro, Maria, Straniero, Oscar, & Lattanzio, John C. 2006. Silicon and Carbon Isotopic Ratios in AGB Stars: SiC Grain Data, Models, and the Galactic Evolution of the Si Isotopes. *The Astrophysical Journal*, **650**(Oct.), 350–373.

Acknowledgements

First and foremost, I would like to thank my wife, without whom I would not have survived the final months of my PhD. I would also like to especially thank my supervisor, Achim Weiss, for his years of supervision, hundereds of group meetings, and many helpful comments. Also, for allowing me the freedom to follow my own interests during the PhD.

There are many other people whom I would like to thank for their support over the course of my PhD:

> Tiara Battich, not only for the use of her post-processing code, but also for the helpful discussions which seeded a number of ideas found in this manuscript.
>
> Teresa Braun, whose careful reading of this manuscript greatly improved its quality.
>
> Maria Lugaro, Lionel Siess, and Arthur Choplin for graciously hosting me for visits and for the fruitful discussions
>
> The secretaries of MPA, in particular Gabi Kratschmann, for her help in dealing with the German bureaucracy.
>
> My friends both inside and outside the institute.

Finally, I would like to thank my parents who have always supported me.